The University Of Sheffield.

Department of Materials Science and Engineering

Investigation of Resistive Switching phenomenon in acceptor-doped oxides: Ca-doped $BiFeO_3$ and Y-doped CeO_2

Submitted for the Degree of Doctor of Philosophy

Fawaz Kahlid Almutairi

Supervisor:Prof. Anthony R. West

April 2023

Dedication

To The Glory of God

To my wife 'Alhanouf'
Who never let me down and always supported me

During this work, I have also involved research, ideas and discussions on resistive switching in Y-doped hafnia and this work was published:

- *Alotaibi, M., F. Almutairi, and A.R. West, Resistive-switching in yttria-stabilized hafnia ceramics. Journal of the American Ceramic Society, 2022. 106(2): p. 822-828.*

This work was part of the overall research programme but the specific results are not included in this thesis.

Acknowledgments

"In the name of Allah, the Most Gracious, the Most Merciful''
First of all, I express my humble thanks to God and then to my mother
"Shaa'a'' without whose blessings, love and prayers I cannot succeed.

I believe that I am a lucky person to has this opportunity to be supervised by prof. Antony West. I am pleased to work with a knowledgeable man like him, just working with him was motivating me to do my best. His words, guidance and treatment helped me to overcome studying in foreign country difficulties. I would like to say to him 'thank you, you have changed me to the best'.

I would like to thank and show my gratitude to all Functional Materials and Device Group members for their help, training and making our life in laboratories easier.

Many thanks to all my friends and colleagues who are too many to be named individually for their help, support in my difficult times 'illness' and discussions which assisted me to finish this journey.

Especial thanks to my uncle 'Saad' for everything your encourage, and especially financial support was a good supporter for me 'you are a father for me'.

I will never forget to thank my life brightness and happiness 'my family', my wife (Alhanouf), my little boys (Khalid and Nahar), my brothers and sisters without their loves and support, it would not be possible achieve this moment 'you are the source of my happiness in my life'.

Finally, I would like to thank the Saudi Government, Imam University, the Royal Embassy, Saudi Cultural Bureau and Ministry of Higher Education for my scholarship and for supporting my study.

Abstract

The effect of application of a small voltage, above the theoretical decomposition voltage, to inorganic materials has become increasingly important in the development of two new emerging areas, resistive switching of memristors and flash sintering of ceramics. Recently, many examples, in bulk, of acceptor-doped fluorite- and perovskite-structured materials show increasing p-type conductivity with increasing voltage. Among these materials, perovskite-structured Ca-doped $BiFeO_3$ showed a dramatic increase in conductivity on application of a small dc bias, and was reversible on removal of the bias. It was the first example of low field resistive switching, OFF-ON, of bulk ceramics.

Fluorite-structured, Y-doped HfO_2 is the second material to show low field resistive switching in bulk. Oxygen exchange between the sample and surrounding atmosphere plays an important role in the switching mechanism. It is attributed to break down of p-i-n junction in which at low field, underbonded oxygen ions undergo single ionisation creating holes on those oxygens at the positive electrode and at higher voltage oxygen ions undergo double ionisation liberating oxygen molecules at the positive electrode and ionised electrons are re-injected at the negative electrode creating an n-type region.

This thesis investigates resistive switching behaviour in Ca-doped $BiFeO_3$, with the aim of understanding the switching mechanism and whether any of the induced p- and n-type behaviour occurs at different or both electrodes and which dominates the sample conductivity during switching. Also, it investigates possible low field resistive switching in another acceptor-doped ceramic, Y-doped CeO_2.

The materials were synthesised by solid state reaction and characterised using x-ray diffraction. The effect of application of a small dc bias on the electrical properties were analysed using impedance spectroscopy as function of different variables such as temperature and pO_2.

Since the electrical properties of Ca-doped $BiFeO_3$ were sensitive to pO_2 during synthesis, three sets of samples, $Bi_{1-x}Ca_xFeO_{3-x/2}$ (where: x =0.23, 0.3 and 0.4) were processed in N_2, air and O_2. The conductivities increased by a few orders of magnitude and the properties changed from mainly oxide ion conductors to p-type semiconductors with increasing pO_2. Circuit fitting was carried out in order to identify electrical microstructure of differently processed samples.

On application of a small dc bias, Ca-doped $BiFeO_3$ samples processed in different atmospheres reversibly switch their resistances, ON-OFF, by 2-5 orders of magnitude with some hysteresis, on removal of the dc bias. This was attributed to a dramatic increase in hole

concentration by internal ionisation of redox active elements, which are believed to be underbonded oxygen ions, and trapping of electrons.

Fluorite-structured, $Ce_{0.84}Y_{0.16}O_{1.92}$ showed mixed n-type and oxide ion conductivity in which oxide-ion conductivity attributed to oxygen vacancies introduced to maintain charge neutrality as a result of lower valence doping, Y^{3+}. The n-type conductivity was attributed to the presence of a transition metal that can easily be reduced, Ce^{4+} to Ce^{3+}. On application of a dc bias, the sample conductivity increased by about two orders of magnitude and was reversible, with hysteresis, on removal of the bias. The increase in conductivity was attributed to an increase in the concentration of n-type carriers as result of oxygen loss. $Ce_{0.84}Y_{0.16}O_{1.92}$ is the third example to show this kind of low field resistive switching, OFF-ON, in bulk ceramics.

$Bi_{0.77}Ca_{0.23}FeO_3$ interestingly showed flash electroluminescence, due to electron-hole recombination, under certain conditions after switching the sample to the highly conductive, ON state. The flash mechanism was sensitive to the level of p-type conductivity and when the sample loses its p-type conductivity by heat treatment close to the sintering temperature (~945 °C) or in low pO_2 just below the sintering temperature, the luminescence effect was suppressed.

Contents

Chapter 1 : Introduction and thesis aims

1.1. Introduction

The effect of a small applied voltage on the electrical properties of materials is not a traditional area of research in the physics and chemistry of solids, but in the last few years has become increasingly of interest in a number of emerging areas.

Memristors [1, 2] are thin film devices in which, after an initial electro-forming treatment, it is possible to switch film resistance between low- and high-resistance, or 'ON' and 'OFF'states, by application of a small bias voltage. Several mechanisms may be involved and although the effect is usually reversible and reproducible, it is not well-understood. The effect has potential memory applications.

In flash sintering of ceramics [3-6], a voltage is applied to a sample that is being heated and, at some temperature, a very rapid increase in temperature commences, the sample luminesces and densification occurs within a few seconds. This is becoming of interest as a new, rapid, low cost method for sintering ceramics but still, the mechanism is not well-understood and the process is not optimised.

In new, high capacity battery cathodes, it is now realised that in addition to the usual redox-active transition elements such as Mn, Fe, Co and Ni, in certain circumstances the oxygen anion may also be redox-active [7]. The effect of an applied voltage is to cause ionisation of some of the lattice oxide ions, as well as the transition metal ion components. There is much interest in understanding this better and using it to develop new high capacity batteries.

It is generally established in Physical chemistry that materials should decompose electrochemically when an applied voltage exceeds their theoretical decomposition voltage, which is typically a few volts. Although many examples of partial decomposition are known especially in battery systems involving (de) intercalation electrodes, the possibility of this happening more widely appears to have deterred researchers from studying the effect of voltage on the stability of materials and possible changes to their properties. Consequently, a knowledge gap was evolved concerning how materials respond to application of a bias voltage.

In research on bulk ceramics (excluding thin films) in the last few years, numerous examples have been found in which the electrical conductivity of a material changes (sometimes

decreases, sometimes increases) on application of a dc bias [8-15]. Initial interest in this effect was associated with possible voltage-induced dielectric breakdown phenomena in ceramics. The effects are usually fully reversible on removing the voltage in which case, no irreversible decomposition occurs. Sometimes, the changes occur slowly and only at high temperatures, but in Ca-doped $BiFeO_3$, the changes occur at room temperature, resistances may switch by several orders of magnitude and are reversible, with some hysteresis, on removing the bias [16].

It is now clear that, although materials should, perhaps theoretically, decompose electrochemically above a certain voltage, they usually do not do this spontaneously in practice but instead, may pass through a number of intermediate stages or processes before complete decomposition occurs. This is a relatively new area of science in which new, unexpected discoveries are possible within the physics and chemistry of solids.

1.2. Aims and objectives of thesis

The aim of this thesis is to investigate the effect of dc bias on mixed conductors of acceptor-doped ceramics and especially low field resistive switching reported, recently, in bulk ceramics.

The main objective was to understand the phenomenon in Ca-doped $BiFeO_3$ and the importance of mixed oxide-ion and p-type conductivity and the presence of oxygen vacancies. The electrical properties of four compositions of Ca-doped $BiFeO_3$ including undoped $BiFeO_3$ were studied using impedance spectroscopy as function of temperature, oxygen partial pressure, pO_2 and dc bias in order to:

I. repeat and extend the experiments reported in the literature and confirm the resistance switching in Ca-doped $BiFeO_3$.
II. analyse data to extract resistance and capacitance values, fit data to equivalent circuits and determine dependence of parameter values on temperature.
III. study the effects of pO_2 and dc bias on electrical properties, determine whether resistive switching occurs and under what conditions.
IV. understand the reactions that occur at the two electrode interfaces.
V. characterise the samples and their electrical properties in ‘ON’ and ‘OFF’ states.

The second objective was to investigate and discover resistive behaviour in other well-known acceptor-doped oxides such as Y-doped CeO_2 which is known to be mixed n-type and oxide-ion conductor. Therefore, the electrical properties of Y-doped CeO_2 was studied by impedance spectroscopy as function of temperature, pO_2, dc bias, and the combination of both dc bias and pO_2.

During the project progress, we have noticed that in some experiments during application of a dc bias, the decrease in conductivity was accompanied by flash luminescence under certain conditions. Such flash events are observed in flash sintering process and the mechanism behind the luminescence is still debatable whether thermoluminescence or electroluminescence. Therefore, the third objective was to investigate the origin of this flash luminescence and under what conditions is observed.

1.3. References

1. Strukov, D.B., F. Alibart, and R. Stanley Williams, *Thermophoresis/diffusion as a plausible mechanism for unipolar resistive switching in metal–oxide–metal memristors.* Applied Physics A, 2012. **107**: p. 509-518.
2. Strukov, D.B., G.S. Snider, D.R. Stewart, and R.S. Williams, *The missing memristor found.* Nature, 2008. **453**(7191): p. 80-3.
3. Biesuz, M. and V.M. Sglavo, *Flash sintering of ceramics.* Journal of the European Ceramic Society, 2019. **39**(2-3): p. 115-143.
4. Perez‐Maqueda, L.A., E. Gil‐Gonzalez, A. Perejon, J.M. Lebrun, P.E. Sanchez‐Jimenez, and R. Raj, *Flash sintering of highly insulating nanostructured phase‐pure BiFeO3.* Journal of the American Ceramic Society, 2017. **100**(8): p. 3365-3369.
5. Kok, D., S.K. Jha, R. Raj, and M.L. Mecartney, *Flash sintering of a three‐phase alumina, spinel, and yttria‐stabilized zirconia composite.* Journal of the American Ceramic Society, 2017. **100**(7): p. 3262-3268.
6. Yu, M., S. Grasso, R. Mckinnon, T. Saunders, and M.J. Reece, *Review of flash sintering: materials, mechanisms and modelling.* Advances in Applied Ceramics, 2017. **116**(1): p. 24-60.
7. Rong, X., E. Hu, Y. Lu, F. Meng, C. Zhao, X. Wang, Q. Zhang, X. Yu, L. Gu, and Y.-S. Hu, *Anionic redox reaction-induced high-capacity and low-strain cathode with suppressed phase transition.* Joule, 2019. **3**(2): p. 503-517.
8. Prades, M., N. Masó, H. Beltrán, E. Cordoncillo, and A.R. West, *Field enhanced bulk conductivity of BaTiO3 : Mg ceramics.* Journal of Materials Chemistry, 2010. **20**(25): p. 5335.
9. Zhang, Q.-L., N. Masó, Y. Liu, H. Yang, and A.R. West, *Voltage-dependent low-field resistivity of CaTiO3:Zn ceramics.* Journal of Materials Chemistry, 2011. **21**(34): p. 12894.

10. Liu, Y. and A.R. West, *Voltage-dependent resistance of undoped rutile, TiO2, ceramics.* Applied Physics Letters, 2013. **103**(26): p. 263508.
11. Alotaibi, M., F. Almutairi, and A.R. West, *Resistive ‐ switching in yttria ‐ stabilized hafnia ceramics.* Journal of the American Ceramic Society, 2022. **106**(2): p. 822-828.
12. Vendrell, X. and A.R. West, *Induced p ‐ type semiconductivity in yttria ‐ stabilized zirconia.* Journal of the American Ceramic Society, 2019. **102**(10): p. 6100-6106.
13. Jovani, M., H. Beltran-Mir, E. Cordoncillo, and A.R. West, *Atmosphere- and Voltage-Dependent Electronic Conductivity of Oxide-Ion-Conducting Zr(1-x)Y(x)O(2-x/2) Ceramics.* Inorg Chem, 2017. **56**(12): p. 7081-7088.
14. Masó, N. and A.R. West, *Electronic conductivity in yttria-stabilized zirconia under a small dc bias.* Chemistry of Materials, 2015. **27**(5): p. 1552-1558.
15. Gil Escrig, L., M. Prades, H. Beltrán, E. Cordoncillo, N. Masó, and A.R. West, *Voltage ‐ Dependent Bulk Resistivity of SrTiO 3: Mg Ceramics.* Journal of the American Ceramic Society, 2014. **97**(9): p. 2815-2824.
16. Masó, N., H. Beltrán, M. Prades, E. Cordoncillo, and A.R. West, *Field-enhanced bulk conductivity and resistive-switching in Ca-doped BiFeO 3 ceramics.* Physical Chemistry Chemical Physics, 2014. **16**(36): p. 19408-19416.

1. Strukov, D.B., F. Alibart, and R. Stanley Williams, *Thermophoresis/diffusion as a plausible mechanism for unipolar resistive switching in metal–oxide–metal memristors.* Applied Physics A, 2012. **107**: p. 509-518.
2. Strukov, D.B., G.S. Snider, D.R. Stewart, and R.S. Williams, *The missing memristor found.* Nature, 2008. **453**(7191): p. 80-3.
3. Biesuz, M. and V.M. Sglavo, *Flash sintering of ceramics.* Journal of the European Ceramic Society, 2019. **39**(2-3): p. 115-143.
4. Perez-Maqueda, L.A., E. Gil-Gonzalez, A. Perejon, J.M. Lebrun, P.E. Sanchez-Jimenez, and R. Raj, *Flash sintering of highly insulating nanostructured phase-pure BiFeO3.* Journal of the American Ceramic Society, 2017. **100**(8): p. 3365-3369.
5. Kok, D., S.K. Jha, R. Raj, and M.L. Mecartney, *Flash sintering of a three-phase alumina, spinel, and yttria-stabilized zirconia composite.* Journal of the American Ceramic Society, 2017. **100**(7): p. 3262-3268.
6. Yu, M., S. Grasso, R. Mckinnon, T. Saunders, and M.J. Reece, *Review of flash sintering: materials, mechanisms and modelling.* Advances in Applied Ceramics, 2017. **116**(1): p. 24-60.
7. Rong, X., E. Hu, Y. Lu, F. Meng, C. Zhao, X. Wang, Q. Zhang, X. Yu, L. Gu, and Y.-S. Hu, *Anionic redox reaction-induced high-capacity and low-strain cathode with suppressed phase transition.* Joule, 2019. **3**(2): p. 503-517.
8. Prades, M., N. Masó, H. Beltrán, E. Cordoncillo, and A.R. West, *Field enhanced bulk conductivity of BaTiO3 : Mg ceramics.* Journal of Materials Chemistry, 2010. **20**(25): p. 5335.
9. Zhang, Q.-L., N. Masó, Y. Liu, H. Yang, and A.R. West, *Voltage-dependent low-field resistivity of CaTiO3:Zn ceramics.* Journal of Materials Chemistry, 2011. **21**(34): p. 12894.

10. Liu, Y. and A.R. West, *Voltage-dependent resistance of undoped rutile, TiO2, ceramics.* Applied Physics Letters, 2013. **103**(26): p. 263508.
11. Alotaibi, M., F. Almutairi, and A.R. West, *Resistive-switching in yttria-stabilized hafnia ceramics.* Journal of the American Ceramic Society, 2022. **106**(2): p. 822-828.
12. Vendrell, X. and A.R. West, *Induced p-type semiconductivity in yttria-stabilized zirconia.* Journal of the American Ceramic Society, 2019. **102**(10): p. 6100-6106.
13. Jovani, M., H. Beltran-Mir, E. Cordoncillo, and A.R. West, *Atmosphere- and Voltage-Dependent Electronic Conductivity of Oxide-Ion-Conducting Zr(1-x)Y(x)O(2-x/2) Ceramics.* Inorg Chem, 2017. **56**(12): p. 7081-7088.
14. Masó, N. and A.R. West, *Electronic conductivity in yttria-stabilized zirconia under a small dc bias.* Chemistry of Materials, 2015. **27**(5): p. 1552-1558.
15. Gil Escrig, L., M. Prades, H. Beltrán, E. Cordoncillo, N. Masó, and A.R. West, *Voltage-Dependent Bulk Resistivity of SrTiO 3: Mg Ceramics.* Journal of the American Ceramic Society, 2014. **97**(9): p. 2815-2824.
16. Masó, N., H. Beltrán, M. Prades, E. Cordoncillo, and A.R. West, *Field-enhanced bulk conductivity and resistive-switching in Ca-doped BiFeO 3 ceramics.* Physical Chemistry Chemical Physics, 2014. **16**(36): p. 19408-19416.

Chapter 2 : Literature Review

2.1. Effect of applied voltage on electrical properties of acceptor-doped oxide materials

2.1.1. Overview

Voltage-dependent conductivity has been observed in a variety of acceptor-doped materials, which change their resistivity by a few orders of magnitude upon application of a small dc bias. This change is fully reversible on removal of the voltage. This type of voltage-dependent conductivity has been observed, for example, in Ca-doped $BiFeO_3$, BCF [1], Mg-doped $BaTiO_3$ [2], $Ca(Ti_{1-x}Zn_x)O_{3-x}$ [3]. The change in conductivity occurs in some materials at high temperature and voltage while in others it happens at lower voltage and temperature or even at room temperature over a different range of timescale [1].

The voltage-dependent conductivity is not observed in undoped materials, is a bulk property, is independent of electrode materials and is not associated with a Schottky barrier [1-3]. For example, $Ba(Ti_{1-x}Mg_x)O_{3-x}$ shows an increase in conductivity by 1-2 orders of magnitude with an application of small dc bias (1 – 50 V/cm) and at temperatures between 200 and 600 °C. The magnitude of change in conductivity and the time to reach the steady state are dependent on the temperature and the magnitude of applied voltage [2].

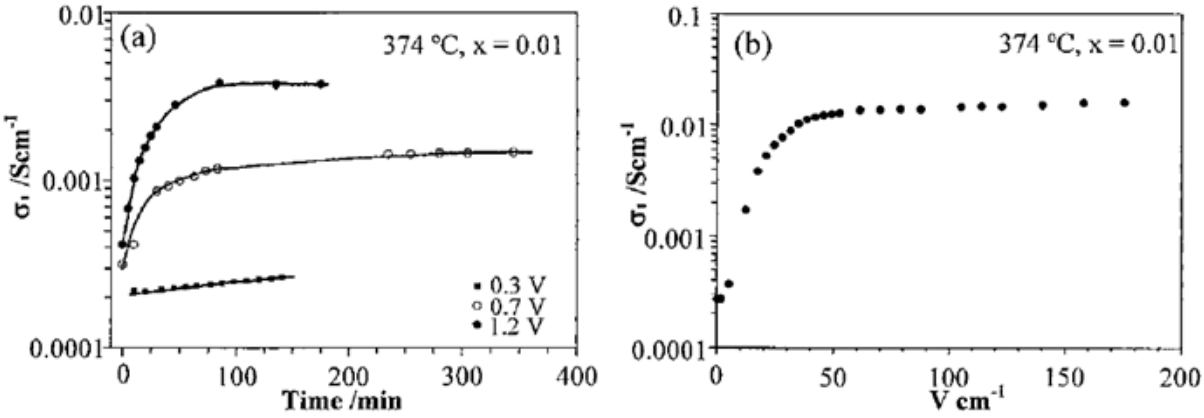

Figure 2.1. a) The bulk conductivity Mg-doped $BaTiO_3$ as fuction of time with application of 0.3, 0.7 and 1.2 V. b) The bulk conductivy as function of applied voltage at 374 °C [2].

Another material that shows bias-conductivity dependent is acceptor-doped $CaTiO_3$ which is not, unlike BFO and BT, ferroelectric indicating that this effect is not related to ferroelectricity [3]. Also, recently, West et al [4] and Maso et al [5] have observed voltage-dependent electronic conductivity in $Ba_{1-x}Sr_xTiO_{3-\delta}$ and $Zr_{1-x}Y_xO_{2-x/2}$ ceramics, respectively.

2.1.2. Source of induced p-type conductivity

The mechanism is estimated to be similar in the reported materials but differs in nature from material to material. The p-type conductivity is commonly observed in acceptor-doped oxides [1-11]. The p-type conductivity in these materials is thermally-activated which means that the holes are located on specific atoms. Since there is no presence of cations that can be readily ionised in most of relevant materials, the holes are traditionally assumed to be located on avoidable impurities such as Fe^{3+}. However, since no similar voltage-dependent conductivity observed in undoped materials and the accumulations studies of p-type conductivity on high purity of acceptor-doped materials, it is believed that the holes are located on underbonded oxygen (i.e. O^{2-} ions that are surrounded by effective charge less than 2+).

A general observation in those studies [1, 4, 6-10, 12-15] that also supports the hole locations being associated with underbonded oxygen is the increase of p-type conductivity with increasing pO_2 in acceptor-doped materials. Oxygen molecules, O_2 dissociate and react with underbonded oxygen, O_o^x to give O^- ions that absorbed by oxygen vacancies according to the following reaction:

$$V_O^{\bullet\bullet} + \frac{1}{2}O_2 + O_O^x \rightarrow 2O_o^{\bullet} \qquad (2.1)$$

Therefore, underbonded oxygen and absorbed O^- ions become the sources of holes.

2.1.3. Mixed electronic and oxide-ion conductivity

As result of doping with lower valence cations, oxygen vacancies are created to provide charge balance in the lattice. They play an important role in observed mixed oxide-ion and electronic conductivity in which sometimes the p-type conductivity dominates the material electrical properties and under certain conditions the material may become mainly an oxide ion conductor and. For example, Ca-doped $BiFeO_3$ [15] is mainly oxide-ion conductor when processed in low pO_2 atmosphere but the p-type conductivity greatly exceeds the oxide-ion conductivity when processed in high pO_2 atmospheres, as discussed later in more details.

Furthermore, n-type conductivity may be observed in ceramics due to oxygen loss (eq 2.2) especially at low pO_2, when materials are donor-doped or in acceptor-doped materials in presence of a cation that can be easily reduced such as Gd-doped ceria [16]. The n-type

conductivity is an important component in two new phenomena, resistive switching and flash luminescence.

$$O_O^x \rightarrow \frac{1}{2} O_2 + V_O^{\bullet\bullet} + 2e' \quad (2.2)$$

2.1.4. Voltage-dependent conductivity mechanism

The voltage-dependent conductivity arises due to electron attraction form the sample interior to react with different oxygen species at the sample surface [8]. Various equilibria may be present at the surface of oxide:

$$O_2(g) \leftrightarrow O_2(ads) \leftrightarrow O_2^- \leftrightarrow O_2^{2-} / O^- \leftrightarrow O^{2-}(surface) \leftrightarrow O^{2-}(bulk) \quad (2.3)$$

The sources of electrons, for n-type materials, is free electrons that are already present while, for p-type materials, it is electrons that result from an ionisation reaction e.g. ionisation of underbonded oxygen:

$$O^{2-} \rightarrow O^- + e^- \quad (2.4)$$

Since electrons are the charge carriers in an n-type material, on application of dc bias, electrons are driven from the sample interior and trapped at the sample-anode interface by forming superoxide or peroxide ions (eq 2.3). Thus, the charge carrier concentration is decreased (eq 2.5) resulting in a reduction of the conductivity [5, 17].

$$O_2 + 4e^- \rightarrow 2O^{2-} \quad (2.5)$$

Since holes are the charge carriers in p-type materials, on application of dc bias, electrons, and the associated holes, are generated by an ionisation process. Again the ionised electrons are attracted to the anode forming ionised oxygen species at the surface as indicated in (eq 2.3), and the created holes remain on oxygen as lattice O^- ions. As a result of the hole creation, the concentration of charge carries increases (eq 2.6) leading to increase p-type conductivity.

$$O_2 \rightarrow 2O^{2-} + 4h^+ \quad (2.6)$$

Alternatively, on application of dc bias, the ionised electron may be trapped at the positive electrode similar to the charging of a capacitor. The third possibility is that electrons may diffuse through the external circuit and be re-injected at the cathode especially in the case of double ionisations of oxide ions which are liberated at the anode according to the following reaction:

$$O_O^x \rightarrow \frac{1}{2} O_2 + V_O^{\bullet\bullet} + 2e' \quad (2.7)$$

Such an effect was observed in yttria-stabilised zirconia [12], YSZ and yttria-sabilised hafnia [18], YSH on application of high dc bias in which the samples start to lose oxygen at one electrode, reaction (2.7) and electrons are re-injected at the other electrode leading to n-type conductivity domination after sufficient time.

2.1.5. Low field resistive switching in bulk ceramics

The induced p-type conductivity has been observed in many acceptor-doped materials such as those mentioned above. Among those materials, BCF [1] and YSH [18] showed remarkably enhanced conductivity on application of a small dc bias. They showed low field bulk resistive switching (RS), ON-OFF in which the sample resistances change reversibly by few orders of magnitude.

At low field, YSH exhibits a small increase in p-type conductivity as a result of hole creation on underbonded oxygen, reaction (2.4) and at high field n-type conductivity is induced due to oxygen loss, reaction (2.7), and electron re-injection, as discussed above. Therefore, an n-i-p junction is created in the sample interior. As the voltage is increased, especially in atmosphere of low pO_2, the sample loses more oxygen leading to injection of more electrons and increase of n-type region initiating the breakdown of the n-i-p junction. Therefore, the conductivity is increased by several orders of magnitude. The breakdown is reversible on removal of the of dc bias and therefore the sample recover its original conductivity.

BCF showed similar RS behaviour at lower temperatures but the mechanism might be different. The RS in BCF was pO_2-independent and the sample did not show any p-n transition during the switching. From the available data, the sample showed no indication of electrons injection and therefore, is probably due to the creation of a hole-conducting layer of O^- and trapping the ionised electrons at the sample anode, as discussed later.

Resistive switching phenomena have been a hot topic over the last few years especially for memristive applications. Memristors are thin film devices in which ON-OFF switching occurs due to the formation and rupturing of conducting filaments [19], for example, TiO_2, ZrO_2 and NiO. Also, RS occurs in other bulks which is associated with a phase transition such as metal-insulator transition in VO_2 and Verwey transition in magnetite [20]. The nature of RS reported

in Ca-doped BF and YSH is different from those associated with the phase transition and conduction filament formation mechanism.

2.1.6. Resistive switching phenomena

Resistive switching (RS) can be defined as a reversible change in dielectric material resistance in response to application of an external electric field which is different from irreversible dielectric breakdown. The RS is an elastic behaviour in which the material can recover and return to its original resistance. The switched state can be retained for a long time even on removal of applied field. RS phenomena have been proposed to be used in many applications, including memories, memristors, logic gate and switches [21, 22]. By far the most studied among these applications is resistive-random access memory (RRAM); so, it is the most important application using RS phenomena [21, 23]. RRAM is a promising candidate for next generation non-volatile memory due to its high density, fast write, read and erase speed, simple constituents, low power and good scalability [23]. Furthermore, this phenomenon occurs in many insulating materials such as oxides, organic materials, nitrides and chalcogenides. However, the observed resistive-switching behaviour varies from material to material. RS can be classified based on conducting path and switching behaviour.

2.1.6.1. Classification of resistive switching phenomena

RS can be classified based on the relationship between the applied voltage polarity and material resistive-switching between high resistance state (HRS) and low resistance state (LRS) into unipolar switching and bipolar switching. In these two switching types, there are two metastable states (i.e. the HRS and LRS) in which the material maintains its resistance state on removal of the applied voltage. Also, some materials exhibit resistive-switching that can involve multiple states in response to applied voltage (threshold switching) but only have one stable state on the removal of the applied voltage.

*2.1.6.1.1. **Unipolar resistive switching***

In this type of switching, resistance can be switched back and forth between LRS and HRS using the same polarity (unipolar) of applied voltage. An as-prepared material is in a HRS, however, it can be switched into LRS by applying a large external voltage ($V_{forming}$) which is called electro-forming process. Then, the resistance can be switched to HRS by applying a

smaller voltage with the same polarity (reset process, V_{Reset}), shown in Figure 2.2a. Increasing the voltage once again switches the resistance to the low state when set voltage (V_{set}) is reached (set process, $V_{reset} < V_{set} < V_{forming}$), shown in Figure 2.2a. The HRS and LRS are metastable for long periods of time on the removal of external bias [21, 22, 24]. This type of RS is also called thermo-chemical resistive switching [19]. For example, TiO_2, NiO, HfO_2, Nb_2O_5, ZnO, and ZrO_2 [19] show unipolar switching.

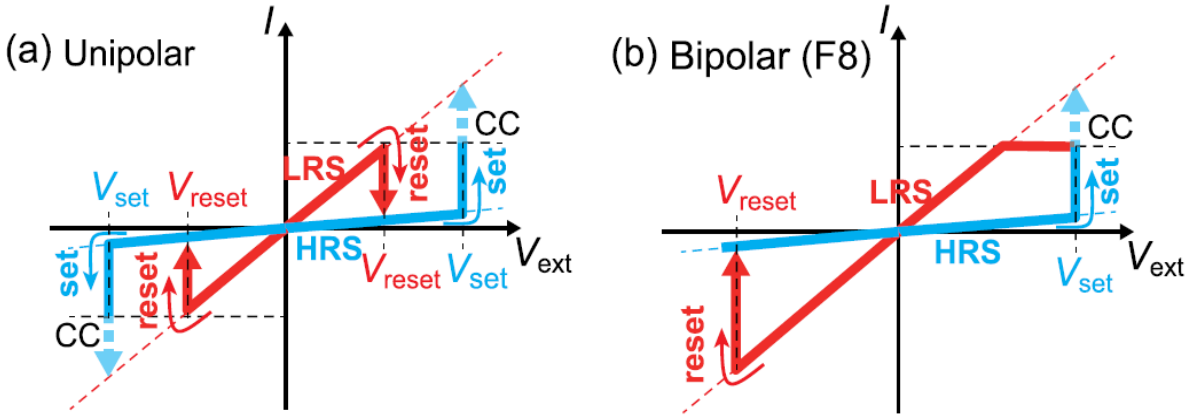

Figure 2.2. I-V curves for a) unipolar switching in which the switching direction depends on the applied voltage amplitude and is symmetric with respect to the polarity and thus the switching can occur with the same polarity, b) bipolar switching which is asymmetric with respect to the polarity and thus the set and rest processes occur with different polarities [21].

Mostly, the switching mechanism in thermo-chemical RS is related the formation and rupture of conducting filaments (CF). These CF can be described by a soft electrical breakdown. Figure 2.3 shows a schematic diagram of formation and rupturing of the CF. In the pristine state the defect density (oxygen vacancies or metal interstitials) is low in the oxide cell and the resistance is high (a). By applying an external field, the oxygen ions are thermally-assisted to migrate toward the anodic interface and that generates and percolates the defects (oxygen vacancies) inside the oxide cell; then nanoscale CFs start forming. Once any of these CFs contacts between the two electrodes the cell enters the LRS(b) [25]. By applying reset voltage, the CF become partially ruptured and the cell enters HRS (C).

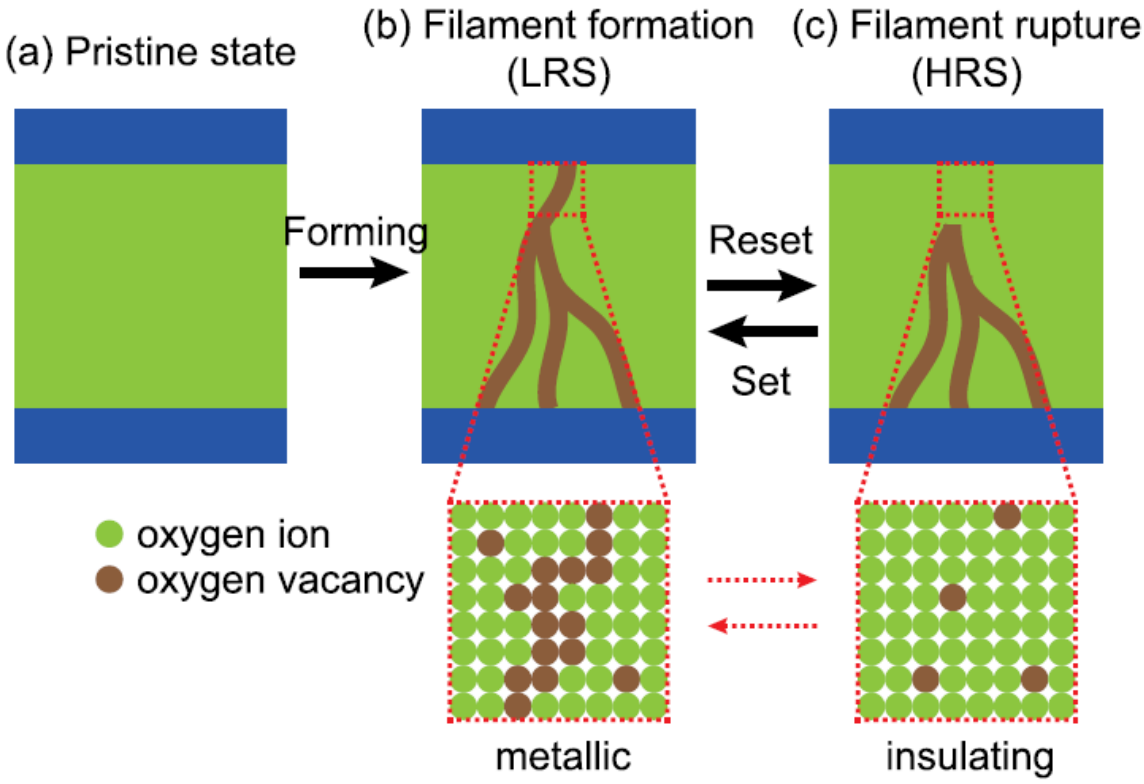

Figure 2.3. Schamatic diagram of unipolar switching mechanism: a) the pristine state befor elecreoforming process, b) the conducting filament is formed switching the cell into LRS after application of forming voltage, c) rupture of conducting filament after switching the back into HRS after of application of rest voltage [21]. The cell can siwtch back and forth between b and c by application of set and reset Voltage.

Many microscopic studies were carried out in order to understand the mechanism involved in unipolar RS [26-31]. Those studies were successfully able to demonstrate the formation and rupturing of CF during switching between the two resistance states. For example, Fujiwara et al showed the formation CF in Ni/CuO/Ni cell after the forming process using SEM (Figure 2.4 a) with resistance value about 3.3 kΩ. Then, they used a focused ion beam, FIB to cut out the filament (b). The sample resistance increased about two orders of magnitude indicating that the formed filament is responsible for the observed reduction in the resistance. Subsequently, forming voltage was applied on the cell again. The cell regained the LRS after re-forming the branch filament that connects between the two electrodes (b).

The origin of the CF and how it is formed and conducting is not well-understood. Also, it is difficult to investigate the structure of the CF by traditional microscopical techniques. The formation of the CF is attributed to local change in the structure of the oxide in which the detailed mechanism of this change varies from one material to another based on its phase diagram. For example, according to the Ti-O binary phase diagram, there are many of intermediate metallic phases known as Magneli phases (Ti_nO_{2n-1} where n is integer). During

the formation of V_O, electrons are released according to Eq. (2.1). These electrons can be captured by the neighbouring Ti^{4+} reducing it as shown below[19]:

$$Ti^{4+} + me^- \leftrightarrow T^{(4-m)+} \quad (2.8)$$

As the Ti reduction increases, the free electron population increases and therefore, the TiO_{2-x} conductivity increases. When x becomes larger, it could introduce phase change to different Magneli phases (Ti_nO_{2n-1}).

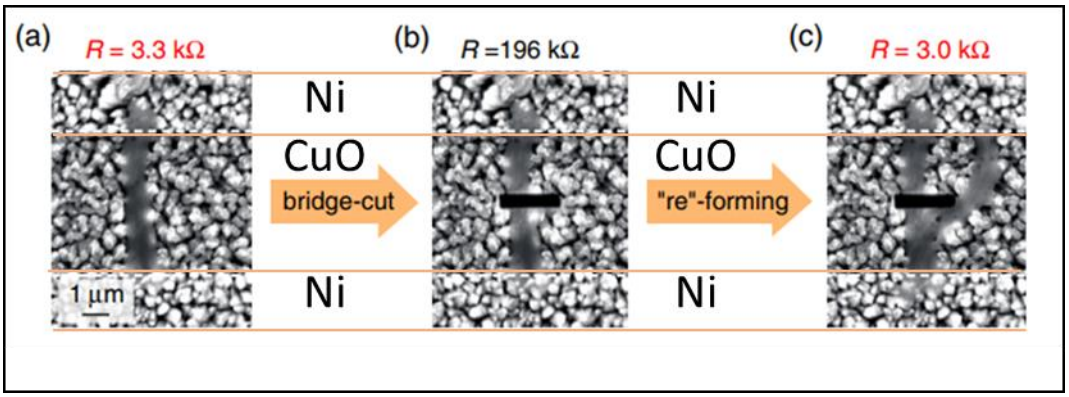

Figure 2.4. Scanning electron microscopy images for formation and cutting of filament in Ni/CuO/Ni cell after: a) applying forming voltage, b) cutting the filament off using FIB, c) applying re-forming voltage.

The mechanism of reset process or CF rupture in unipolar RS is not clear in the literature. There is an argument that attributes the rupture of CF to Joule heating that produced from the current. There is no direct evidence of such effect but indirectly, since the time of resting process is much longer than setting process time, some studies argue that the reset process is consistent with the slow thermal process [32].

Therefore, the thermal stability of CF can be effected due to the local Joule heating that produced from the current. It can raise the temperature in the CF vicinity to several hundred Kelvins (approaching the processing temperature) and results in increasing sample homogeneity by solid state diffusion [21].

It is suggested that [33] on application of an external electrical field, oxygen vacancies could be provided with sufficient thermal energy by the generated Joule heating and overcome the energy barrier for hopping. Due to the Joule heating, there are two microscopic forces which work perpendicular to the electric field: i) Soret force (dominant in forming/ set process), ii) Fick force (dominant in reset process). The temperature gradient can result in oxygen ion migration form hotter region to cooler region to minimise its energy and attract oxygen vacancies to the CF which give rise to the oxygen vacancy-rich region (Soret force). In

contrast, in the reset process, oxygen vacancies cluster and are non-uniformly distributed and concentrated in the CF. The density gradient repels them, by diffusion, to minimise the free energy by increasing the entropy term. Thus the CF become ruptured.

2.1.6.1.2. ***Bipolar RS***

In this type of switching, the RS shows polarity dependence in which switching into LRS (HRS) occurs at a positive voltage, then the switching into HRS (LRS) will occur at a negative voltage (Figure 2.2b). The polarity dependence indicates that charged species are involved in switching mechanism. Oxygen vacancies and electrons are assumed to be the most important species that play a role in bipolar switching mechanism. In most bipolar switching an electroforming process is required and is similar to the CF formation in unipolar switching. However, the cell switches between HRS and LRS by changing the polarity of applied voltage. Also, this type of switching can be achieved by modifying Schottky barrier width using the dependence of oxygen vacancy migration on the applied voltage polarity [19, 21, 34]. There are different materials which exhibit bipolar switching such as TiO_2/TiO_{2-x}, Cr_2O_3 [34], $BiFeO_3$ (thin film) [35], $Pr_{1-x}Ca_xMnO_3$ [36] and Cr-doped $SrZrO_3$ [21].

2.1.6.1.2.1 Schottky barrier effects

A Schottky barrier is a potential barrier that arises from charge transfer when a metal and a semiconductor become in contact. The formation of the barrier is due to the difference in work function, which is the required energy to transfer an electron from the Fermi level to vacuum level, between the metal and semiconductor [37]. This phenomenon is utilised in different applications such as photocatalysis, photovoltaics, memristors and gas sensors [38].

When a metal and a semiconductor become in non-ohmic contact due to the difference in their Fermi energy (E_f), electrons spill over from the substance that has higher E_f. These electrons build up charge on one side of the interface leaving behind positive charge on the other side creating a charged capacitor. Consequently, a barrier height is generated (i.e. space charge separation produces the barrier height) that is sensitive to a dc bias. The dc bias can modify the barrier height and reduce its resistance.

Another consequence of charge build-up is the formation of a depletion layer. For example, electrons may spill over from the semiconductor surface to the metal resulting in formation of

an electron-deficient depletion layer with resistivity higher than that of the material interior [39].

Various materials exhibit bipolar resistive switching as a consequence of modification of Schottky barrier height. Rubi et al reported bipolar resistive switching in $Bi_{0.9}Ca_{0.1}FeO_3$ by modifying the Schottky barrier height [40]. They argued that the application of an electrical pulse changes the V_O concentration near the metal-sample interface and therefore changes its resistivity. On application of a negative voltage, the oxygen vacancies are attracted toward the electrode-sample interface resulting in reduced Schottky potential barrier and a low resistance state, and vice versa in case of application of positive voltage. Further investigations have been done by Rubi et al [41] in order to confirm whether this resistive switching is related to metal-semiconductor mismatch or not. They varied the electrode from Ag to Ti and Al and they did not observe RS when Ti and Al were used as electrode.

2.1.6.1.3. ***Threshold RS***

In this type of switching, there is one stable state (HRS) without application of external bias. The materials switch their resistance into LRS after applying a set voltage which is stable only under this applied voltage (V_{set}); when the applied voltage falls below V_{set} the resistance recovers to its original state (HRS) [25].

RS that has been reported in different materials such as acceptor-doped $ATiO_3$ (where A = Ba, Ca, Sr) and Ca-doped $BiFeO_3$ [14, 42, 43] is most likely a type of threshold RS. It is different from those reported in unipolar and bipolar switching that required a rest voltage with the same/ different polarity to switch back to HRS. Also, it shows only one stable state in the absence of the applied bias, while RS associated with formation and rupturing of conduction filaments shows two or multiple stable states.

The mechanism behind threshold switching is not well understood but is clearly different from filamentary. It is clearly electronic in origin, and probably does not involve any structural change like those associated with CF formation.

2.2. Bismuth Ferrite ($BiFeO_3$)

Bismuth ferrite, BF is currently attracting considerable attention due to its multiferroic properties, which can be utilised in various applications such as spintronics, data storage and microelectronic devices [44]. It shows both ferroelectricity below the Curie temperature (1100 K) and G-type anti-ferromagnetism below the Neel temperature (640 K). However, these useful properties are not usually present in perovskite-structureed simultaneously. Multiferroic mechanisms can arise in a perovskite structure when the A-site is occupied by a polar cation such as Bi^{3+} and a magnetic cation is present in the B-site. The main reason for the ferroelectricity is the off-centre displacement of A-cation due to the lone pair effect. In $BiFeO_3$ (BFO) the outer electrons $6s^2$ in Bi^{3+} are not participants in chemical bonds which causes the lone pairs to distort the structure. As result of this distortion, Bi^{3+} ions displace off their centro-symmetric positions giving rise to the ferroelectricity in BF [45]. The ferromagnetism is due to long-range magnetic order that is caused by coupling of magnetic cation spins [45]. The magnetic moments of Fe^{3+} are G-type AFM which means each spin is surrounded by another six antiparallel spins. However, small canted moments exist due to imperfection in the anti-parallel spin arrangement[46, 47].

2.2.1. Crystal structure of BF

Bulk BF has a rhombohedral distorted perovskite structure with space group R3c at room temperature with lattice parameter a = 5.64 Å and rhombohedral angle about 59º, where Bi^{3+} occupies cubo-octahedral sites in a perovskite structure while the Fe^{3+} ions occupy octahedra (FeO_6) (Figure 2.5 a & b). It also can be described in a hexagonal setting with lattice parameters a = 5.53 Å and c = 13.90 Å (Figure 2.5 c) [46]. The tolerance factor for BF was calculated using Shannon ionic radii [47] to be 0.97 [48]. Since the tolerance factor of BF is less than one, Bi^{3+} is too small to fit A-site and therefore, the oxygen octahedra tilt to reduce A cation. The FeO_6 octahedra rotate antiphase around the rhombohedral (Glazer notation $a^- a^- a^-$) $[111]_c$ direction [46, 47].

Haumont et al investigated the ferroelectric phase transition in BF and reported that BF undergoes a phase transition from ferroelectric rhombohedral to cubic paraelectric at T_c (825 ℃) [49]. However, Palai et al reported that, in their phase diagram study of BF based on results obtained using differential thermal analysis, high temperature and polarized Raman spectroscopy and other methods, there are three solid phases between RT temperature and the melting point (961 ℃) [50]. They reported that, below T_c, the structure of BF is rhombohedral

(α-phase) and it undergoes a phase transition from the ferroelectric α-phase to paraelectric β-phase just above T_c (orthorhombic phase) and it changes to the cubic γ-phase between (925-933) ℃ before decomposition (Figure 2.6). This study is consistent with a recent study that shows the ferroelectric- paraelectric phase transition was from rhombohedral (space group R3c) to orthorhombic (space group Pbnm) between 820 ℃ and 830 ℃ using variable temperature powder neutron diffraction[44].

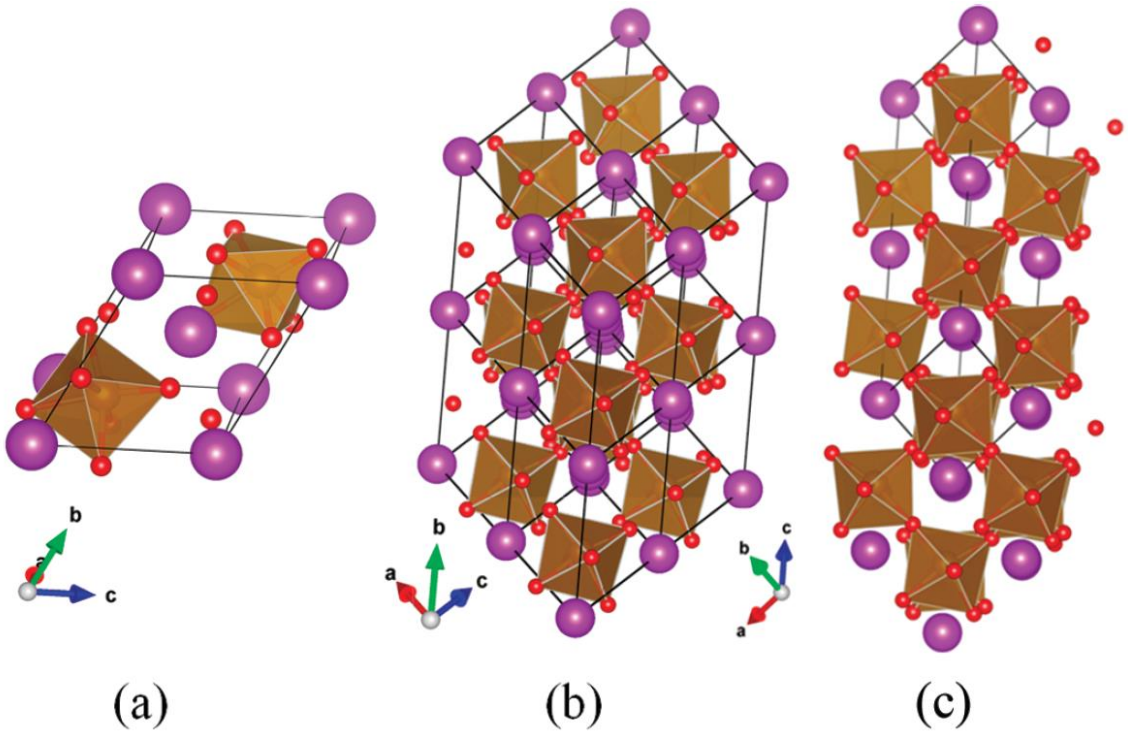

Figure 2.5. Schematic diagram of BF in different settings: a) a single rhombohedral unit cell, b) multiple unit cells in rhombohedral setting, c) hexagonal setting, where the red spheres represent oxygen, purple spheres represent the Bi ions and brown squares represent the FeO_6 octahedra [46]

2.2.2. Functional properties of BF

There is clear disagreement in the literature regarding the electrical properties of BF which is mostly found to be a semiconductor with low resistivity [51]. It is well known that bismuth ferrite is both ferroelectric and antiferromagnetic at RT. BF shows ferroelectricity below Curie temperature about 830 ℃. However, the small value of polarisation of single crystal BFO, 6 μC/ cm^2 and the lack of saturation polarisation even at low temperature were reported by [52]. Theoretically, BF shows large spontaneous polarisation as a result of large cation displacement [53]. The spontaneous polarisation of high quality thin films was consistent with this theoretical calculation but this was attributed to the effect of the substrate strain enhancement. Recently, Shvartsman et al reported that the spontaneous polarisation of bulk BF was

intrinsically high and is consistent with theoretical calculations which was about 75-80 μC/ cm^2 [54].

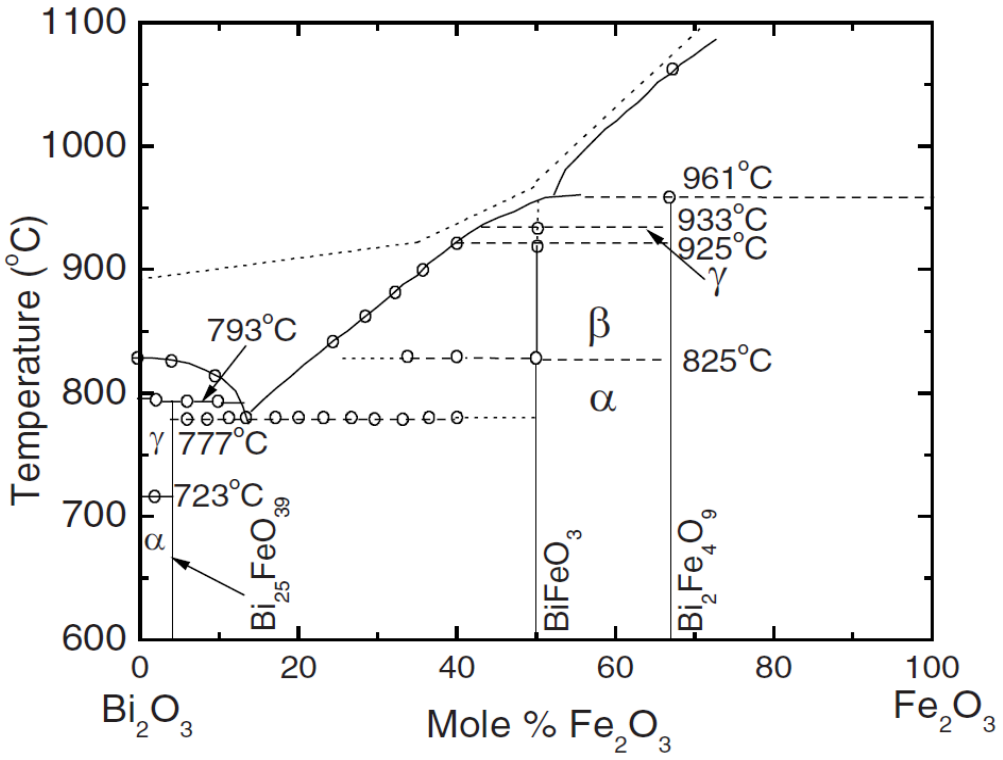

Figure 2.6. Phase diagram of Bi_2O_3 – Fe_2O_3 system. Open circles show the data points obtained by DTA. The dotted line above the liquidus represents the approximate temperature limit not to be surpassed for avoiding decomposition. The α, β and γ phases are rhombohedral, orthorhombic, and cubic, respectively. [50]

In most of the literature, the absence of the saturation of P-E loops is reported and this is attributed to the electrical breakdown of processed samples at fields less than the coercive field. Moreover, the obtained low remanent polarisation in most previous studies resulted from high leakage current [46]. The difficulty in preparation of phase-pure BF is the main reason for low resistivity of these samples and therefore the leakage. Another reason suggested for the high conductivity is associated with the volatile nature of Bi beyond 810 °C which leads to oxygen vacancies and reduction of Fe^{3+} to Fe^{2+} during synthesis. Consequently, less desirable properties are raised such as leakage current [46]. In contrast, a good quality single crystal of BF has been reported which shows high resistivity at room temperature of about 10^{16} S/cm as well as high quality of phase pure BF ceramics [51].

2.2.3. Problems with BF

The difficulty in fabrication of phase-pure BF and appearance of secondary phases such as $Bi_2Fe_4O_9$ or $Bi_{25}FeO_{39}$, may be a result of the small stabilised area of BF on the phase diagram (Figure 2.6). Bismuth volatilisation and cation deficiency, are the major problems that hinder

BF from being used in commercial applications. The presence of these impurity phases and Bi volatilisation would cause the high conductivity in BF mentioned above and clearly is the main reason for significant disagreements in the literature. BF based ceramics also suffer from low remanent polarisation and weak magnetoelectric coupling [46]. Many authors have tried different techniques to avoid the formation of secondary phase and improve BF properties by varying the processing methods or doping on both A and B sites (discussed in the next section).

Different synthesis methods have been used in order to prepare single phase BF. Some of these processes, such as mechanosynthesis [51], sol-gel method [55] and high pressure annealing synthesis [56], have successfully made phase pure BF. Another technique used to prepare single phase BF is by leaching secondary phase with nitric acid [57].

2.2.4. Doped BF

An alternative route has been used to suppress formation of secondary phase and improve the properties of BF-based materials by doping strategies. A-site substitution of, for example, acceptors such as Ca^{2+} [14, 15] and Pb^{2+}, or isovalent ions such as La^{3+} and Nd^{3+} [46]; B-site substitution such as Mn^{4+} and Ti^{4+} [58] or A- and B-site co-doped such as $BiFeO_3$- $PbTiO_3$ [59].

2.2.4.1. A-site doping in BF

2.2.4.1.1. ***Rare earth doped BF***

Generally, A-site doping of BF with rare-earth (RE) elements, for example La^{3+}, Sm^{3+}, Nd^{3+} and Eu^{3+}, eliminates formation of secondary phase and therefore, single phase ceramics can be prepared by conventional solid state reaction. It also improves dielectric properties and reduces leakage current and consequently, gives better ferroelectric properties.

A-site doping of BFO with La^{3+} is the most studied material among RE-doped BF. Low La^{3+} dopant concentration shows rhombohedral structure with R3c space group (i.e. in $Bi_{1-x}La_xFeO_3$ $x \leq 0.125$) [46, 60]. However, for $x > 0.125$ other phases are reported and some authors give the rhombohedral phase limit until $x \leq 0.3$ for $Bi_{1-x}La_xFeO_3$ [46]. The presence of La^{3+} hinders the formation of impurity phases and increases the resistivity of the material [60, 61]. As result of La^{3+} doping in BF, leakage current is reduced and therefore, ferroelectricity is enhanced and P-E loop can be observed [60]. Likewise, doping with Nd^{3+} [62] and Gd^{3+} [63] help to eliminate impurities and reduce leakage current. Similarly, Sm-doping on the A-site of perovskite has been reported to eliminate impurity phases [64, 65]. It also improves

antiferromagnetic behaviour in which Sm-doped sample showed large enhancement in the magnitude of remnant magnetisation T_N ~ 370 ℃, similar to un-doped sample. This is not clear why especially AFM is based on Fe concentration but this may be due to Sm-doped sample did not show any secondary phases that may affect AFM behaviour. However, unlike other RE-doped BF, Sm-doped BF shows an order of magnitude higher leakage current than un-doped sample [65]. This is probably attributed to domination of high conductive grain boundaries due to small size of grain and therefore, larger grain boundary area.

As discussed early, besides impurity phases, Bi^{3+} volatility, which leads to oxygen vacancies and mixed oxidation state of Fe^{3+} and Fe^{2+}, are considered as major issues that cause less desirable properties of pure $BiFeO_3$. It is believed that introduction of RE stabilises oxygen in the lattice due to higher bond enthalpy of RE with oxygen [46, 66]. This may cause reduction in enthalpy of formation (ΔH_f) and therefore, reduction of free energy of formation (ΔG_f) of more stable material than undoped $BiFeO_3$ [46].

2.2.4.1.2. ***Y-doped BF***

It is also accepted that the change in multiferroic properties of RE-doped $BiFeO_3$ is attributed to the effect of cation size. If so, substitution of Bi by non-rare earth with comparable ionic radius such as Y^{3+} should be valid. Mishra et al [67] have made a systematic study on the influence of Y doping on BF properties. They reported that similar to RE doping, doping BFO with Y^{3+} eliminates the formation of secondary phase, increases the resistivity and reduces the leakage current.

2.2.4.1.3. ***Ca-doped BF***

Another possible choice to enhance multiferroic properties of BF is doping with alkaline earth metals such as Ca^{2+} and Ba^{2+}. Doping with Ca^{2+} reduces the resistivity and causes the activation energy for the electrical conductivity to be in the range 0.27 to 0.5 eV. It is also difficult to observe saturation of the P-E loop due to high intrinsic conductivity [68]. The phase diagram of $Bi_{1-x}Ca_xFeO_{3-\delta}$ solid solutions contains several phases but there is disagreement over the phase limits.

Recently, it is reported that compositions $0.2 \leq x \leq 0.6$ show cubic phase while those with $0 \leq x \leq 0.07$ are rhombohedral with R3c space group and coexistence of the cubic and rhombohedral phases for intermediate compositions [15, 45]. It appears that the charge

compensation in Ca-doped BF mainly involves oxygen vacancies. Schiemer et al showed in their study no evidence of existence of Fe^{4+} using Mossbauer spectroscopy [68].

However, there are differences regarding the nature of Ca-doped BFO electrical properties which is reported to be a leaky dielectric. This is attributed in some reports to hole conduction that comes from oxidation of Fe^{3+} to Fe^{4+} and others attributed the conduction to oxygen vacancies. Recently, Maso and West studied the electrical properties of Ca-doped BFO and showed that it is sensitive to oxygen partial pressure during sintering and subsequent cooling [15]. They showed that the conductivity varies from p-type semiconductor to oxide-ion conductor with decreasing oxygen partial pressure during synthesis.

They concluded that a sample processed in N_2 atmosphere was an oxide-ion conductor, comparable to that well-known oxide-ion conductor, 8 mol % YSZ. However, samples processed in air and O_2 were p-type semiconductors. They attributed this electronic conductivity to existence of Fe^{3+} and Fe^{4+} that arises from absorption of small amount of oxygen (e.g. 3.2 % expanding formula to $Bi_{0.7}Ca_{0.3}Fe^{3+}_{0.968}\ Fe^{4+}_{0.032}O_{2.866}$) for a sample processed in O_2/ air.

Despite those reports (e.g. [68]) showing no evidence of the existence of Fe^{4+} using Mossbauer spectroscopy, they showed a slight increase in sample weight with increasing oxygen partial pressure in processing atmosphere indicating absorption of a small amount of oxygen and consequently small amount of Fe^{4+}. This small amount of Fe^{4+} probably cannot be detected by Mossbauer spectroscopy. Figure 2.7 shows the dependence of Ca-doped $BiFeO_3$ conductivity on atmosphere which falls within the electrolytic domain (sample processed in N_2) in the absence of electronic conductivity that arises from hole conduction via Fe^{4+} (samples processed in O_2/ air). The dependence of conductivity on oxygen partial pressure during processing and subsequent cooling atmosphere is fully reversible.

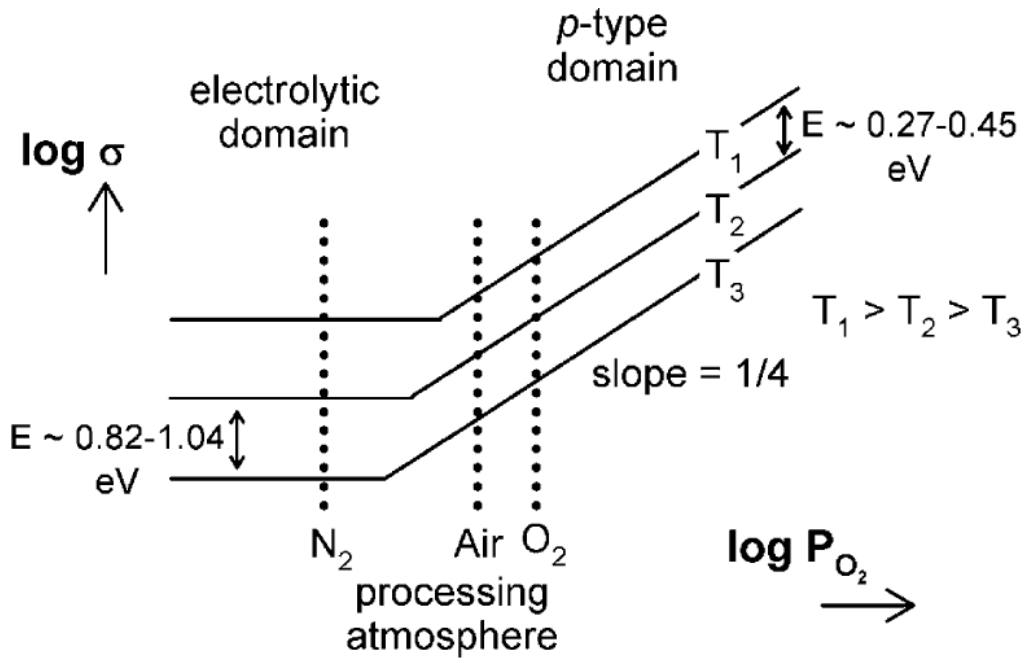

Figure 2.7. Schematic diagram of conductivity dependency on processing atmosphere and temperature [15].

Recently, Maso et al [14] reported resistive-switching behaviour in Ca-doped $BiFeO_3$ which differs from that associated with a Schottky barrier (discussed above) reported by [40]. They concluded that the material conductivity is enhanced, reversibly, by several orders of magnitude for both bulk and grain boundary regions on application of a small dc bias voltage.

It is worth mentioning that this change in conductivity was independent of electrode material and atmosphere (N_2, O_2 and air) during measurement indicating that this change was not associated with oxygen exchange between the atmosphere and sample.

On application of a small dc bias voltage in the range 5 to 30 V (≥ onset voltage) across 1.5 mm of pellet thickness, the conductivity increased steadily before a rapid increase occurred after some time and then levelled off. The time taken to achieve enhanced conductivity and then reach a steady state was dependent on the magnitude of applied voltage and temperature. On increasing the voltage, the time taken to reach a steady state decreased (Figure 2.8b) as well as the temperature (Figure 2.8c). The onset voltage decreased with increasing temperature (Figure 2.5a). On removal of dc bias the material recovered and returned to its original conductivity within a short time which was independent of temperature (Figure 2.8).

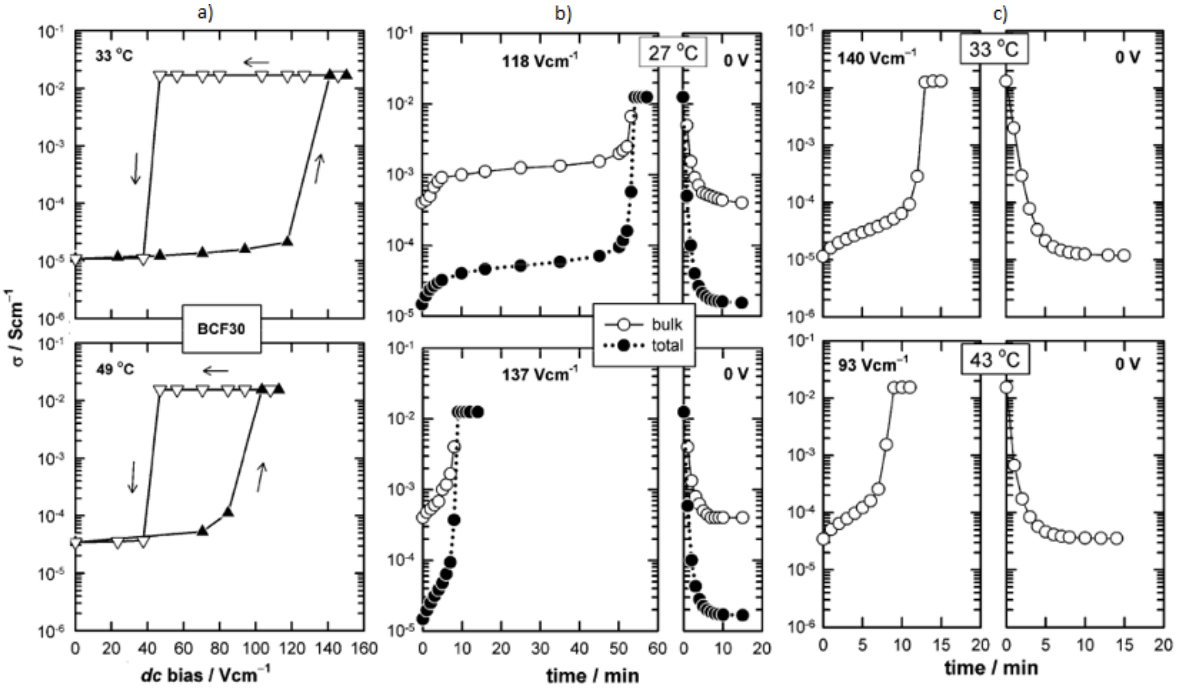

Figure 2.8. a) The total conductivity of $Bi_{0.7}Ca_{0.3}FeO_{2.85}$ vs. applied voltage at two temperatures; b) the bulk and total conductivity of $Bi_{0.95}Ca_{0.05}FeO_{2.975}$ vs. time affter different voltages were applied c) The total conductivity of $Bi_{0.7}Ca_{0.3}FeO_{2.85}$ vs. time affter different voltages were applied at different tmperatures [14].

So, they proposed a new resistive-switching mechanism which is not associated with Schottky barrier but was similar to that observed in acceptor-doped perovskites $ATiO_3$ (where A = Ba, Ca, Sr) that occurs at high temperature and over much longer time scale.

It appears to be that the key material requirement is to have acceptor dopants that lead to the presence of underbonded oxygen which can readily ionise to O^-. They believed [1] that the proposed resistive-switching mechanism, on application of a dc bias, includes a combination of capacitive charging and internal ionisation in which the underbonded O^{2-} ionise to O^- creating a hole-conducting layer of O^- and trapping the ionised electrons at the sample anode (Figure 2.9).

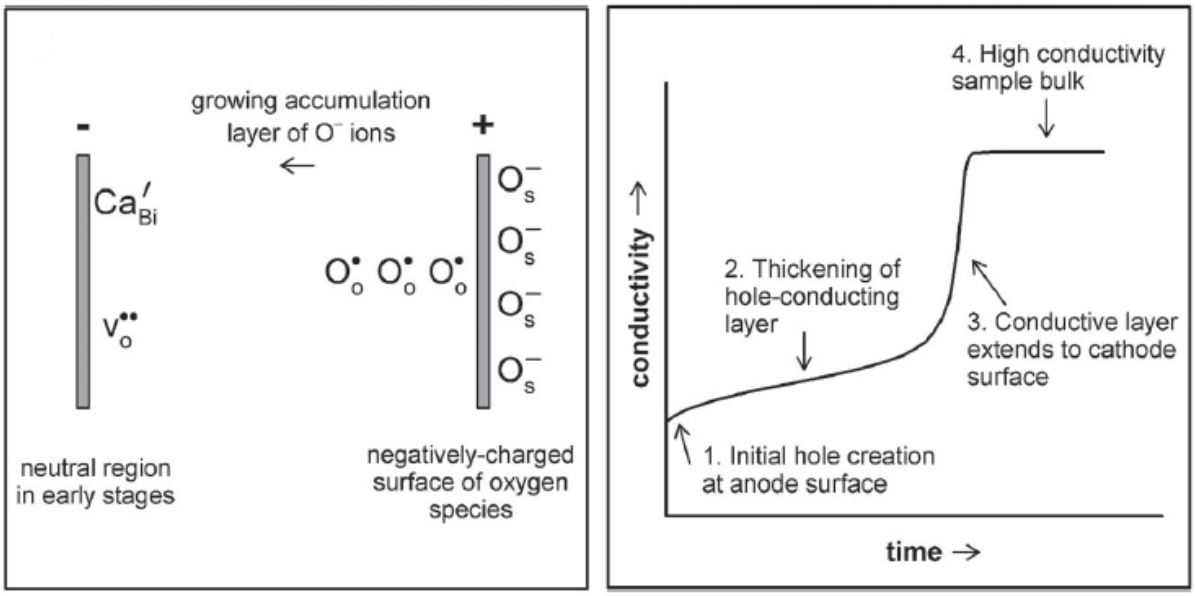

Figure 2.9. Capacitive model for voltage-dependent resistance (left), capacitive charging process stages on application of dc bias (right) [14].

2.2.4.2. B-site doping

Besides the fact that A-site doping eliminates or reduces the existence of impurity phases and improves the dielectric properties, the leakage current issue also can be reduced by B-site doping. Several studies have proposed that the existence of multi valence of Fe^{2+} and Fe^{3+} results in high conductivity in BF which has oxygen vacancies for charge neutrality. B-site doping of BF with donor dopants, such as V^{5+}, Nb^{5+} and Ti^{4+}, reduces the oxygen vacancy concentration, and results in increasing the resistivity and reducing leakage current [69]. For example, partial substitution of Fe^{3+} with Ti^{4+} increased the resistivity by six orders of magnitude and reduced the leakage current [58]. Similarly, substitution of Fe^{3+} with Nb^{5+} increased the resistivity by six orders of magnitude [70].

2.3. References

1. Maso, N., H. Beltran, M. Prades, E. Cordoncillo, and A.R. West, *Field-enhanced bulk conductivity and resistive-switching in Ca-doped BiFeO3 ceramics.* Phys Chem Chem Phys, 2014. **16**(36): p. 19408-16.
2. Prades, M., N. Masó, H. Beltrán, E. Cordoncillo, and A.R. West, *Field enhanced bulk conductivity of BaTiO3 : Mg ceramics.* Journal of Materials Chemistry, 2010. **20**(25).
3. Zhang, Q.-L., N. Masó, Y. Liu, H. Yang, and A.R. West, *Voltage-dependent low-field resistivity of CaTiO3:Zn ceramics.* Journal of Materials Chemistry, 2011. **21**(34).
4. Guo, M., N. Masó, Y. Liu, and A.R. West, *Electrical Properties and Oxygen Stoichiometry of Ba1–xSrxTiO3−δ Ceramics.* Inorganic Chemistry, 2017. **57**(1): p. 64-71.
5. Jovaní, M., H. Beltrán-Mir, E. Cordoncillo, and A.R. West, *Atmosphere- and Voltage-Dependent Electronic Conductivity of Oxide-Ion-Conducting Zr1–xYxO2–x/2 Ceramics.* Inorganic Chemistry, 2017. **56**(12): p. 7081-7088.
6. Alotaibi, M., L. Li, and A.R. West, *Electrical properties of yttria-stabilised hafnia ceramics.* Phys Chem Chem Phys, 2021. **23**(45): p. 25951-25960.
7. Vendrell, X. and A.R. West, *Induced p-type semiconductivity in yttria-stabilized zirconia.* Journal of the American Ceramic Society, 2019. **102**(10): p. 6100-6106.
8. Jovani, M., H. Beltran-Mir, E. Cordoncillo, and A.R. West, *Atmosphere- and Voltage-Dependent Electronic Conductivity of Oxide-Ion-Conducting Zr(1-x)Y(x)O(2-x/2) Ceramics.* Inorg Chem, 2017. **56**(12): p. 7081-7088.
9. Masó, N. and A.R. West, *Electronic Conductivity in Yttria-Stabilized Zirconia under a Small dc Bias.* Chemistry of Materials, 2015. **27**(5): p. 1552-1558.
10. Gil Escrig, L., M. Prades, H. Beltrán, E. Cordoncillo, N. Masó, and A.R. West, *Voltage-Dependent Bulk Resistivity of SrTiO 3: Mg Ceramics.* Journal of the American Ceramic Society, 2014. **97**(9): p. 2815-2824.
11. Ren, P., N. Masó, Y. Liu, L. Ma, H. Fan, and A.R. West, *Mixed oxide ion and proton conduction and p-type semiconduction in BaTi0.98Ca0.02O2.98 ceramics.* Journal of Materials Chemistry C, 2013. **1**(13).
12. Jovaní, M., H. Beltrán-Mir, E. Cordoncillo, and A.R. West, *Field-induced pn transition in yttria-stabilized zirconia.* Scientific Reports, 2019. **9**(1): p. 18538.
13. Guo, M., N. Maso, Y. Liu, and A.R. West, *Electrical Properties and Oxygen Stoichiometry of Ba(1-x)Sr(x)TiO(3-delta) Ceramics.* Inorg Chem, 2018. **57**(1): p. 64-71.
14. Masó, N., H. Beltrán, M. Prades, E. Cordoncillo, and A.R. West, *Field-enhanced bulk conductivity and resistive-switching in Ca-doped BiFeO 3 ceramics.* Physical Chemistry Chemical Physics, 2014. **16**(36): p. 19408-19416.
15. Masó, N. and A.R. West, *Electrical Properties of Ca-Doped BiFeO3 Ceramics: From p-Type Semiconduction to Oxide-Ion Conduction.* Chemistry of Materials, 2012. **24**(11): p. 2127-2132.
16. Navarro, L., F. Marques, and J. Frade, *n-Type conductivity in gadolinia-doped ceria.* Journal of The Electrochemical Society, 1997. **144**(1): p. 267.
17. Liu, Y. and A.R. West, *Voltage-dependent resistance of undoped rutile, TiO2, ceramics.* Applied Physics Letters, 2013. **103**(26): p. 263508.
18. Alotaibi, M., F. Almutairi, and A.R. West, *Resistive-switching in yttria-stabilized hafnia ceramics.* Journal of the American Ceramic Society, 2022. **106**(2): p. 822-828.
19. Kim, K.M., D.S. Jeong, and C.S. Hwang, *Nanofilamentary resistive switching in binary oxide system; a review on the present status and outlook.* Nanotechnology, 2011. **22**(25): p. 254002.

20. Walz, F., *The Verwey transition-a topical review.* Journal of Physics: Condensed Matter, 2002. **14**(12): p. R285.
21. Lee, J.S., S. Lee, and T.W. Noh, *Resistive switching phenomena: A review of statistical physics approaches.* Applied Physics Reviews, 2015. **2**(3): p. 031303.
22. Sawa, A., *Resistive switching in transition metal oxides.* Materials Today, 2008. **11**(6): p. 28-36.
23. Kumar, D., R. Aluguri, U. Chand, and T.Y. Tseng, *Metal oxide resistive switching memory: Materials, properties and switching mechanisms.* Ceramics International, 2017. **43**: p. S547-S556.
24. Panda, D. and T.-Y. Tseng, *Perovskite Oxides as Resistive Switching Memories: A Review.* Ferroelectrics, 2014. **471**(1): p. 23-64.
25. Lee, J.S., S. Lee, and T.W. Noh, *Resistive switching phenomena: A review of statistical physics approaches.* Applied Physics Reviews, 2015. **2**(3).
26. Waser, R., R. Dittmann, G. Staikov, and K. Szot, *Redox-based resistive switching memories–nanoionic mechanisms, prospects, and challenges.* Advanced materials, 2009. **21**(25-26): p. 2632-2663.
27. Bocquet, M., D. Deleruyelle, C. Muller, and J.-M. Portal, *Self-consistent physical modeling of set/reset operations in unipolar resistive-switching memories.* Applied Physics Letters, 2011. **98**(26): p. 263507.
28. Chae, S.C., J.S. Lee, S. Kim, S.B. Lee, S.H. Chang, C. Liu, B. Kahng, H. Shin, D.W. Kim, and C.U. Jung, *Random circuit breaker network model for unipolar resistance switching.* Advanced Materials, 2008. **20**(6): p. 1154-1159.
29. Sim, H., D. Choi, D. Lee, S. Seo, M.-J. Lee, I.-K. Yoo, and H. Hwang, *Resistance-switching Characteristics of polycrystalline Nb/sub 2/O/sub 5/for nonvolatile memory application.* IEEE electron device letters, 2005. **26**(5): p. 292-294.
30. Cagli, C., F. Nardi, B. Harteneck, Z. Tan, Y. Zhang, and D. Ielmini, *Resistive-Switching Crossbar Memory Based on Ni–NiO Core–Shell Nanowires.* Small, 2011. **7**(20): p. 2899-2905.
31. Fujiwara, K., T. Nemoto, M.J. Rozenberg, Y. Nakamura, and H. Takagi, *Resistance switching and formation of a conductive bridge in metal/binary oxide/metal structure for memory devices.* Japanese Journal of Applied Physics, 2008. **47**(8R): p. 6266.
32. Chang, S., S. Chae, S. Lee, C. Liu, T. Noh, J. Lee, B. Kahng, J. Jang, M. Kim, and D.-W. Kim, *Effects of heat dissipation on unipolar resistance switching in Pt/ Ni O/ Pt capacitors.* Applied Physics Letters, 2008. **92**(18): p. 183507.
33. Strukov, D.B., F. Alibart, and R. Stanley Williams, *Thermophoresis/diffusion as a plausible mechanism for unipolar resistive switching in metal–oxide–metal memristors.* Applied Physics A, 2012. **107**: p. 509-518.
34. Jeong, D.S., R. Thomas, R.S. Katiyar, J.F. Scott, H. Kohlstedt, A. Petraru, and C.S. Hwang, *Emerging memories: resistive switching mechanisms and current status.* Reports on Progress in Physics, 2012. **75**(7): p. 076502.
35. Yin, K., M. Li, Y. Liu, C. He, F. Zhuge, B. Chen, W. Lu, X. Pan, and R.-W. Li, *Resistance switching in polycrystalline BiFeO3 thin films.* Applied Physics Letters, 2010. **97**(4): p. 042101.
36. Ignatiev, A., N.J. Wu, X. Chen, S.Q. Liu, C. Papagianni, and J. Strozier, *Resistance switching in perovskite thin films.* physica status solidi (b), 2006. **243**(9): p. 2089-2097.
37. Adams, T.B., D.C. Sinclair, and A.R. West, *Characterization of grain boundary impedances in fine- and coarse-grainedCaCu3Ti4O12ceramics.* Physical Review B, 2006. **73**(9).
38. Jiao, Y., A. Hellman, Y. Fang, S. Gao, and M. Käll, *Schottky barrier formation and band bending revealed by first- principles calculations.* Scientific Reports, 2015. **5**(1).

39. Biendicho, J.J. and A.R. West, *Impedance characterisation of LiFePO4 ceramics.* Solid State Ionics, 2012. **226**: p. 41-52.
40. Rubi, D., F. Gomez-Marlasca, P. Bonville, D. Colson, and P. Levy, *Resistive switching in ceramic multiferroic Bi0.9Ca0.1FeO3.* Physica B: Condensed Matter, 2012. **407**(16): p. 3144-3146.
41. Rubi, D., F.G. Marlasca, M. Reinoso, P. Bonville, and P. Levy, *Magnetism and electrode dependant resistive switching in Ca-doped ceramic bismuth ferrite.* Materials Science and Engineering: B, 2012. **177**(6): p. 471-475.
42. Prades, M., N. Masó, H. Beltrán, E. Cordoncillo, and A.R. West, *Field enhanced bulk conductivity of BaTiO3 : Mg ceramics.* Journal of Materials Chemistry, 2010. **20**(25): p. 5335.
43. Zhang, Q.-L., N. Masó, Y. Liu, H. Yang, and A.R. West, *Voltage-dependent low-field resistivity of CaTiO3:Zn ceramics.* Journal of Materials Chemistry, 2011. **21**(34): p. 12894.
44. Arnold, D.C., K.S. Knight, F.D. Morrison, and P. Lightfoot, *Ferroelectric-Paraelectric Transition inBiFeO3: Crystal Structure of the OrthorhombicβPhase.* Physical Review Letters, 2009. **102**(2).
45. Chen, W.-t., A.J. Williams, L. Ortega-San-Martin, M. Li, D.C. Sinclair, W. Zhou, and J.P. Attfield, *Robust Antiferromagnetism and Structural Disorder in Bi x Ca1− x FeO3 Perovskites.* Chemistry of Materials, 2009. **21**(10): p. 2085-2093.
46. Arnold, D., *Composition-driven structural phase transitions in rare-earth-doped bifeo₃ ceramics: a review.* IEEE Transactions on Ultrasonics, Ferroelectrics, and Frequency Control, 2015. **62**(1): p. 62-82.
47. Catalan, G. and J.F. Scott, *Physics and Applications of Bismuth Ferrite.* Advanced Materials, 2009. **21**(24): p. 2463-2485.
48. Chang, W.S., C.-S. Tu, P.-Y. Chen, C.-S. Chen, C.-Y. Lin, K.-C. Feng, Y.L. Hsieh, and Y.H. Huang, *Effects of Fe 3d–O 2p and Bi 6sp–O 2p orbital hybridizations in Nd doped BiFeO3 ceramics.* Journal of Alloys and Compounds, 2017. **710**: p. 670-679.
49. Haumont, R., J. Kreisel, P. Bouvier, and F. Hippert, *Phonon anomalies and the ferroelectric phase transition in multiferroicBiFeO3.* Physical Review B, 2006. **73**(13).
50. Palai, R., R.S. Katiyar, H. Schmid, P. Tissot, S.J. Clark, J. Robertson, S.A.T. Redfern, G. Catalan, and J.F. Scott, *βphase andγ−βmetal-insulator transition in multiferroicBiFeO3.* Physical Review B, 2008. **77**(1).
51. Perejón, A., N. Masó, A.R. West, P.E. Sánchez-Jiménez, R. Poyato, J.M. Criado, L.A. Pérez-Maqueda, and D. Viehland, *Electrical Properties of Stoichiometric BiFeO3Prepared by Mechanosynthesis with Either Conventional or Spark Plasma Sintering.* Journal of the American Ceramic Society, 2013. **96**(4): p. 1220-1227.
52. Teague, J.R., R. Gerson, and W.J. James, *Dielectric hysteresis in single crystal BiFeO3.* Solid State Communications, 1970. **8**(13): p. 1073-1074.
53. Neaton, J.B., C. Ederer, U.V. Waghmare, N.A. Spaldin, and K.M. Rabe, *First-principles study of spontaneous polarization in multiferroicBiFeO3.* Physical Review B, 2005. **71**(1).
54. Shvartsman, V.V., W. Kleemann, R. Haumont, and J. Kreisel, *Large bulk polarization and regular domain structure in ceramic BiFeO3.* Applied Physics Letters, 2007. **90**(17): p. 172115.
55. Kim, J.K., S.S. Kim, and W.-J. Kim, *Sol–gel synthesis and properties of multiferroic BiFeO3.* Materials Letters, 2005. **59**(29-30): p. 4006-4009.
56. Zhai, L., Y.G. Shi, J.L. Gao, S.L. Tang, and Y.W. Du, *Ferroelectric and magnetic properties in high-pressure synthesized BiFeO3 compound.* Journal of Alloys and Compounds, 2011. **509**(28): p. 7591-7594.

57. Kumar, M.M., V.R. Palkar, K. Srinivas, and S.V. Suryanarayana, *Ferroelectricity in a pure BiFeO3 ceramic.* Applied Physics Letters, 2000. **76**(19): p. 2764-2766.
58. Kumar, M. and K.L. Yadav, *Study of room temperature magnetoelectric coupling in Ti substituted bismuth ferrite system.* Journal of Applied Physics, 2006. **100**(7): p. 074111.
59. Comyn, T.P., T. Stevenson, M. Al-Jawad, S.L. Turner, R.I. Smith, W.G. Marshall, A.J. Bell, and R. Cywinski, *Phase-specific magnetic ordering in BiFeO3−PbTiO3.* Applied Physics Letters, 2008. **93**(23): p. 232901.
60. Cheng, Z., A. Li, X. Wang, S.X. Dou, K. Ozawa, H. Kimura, S. Zhang, and T.R. Shrout, *Structure, ferroelectric properties, and magnetic properties of the La-doped bismuth ferrite.* Journal of Applied Physics, 2008. **103**(7): p. 07E507.
61. García-Zaleta, D.S., A.M. Torres-Huerta, M.A. Domínguez-Crespo, J.A. Matutes-Aquino, A.M. González, and M.E. Villafuerte-Castrejón, *Solid solutions of La-doped BiFeO3 obtained by the Pechini method with improvement in their properties.* Ceramics International, 2014. **40**(7): p. 9225-9233.
62. Yuan, G. and S.W. Or, *Enhanced piezoelectric and pyroelectric effects in single-phase multiferroic Bi 1− x Nd x Fe O 3 (x= 0–0.15) ceramics.* Applied physics letters, 2006. **88**(6): p. 062905.
63. Fanggao, C., S. Guilin, F. Kun, Q. Ping, and Z. Qijun, *Effect of Gadolinium Substitution on Dielectric Properties of Bismuth Ferrite.* Journal of Rare Earths, 2006. **24**(1): p. 273-276.
64. Schiemer, J., R.L. Withers, M.A. Carpenter, Y. Liu, J.L. Wang, L. Norén, Q. Li, and W. Hutchison, *Temperature-dependent electrical, elastic and magnetic properties of sol–gel synthesized Bi0.9Ln0.1FeO3(Ln = Nd, Sm).* Journal of Physics: Condensed Matter, 2012. **24**(12): p. 125901.
65. Nalwa, K.S. and A. Garg, *Phase evolution, magnetic and electrical properties in Sm-doped bismuth ferrite.* Journal of Applied Physics, 2008. **103**(4): p. 044101.
66. Khodabakhsh, M., C. Sen, H. Khassaf, M.A. Gulgun, and I.B. Misirlioglu, *Strong smearing and disappearance of phase transitions into polar phases due to inhomogeneous lattice strains induced by A-site doping in Bi1−xAxFeO3 (A: La, Sm, Gd).* Journal of Alloys and Compounds, 2014. **604**: p. 117-129.
67. Mishra, R.K., D.K. Pradhan, R.N.P. Choudhary, and A. Banerjee, *Effect of yttrium on improvement of dielectric properties and magnetic switching behavior in BiFeO3.* Journal of Physics: Condensed Matter, 2008. **20**(4): p. 045218.
68. Schiemer, J., R. Withers, L. Norén, Y. Liu, L. Bourgeois, and G. Stewart, *Detailed Phase Analysis and Crystal Structure Investigation of a Bi1−xCaxFeO3−x/2Perovskite-Related Solid Solution Phase and Selected Property Measurements Thereof.* Chemistry of Materials, 2009. **21**(18): p. 4223-4232.
69. Yu, B., M. Li, J. Wang, L. Pei, D. Guo, and X. Zhao, *Enhanced electrical properties in multiferroic BiFeO3ceramics co-doped by La3+and V5+*. Journal of Physics D: Applied Physics, 2008. **41**(18): p. 185401.
70. Jun, Y.-K., W.-T. Moon, C.-M. Chang, H.-S. Kim, H.S. Ryu, J.W. Kim, K.H. Kim, and S.-H. Hong, *Effects of Nb-doping on electric and magnetic properties in multi-ferroic BiFeO3 ceramics.* Solid State Communications, 2005. **135**(1-2): p. 133-137.

Chapter 3 : Experimental Procedures

3.1. Solid state synthesis

Polycrystalline ceramic Samples were synthesised by solid state reaction. Reagents in Table 3.1 were used to prepare Ca-doped $BiFeO_3$ (BCF) and Y-doped CeO_2 (YDC). Each reagent was dried overnight before weighing at suitable temperature as shown in Table 3.1. Then, all-samples were manually mixed in conventional mortar and pestle with acetone and reacted in an alumina crucible at suitable temperature, as mentioned in Table 3.2, in wanted atmosphere. The reacted powders were re-ground and pressed into pellets, 10 mm diameter, using a uniaxial press. Pellets of BCF and YDC were sintered at around 945 and 1500 ℃, respectively.

Table 3.1. Reagent sources, drying temperatures and purities.

Reagent	**Drying T (℃)**	**Purity**	**Supplier**
Bi_2O_3	180	99 %	Sigma-Aldrich
$CaCO_3$	180	99 %	Sigma-Aldrich
Fe_2O_3	400	99.9 %	Alfa Aesar
CeO_2	900	99 %	Sigma-Aldrich
Y_2O_3	900	99.99 %	Alfa Aesar

Table 3.2. Ceramic processing parameters for each composition.

Composition	**pre-heating / Reaction temperature (℃)**	**Pressure (MPa)**	**Sintering temperature (℃)**
$BiFeO_3$	830	225	870
$Bi_{0.77}Ca_{0.23}FeO_{2.885}$	830	225	950
$Bi_{0.70}Ca_{0.30}FeO_{2.85}$	830	225	950
$Bi_{0.60}Ca_{0.40}FeO_{2.80}$	830	225	950
$Ce_{0.84}Y_{0.16}O_{2.92}$	1400	125	1500

3.2. Phase identification

The sintered pellets were crushed and analysed using X-ray diffraction for phase identification. A Bruker D2 phaser were used with Cu Kα radiation (λ= 1.541 Å) in this project. The data were collected over the range 20˚ < 2θ < 90˚. The date was collected and compered with literature and different XRD pattern using the JCPDS database.

3.3. Impedance spectroscopy (IS)

Impedance spectroscopy (IS) is powerful technique to measure and especially distinguish between different electrical regions of a ceramic sample in which its electrical properties depend on individual grain, grain boundary or surface properties [1-5]. In this project, ceramic electrical properties were measured and analysed using impedance spectroscopy.

3.3.1. Sample preparation and Instrumentation

For impedance measurements, Au paste was attached to both side of sintered pellets and dried at 850 ℃ for 2 hours. A pellet with attached electrodes was placed between Pt leads in measuring jig and placed in a tube furnace. Impedance measurements were performed as a function of different variables: i) temperatures, ii) oxygen partial pressure (pO_2), iii) dc bias and iv) combination of both dc bias and pO_2. Three impedance analysers were used in this study which were Modulab XM Solartron with a frequency range 0.1 Hz-1000 kHz, Solartron SI 1260 with a frequency range 0.1 Hz-1000 kHz and Agilent 4294A with a frequency range 0.04-1000 kHz. Z-view software was used for IS data analysis and equivalent circuit fitting.

3.3.2. Data correction

The collected data were corrected for the jig characteristics in which closed circuit measurements were performed to eliminate the lead inductance and resistance, and open circuit measurements were performed to eliminate the blank capacitance of the jig. Also, the data were corrected for the overall sample geometries in which the specific values of sample resistance, R and capacitance, C, i.e. resistivity, ρ and permittivity, ε are given by eqs 3.1 and 3.2, respectively:

$$\rho = RA/d \tag{3.1}$$

$$\varepsilon = \mathrm{Cd/A} \tag{3.2}$$

where A is the cross sectional area of the pellet and d its thickness. Therefore, the resistivity and permittivity units are Ω cm and F cm^{-1}, respectively.

3.3.3. Data analysis and their equivalent circuits

IS is a useful technique to measure and distinguish between different electrical regions of a polycrystalline material. Each electrically-distinct region of a heterogeneous material, that contains, for example, grain, grain boundary, surface layer and/ or sample-electrode interface, can be represented by its own parallel RC element. The distinct region is characterised and separated by a time constant, τ, given by [1]:

$$\tau = RC = \rho\varepsilon \tag{3.3}$$

The time constant is a dimensionless quantity and depends only on the intrinsic properties, ρ and ε, of the corresponding region. Each region, therefore, can be identified and separated on a frequency scale based on its τ, which relaxes-out at its ω_{max} ($\omega = 2\pi f$), by the following equation:

$$\omega_{max}\tau = \omega_{max}RC = 1 \tag{3.4}$$

In this project, R and C data were represented using four formalisms: impedance, Z*, admittance, Y*, electrical modulus, M*, permittivity, ε*. These formalisms are inter-larded by the following [1]:

$$Z^* = (Y^*)^{-1} \tag{3.5}$$

$$Y^* = j\omega C_0\varepsilon^* \tag{3.6}$$

$$M^* = j\omega C_0 Z^* \tag{3.7}$$

$$\varepsilon^* = (M^*)^{-1} \tag{3.8}$$

Where $j = \sqrt{-1}$, C_0 is the blank capacitance and ω is the angular frequency. Each formalism has real and imaginary components given by:

$$Z^* = Z' - jZ''; \; Y^* = Y' - jY''; \; M^* = M' - jM''; \; \varepsilon^* = \varepsilon' - j\varepsilon''; \tag{3.9}$$

Here, the data were measured directly in terms of in impedance formalism and converted to other formalism using equations 3.5 to 3.8. The data were presented in four different graphs:

impedance complex plane plot in which the imaginary part (Z'') is plotted against the real part (Z'); spectroscopic plots in which the real parts on logarithmic scales are plotted against the frequency on logarithmic scale, i.e. log Y' vs log *f*, log C' vs log *f*, and the imaginary parts on liner scales are plotted against the frequency on logarithmic scale, i.e. Z", M" vs log *f*.

Figure 3.1 shows the ideal appearance of two parallel RC elements connected in series in different graphical representations. The data were simulated using Z-view software for well-defined inputs in which $R_1 > R_2$ and $C_1 <<< C_2$, and therefore $\tau_1 <<< \tau_2$, over the frequency range 10^{-2}-10^6 Hz. The impedance complex plane plot (a) shows two ideal, well-separated, semicircles at low and high frequencies. Representing the same data in Z"/ M" spectroscopic plots (b) showed a peak at high frequency for both Z" and M", which overlap, representing high frequency semicircle, Z_1^*; since the M" plot is dominated by the lowest capacitance, only the Z" plot showed a peak at low frequency related to Z_2^*. The C' spectroscopic plot (c) shows two plateaux in which the high frequency plateau represents C_1. The Y' spectroscopic plot (d) shows two plateaux in which the low frequency peak represents $1/R_t$. Low and high frequency plateaux in both C' and Y' plots (c and d) were single-valued and frequency-independent.

In reality, many ceramics show non-ideal response and their conductivities and capacitances show frequency-dependent behaviour at the high and low frequency, respectively, due to the power low response. Recently, a constant phase element, CPE, which is combination of variable R and C, is used to fit such frequency-dependent response in which CPE is added in parallel with the parallel RC element. The admittance of the CPE is given by [1, 2, 6-8]:

$$Y_{CPE}^* = A\omega^n + jB\omega^n = Y' + jY'' \qquad (3.10)$$

Where n is the ratio of the numbers of series and parallel *R-C* connections in the network ($0 < n < 1$) and $B/A = \tan n\pi/2$. The Y* of a circuit consisting of parallel R-CPE-C is given by the following equation:

$$Y^* = \frac{1}{R} + A\omega^n + j(B\omega^n + \omega C) = Y' + jY'' \qquad (3.11)$$

Figure 3.2 shows the effect of CPE inclusion on the data appearance in the different graphical representations. The semicircle in Z* plot became distorted and both C' and Y' plots became frequency-independent over limited frequency range at high and low frequency, respectively. At low frequency, the C' plot shows linear increase in the capacitance with slope = n-1 while a

linear increase of slope n is shown at high frequency in Y'. If n = 1, the CPE is capacitive and if n =0, the CPE is resistive and in both cases no CPE are detected.

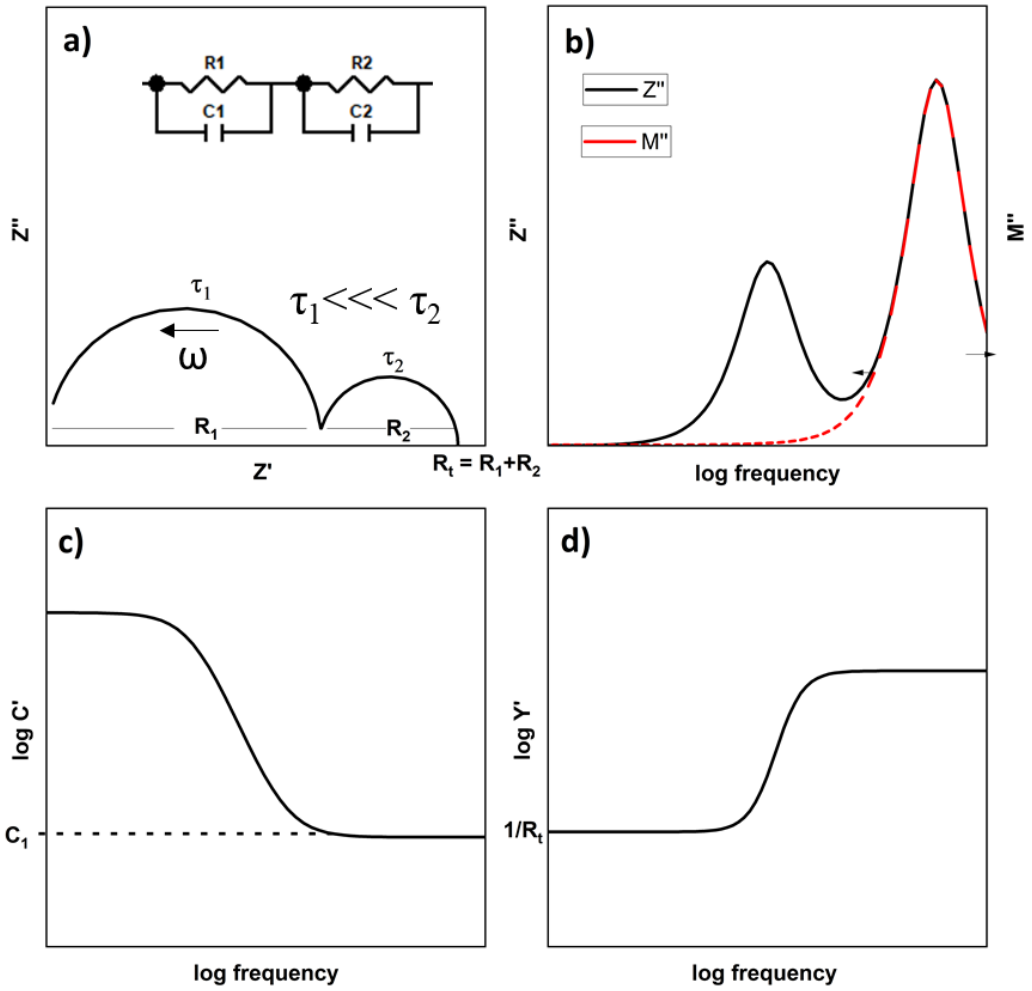

Figure 3.1 Simulation of typical impedance data for a sample containing two electrically-distinct regions with $\tau_1 <<< \tau_2$.

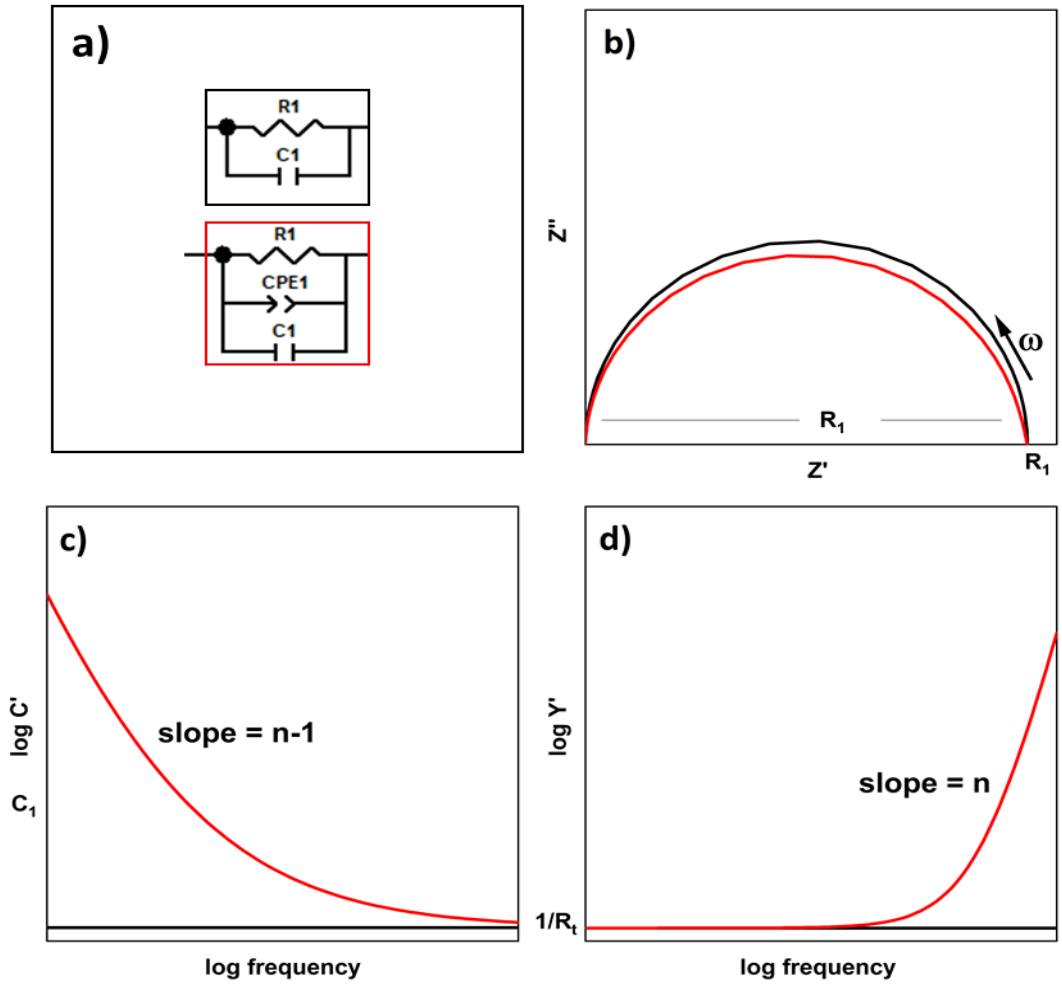

Figure 3.2 Simulation of the effect of CPE inclusion on impedance data.

In practice, there are many complicated cases in which presenting the data in one formalism would lead to miss-interpreting the data origin. For example, the impedance response is shown in Figure 3.3 for a sample containing grain, bulk, and grain boundaries in which each region is modelled by a parallel RC where $R_b <<< R_{gb}$ and $C_b < C_{gb}$. The impedance complex plane plot (a) shows only one semicircle which could be incorrectly attributed to the bulk. Presenting the data in the Z"/ M" plots (b) clearly shows that the arc in Z* plot is related to the low frequency region and there is another region at high frequency shown in M" plot, even though its resistance is too small to appear in Z* plot (a). The Y' spectroscopic plot (d) shows that the sample contains a high frequency region whose resistance much smaller than its total resistance which is dominated by the resistance of the low frequency region. The C' spectroscopic plot (c) shows that the sample contains two capacitive regions of different thicknesses at high and low frequencies. Thus, it is useful to present the data in different formalisms in order to fully interpret the electrical make-up of a sample.

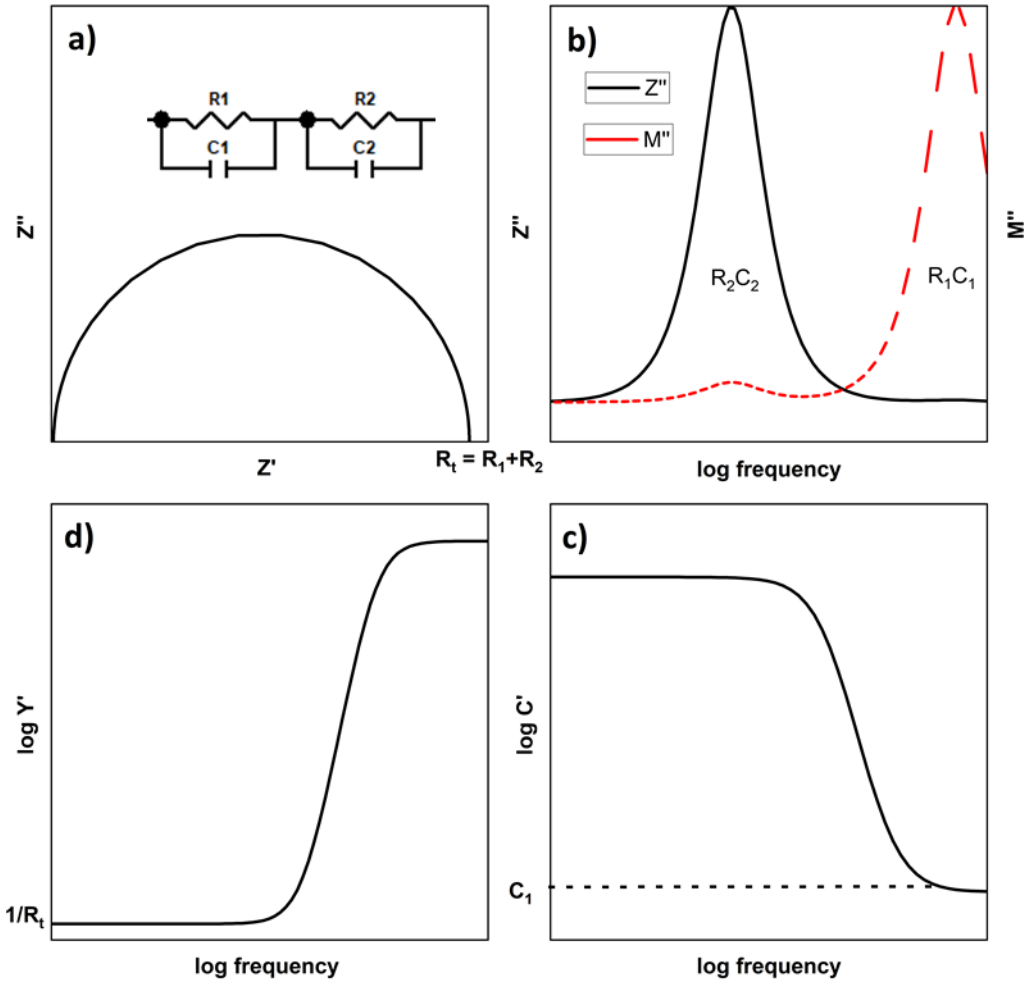

Figure 3.3. Simulation of typical impedance response for a sample with R_1 <<< R_2

Measuring the sample at fixed temperature would not allow us to see all the different regions of the sample due to the frequency window limit of the instrumentations. Therefore, performing impedance measurement as function of temperature allows us to observe all sample elements or regions. Also, measuring impedance as function of temperature allows Arrhenius plots to be constructed in which the reciprocal of R_1 and R_2 are plotted against the reciprocal of temperature, and therefore activation energies, E_σ, are obtained using:

$$\sigma = A \exp(\frac{Ea}{kT}) \qquad (3.12)$$

Where, σ is R^{-1}, E_a is the activation energy of the region (eV), k is Boltzmann's constant (8.613×10^{-5} eV/K) and T is the temperature (K).

3.3.4. Data interpretation

Each electrically-distinct region can be identified based on the magnitude of its capacitance using a brickwork model in which the main difference between various regions in a ceramic sample, that contains grain (bulk), b, grain boundaries, gb, and sample electrode interface, el, is the thickness, i.e. $t_b < t_{gb} < t_{el}$ (Figure 3.4). Each region capacitance can vary few orders of magnitude based on the following equation:

$$C = \varepsilon_r \varepsilon_0 \left({}^{A}/_{t}\right) \tag{3.13}$$

Where ε_r is the relative permittivity, ε_0 is the permittivity of free space, A is the sample surface area and t is the sample thickness. Therefore, each region can be identified using Table 3.3 based on the inverse relationship between C' and t.

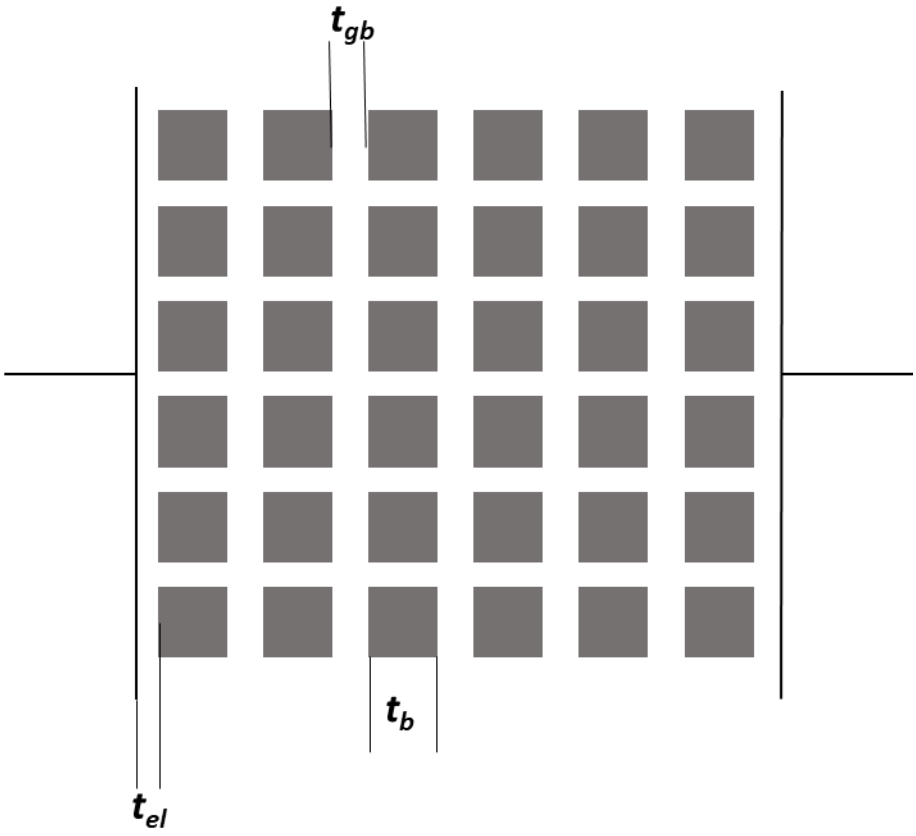

Figure 3.4. The Brickwork model illustrating the thickness of the grains, grain boundaries and sample-electrode interface.

Table 3.3. Possible interpretation for capacitance value [1, 5].

Normalised Capacitance (F/cm)	Origin of the RC element
10^{-12}	Bulk
10^{-11}	Minor, second phase
10^{-11} - 10^{-9}	Grain boundary
10^{-10} - 10^{-9}	Bulk ferroelectric near T_c (Curie temperature)
10^{-9} - 10^{-7}	Surface layer
10^{-7} - 10^{-5}	Sample-electrode interface
10^{-4}	Electrochemical reactions

The sample-electrode interface impedance is greatly affected by the nature of the sample conductivity whether it is electronic or ionic. It is a useful advantage which can be utilised to determine the type of the sample conductivity. For an oxide-ion conductor, the sample-electrode contact is not blocking due to the redox reaction occurs between the sample O^{2-} ions and oxygen gas, O_2, in which the O_2 molecules diffuse toward and/or away from the sample interface.

The sample discharges O^{2-} ions from the sample interior at one electrode and adsorbs O_2 molecules that are reduced to O^{2-} ions and diffuse into the sample at the other electrode. During the O^{2-} discharge electrons are liberated and injected through the external circuit. This redox reduction is quantified by the resistance of the charge transfer, R_{CT} which is in parallel with sample-electrode interface capacitance. At lowest frequencies, it may be difficult for O_2 diffuse towards and/or away from the sample which appear as a Warburg impedance or inclined spike of angle 45˚ in Z* plot. It is usually represented by a CPE with an ideal n value of ½, connected in series with the sample RC.

The type of electronic conductivity, whether it is n- or p-type, can be determined by IS if the material exhibits modest electronic conductivity and is sensitive to the pO_2. The equilibria at the surfaces of oxides can be affected by oxygen molecule adsorption, dissociation and ionisation reactions in eq 3.13 and 3.14.

$$O_2 + 4e^- \rightarrow 2O^{2-} \qquad (3.14)$$

$$O_2 \leftrightarrow 2O^{2-} + 4h^+ \quad (3.15)$$

In both cases, electron participation from the sample is required. For an n-type material, the conductivity decreases due to removal of the carriers (electrons) form the sample eq 3.13. For a p-type material, the conductivity increases since the captured electrons arises from ionising of the redox active element and therefore more holes are created eq 3.14.

3.4. References

1. West, A.R., *Solid state chemistry and its applications*. 2022: John Wiley & Sons.
2. E.J. ABRAM, D.C.S.A.R.W., *A Strategy for Analysis and Modelling of Impedance Spectroscopy Data of Electroceramics: Doped Lanthanum Gallate.* Journal of Electroceramics, 2003.
3. West, A.R., D.C. Sinclair, and N. Hirose, *Characterization of electrical materials, especially ferroelectrics, by impedance spectroscopy.* Journal of electroceramics, 1997. **1**(1): p. 65-71.
4. Sinclair, D.C. and A.R. West, *Impedance and modulus spectroscopy of semiconducting BaTiO3showing positive temperature coefficient of resistance.* Journal of Applied Physics, 1989. **66**(8): p. 3850-3856.
5. Sinclair, D.C., *Characterisation of electro-materials using ac impedance spectroscopy.* Boletín de la Sociedad Española de Cerámica y Vidrio, 1995. **34**(2): p. 55-65.
6. Hernández, M.A., N. Masó, and A.R. West, *On the correct choice of equivalent circuit for fitting bulk impedance data of ionic/electronic conductors.* Applied Physics Letters, 2016. **108**(15): p. 152901.
7. Osman, R.A. and A.R. West, *Electrical characterization and equivalent circuit analysis of (Bi1. 5Zn0. 5)(Nb0. 5Ti1. 5) O7 Pyrochlore, a relaxor ceramic.* Journal of Applied Physics, 2011. **109**(7): p. 074106.
8. Masó, N., X. Yue, T. Goto, and A.R. West, *Frequency-dependent electrical properties of ferroelectric BaTi 2 O 5 single crystal.* Journal of Applied Physics, 2011. **109**(2): p. 024107.

Chapter 4 : Electrical properties of Ca-doped $BiFeO_3$

4.1. Introduction

Bismuth ferrite (BF) is currently attracting considerable attention due to its multiferroic properties, which can be utilised in various applications such as spintronics, data storage and microelectronic devices [1-3]. BF suffers from some problems that hinder it from being used in commercial applications such as the difficulty in preparation of phase-pure BF and leakage conductivity. Doping BF with other materials is an effective way to solve some of these problems. Recently, Ca-doped BF (BCF) shows interesting electrical properties and especially, in response to a dc bias.

The conductivity of BCF varies from p-type semiconduction to oxide ion conduction depending on pO_2 at the processing temperature and during subsequent cooling [4]. More interestingly, the conductivity of BCF increases by several orders of magnitude on application of a small dc bias at room temperature and is reversible, with some hysteresis, on removing the bias [5]. Such a phenomenon has been observed previously in thin film memristors but BCF is the first bulk ceramic to show this switching behaviour. Recently, similar low field bulk resistive switching was observed in hafnia stabilised zirconia, HSZ [6].

In this chapter, we have studied and confirmed the electrical properties of Ca-doped BF that have been reported in the literature, and extended the study by including new compositions of BCF to study the effect of composition on the electrical properties. We studied four compositions of $Bi_{1-x}Ca_xFeO_{3-x/2}$ (where x = 0, 0.23, 0.3 and 0.4) processed in different levels of pO_2. The phase present and its crystal structure was analysed by x-ray powder diffraction. The electrical properties were studied by impedance spectroscopy and were measured as a function of temperatures and pO_2.

4.2. Results

4.2.1. X-ray diffraction

Four compositions of $Bi_{1-x}Ca_xFeO_{3-x/2}$ (where: x = 0, 0.23, 0.3 and 0.4 which are labelled as BF, BCF23, BCF30 and BCF40 respectively) were synthesised by high-temperature solid state reaction. The samples were almost single phase with small impurity of Fe_2O_3 (Figure 4.1). BF was indexed on rhombohedral unit cell, with space group R3c, by X-ray diffraction, while the other three compositions showed no splitting in all XRD peaks, which were indexed on a cubic unit cell ($Pm\bar{3}m$ space group) with small shift in diffraction peak positions toward higher angle with increasing x.

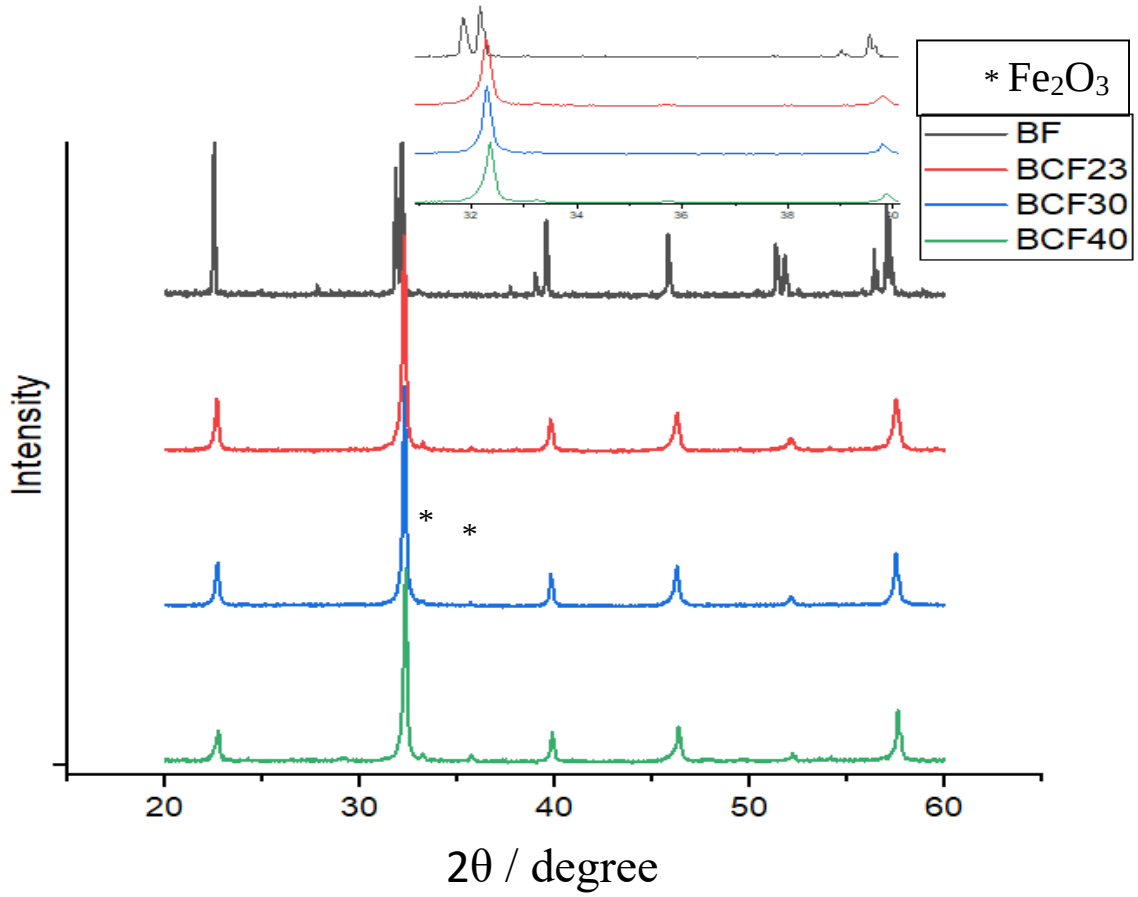

Figure 4.1. X-ray diffraction patterns of $Bi_{1-x}Ca_xFeO_{3-x/2}$ where x = 0, 0.23, 0.30 and 0.40. The inset shows the reflections between 32 and 40 degrees on expanded scale.

4.2.2. Impedance spectroscopy

A detailed survey of the electrical properties of the $Bi_{1-x}Ca_xFeO_{3-x/2}$ ceramics were carried out by impedance spectroscopy. Impedance results were obtained after three sets of processing conditions for x = 0.23, 0.30 and 0.40. Each composition was heated to 900 ℃ and slow-cooled in atmosphere of either air, O_2 or N_2. The same pellets were used for each composition without removing the electrodes between subsequent heat treatments. For BF, impedance measurements were only performed for the air-processed sample and measured over the temperature range RT- 100 ℃. For doped samples, the O_2 and air-processed samples were more conducting and, therefore, they were measured over the temperature range RT- 100 ℃, while the N_2-processed samples were less conductive and were measured over the range 150-350 ℃. The measurements were taken on heating and cooling to check the data reversibility.

4.2.2.1. Air-processed samples

BF impedance data at 32 ℃ are shown in Figure 4.2. The Z* complex plane plot shows two arcs (Figure 4.2a) which from their intercepts with the real Z` axis, the resistivity values R_1 and R_2 were obtained that together (R_1+R_2) dominated the total sample resistance. The high frequency region spectra had moved to higher frequency in Z" / M" spectroscopy plots at measured temperatures and only the low frequency region peak is shown in Z" plot. The capacitance data (Figure 4.2c) show two plateaus at low and high frequencies. Thus, these data can be represented initially by two parallel RC circuits connected in series. From the associated capacitance values, the high frequency region was attributed to the bulk effect (C_1~ 9 pF at 32 ℃) and the low frequency (Figure 4.2 c) region was attributed to the conventional grain boundary (C_2~ 2 nF at 32 ℃). The admittance (Y') plot shows two plateaus at high and low frequencies (Figure 4.2d).

Impedance responses of BCF23, 30 and 40 processed in air were measured between 20 and 100 ℃ in dry air. The responses of all three compositions were similar and similar data sets were obtained. The impedance data for BCF23, 30 and 40 are shown in Figure 4.3 and Figure 4.4 at selected temperatures. The Z* complex plane plots show a single, almost ideal semicircle for all compositions (Figure 4.3a,Figure 4.4a). The same data, for BCF23, in Z"/ M" spectroscopic plots show a single peak in both cases which overlap and indicate electrical homogeneity of the samples (Figure 4.3b). The capacitance data show one plateau at high frequency (Figure 4.3c,Figure 4.4b). They can be modelled ideally by a single parallel RC element in which R is the bulk resistance and C is its capacitance. The bulk capacitances for all compositions were in the range between 9 and 12 pF/cm at about 32 ℃ (Figure 4.3c, Figure

4.4b). The admittance (Y') plot, for BCF23, shows one plateau over the frequency range (Figure 4.3d).

At low frequency, the C' data (Figure 4.3c) show an approximate linear increase in capacitance, and at high frequency, the Y' data (d) show a dispersion indicating a possible power law response. The probable equivalent circuit to represent the electrical property, therefore, is a parallel R-CPE-C element. A detailed analysis of the data and equivalent circuit fitting will be shown in chapter 5.

The conduction type is electronic in all air-processed samples since there is no evidence ionic conduction from impedance results and low activation energies. The Z* complex plane plot showed no evidence of any additional impedance related to a charge transfer process at the sample-electrode interface (Figure 4.3a, Figure 4.4a) which is a key result obtained in different processing conditions experiments as shown later.

From the above data, the bulk resistances were obtained from the intercepts of the arc on the real axis, Z' and are shown as conductivity Arrhenius plots (Figure 4.5). The bulk conductivity of $Bi_{1-x}Ca_xFeO_{3-x/2}$ solid solutions decreased with increasing x; activation energies were in the range 0.53 - 0.63 eV. The impedance measurements were taken on heating and cooling and the obtained data were similar, showing linear behaviour as represented in Figure 4.5.

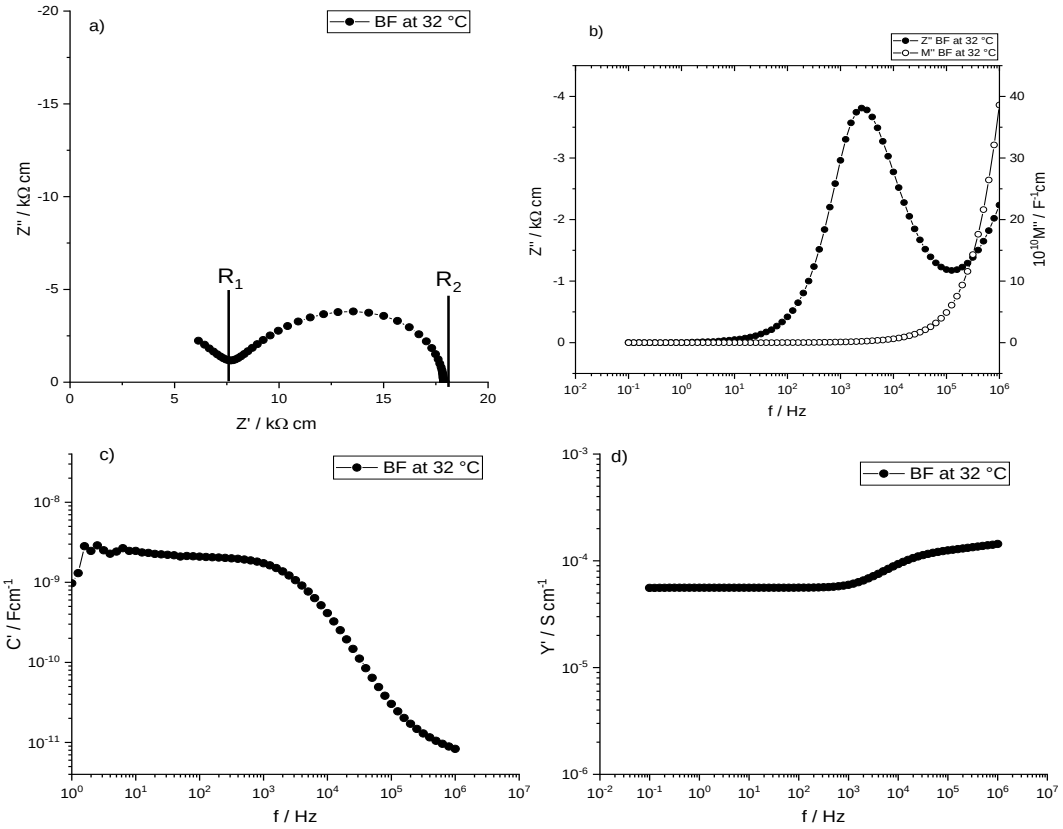

Figure 4.2. Impedance data for BF at 32 ℃: a) Z complex plane plot, spectroscopic plots of (b) Z''/ M'', (c) capacitance, C' and (d) admittance, Y'.*

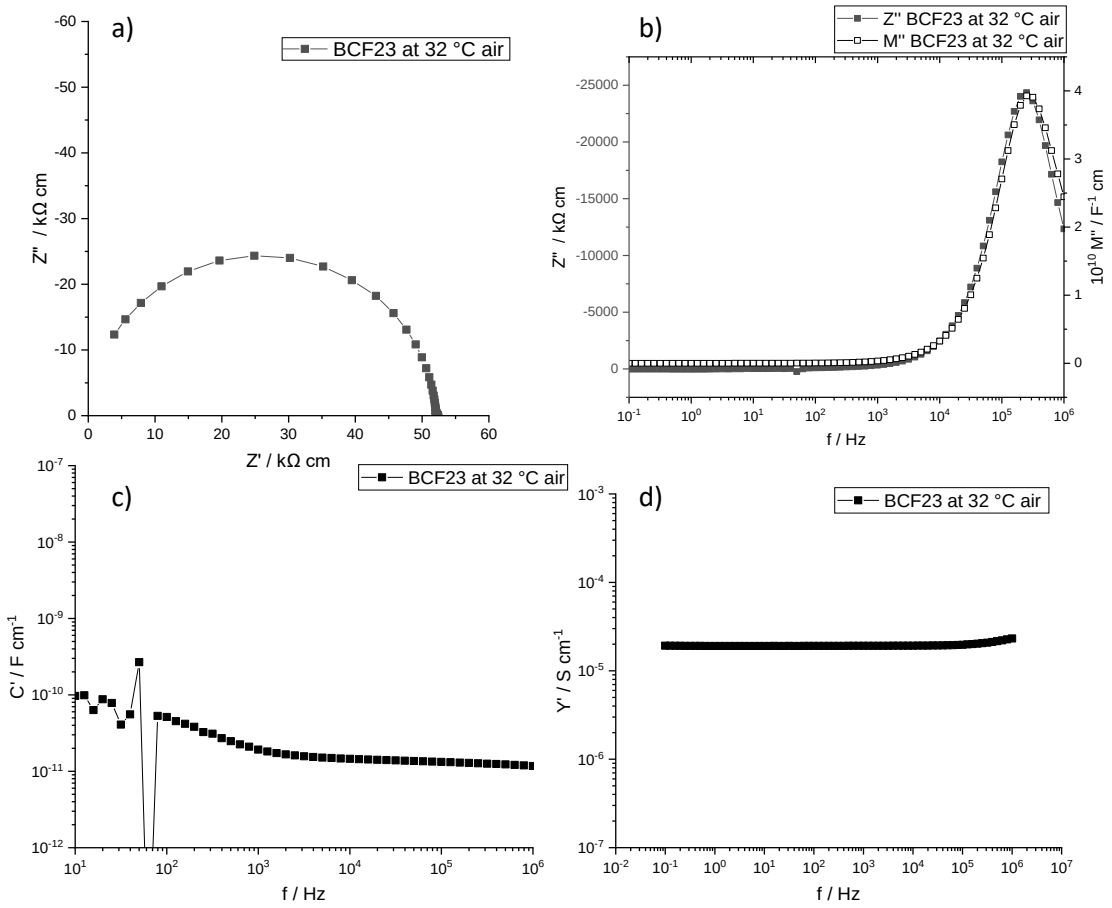

Figure 4.3. Impedance data for BCF23 processed in air at 32 ℃: a) Z complex plane plot, spectroscopy plots of (b) Z''/ M'', (c) capacitance and (d) admittance.*

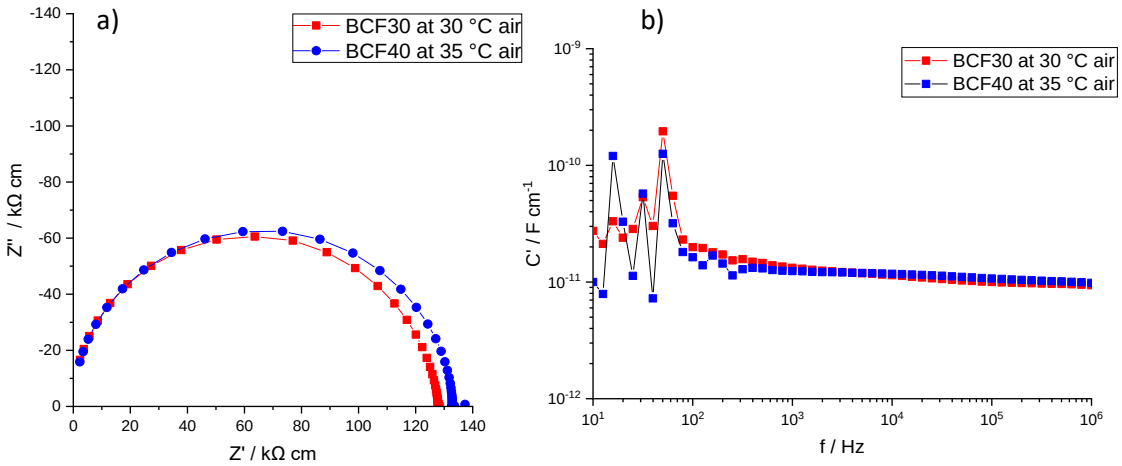

Figure 4.4. (a) Impedance complex plane plots, (b) capacitance spectroscopic plots, for BCF30 and BCF40 processed in air at 30 and 35 ℃, respectively.

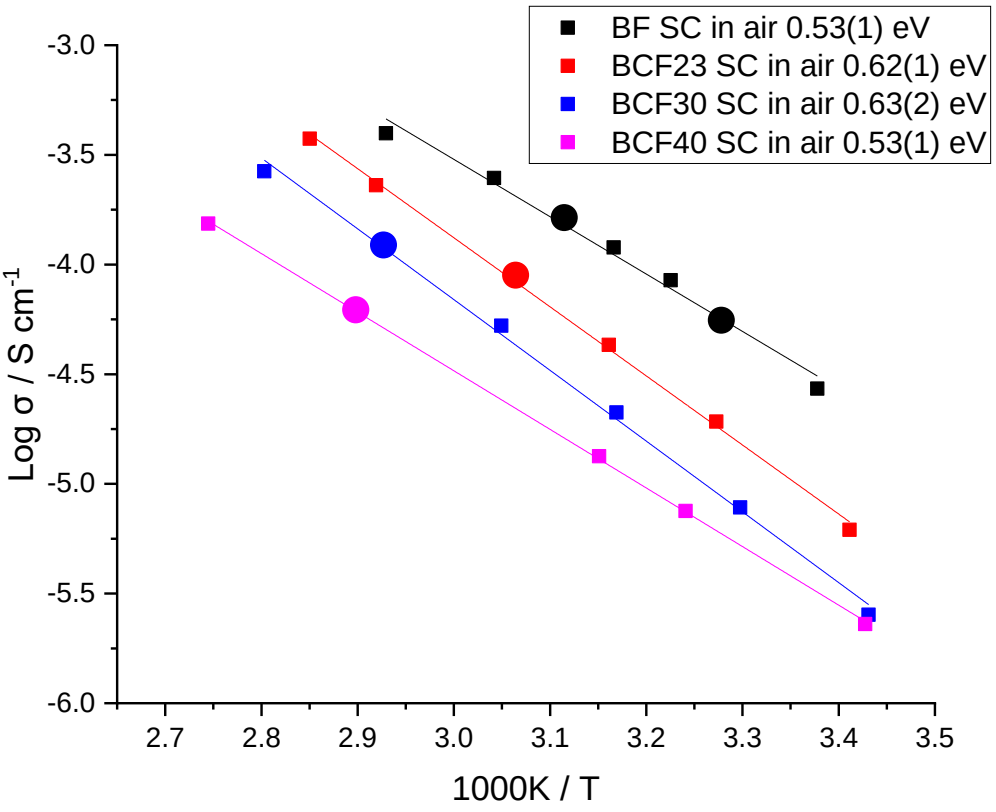

Figure 4.5. Arrhenius plots of the bulk conductivities for air-processed samples. The activation energies (eV) are shown beside each composition label. The circle points represent the data that were taken on cooling.

Further investigations of the materials' conduction mechanism were carried out by performing impedance spectroscopy as a function of pO_2 for all compositions processed in air. Impedance data of BCF23 and 30 (Figure 4.6) showed no obvious dependence on pO_2 at the measured temperatures (< 100 °C). The conductivities were almost identical and did not change with changing the atmosphere from oxygen to nitrogen (Figure 4.6). BF and BCF40, processed in air, behaved similarly (not shown).

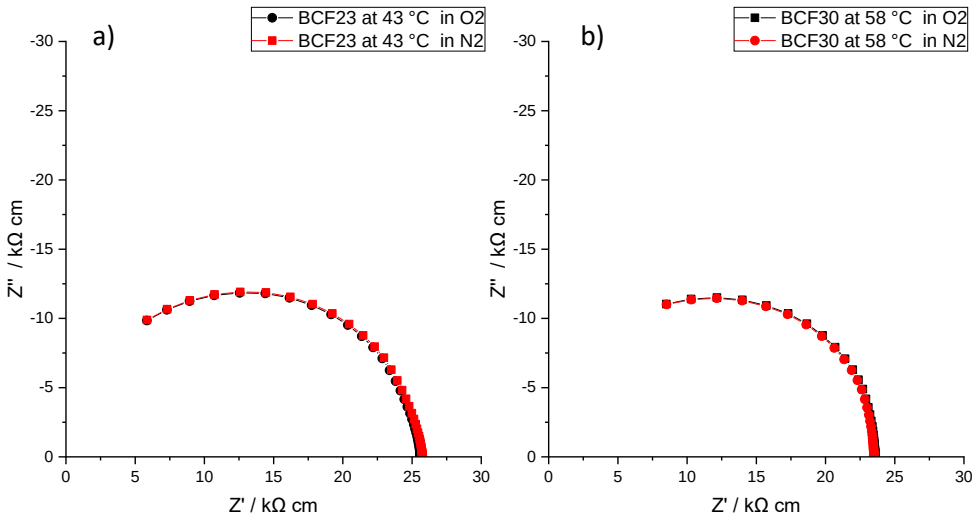

Figure 4.6. Impedance complex plane plots, Z, for (a) BCF23 and (b) BCF30 processed in air at 43 and 58 ℃, respectively, measured in dry O_2 and N_2.*

4.2.2.2. O_2-processed samples

The impedance response of BCF23, 30 and 40 processed in O_2 was measured between 20 and 100 ℃ in dry air. The impedance data sets were similar to those of air-processed samples. The Z* complex plane plots show one semicircle (Figure 4.7) that represents the bulk response based on the capacitance values (d). Both air- and O_2-processed samples impedance response were similar, but the conductivities of O_2-processed samples were higher (Figure 4.7a, b & c) indicating p-type conduction mechanism. The hole concentration was controlled by:

$$V_O^{\bullet\bullet} + \frac{1}{2}O_2 \rightarrow O_O^x + 2h^{\bullet} \qquad (4.1)$$

and therefore, the hole concentration increased with increasing pO_2 of the processing atmosphere. The holes are probably located in underbonded O^{2-} ions or alternatively, the location of holes might be on Fe as Fe^{4+}, as discussed in 4.3.

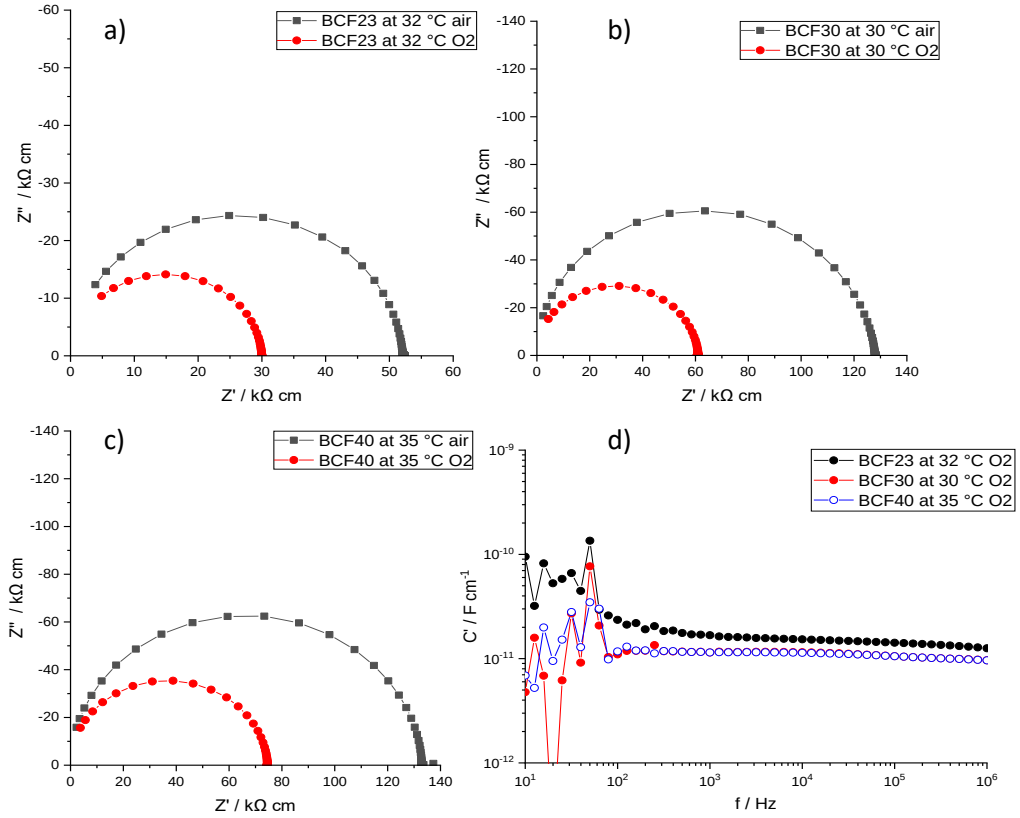

Figure 4.7. Impedance complex plane plots, Z, for (a) BCF23, (b) BCF30 and (c) BCF40 processed in air and O_2, (d) capacitance spectroscopic plots, for BCF23, BCF30 and BCF40 measured in O_2.*

4.2.2.3. N_2-processed samples

For the N_2-processed samples, the impedance measurements were performed in N_2 atmosphere to prevent the samples from being reoxidised. They were insulating at lower temperatures with $\sigma << 10^{-7}$ S/ cm (Figure 4.8a); so, the measurements were performed between 150 and 350 °C. Impedance data, for the N_2-processed samples, are summarised in Figure 4.8. The response of all three compositions was similar. The Z* complex plane plots (a) show a single semicircle at high frequencies with a low frequency Warburg spike (e.g. inset in b). The Z‟/ M‟ spectroscopic plots, for BCF23, show single overlapping peaks (c) at high frequencies indicating (a) sample homogeneity and (b) the sample contained one electrical component which represents the bulk effect. Also, the Z‟ spectroscopic plot shows a gradually increasing incline at low frequency.

The C‟ against frequency plots (d) show a plateau at high frequency representing the bulk capacitance of the samples with values, for example, around $2x10^{-11}$ F/cm at 288 °C for BCF23. The capacitance increased significantly reaching about 10^{-4} F/ cm at 10^{-2} Hz which is characteristic of ion blocking at a sample-electrode interface and double layer phenomena. The

combination of Warburg spike at low frequency (b), that represents diffusion of oxygen molecules towards, and away from, the sample electrode-interfaces, and the high capacitance value are evidence of oxide-ion conduction.

It appears that these acceptor-doped perovskite materials are good oxide-ion conductors, with activation energies in the range 0.80- 0.90 eV (Figure 4.9), under appropriate circumstances. It is important that the samples do not pick up oxygen in order to remain as predominantly oxide-ion conductors as if that happened, they would change from being oxide-ion conductors to p-type semiconductors with higher conductivity and lower activation energy (0.53-0.63 eV) (Figure 4.9 a-c). Figure 4.9 (d-f) show the effect of increasing doping concentration on the material conductivities. Air- and O_2-processed sample conductivities decreased slightly with increasing Ca^{2+} concentration while N_2-processed sample conductivities did not show obvious dependence on dopant concentration and only the conductivity of the sample with highest Ca^{2+} concentration, BCF40 slightly decreased

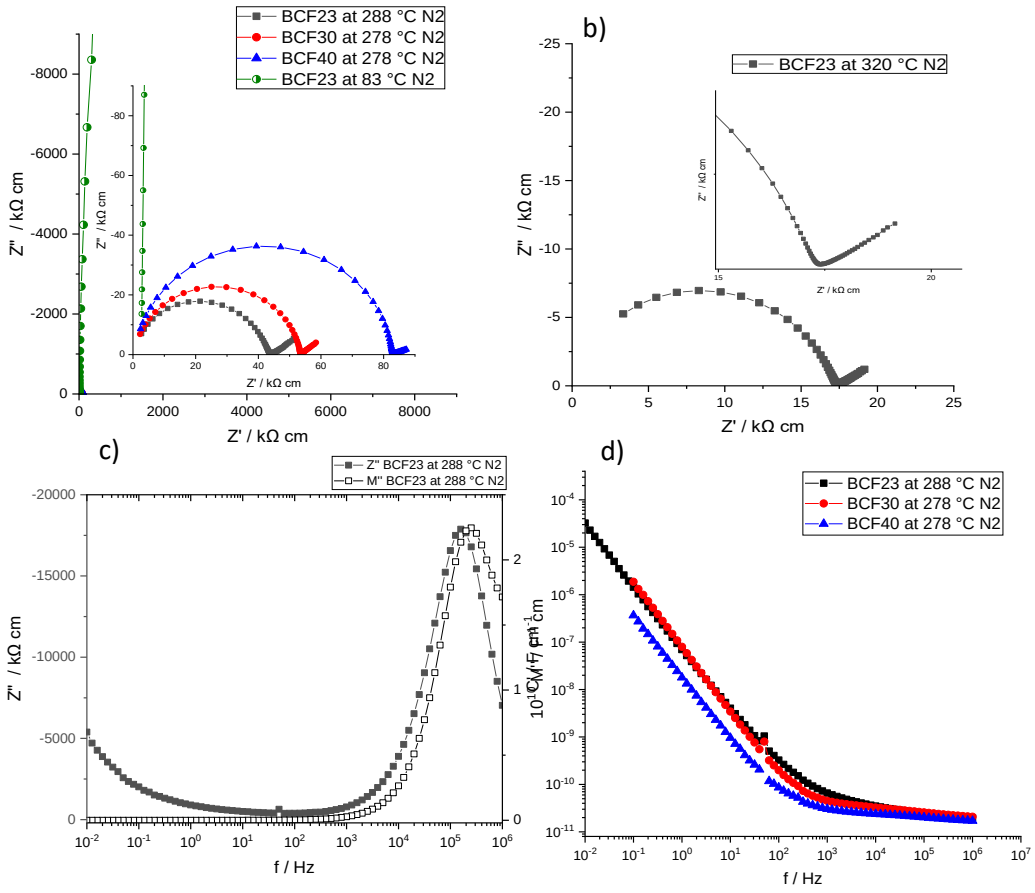

Figure 4.8. (a and b) impedance complex plane plots, Z, for the N_2-processed samples at different temperatures, as noted beside each graph, (c) Z''/ M'' spectroscopic plots for BCF23, processed in N_2, at 288 ℃, (d) capacitance spectroscopy plots, for BCF23, BCF30 and BCF40, that processed in N_2.*

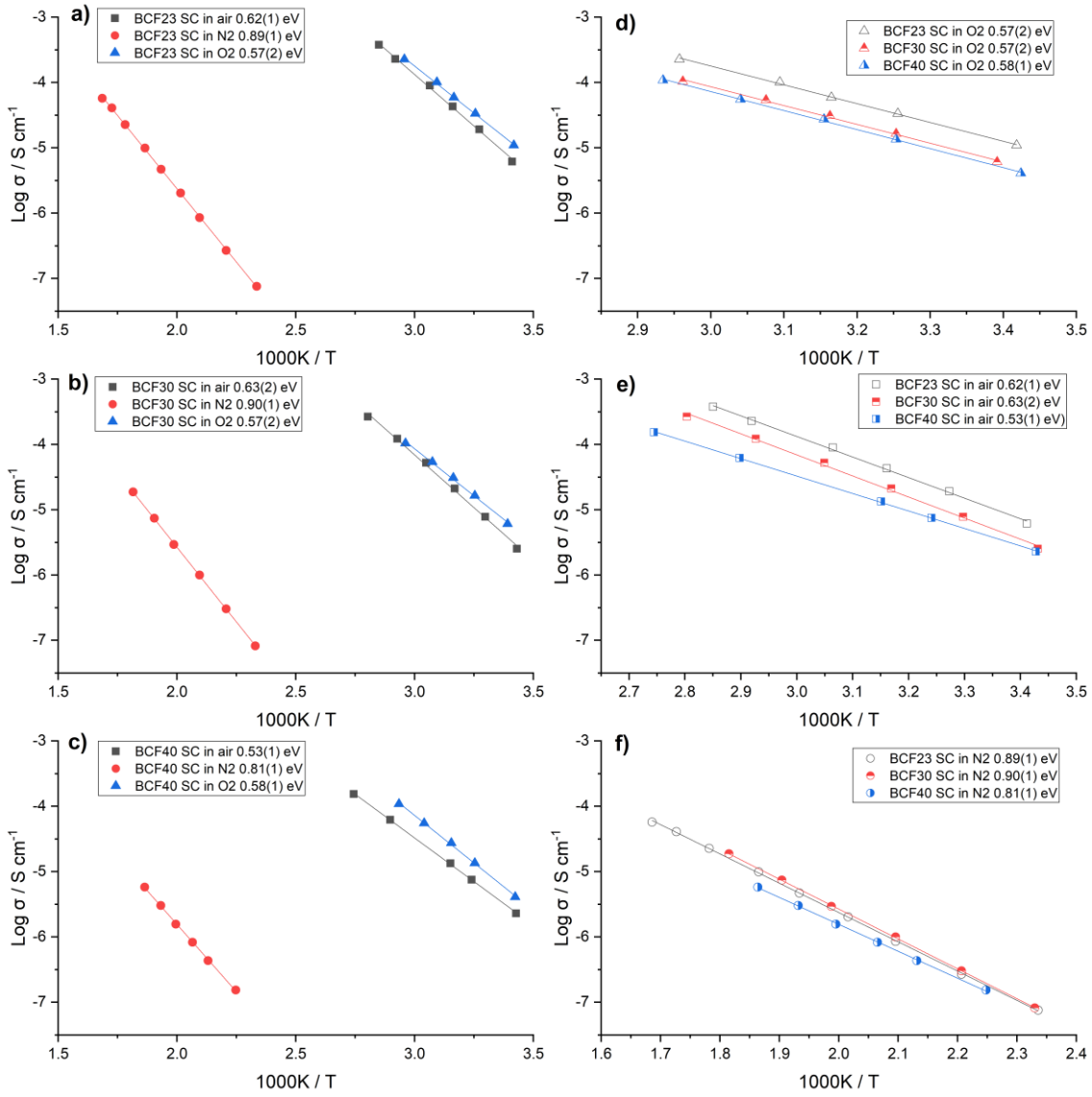

Figure 4.9. Arrhenius plots of the bulk conductivities for each sample in different processing conditions (a –c), and (d-f) Arrhenius plots of the bulk conductivities for different compositions in each processing atmosphere, as noted beside each graph. The activation energies in (eV) are shown beside each composition label.

The effect of changing the measuring atmosphere from N_2 to O_2 during impedance measurements was studied at different temperatures for all N_2-processed samples. The impedance was measured as a function of time after switching from N_2 to O_2 and back to N_2. Results are shown in Figure 4.10 and Figure 4.12. As the atmosphere changed from N_2 to O_2, the conductivities increased significantly, and the low frequency spike contracted or disappeared, as shown in Figure 4.10a, c and e. The C‘ plots show that the low frequency data were noisy (Figure 4.10d and f), indicating the reduced absence of ion blocking phenomena.

The impedance data, for the samples measured in O_2, showed less evidence of ionic conduction, and therefore, the conduction mechanism is primarily electronic.

In other words, the increase of pO_2 introduced p-type semi-conduction in all N_2-processed samples in which hole creation is controlled by eq 4.1. The effect of increasing pO_2 was not instantaneous but the sample conductivity took some time to reach the steady state, as shown in Figure 4.11.

The effect of increase of pO_2 and introduction of hole conduction depended on composition and temperature. The effect of pO_2 increased with increasing Ca^{2+} content in which the conductivity increased most in the sample with the highest Ca^{2+} content (i.e. with the highest number of oxygen vacancies) with increasing pO_2 at all temperatures (Figure 4.11). For example, the conductivity of BCF40 (c) increased by about half an order of magnitude at 250 ℃ while it increased slightly and by a factor of about two for BCF23 (a) and BCF30 (b), respectively at similar temperature.

Another important observation was that the effect of changing pO_2 was more noticeable at higher temperature. The conductivity increased slightly at lower temperature in O_2 while it increased significantly at temperatures higher than 250 ℃ (Figure 4.11). For example, the conductivity of BCF23 (a) increased slightly in O_2 at 250 ℃ while it increased about an order of magnitude at 328 ℃.

When the atmosphere was switched back to N_2, the sample conductivities fully recovered their original state at the lower and intermediate temperatures, and partially recovered them at higher temperatures (Figure 4.11). For example, BCF30 conductivity (b) was fully recovered at 250℃ and partially recovered at 280 ℃ after switching the atmosphere back to N_2 while BCF40 conductivity had not recovered at 280℃ (c).

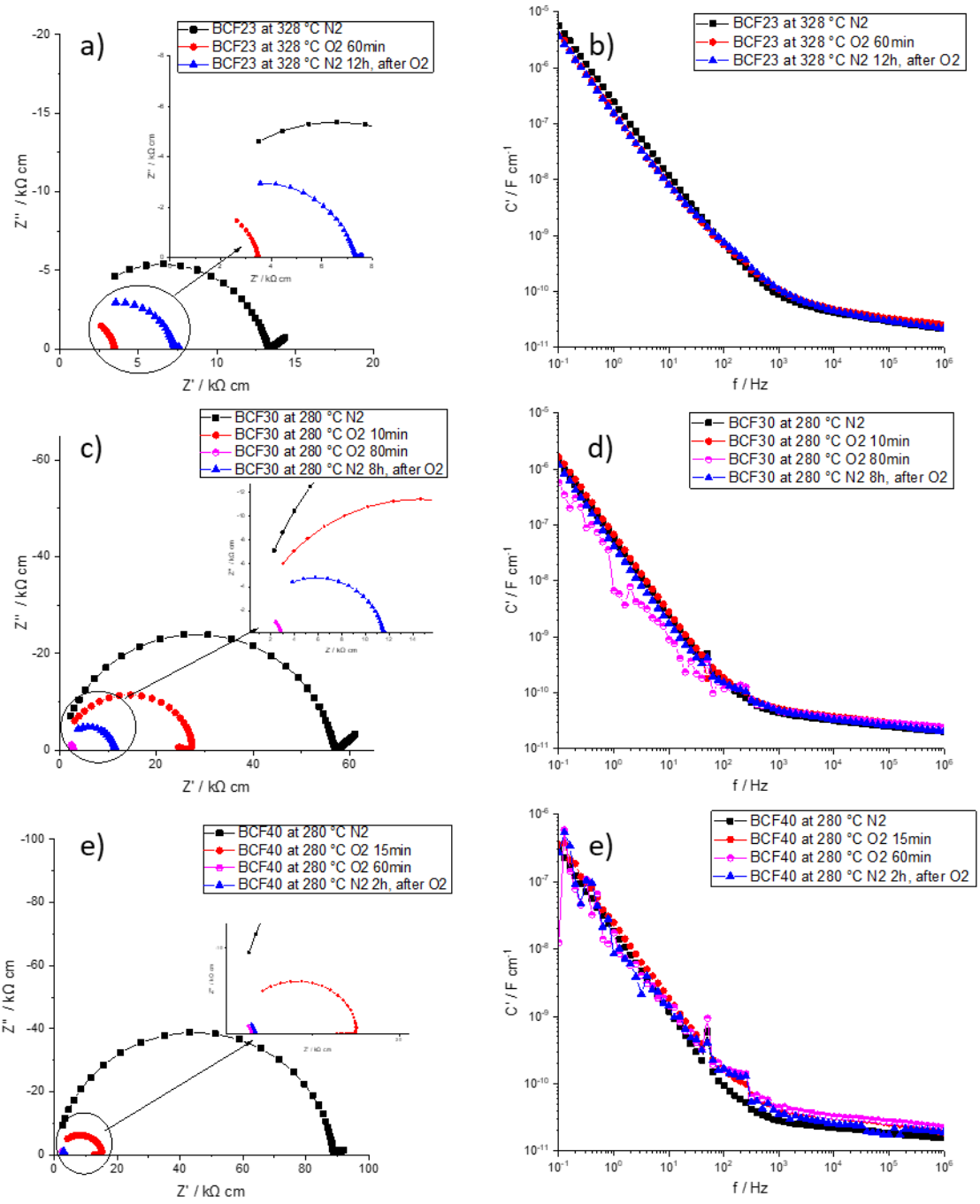

Figure 4.10. (a, c and e) Impedance complex plane plots, Z, for the N_2 processed samples, measured as function of pO_2, (b, d and f) capacitance spectroscopy plots, for the same samples, as noted beside each graph.*

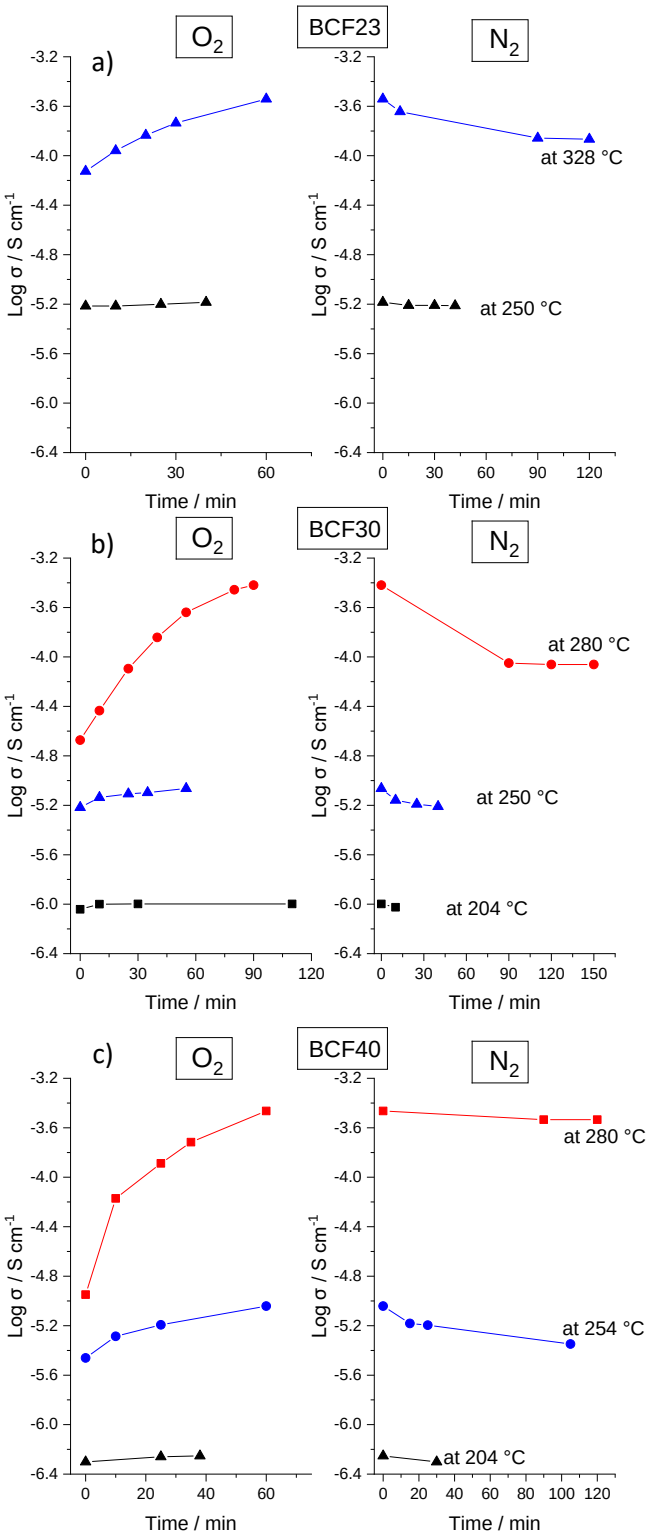

Figure 4.11. The measured conductivity of N_2-processed samples as function of time through the switching between O_2 and N_2 at different temperatures for (a) BCF23, (b) BCF30 and (c) BCF40.

The impedance of BCF40 was measured as a function of temperature after it had decreased by about two orders of magnitude in O_2 at 280 ℃ and did not recover after switching back to N_2. The impedance data are summarised in Arrhenius plots of the sample conductivity in Figure 4.12. The data were recorded after the sample reached a steady state in O_2 at 280 ℃ on cooling and was higher by about two orders of magnitude over the temperature range with a slight decrease in activation energy.

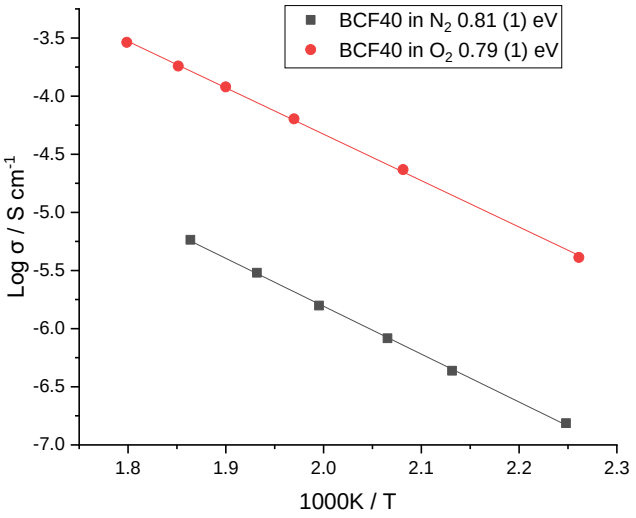

Figure 4.12. Arrhenius plots of the bulk conductivities for BCF40, processed in N_2, which was first measured in N_2, and second in O_2 on cooling after reaching a steady state at 280 ℃.

4.3. Discussion

Single-phase $BiFeO_3$ (BF) with a rhombohedrally-distorted perovskite structure was formed with small amount of Fe_2O_3 impurity. The existence of this impurity in BF is attributed to the volatilisation of Bi_2O_3 above 810 ℃. Homogeneous solid solutions of $Bi_{1-x}Ca_xFeO_{3-x/2}$ were formed where x = 0.23, 0.30 and 0.40. All XRD peaks of all three compositions showed no splitting indicating phase transformation to cubic perovskite. This result suggests that the rhombohedral distortion can be reduced and cubic phase of the perovskite can be stabilised by Ca^{2+} doping. As the Ca^{2+} content increases, all XRD peaks shifted slightly toward higher angle indicating a decrease in the lattice parameter. In many cases in literature, this was attributed to smaller radius of Ca^{2+} compared with Bi^{3+}, but this may not fully true since Bi and Ca have similar ionic radius in environment of CN12 and such effect could be counteracted by the repulsive effect of oxygen vacancy which can reduce the lattice strain caused by Ca-doping in BF. These results indicate that Ca^{2+} substitutes for Bi^{3+} on the A-sites of the perovskite structure. Oxygen vacancies are introduced to maintain charge neutrality due to the

substitution of higher valence Bi^{3+} by lower valence Ca^{2+}. These results are consistent with literature [4, 7, 8].

The electrical properties of $Bi_{1-x}Ca_xFeO_{3-x/2}$ studied here are sensitive to pO_2 both during the processing and subsequent cooling and also during impedance measurements. The conductivity of these materials varies from p-type semiconduction to oxide ion conduction, depending on pO_2 during the processing and subsequent cooling. Oxide ion conduction is well-established in other acceptor-doped perovskites such as $(La_{1-x}Sr_x)(Ga_{1-x}Mg_x)O_{3-x}$ [9]. So, it is no surprise that Ca-doped BF shows oxide ion conduction. However, BCF ceramics are good oxide ion conductors only in the absence of electronic conductivity that can be greatly reduced by processing and cooling in low pO_2. Recently, another acceptor-doped perovskite shows oxide-ion conduction, Ca-doped $BaTiO_3$, in which the conductivity varies from p-type to oxide ion conduction depending on the processing conditions [9]. So, oxide ion conduction might be a common feature of acceptor-doped of perovskite materials. This has been established recently in many examples of acceptor-doped $Ni_{0.5}Bi_{0.5}TiO_3$ perovskite which show good enhancement in oxide-ion conductivity [10].

The effect of oxygen partial pressure, during the processing and subsequent cooling, on electrical properties of all BCF compositions may be interpreted using Figure 4.13, in which oxide ions are the current carriers in the electrolytic domain, but below and above a certain pO_2,–electrons in the n-type domain and holes in p-type domain, become the main charge carriers, respectively. The change in all BCF conductivities were fully reversible in response to increase/ decrease in pO_2 during processing. BCF processed in N_2 falls in the electrolytic domain with activation energy in the range 0.80 to 0.91 eV while the air and O_2-processed samples fall in the p-type domain with activation energy in the range 0.53 to 0.63 eV.

The effect of changing pO_2 during impedance measurement is seen in N_2-processed samples but only at temperatures above 200 °C. The effect became obvious with increasing both temperature and Ca^{2+} content (i.e. with increasing oxygen vacancy concentration). The samples were oxide ion conductors in the electrolytic domain. However, with increasing pO_2, they entered the p-type domain giving rise to mixed p-type/ oxide ion conduction. In contrast, changing pO_2 during impedance measurements showed no effect on the conductivity of air-

and O_2-processed samples but these were measured only over the more limited temperature range between 20 and 100 ℃.

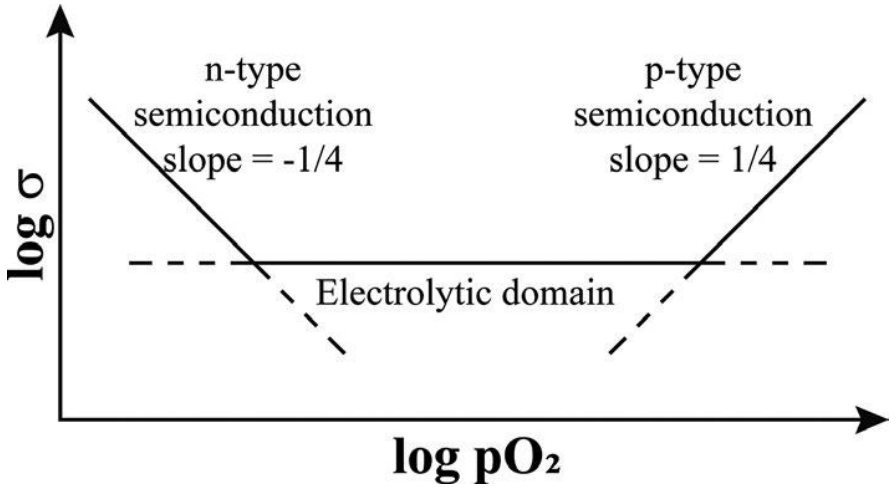

Figure 4.13. Schematic ionic and electronic conductivity domains as function of pO_2.

The reason for the variety of electrical properties of BCF is probably attributed to the presence of oxygen vacancies. These can absorb oxygen by dissociation and ionisation according to eq1 leading to variable oxygen content, given by the general formula $Bi_{1-x}Ca_xFeO_{(3-x/2)+\delta}$, in which δ depends on oxygen partial pressure during processing. Thus, if the samples are processed in high pO_2, they absorb oxygen and δ increases ($\delta > 0$) leading to hole creation and the observed p-type conductivity. By contrast, if they are processed in N_2, they are oxygen stoichiometric (i.e. $\delta \sim 0$) and therefore, are oxide ion conductors [11].

Since the p-type conductivity is thermally activated, the holes must be created on specific atom species. In the ceramic literature, the hole locations are widely assumed, but not proven, to be on unavoidable impurities such as Fe. Recent studies of high purity, acceptor-doped oxide ceramics show that in many cases, the only realistic location of holes is on oxygen (underbonded oxygen) as O^- ions, since there are no cations present that can be ionised to higher oxidation state [11-14]. In order to create those holes on the oxide ions, they should ionise readily.

We recall that O^{2-} ion is thermodynamically unstable in the gas phase and should spontaneously ionise to O^-. It is stabilised in a crystal lattice by the additional lattice energy associated with formation of O^{2-} ions. So, oxygen ions, that are surrounded by positive charge less than 2+, can ionise readily to O^-. Oxygen ions, that are in the vicinity of accepter dopant,

Ca, at a sample surface or/ and at a grain boundary, might be regarded as underbonded and therefore, can ionise readily.

In the present materials, Fe^{3+} ion is the alternative source of holes, since there are no other cations that can be oxidised any further. In principle, formation of Fe^{4+} can be the alternative charge composition mechanism to the creation of oxygen vacancies in BCF. However, there is clear evidence for oxide ion conduction in the N_2-processed samples (Figure 4.8) and therefore, for creation of oxygen vacancies as the main charge compensation mechanism. Furthermore, Mossbauer spectroscopy studies show no existence of Fe^{4+} in BCF processed in air indicating that the oxygen vacancy is the main charge compensation mechanism [15-19]. Also Rubi et al showed no evidence of Fe^{4+} existence and the main charge compensation mechanism is creation of oxygen vacancies using Mossbauer spectroscopy and also found that the magnetic behaviour for both doped and undoped samples qualitatively similar indicating no change in Fe^{3+} oxidation state [20].

We conclude that, O^{2-} ions are the main source of holes similar to other accepter doped perovskite such as Ca-doped BT, but Fe^{3+} ions might be included somehow. Moreover, processing the samples in air or O_2 lead to oxygen absorption, and therefore p-type conduction, in which the holes are mainly located on oxygen as O^-.

4.4. Conclusions

Solid solutions of $Bi_{1-x}Ca_xFeO_{3-x/2}$ (where: x = 0, 0.23, 0.3 and 0.4) were formed by conventional solid state reaction. The higher valence Bi^{3+} was substituted by lower valence Ca^{2+} and charge neutrality was maintained by creation of oxygen vacancies. The rhombohedral distortion of the perovskite structure of BF was stabilised towards cubic by Ca^{2+} doping.

The electrical properties of all three compositions of Ca-doped BF were sensitive to the pO_2 during the processing and subsequent cooling. The conductivity of these materials changed by few orders of magnitude, and the properties varied from oxide ion conduction to p-type semiconduction with increasing pO_2 during the processing and subsequent cooling.

The variety of the electrical properties of BCF is probably attributed to the presence of oxygen vacancies. These can absorb oxygen by dissociation and ionisation according to eq 4.1 leading to variable oxygen content, given by the general formula $Bi_{1-x}Ca_xFeO_{(3-x/2)+\delta}$, in which δ depends on oxygen partial pressure during processing. Thus, if the samples are processed in high pO_2, they absorb oxygen and δ increases ($\delta > 0$) leading to hole creation and the observed

p-type conductivity. The holes are believed to be located mainly on under bonded oxygen but oxidation of Fe^{3+} ions might be involved somehow. By contrast, if they are processed in N_2, they are oxygen stoichiometric (i.e. $\delta \sim 0$) and therefore, are oxide ion conductors.

The conductivities of N_2-processed samples showed pO_2-dependence during impedance measurements at temperatures above 200 °C. With increasing pO_2, the p-type conductivity was introduced and the samples became mixed p-type/ and oxide ion conductor. This change was dependent on Ca^{2+} content and temperature. The conductivity of the sample with highest Ca^{2+} content increased the most and this increase was about two of orders of magnitude at the highest temperature.

4.5. References

1. Arnold, D., *Composition-driven structural phase transitions in rare-earth-doped bifeo₃ ceramics: a review.* IEEE Transactions on Ultrasonics, Ferroelectrics, and Frequency Control, 2015. **62**(1): p. 62-82.
2. Arnold, D.C., K.S. Knight, F.D. Morrison, and P. Lightfoot, *Ferroelectric-Paraelectric Transition inBiFeO3: Crystal Structure of the OrthorhombicβPhase.* Physical Review Letters, 2009. **102**(2).
3. Catalan, G. and J.F. Scott, *Physics and Applications of Bismuth Ferrite.* Advanced Materials, 2009. **21**(24): p. 2463-2485.
4. Masó, N. and A.R. West, *Electrical Properties of Ca-Doped BiFeO3 Ceramics: From p-Type Semiconduction to Oxide-Ion Conduction.* Chemistry of Materials, 2012. **24**(11): p. 2127-2132.
5. Maso, N., H. Beltran, M. Prades, E. Cordoncillo, and A.R. West, *Field-enhanced bulk conductivity and resistive-switching in Ca-doped BiFeO3 ceramics.* Phys Chem Chem Phys, 2014. **16**(36): p. 19408-16.
6. Alotaibi, M., F. Almutairi, and A.R. West, *Resistive‐switching in yttria‐stabilized hafnia ceramics.* Journal of the American Ceramic Society, 2022. **106**(2): p. 822-828.
7. Chen, W.-t., A.J. Williams, L. Ortega-San-Martin, M. Li, D.C. Sinclair, W. Zhou, and J.P. Attfield, *Robust Antiferromagnetism and Structural Disorder in Bi x Ca1− x FeO3 Perovskites.* Chemistry of Materials, 2009. **21**(10): p. 2085-2093.
8. Tu, C.S., C.M. Hung, Z.R. Xu, V.H. Schmidt, Y. Ting, R.R. Chien, Y.T. Peng, and J. Anthoninappen, *Calcium-doping effects on photovoltaic response and structure in multiferroic BiFeO3 ceramics.* Journal of Applied Physics, 2013. **114**(12): p. 124105.
9. Ren, P., N. Masó, Y. Liu, L. Ma, H. Fan, and A.R. West, *Mixed oxide ion and proton conduction and p-type semiconduction in BaTi0.98Ca0.02O2.98 ceramics.* Journal of Materials Chemistry C, 2013. **1**(13): p. 2426.
10. Ren, P., N. Masó, and A.R. West, *Hole conductivity in oxygen-excess BaTi1−xCaxO3−x+δ.* Physical Chemistry Chemical Physics, 2013. **15**(48): p. 20943.
11. Masó, N. and A.R. West, *Electronic Conductivity in Yttria-Stabilized Zirconia under a Small dc Bias.* Chemistry of Materials, 2015. **27**(5): p. 1552-1558.
12. Guo, M., N. Masó, Y. Liu, and A.R. West, *Electrical Properties and Oxygen Stoichiometry of Ba1–xSrxTiO3−δ Ceramics.* Inorganic Chemistry, 2017. **57**(1): p. 64-71.

13. Prades, M., N. Masó, H. Beltrán, E. Cordoncillo, and A.R. West, *Field enhanced bulk conductivity of BaTiO3 : Mg ceramics.* Journal of Materials Chemistry, 2010. **20**(25): p. 5335.
14. Schiemer, J., R. Withers, L. Norén, Y. Liu, L. Bourgeois, and G. Stewart, *Detailed Phase Analysis and Crystal Structure Investigation of a Bi1−xCaxFeO3−x/2 Perovskite-Related Solid Solution Phase and Selected Property Measurements Thereof.* Chemistry of Materials, 2009. **21**(18): p. 4223-4232.

1. Arnold, D., *Composition-driven structural phase transitions in rare-earth-doped bifeo₃ ceramics: a review.* IEEE Transactions on Ultrasonics, Ferroelectrics, and Frequency Control, 2015. **62**(1): p. 62-82.
2. Arnold, D.C., K.S. Knight, F.D. Morrison, and P. Lightfoot, *Ferroelectric-Paraelectric Transition inBiFeO3: Crystal Structure of the OrthorhombicβPhase.* Physical Review Letters, 2009. **102**(2).
3. Catalan, G. and J.F. Scott, *Physics and Applications of Bismuth Ferrite.* Advanced Materials, 2009. **21**(24): p. 2463-2485.
4. Masó, N. and A.R. West, *Electrical Properties of Ca-Doped BiFeO3 Ceramics: From p-Type Semiconduction to Oxide-Ion Conduction.* Chemistry of Materials, 2012. **24**(11): p. 2127-2132.
5. Maso, N., H. Beltran, M. Prades, E. Cordoncillo, and A.R. West, *Field-enhanced bulk conductivity and resistive-switching in Ca-doped BiFeO3 ceramics.* Phys Chem Chem Phys, 2014. **16**(36): p. 19408-16.
6. Alotaibi, M., F. Almutairi, and A.R. West, *Resistive-switching in yttria-stabilized hafnia ceramics.* Journal of the American Ceramic Society, 2022. **106**(2): p. 822-828.
7. Chen, W.-t., A.J. Williams, L. Ortega-San-Martin, M. Li, D.C. Sinclair, W. Zhou, and J.P. Attfield, *Robust Antiferromagnetism and Structural Disorder in Bi x Ca1− x FeO3 Perovskites.* Chemistry of Materials, 2009. **21**(10): p. 2085-2093.
8. Tu, C.S., C.M. Hung, Z.R. Xu, V.H. Schmidt, Y. Ting, R.R. Chien, Y.T. Peng, and J. Anthoninappen, *Calcium-doping effects on photovoltaic response and structure in multiferroic BiFeO3 ceramics.* Journal of Applied Physics, 2013. **114**(12): p. 124105.
9. Ren, P., N. Masó, Y. Liu, L. Ma, H. Fan, and A.R. West, *Mixed oxide ion and proton conduction and p-type semiconduction in BaTi0.98Ca0.02O2.98 ceramics.* Journal of Materials Chemistry C, 2013. **1**(13): p. 2426.
10. Yang, F., M. Li, L. Li, P. Wu, E. Pradal-Velázque, and D. Sinclair, *Optimisation of oxide-ion conductivity in acceptor-doped Na 0.5 Bi 0.5 TiO 3 perovskite: approaching the limit?* Journal of Materials Chemistry A, 2017. **5**(41): p. 21658-21662.
11. Ren, P., N. Masó, and A.R. West, *Hole conductivity in oxygen-excess BaTi1−xCaxO3−x+δ.* Physical Chemistry Chemical Physics, 2013. **15**(48): p. 20943.
12. Masó, N. and A.R. West, *Electronic Conductivity in Yttria-Stabilized Zirconia under a Small dc Bias.* Chemistry of Materials, 2015. **27**(5): p. 1552-1558.
13. Guo, M., N. Masó, Y. Liu, and A.R. West, *Electrical Properties and Oxygen Stoichiometry of Ba1–xSrxTiO3−δ Ceramics.* Inorganic Chemistry, 2017. **57**(1): p. 64-71.
14. Prades, M., N. Masó, H. Beltrán, E. Cordoncillo, and A.R. West, *Field enhanced bulk conductivity of BaTiO3 : Mg ceramics.* Journal of Materials Chemistry, 2010. **20**(25): p. 5335.

15. Schiemer, J., R. Withers, L. Norén, Y. Liu, L. Bourgeois, and G. Stewart, *Detailed Phase Analysis and Crystal Structure Investigation of a Bi1−xCaxFeO3−x/2 Perovskite-Related Solid Solution Phase and Selected Property Measurements Thereof.* Chemistry of Materials, 2009. **21**(18): p. 4223-4232.
16. Chauhan, S., M. Kumar, S. Chhoker, S. Katyal, and M. Singh, *Substitution driven structural and magnetic transformation in Ca-doped BiFeO 3 nanoparticles.* RSC advances, 2016. **6**(49): p. 43080-43090.
17. Rubi, D., F.G. Marlasca, M. Reinoso, P. Bonville, and P. Levy, *Magnetism and electrode dependant resistive switching in Ca-doped ceramic bismuth ferrite.* Materials Science and Engineering: B, 2012. **177**(6): p. 471-475.
18. Bhushan, B., D. Das, A. Priyam, N. Vasanthacharya, and S. Kumar, *Enhancing the magnetic characteristics of BiFeO3 nanoparticles by Ca, Ba co-doping.* Materials Chemistry and Physics, 2012. **135**(1): p. 144-149.
19. Bhushan, B., A. Basumallick, S. Bandopadhyay, N. Vasanthacharya, and D. Das, *Effect of alkaline earth metal doping on thermal, optical, magnetic and dielectric properties of BiFeO3 nanoparticles.* Journal of Physics D: Applied Physics, 2009. **42**(6): p. 065004.
20. Rubi, D., F. Marlasca, M. Reinoso, P. Bonville, and P. Levy, *Magnetism and electrode dependant resistive switching in Ca-doped ceramic bismuth ferrite.* Materials Science and Engineering: B, 2012. **177**(6): p. 471-475.

Chapter 5 . Equivalent circuit modelling of Ca-doped $BiFeO_3$

5.1. Introduction

In order to analyse impedance data further and interpret the electrical behaviour of samples, the modelling of experimental data and finding the most appropriate equivalent circuit is an essential step that leads to accurate extraction of impedance parameters. To achieve this step, the data were presented in different formats to find the best equivalent circuit that fits data sets in various formalisms. The quality and accuracy of fitting was assessed by (i) visual inspection of the data, (ii) the quality of agreement between experimental and fitted data and (iii) realistic values of extracted parameters[1-4].

In this section, several data sets of three compositions of $Bi_{1-x}Ca_xFeO_3$ (where x= 0.23, 0.30 and 40) processed in different atmospheres were analysed to find the most appropriate equivalent circuits. First, data sets for BCF30 samples processed in air and N_2 were fitted to find their best equivalent circuit, which was then used to fit data of other compositions.

The conductivity of these materials changed by many orders of magnitude and the properties varied from p-type semi-conduction to oxide-ion conduction with decreasing pO_2 during the processing and subsequent cooling. Air- and O_2-processed sample impedances were similar and their impedance complex plane plots showed only a single semicircle related to the bulk with no clear evidence of the existence of other electrical regions such as grain boundaries or electrode response (fig 3, 4 & 7 in chapter 4), while N_2-processed samples showed a single semicircle at high frequencies with a Warburg spike at low frequency (fig 8 in chapter 4).

The C` plot, for example fig 3c, of the air- and O_2-processed samples shows another possible electrical region at low frequency not seen in the Z* complex plane plot and M`` / Z`` spectroscopy plots (fig 3a & b in chapter 4). So, fitting is an important step, especially in this case, to find the right equivalent circuit and therefore extract different impedance parameters.

A number of possible circuits, that could represent the impedance response in such materials are shown in Figure 5.1. These include only the bulk response in circuits A and B, bulk with a possible series response such as gb (circuit C) and bulk with a parallel dielectric response (circuits D and E). These circuits were considered and tested in order to find the most appropriate equivalent circuit.

Fitting impedance data at lower temperatures is considered first to examine the bulk response separately. This would help to know the bulk parameters and their temperature dependence before subsequent fitting of more complex circuits, that might include grain boundary (gb) and electrode responses, at higher temperatures.

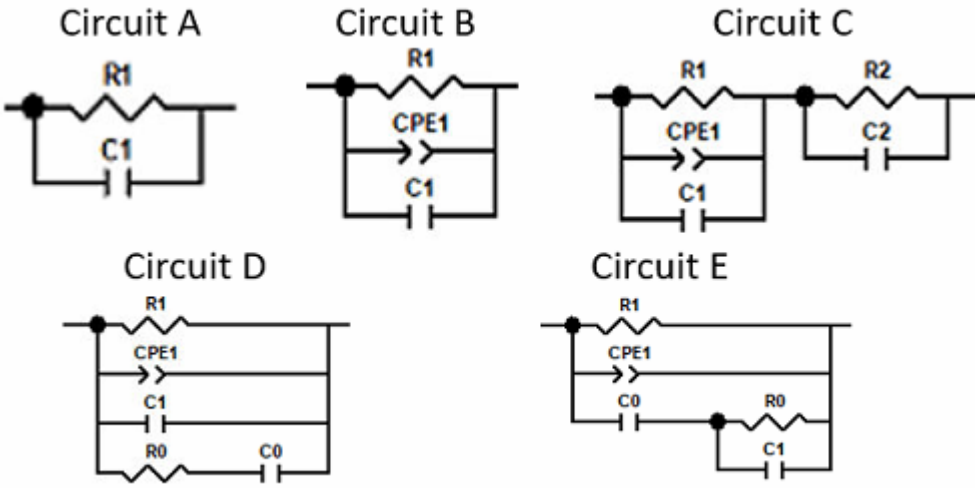

Figure 5.1. Possible equivalent circuits used to model impedance data.

5.2. Results and discussion

5.2.1. BCF30 fitting data

5.2.1.1. Air-processed sample

Impedance Z* data for BCF30 processed in air showed only a single semicircle that, at first sight, can be modelled by a parallel RC element (circuit A), where R represent the resistance and C its capacitance. This circuit represents an ideal Debye-like behaviour where R and C are single-valued and therefore, C` and Y` are frequency-independent. However, in reality C` and Y` are rarely frequency-independent which is the case here and this circuit does not fit the experimental data at all measured temperatures and frequencies (Figure 5.2).

In practice most electroceramics show non-ideal Debye-like data and C` and Y` are often frequency-dependent (Figure 5.2c & d), at intermediate and high frequency respectively due to Jonscher power law behaviour. This power law response can usually be modelled by inclusion of a parallel CPE in circuit A (i.e. parallel R-C-CPE (circuit B)) [2, 5-7]. Figure 5.3 shows fitting to the data for circuit B. The quality and visual inspection of the fitting improved for all different formalisms. However, the C` plot showed a second plateau at low frequency and clear

deviation between fitting and experimental data especially at higher temperature (Figure 5.3C). This probably indicates the existence of a second electrical region.

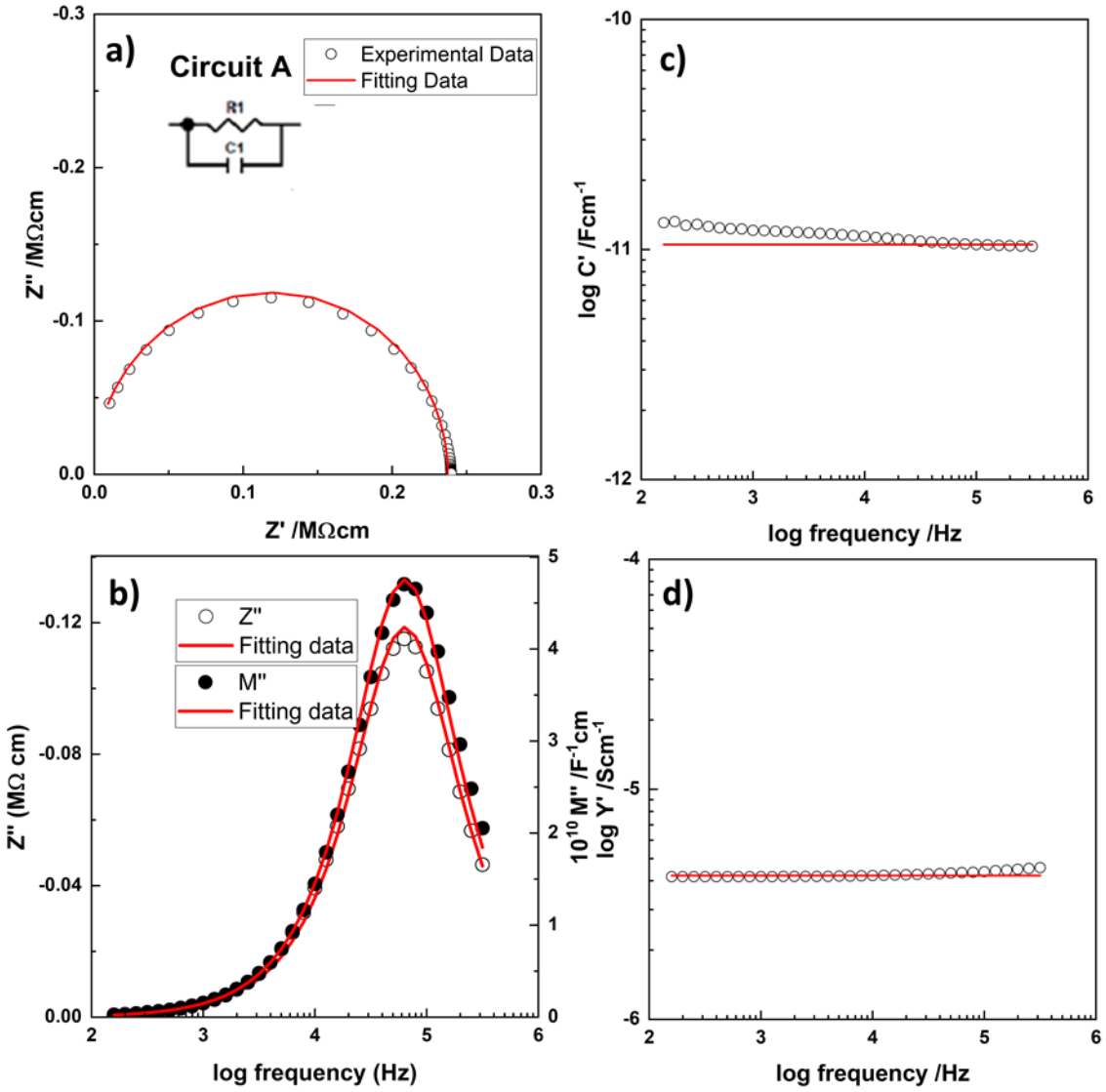

Figure 5.2. The impedance response for BCF30 at 21 ℃, fitted to circuit A.

In order to fit this extra capacitance, a parallel R-C element was added in series with circuit B (i.e. parallel R_1- C_1-CPE in series with parallel R_2-C_2 (circuit C)). This circuit showed high quality fitting and excellent agreement between experimental and fitted data for all four impedance formalisms (Figure 5.4), with low residuals (Figure 5.5) and logical values for impedance parameters at all measured temperatures. In such cases where R_2 is much smaller than R_1 (i.e. ~$R_2 < 0.05R_1$) and C_2 larger than C_1 by two orders of magnitude (Table 5.1), the R_2-C_2 region cannot be seen either in impedance complex plane plot or in modulus spectroscopy plots since Z* highlights the region with largest resistance and M`` is dominated

by the region with the smallest capacitance. So, this circuit can be interpreted by the following: i) the high frequency electrical region is attributed to the bulk where R_1= 230 kΩ.cm and C_1= 9.98 pF/cm at 20 °C, ii) the low frequency electrical region probably is attributed to grain boundaries based on its capacitance (C_2= 797 pF/cm, R_2= 9.90 kΩ.cm at 21 °C).

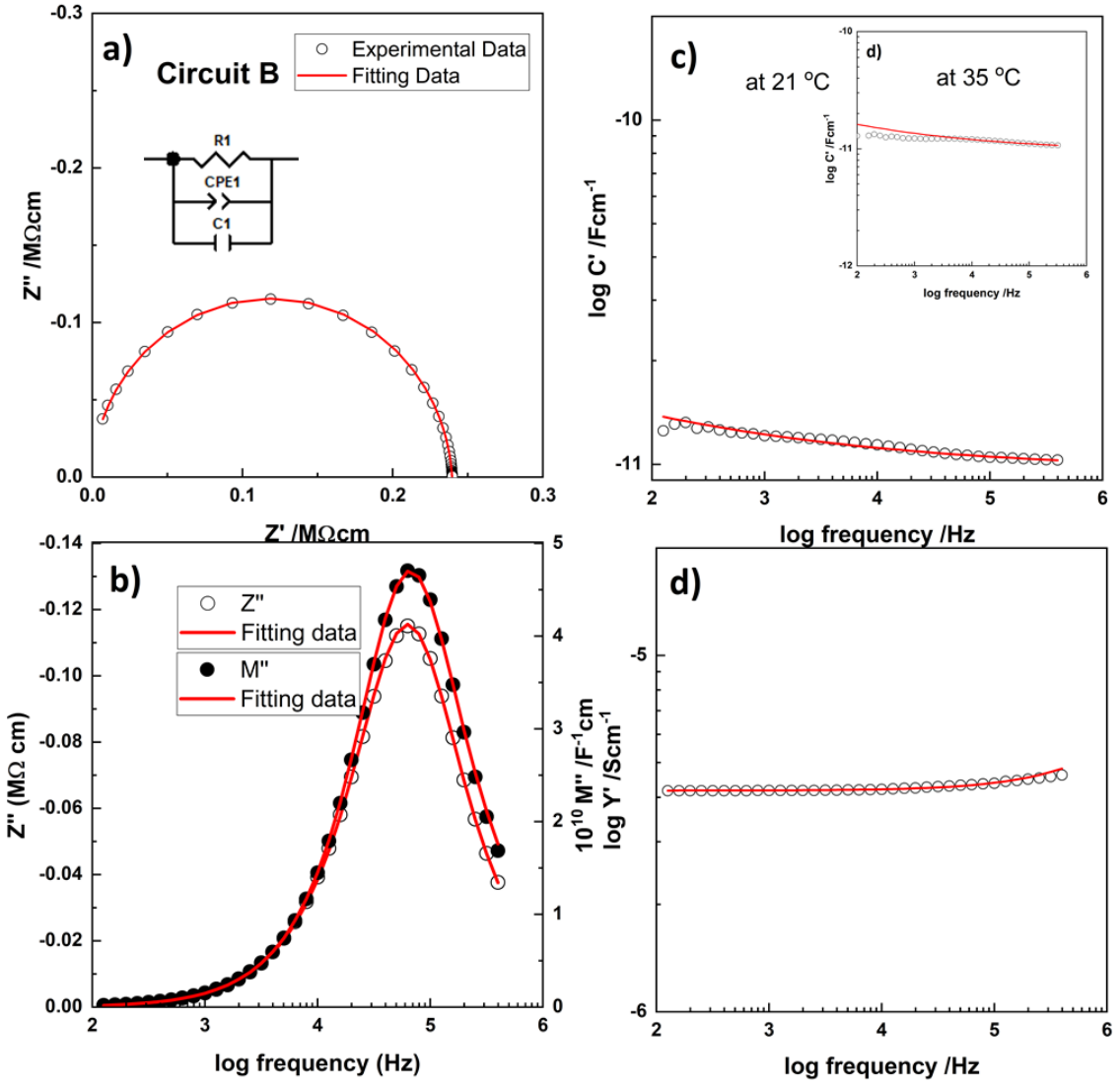

Figure 5.3. The impedance response for BCF30 at 21 °C, fitted to circuit B and at 35°C, inst(c).

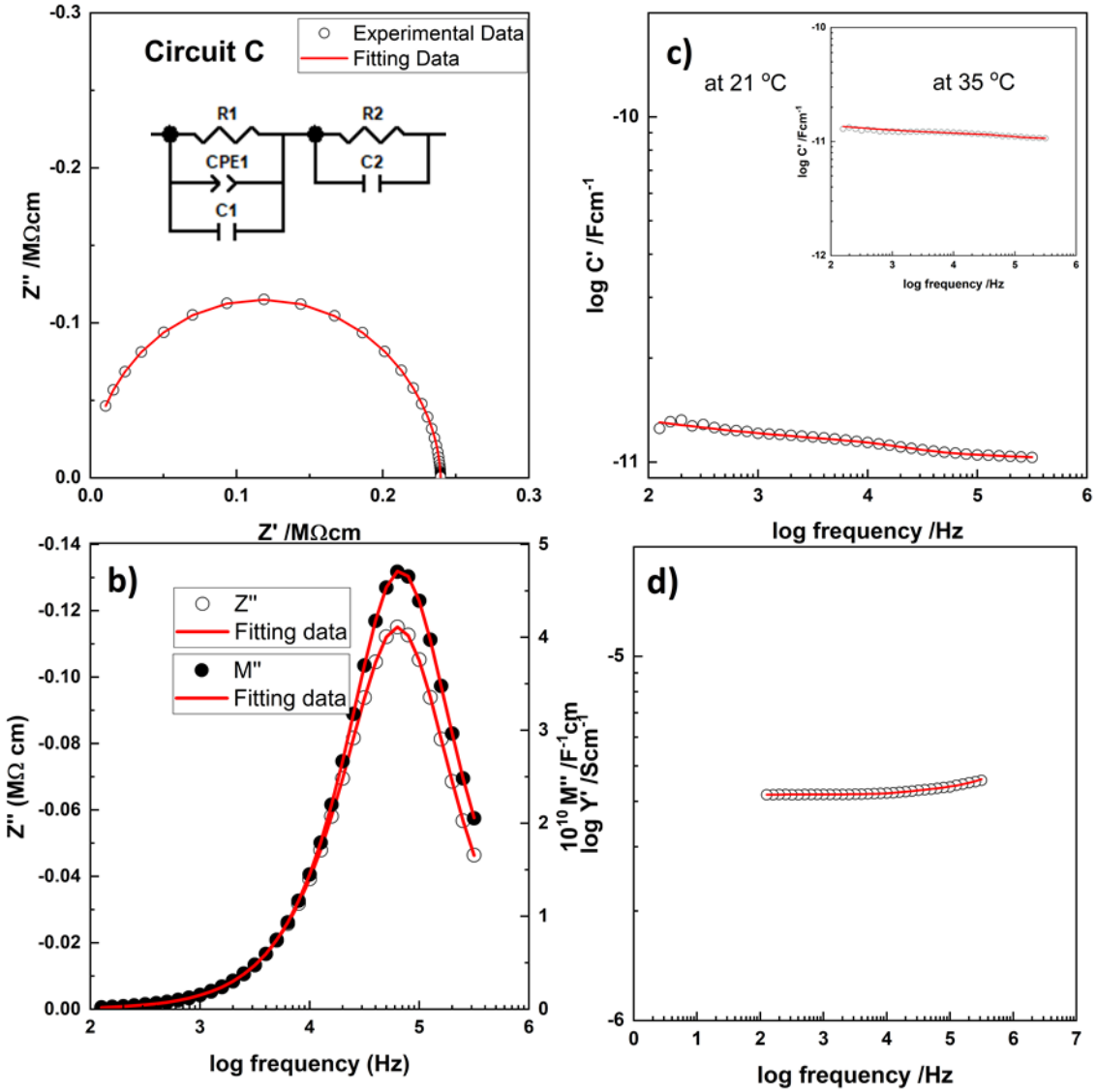

Figure 5.4. The impedance response for BCF30 at 21 °C, fitted to circuit C.

Recently, circuit D (Figure 5.1) was used for accurate fitting of single crystal impedance data of YSZ [4], where the data showed no contribution from grain boundaries, but appeared to highlight the existence of parallel dielectric relaxation phenomena. Also, other oxide ion conductors such as calcia-stabilised zirconia [8] and yttria-stabilised hafnia [9] were fitted to the same circuit as YSZ to fit a dipole re-orientation effect. The logical origin of the dipoles is the attraction between the oppositely charged acceptor dopants and positively-charged oxygen vacancies, for example $V_o^{\bullet\bullet}$ - $Y_{Zr}^{`}$.

The existence of oxygen vacancies as the main charge compensation mechanism and associated oxide-ion conduction, especially in N_2-processed samples, are reported for BCF [10-13]. It is possible that dielectric relaxation processes could be present here, and therefore it is

worthwhile to examine the inclusion of a dielectric response in the equivalent circuit and its effect on fitting quality. Also, since BF is ferroelectric below T_c=830 ℃ [11, 12, 14, 15], a dielectric response due to reorientation of ferroelectric domains or dipoles is another possibility.

A series R_0C_0 element is added in circuit D and E that could represent dielectric relaxation processes. These circuits were then used to fit data. The residuals together with the equivalent circuits are shown in Figure 5.5 and the extracted parameters are listed in Table 5.1. Both circuits showed good agreement between calculated and experimental data, and the residuals are as low as those of circuit C (Figure 5.5c, d & e). Circuit E showed reasonable values for the bulk capacitance and resistance (Table 5.1) and so, it is difficult to distinguish and choose the best circuit between circuit C and E at this point. However, circuit D become less favourable among the three circuits due to unrealistically high bulk capacitance (Table 5.1).

Table 5.1. Fitted parameters of the different circuit, for BCF30, processed in air at 21 ℃.

Circuit	T (℃)	R_1 (KΩcm)	R_2 (KΩcm)	R_0 (KΩcm)	A_1 ($pScm^{-1}$)	n_1	C_1 ($pFcm^{-1}$)	C_2 ($pFcm^{-1}$)	C_0 ($pFcm^{-1}$)	Weighted sum of squares ($x10^{-3}$)
A	21	237(1)	-		-	-	10.5(1)	-		125
B	21	240(1)	-		19.72(47)	0.78	9.55(3)	-		4
C	21	195(5)	45(5)	-	12.63(27)	0.78	9.98(2)	797(66)		0.2
D	21	240(1)	-	40.4(18)	12.31(27)	0.78	169(4)		10.47(3)	0.2
E	21	240(1)	-	$11.9(45)x10^3$	12.31(27)	0.78	9.86(1)		0.61(2)	0.2

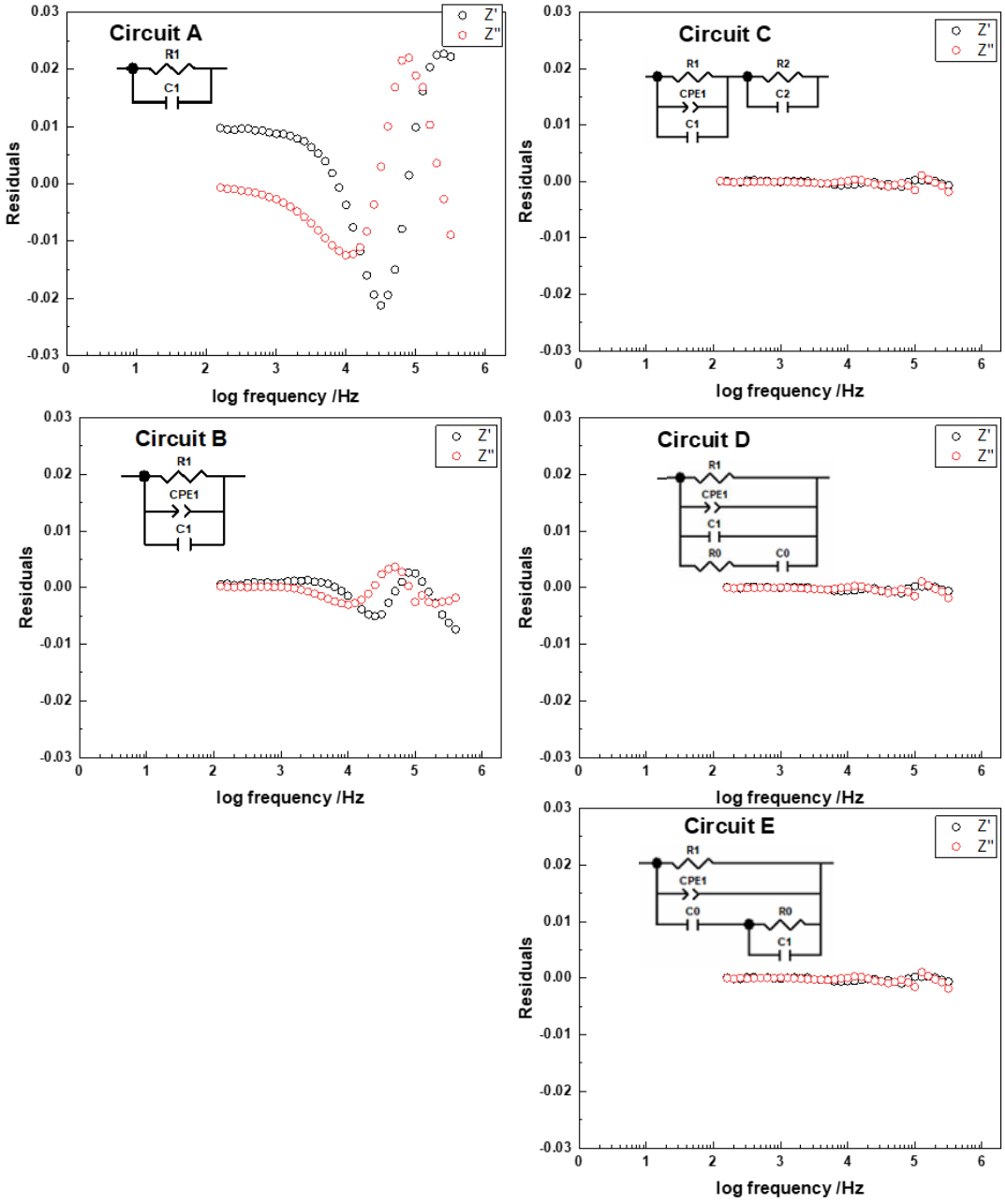

Figure 5.5. Fitting residuals from different possible circuits, for CBF30, processed in air, at 21℃.

5.2.1.2. N_2-processed sample

Samples processed in N_2 showed much higher resistivity and the impedance measurements have been performed at higher temperatures (130 – 300 ℃). Unlike air-processed samples, at the lowest temperature, the sample impedance is dominated by the bulk which allows us to find a partial circuit that fits the data sets at this temperature.

Circuit B showed an excellent agreement between fitted and experimental data at 130℃ (Figure 5.6) and logical impedance parameter values (Table 5.2). It is the only temperature that circuit B gave high quality fitting with low residuals (Figure 5.7). Also, circuits C to E showed good agreement between fitted and experimental data at this temperature and their residuals are as low as those of Circuit B (Figure 5.7). However, the error in in R_2/ R_0 and C_2/ C_0 values is so high (> 60%) (Table 5.2) which indicates that use of these more complex circuits cannot be justified to fit data sets at lower temperature. These results indicate that circuit B is the most appropriate equivalent circuit since the bulk response only was detected at lower temperatures over the measured frequency range.

At intermediate temperatures, circuit B fitting became poorer with high residuals (Figure 5.8). In contrast, circuits C (Figure 5.9) to E showed high fitting accuracy with low residuals (Figure 5.8) between calculated and experimental data. All three circuits, for example at 180℃, showed reasonable fitted parameters(Table 5.2).

It is more reasonable that circuit C does not fit lower temperature data, since the series region is out of the measurement window and only the bulk response is detected. As R_0C_0 element is in parallel with the bulk response in circuits D and E, therefore, in principle, it is more likely to be detected and fitted even at lower temperatures. However, fitting results showed high errors in R_0 and C_0 values in circuits D and E at 130℃ (Table 5.2). This high error is a good indication that these circuits are not appropriate to fit BCF30 data. Another possible reason for this high error is that it could be due to the limited amount of data at lower temperatures.

It is commonly recognised that there is always more than one possible circuit to fit a particular impedance response and these data represent a good example of it. Once a circuit has been identified, it is necessary somehow to link between the chosen circuit and the region of the sample that is responsible. Here, it is clear that at the lowest temperature, for N_2-

processed samples, the partial circuit B is the best equivalent circuit since it is the only circuit that fits the data set (Figure 5.6).

However, since there are more than one circuit (i.e. circuits C to E) to fit the data of N_2-processed samples at intermediate temperatures as well as air-processed samples, circuit C is the most logical circuit which is usually appropriate for ceramics containing bulk and gb components. Polycrystalline materials such as ceramics, of course, always contain grain boundaries and different composition of Ca-doped BF showed that the effect of grain boundaries can be seen using impedance spectroscopy [10]. It showed that the capacitance value of gb is similar to those C_2 extracted from circuit C (Table 1&2) with much higher resistance. So, circuit C will be used in upcoming fitting for BCF23 and BCF40 data and as the partial circuit to fit highest temperature data for N_2 processed samples.

The final step is to analyse the sample-electrode impedance that is seen at low frequency with increasing temperature (i.e. 204 – 300 °C). It was found that circuit C is part of the complete circuit F, that consist of a parallel R_1-C_1-CPE_1 to represent bulk response connected in series with parallel R_2-C_2 and CPE_2 to model grain boundaries and sample-electrode impedances, respectively, which fitted the data over wide range of temperatures. However, due to the limited range of experimental frequencies, this circuit did not fit N_2-proceseed data at all temperatures. Fits to circuit F for BCF30 processed in N_2 at 230 °C are shown in Figure 5.10 together with the residuals and its equivalent circuit, and the fitted parameter values are listed in Table 2. Circuit F shows good agreement between calculated data and experimental data in various formalisms with low residuals indicating good quality of fitting.

The Arrhenius plots for σ_1 and σ_2 for BCF30 processed in air and N_2 are shown in Figure 5.11. These show that the bulk conductivity is about 1.5 orders of magnitude smaller than gb conductivity (i.e σ_2) and the activation energies for the bulk and gb within errors are similar in both processing atmospheres. The gb conductivities are corrected only for the overall sample geometry, and in order to obtain true values of gb conductivities, they should be corrected for their geometry that can be estimated based on brickwork model of grain and gb. Since the thickness of the region is the main variable that affects the capacitances of different regions, we can use the difference in the bulk and gb capacitances to estimate the thickness of gb. The gb capacitance values are about one order of magnitude larger than bulk capacitance (Table 5.1 and Table 5.2). Since gb resistances are ~1.5 orders of magnitude smaller than bulk resistances, the net effect is that the gb resistivities are about 0.5 order of magnitude smaller than bulk.

However, the similarity in activation in the two region indicates that the gb and bulk structure are similar and the difference in the conductivity is probably due to a higher concentration of carriers in the grain boundaries.

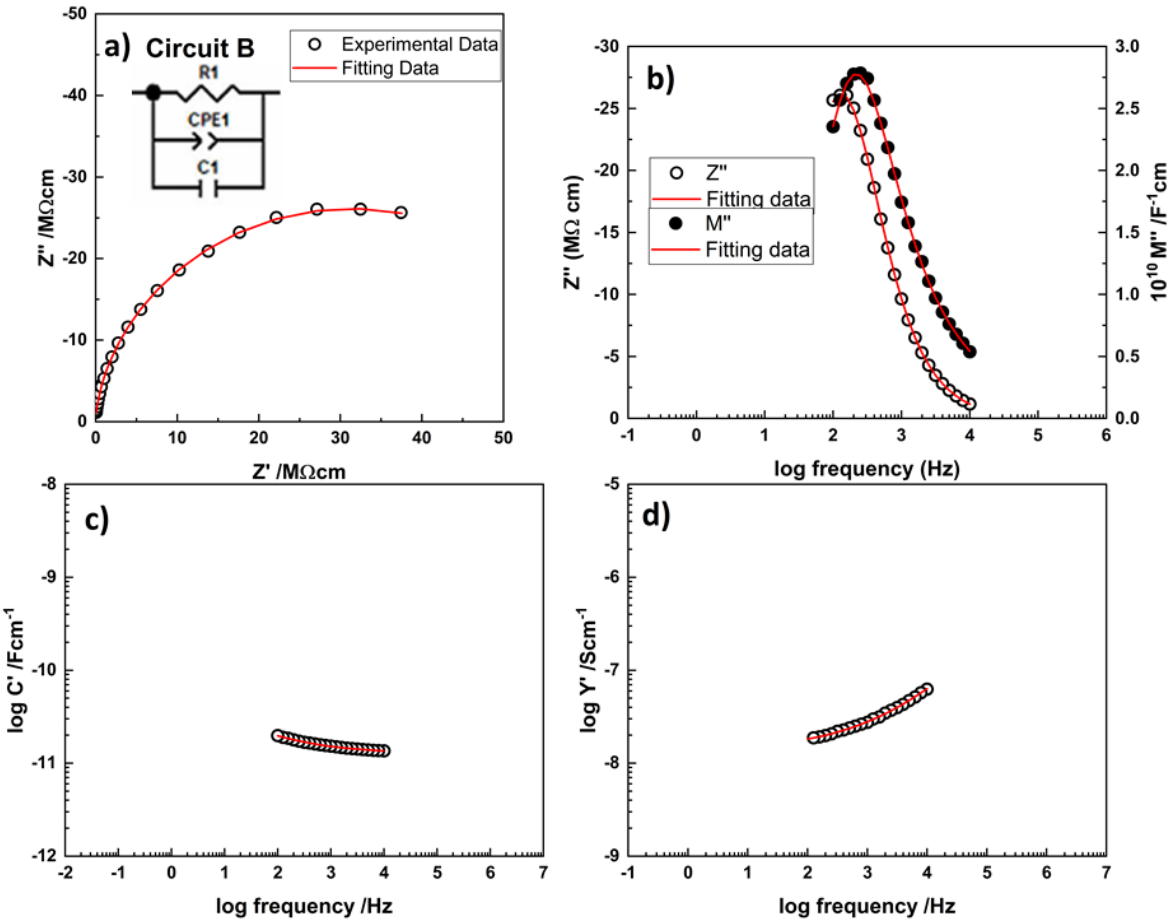

Figure 5.6. The impedance response for BCF30, processed in N_2, at 130 ℃, fitted to circuit B.

Table 5.2. Fitted parameters of the different circuit, for BCF30, processed in N_2, at indicated temperatures.

Circuit	T (℃)	R_1 (MΩcm)	R_2 (MΩcm)	R_0 (MΩcm)	A_1 ($pScm^{-1}$)	n_1	C_1 ($pFcm^{-1}$)	C_2 ($pFcm^{-1}$)	C_0 ($pFcm^{-1}$)	Weighted sum of

										squares ($x10^{-3}$)
B	129	69.4(6)	-	-	170(11)	0.55(1)	12.69(8)	-	-	1.4
C	129	66.8(18)	1.1(8)	-	133(25)	0.58(2)	13.1(3)	336(241)	-	1.4
D	129	67.2(13)	-	1320(829)	119(29)	0.59(3)	12.6(1)	-	0.54(36)	1.4
E	129	67.2(14)	-	2.2(17)	117(29)	0.59(3)	308(205)	-	13.1(3)	1.4
B	180	3.32(1)	-	-	139(8)	0.70(1)	13.3(1)	-	-	4.1
C	180	3.16(11)	0.13(1)	-	89(3)	0.77(1)	13.9(1)	158(9)	-	0.4
D	180	3.29(1)	-	34 (2)	93(3)	0.74(1)	13.2(1)	-	1.1(1)	0.4
E	180	3.29(1)	-	0.204(16)	93(3)	0.74(1)	170(8)	-	14.3(6)	0.4
F	230	0.330(1)	0.011(1)	-	151(1)	0.77	16.1(1)	157	-	8

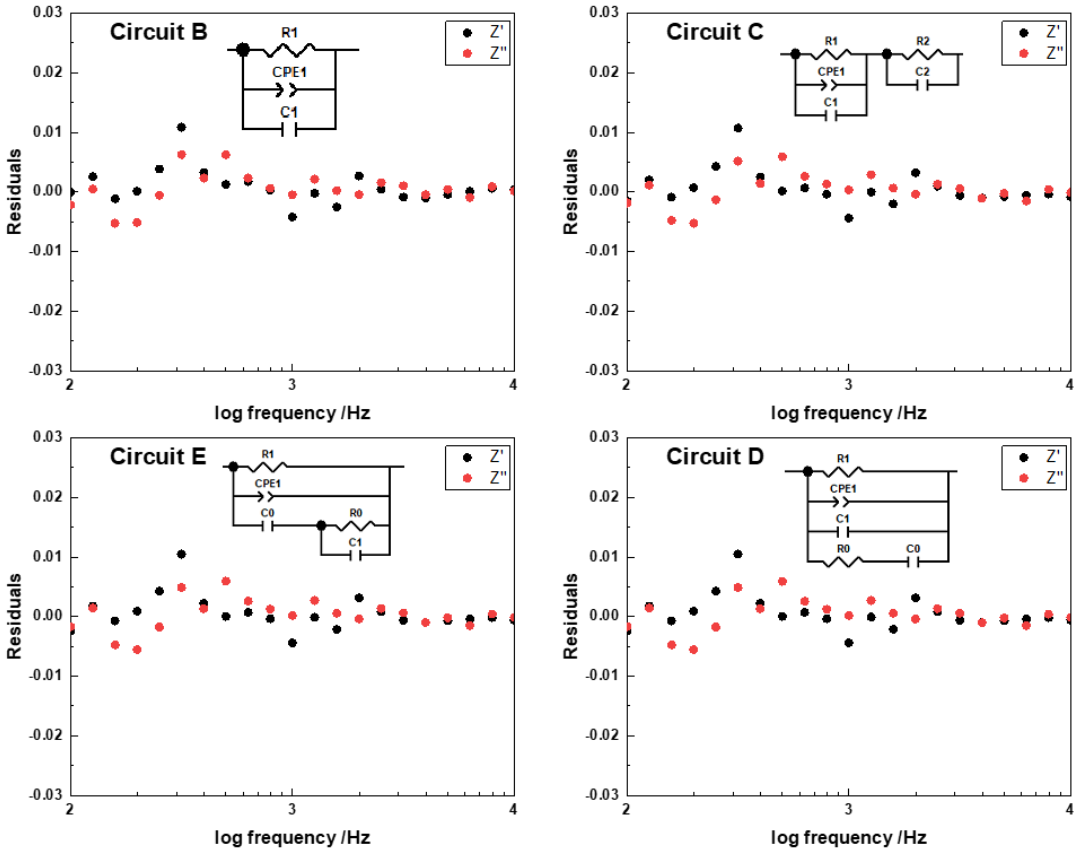

Figure 5.7. Fitting residuals from different possible circuits, for CBF30, processed in N_2, at 130°C.

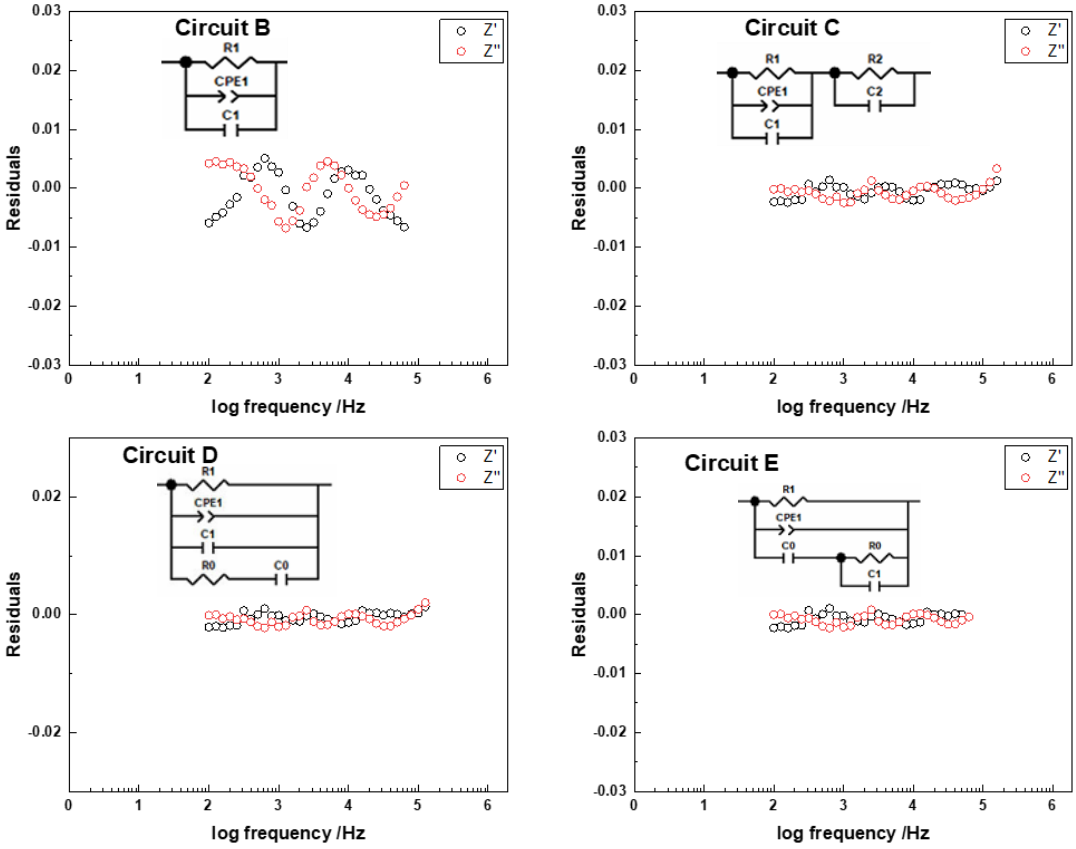

Figure 5.8. Fitting residuals from different possible circuits, for CBF30, processed in N_2, at 180℃.

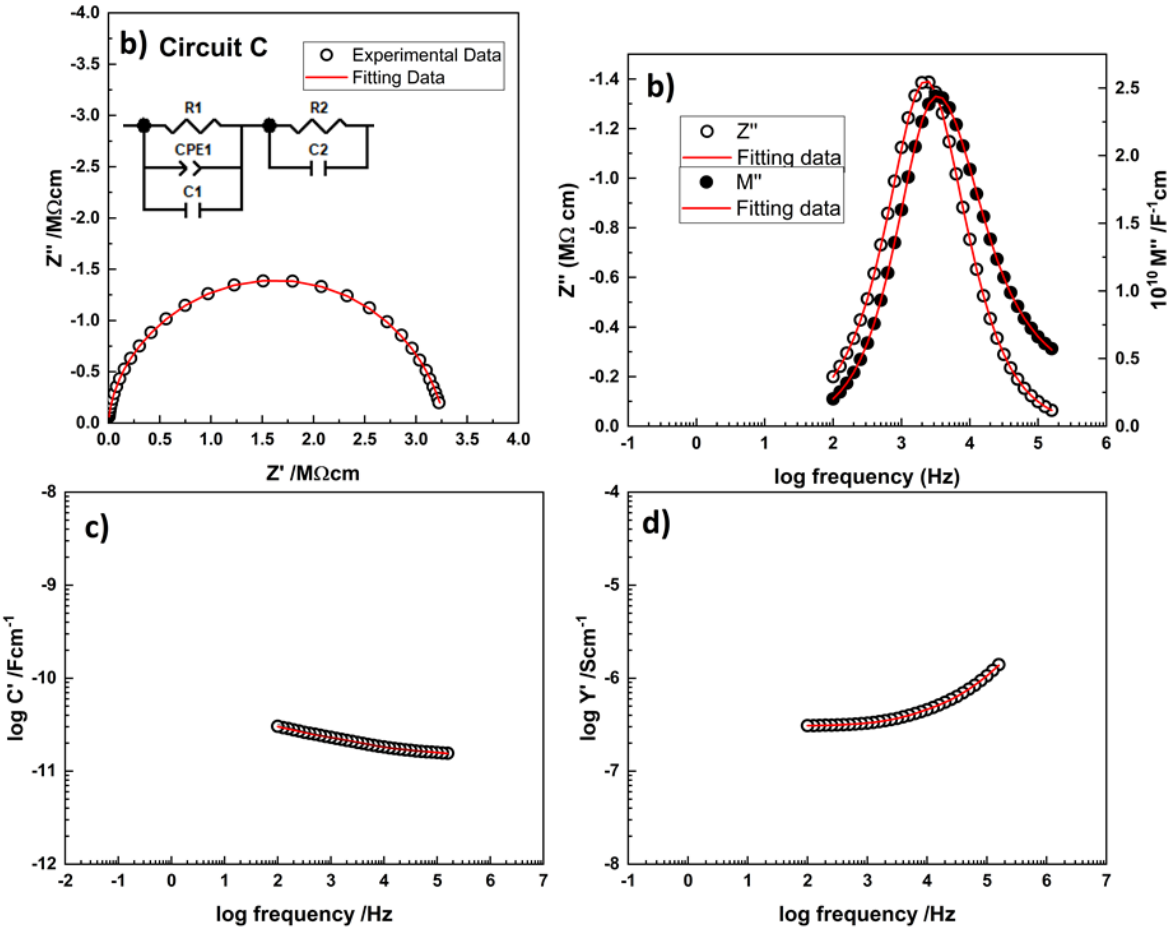

Figure 5.9. The impedance response for BCF30, processed in N_2, at 180 ℃, fitted to circuit C.

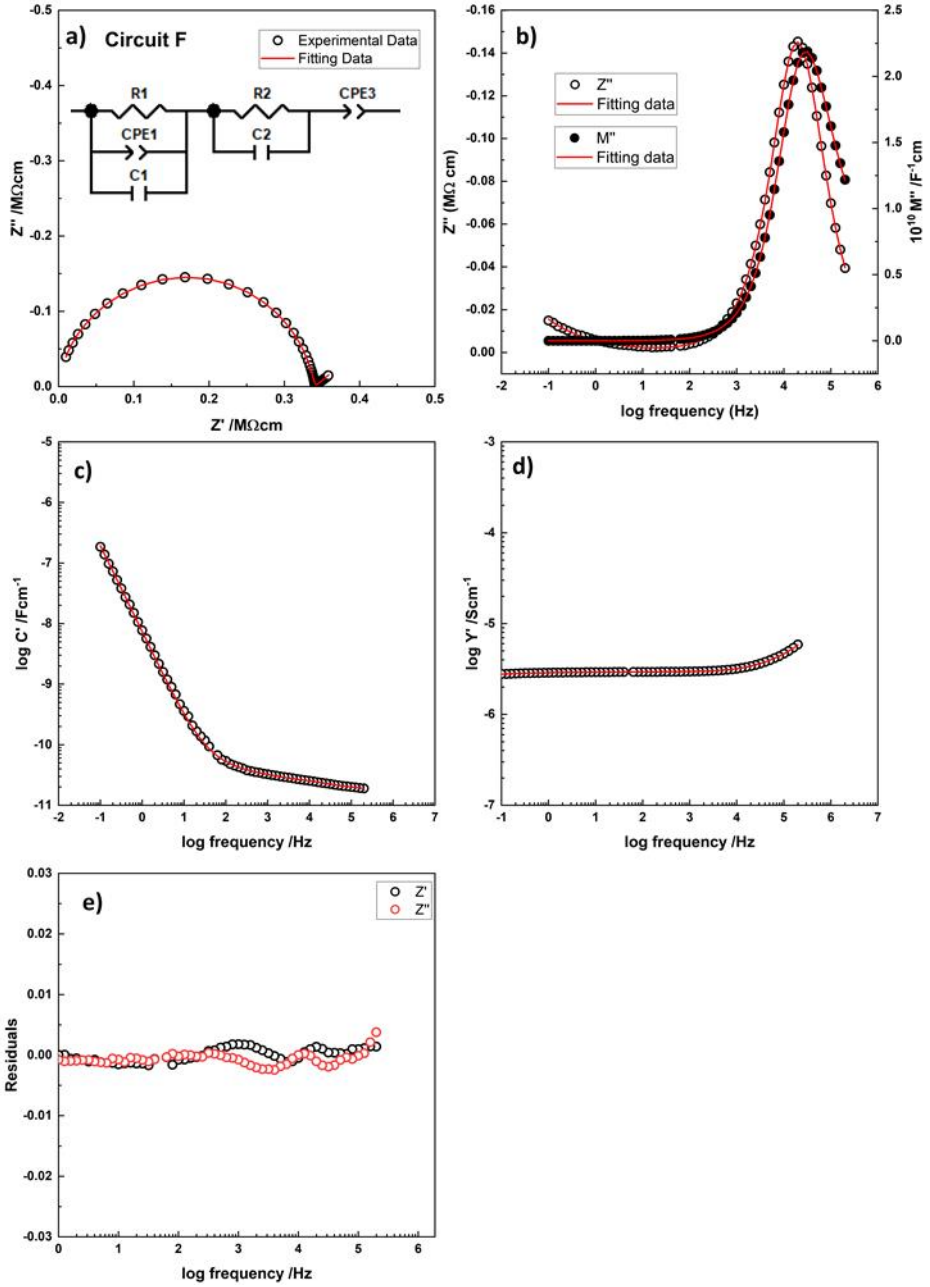

Figure 5.10. The impedance response for BCF30, processed in N_2, at 230 °C, fitted to circuit F with its residuals.

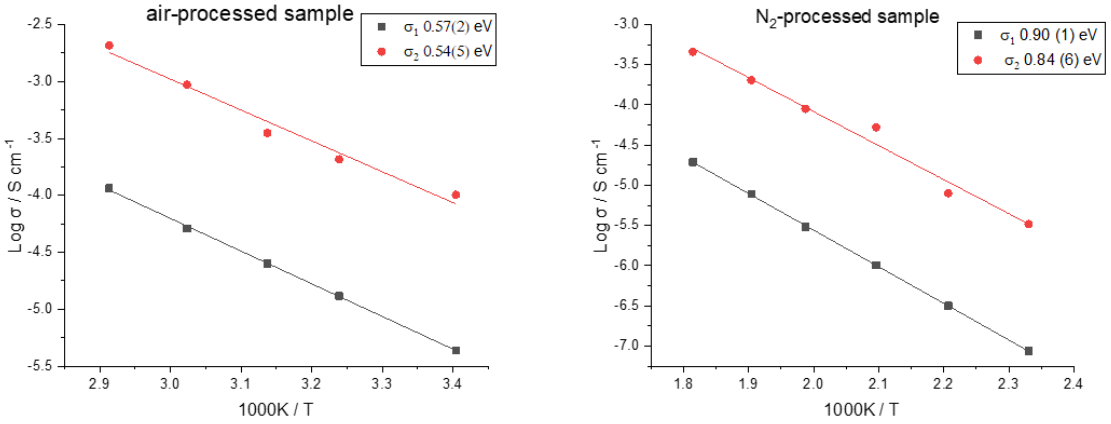

Figure 5.11. Conductivity Arrhenius plots of: bulk and grain boundaries for air-processed BCF30 (lift), and N_2-processed BCF30 (right).

5.2.2. BCF23 and BCF40 fitting data

Both compositions were fitted to the equivalent circuits that best fitted air- and N_2 processed data for BCF30. It was found that similarly, BCF40 data, for both air- and N_2-processed samples, fitted accurately to circuit C for air-processed sample and the partial circuit C at low temperature and to the complete circuit F at high temperatures for N_2-processed sample. The fitting data at different temperatures are shown in Figure S 5.2 to Figure S 5.5 and fitting parameters are listed in Table S 5.3and Table S 5.4.

Also, BCF23 data processed in N_2 fitted accurately to circuits C and F at low and high temperatures, respectively, similar to BCF30 and 40 Figure S 5.6,Figure S 5.7 and Table S 5.6. However, air-processed data for BCF23 did not fit circuit C. It was found that there was no need to include the bulk capacitance in the equivalent circuit and the data fitted accurately with very low residuals to circuit G which consist of parallel R_1- CPE1 connected in series with parallel R_2-C_2. This circuit is a reasonable circuit for air-processed BCF23, since its conductivity is lower than those of BCF30 and 40 and the bulk capacitance is out of the measurement window at the measured temperatures. The fitting data of BCF23 processed in air at 46 ℃ are shown in Figure 5.12, at 21 ℃ in Figure S 5.8 and the fitting parameters are shown in Table S 5.5.

Figure 5.13 shows Arrhenius plots for σ_1 and σ_2 for both air- and N_2-processed sample as a function of composition. It concludes that the bulk conductivities are smaller than those of gb by about 1.5 order of magnitude for air-processed samples and a factor of about three for N_2-processed samples. Secondly, both σ_1 and σ_2 have similar activation energies for each

processing atmosphere indicating the similarity of gb and bulk structure and the difference in the conductivity is probably attributed to a higher concentration of carriers in the grain boundaries. Thirdly, the total conductivity decreased with increasing Ca content with no change in activation energies.

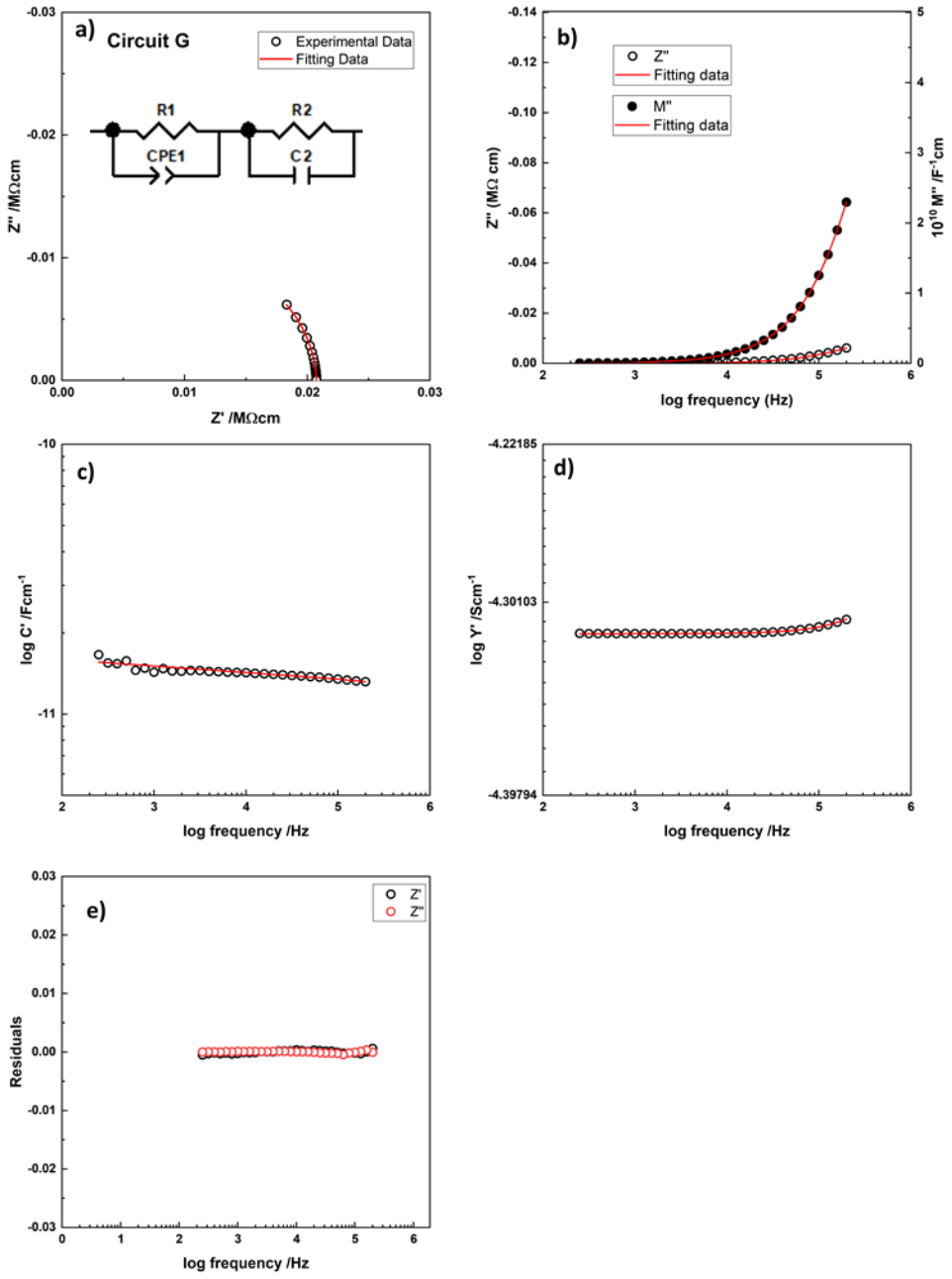

Figure 5.12. The impedance response for BCF23, processed in air, at 45 ℃, fitted to circuit G.

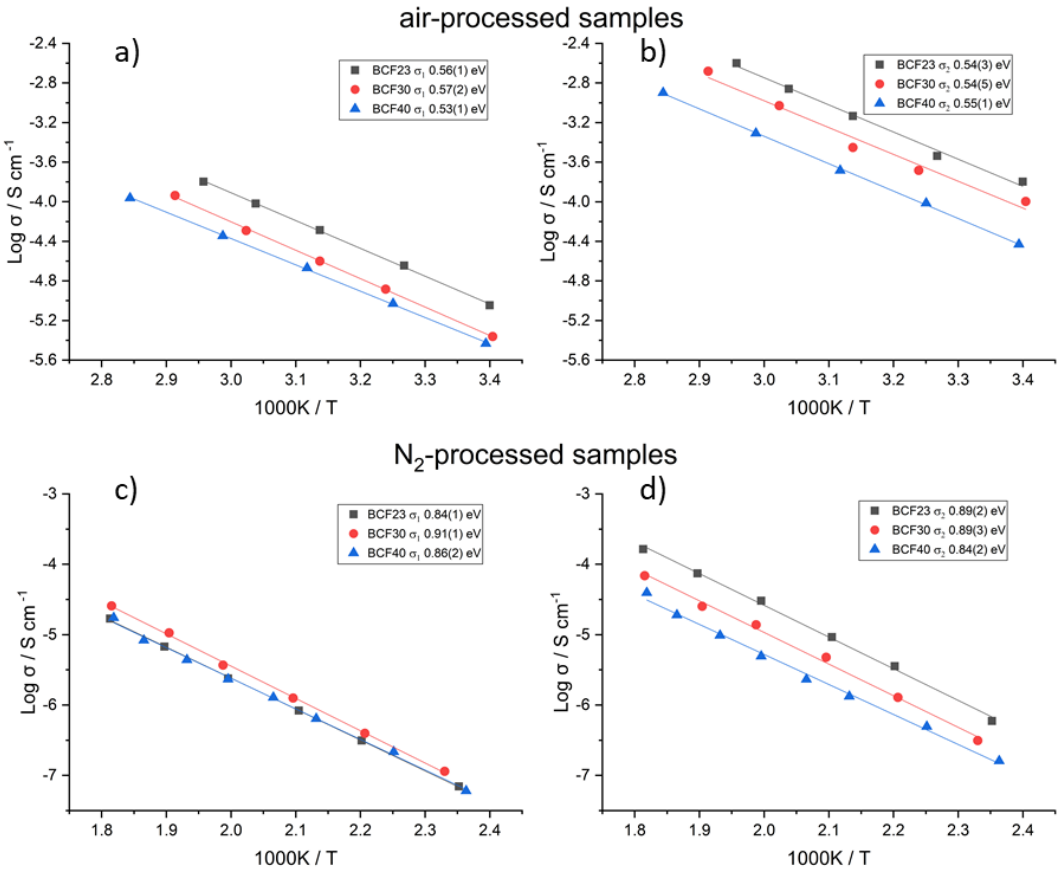

Figure 5.13. Conductivity Arrhenius plots of: bulk (a) and grain boundaries (b) for air-processed samples, and bulk (c) and grain boundaries (d) for N_2-processed sample.

5.3. Conclusions

Impedance data of $Bi_{1-x}Ca_xFeO_{3-x/2}$ (where: x = 0.23, 0.3 and 0.4) was dominated by the bulk response with no obvious additional response from other regions such as grain boundaries or sample-electrode interface for air- and O_2-processed samples. N_2-processed samples showed additional low frequency response that attributed to sample-electrode interface at high temperatures. Fitting the data to the circuits that usually used to represent bulk response of a ceramic such as a parallel R-C or R-CPE-C did not produce an acceptable fit.

Therefore, accurate representation of impedance data of all compositions required inclusion of additional elements to those usually used to fit the bulk response for all samples processed in different atmospheres. Different circuits were tested in order to find the best equivalent circuit that represents the full response of impedance data.

It is found that circuits C, D and E (Figure 5.1) showed good fitting and it was difficult to choose the best equivalent circuit from just visual inspection. The partial circuit C (i.e. parallel R_1-CPE_1-C_1 in series with parallel R_2-C_2) is the most logical circuits for air-, O_2-procesd

samples and for N_2-processed samples at low temperatures in which R_1 and C_1 attributed to the bulk resistivity and capacitance, respectively and R_2 and C_2 are attributed to grain boundaries resistivity and capacitance, respectively. CPE_3 was added in series with circuit C, the complete circuit F, to fit sample-electrode interface response in N_2-processed samples at high temperatures (> 200°C).

5.4. References

1. Vendrell, X. and A.R. West, *Induced p-type semiconductivity in yttria-stabilized zirconia.* Journal of the American Ceramic Society, 2019. **102**(10): p. 6100-6106.
2. Hernández, M.A., N. Masó, and A.R. West, *On the correct choice of equivalent circuit for fitting bulk impedance data of ionic/electronic conductors.* Applied Physics Letters, 2016. **108**(15): p. 152901.
3. Masó, N. and A.R. West, *Electronic conductivity in yttria-stabilized zirconia under a small dc bias.* Chemistry of Materials, 2015. **27**(5): p. 1552-1558.
4. Vendrell, X. and A.R. West, *Electrical properties of yttria-stabilized zirconia, YSZ single crystal: local AC and long range DC conduction.* Journal of The Electrochemical Society, 2018. **165**(11): p. F966.
5. Osman, R.A. and A.R. West, *Electrical characterization and equivalent circuit analysis of (Bi1. 5Zn0. 5)(Nb0. 5Ti1. 5) O7 Pyrochlore, a relaxor ceramic.* Journal of Applied Physics, 2011. **109**(7): p. 074106.
6. Masó, N., X. Yue, T. Goto, and A.R. West, *Frequency-dependent electrical properties of ferroelectric BaTi 2 O 5 single crystal.* Journal of Applied Physics, 2011. **109**(2): p. 024107.
7. E.J. ABRAM, D.C.S.A.R.W., *A Strategy for Analysis and Modelling of Impedance Spectroscopy Data of Electroceramics: Doped Lanthanum Gallate.* Journal of Electroceramics, 2003.
8. Ramírez-González, J. and A.R. West, *Electrical properties of calcia-stabilised zirconia ceramics.* Journal of the European Ceramic Society, 2020. **40**(15): p. 5602-5611.
9. Alotaibi, M., L. Li, and A.R. West, *Electrical properties of yttria-stabilised hafnia ceramics.* Phys Chem Chem Phys, 2021. **23**(45): p. 25951-25960.
10. Masó, N. and A.R. West, *Electrical Properties of Ca-Doped BiFeO3 Ceramics: From p-Type Semiconduction to Oxide-Ion Conduction.* Chemistry of Materials, 2012. **24**(11): p. 2127-2132.
11. Costa, L.V., L.S. Rocha, J.A. Cortés, M.A. Ramirez, E. Longo, and A.Z. Simões, *Enhancement of ferromagnetic and ferroelectric properties in calcium doped BiFeO3 by chemical synthesis.* Ceramics International, 2015. **41**(8): p. 9265-9275.
12. Costa, L.V., R.C. Deus, C.R. Foschini, E. Longo, M. Cilense, and A.Z. Simões, *Experimental evidence of enhanced ferroelectricity in Ca doped BiFeO3.* Materials Chemistry and Physics, 2014. **144**(3): p. 476-483.
13. Schiemer, J., R. Withers, L. Norén, Y. Liu, L. Bourgeois, and G. Stewart, *Detailed Phase Analysis and Crystal Structure Investigation of a Bi1−xCaxFeO3−x/2 Perovskite-Related Solid Solution Phase and Selected Property Measurements Thereof.* Chemistry of Materials, 2009. **21**(18): p. 4223-4232.

14. Arnold, D.C., *Composition-driven structural phase transitions in rare-earth-doped BiFeO3 ceramics: a review.* IEEE Trans Ultrason Ferroelectr Freq Control, 2015. **62**(1): p. 62-82.
15. Zhai, L., Y.G. Shi, J.L. Gao, S.L. Tang, and Y.W. Du, *Ferroelectric and magnetic properties in high-pressure synthesized BiFeO3 compound.* Journal of Alloys and Compounds, 2011. **509**(28): p. 7591-7594.

5.5. Supplementary data

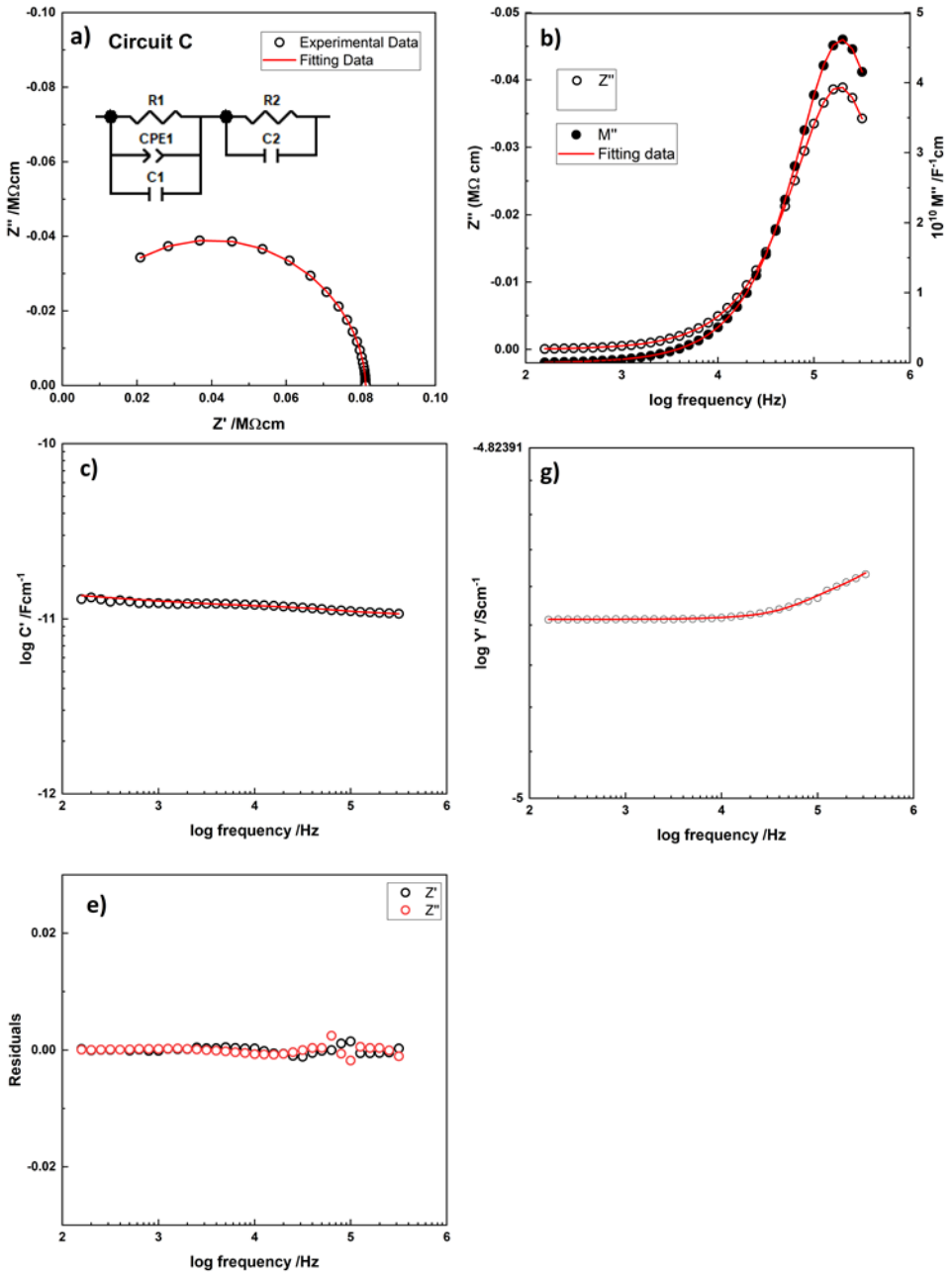

Figure S 5.1. The impedance response for BCF30, processed in air, at 35 ℃, fitted to circuit C.

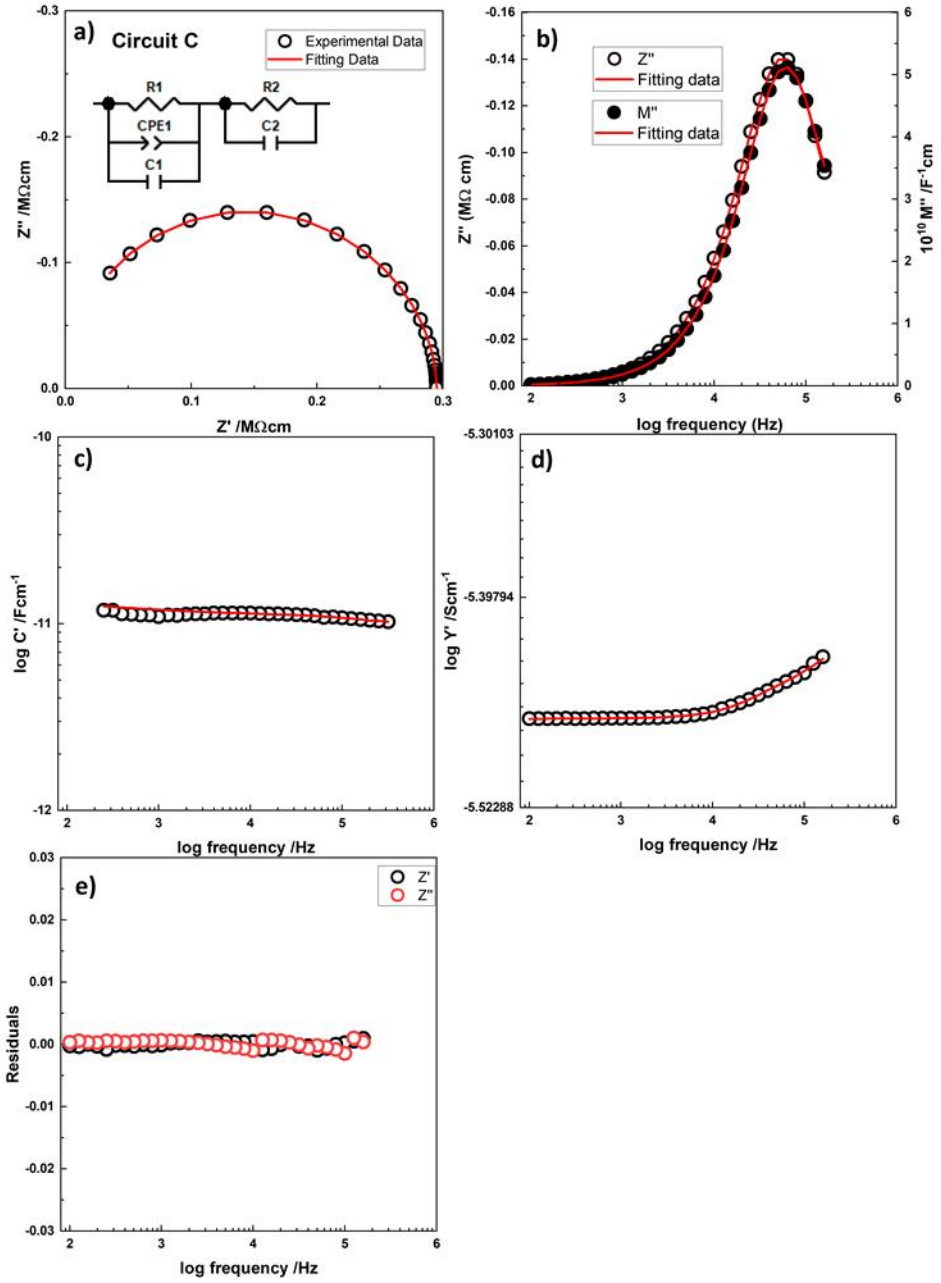

Figure S 5.2. The impedance response for BCF40, processed in air, at 21.5 °C, fitted to circuit C.

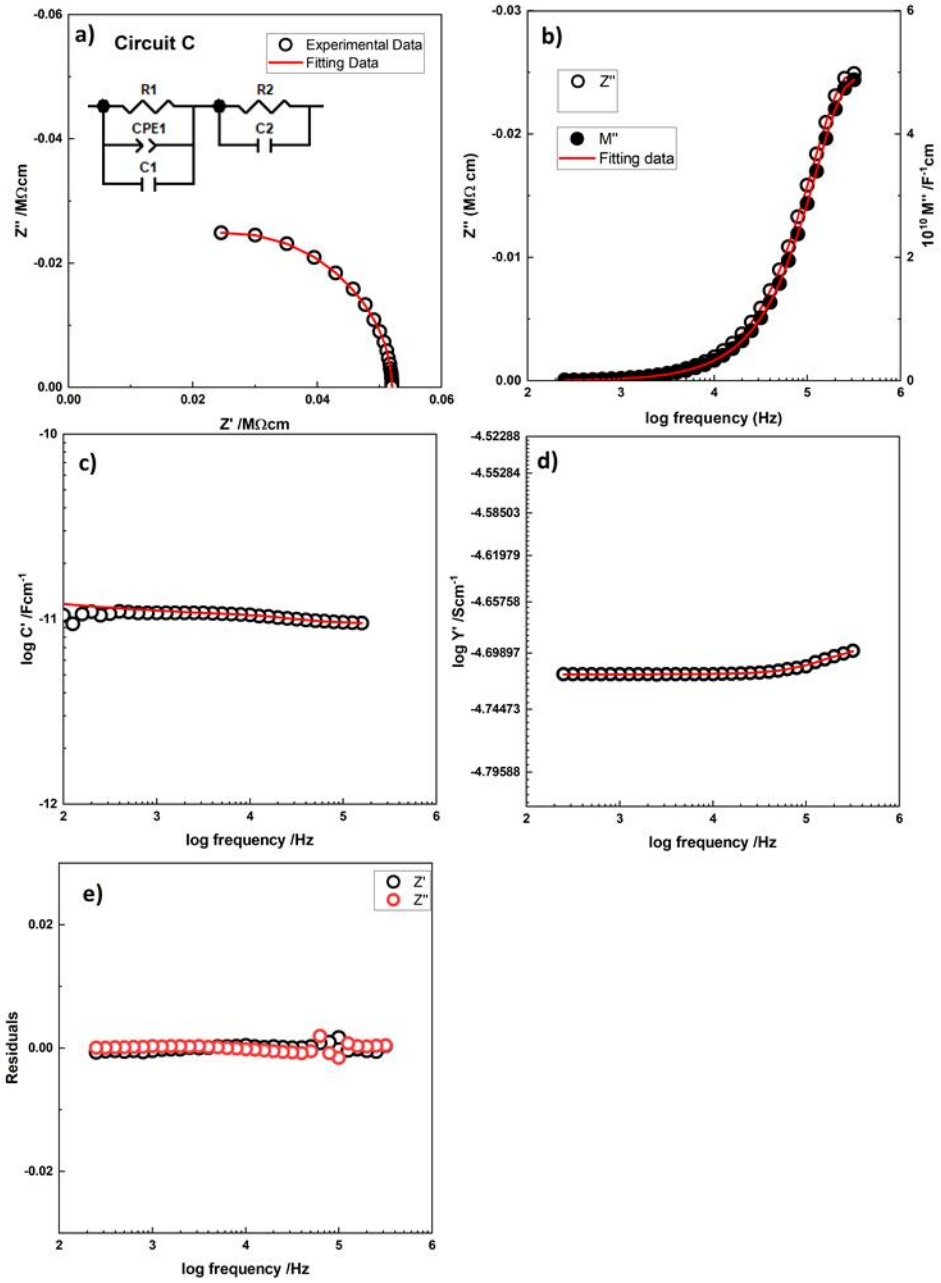

Figure S 5.3. The impedance response for BCF40, processed in air, at 48 ℃, fitted to circuit C.

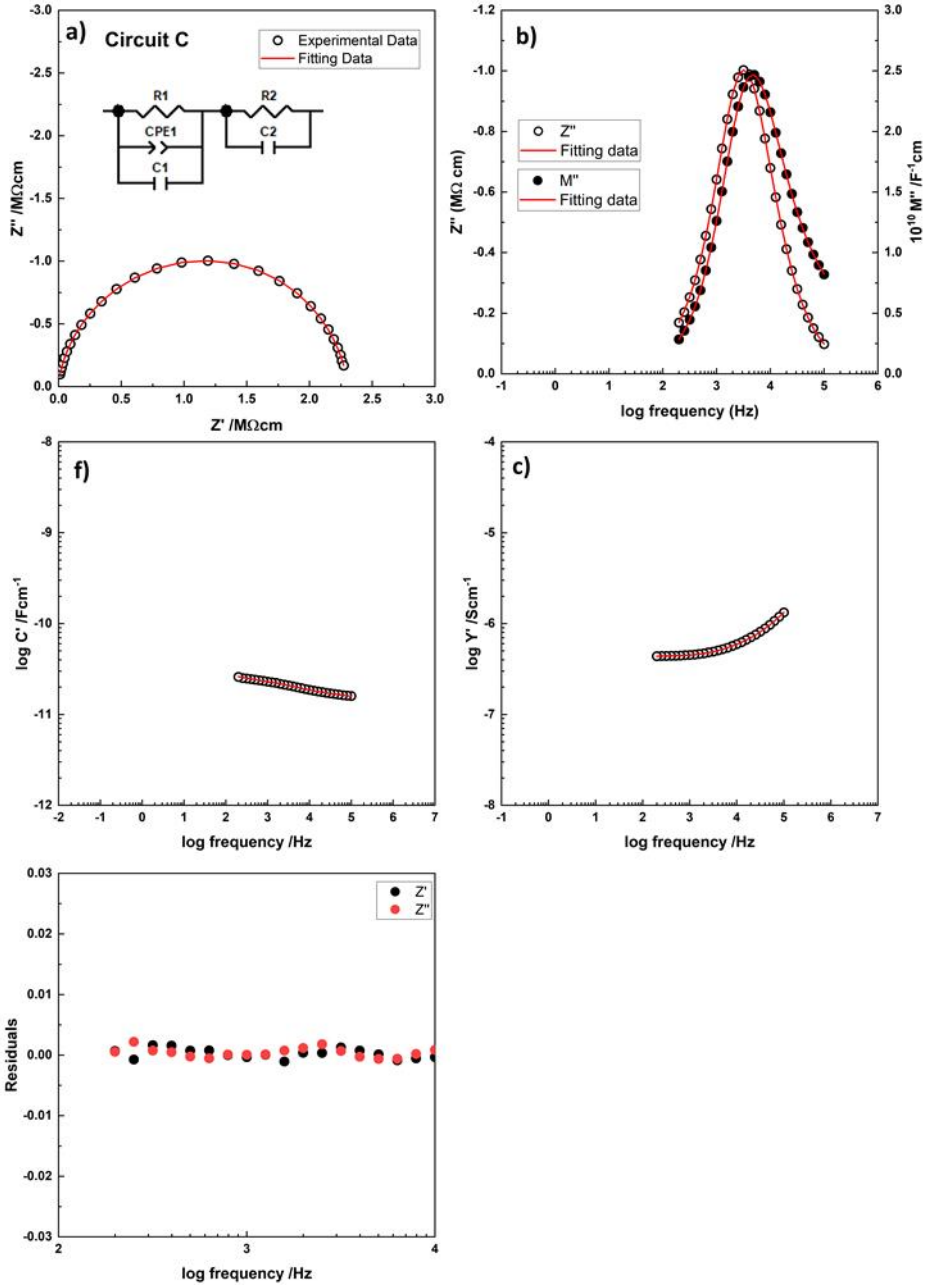

Figure S 5.4. The impedance response for BCF40, processed in N_2, at 196 ℃, fitted to circuit C.

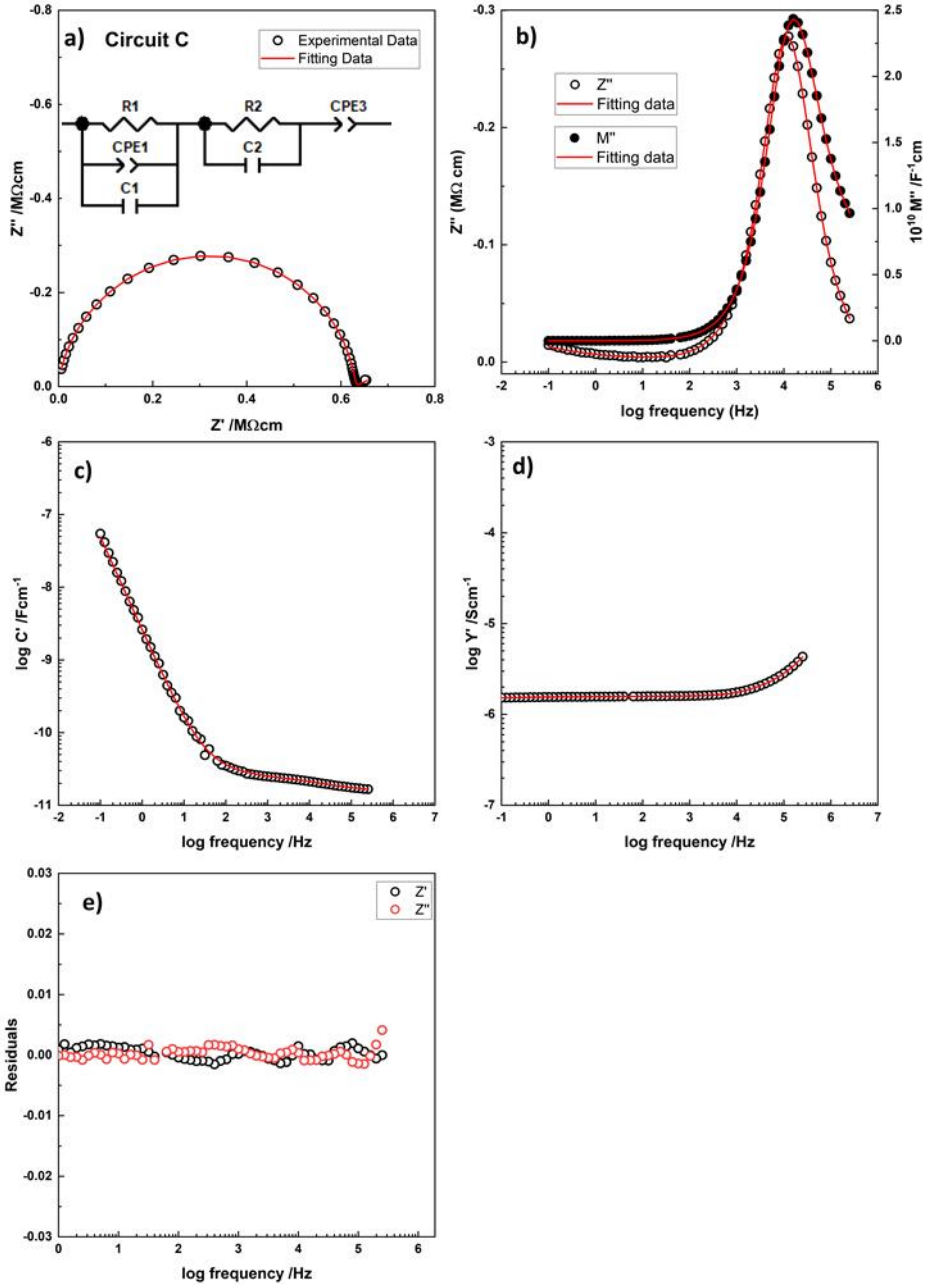

Figure S 5.5. The impedance response for BCF40, processed in N_2, at 228 ℃, fitted to circuit F.

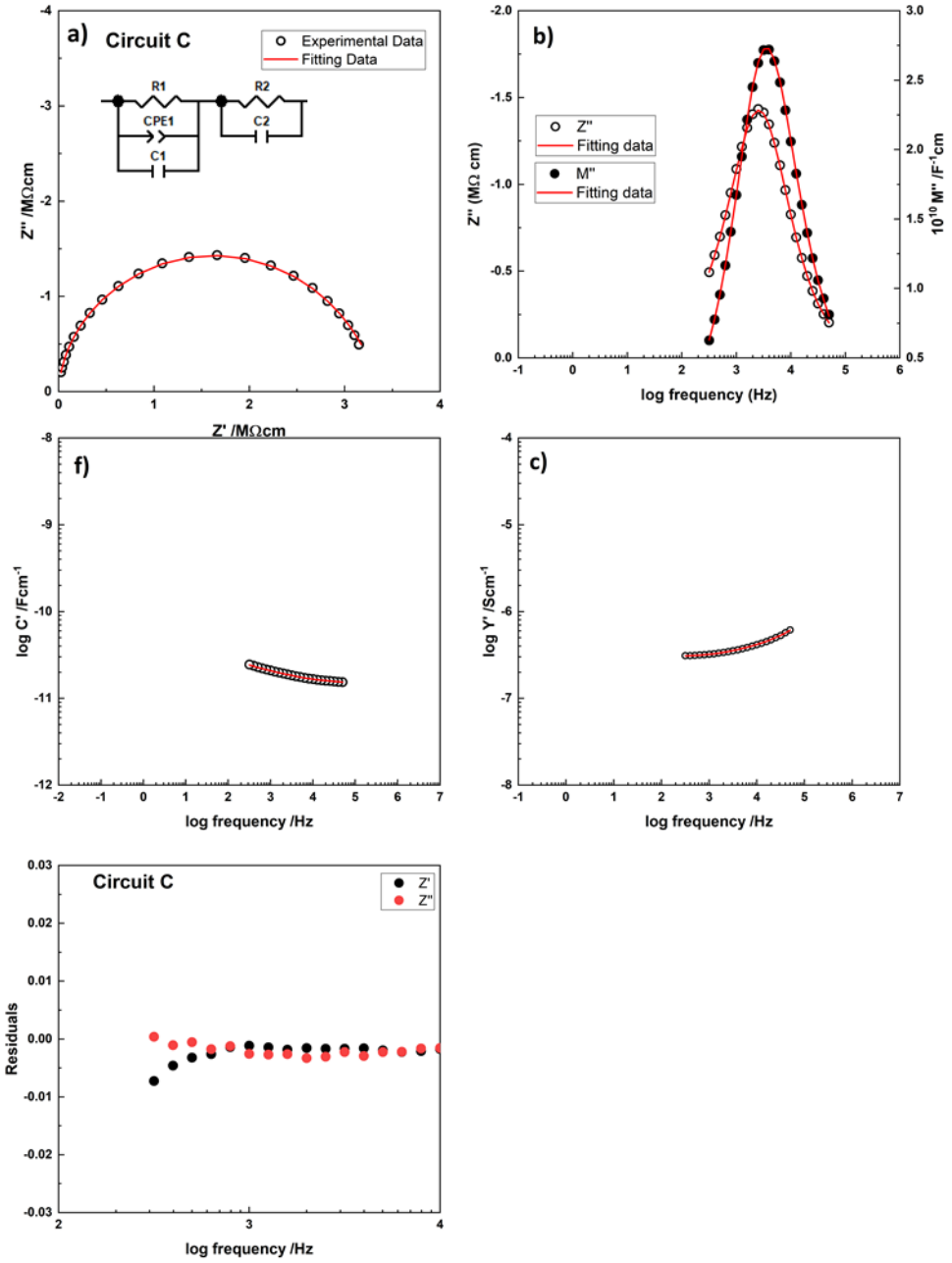

Figure S 5.6. The impedance response for BCF23, processed in N_2, at 181 ℃, fitted to circuit C.

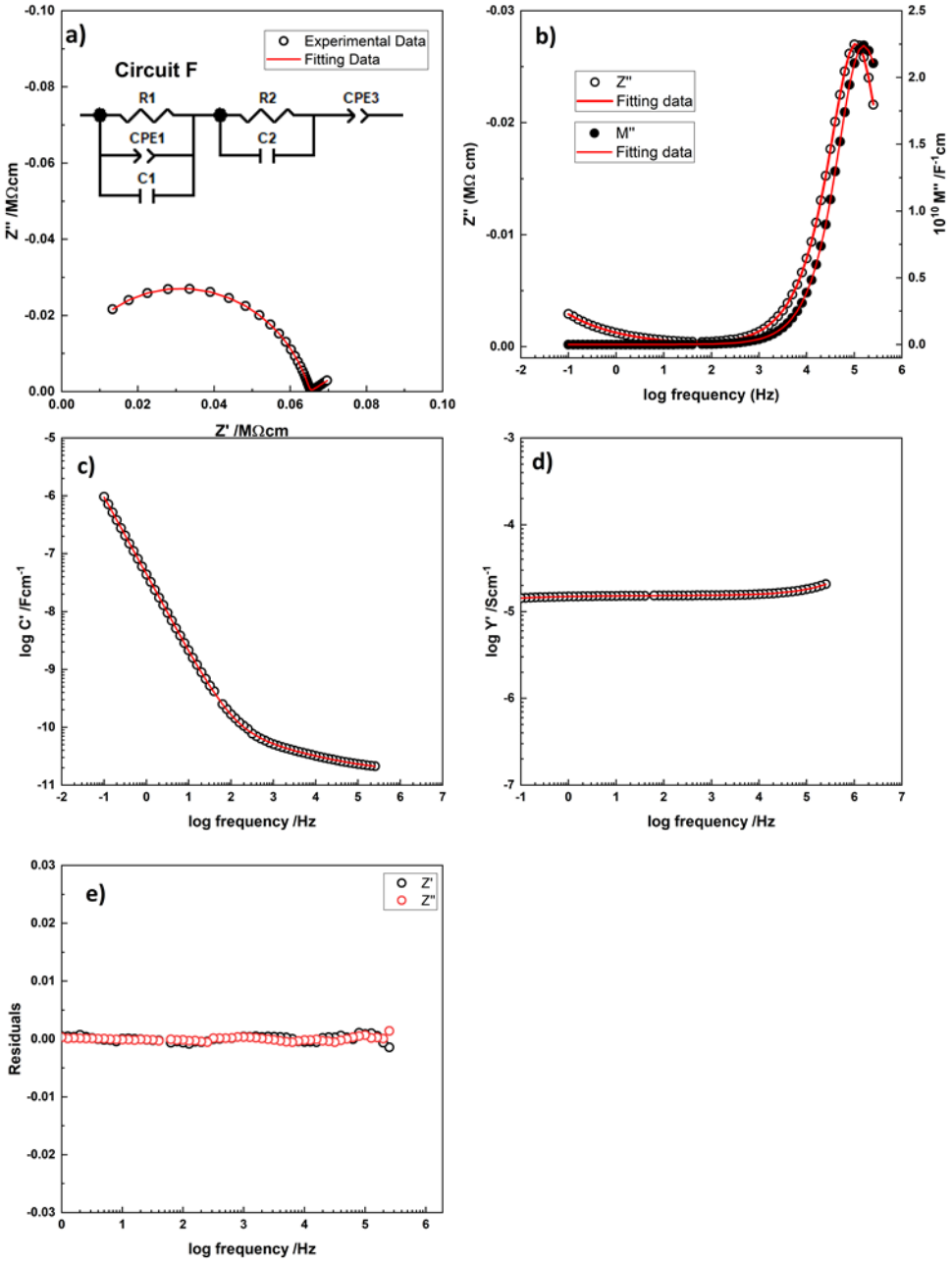

Figure S 5.7. The impedance response for BCF23, processed in N_2, at 278 ℃, fitted to circuit F.

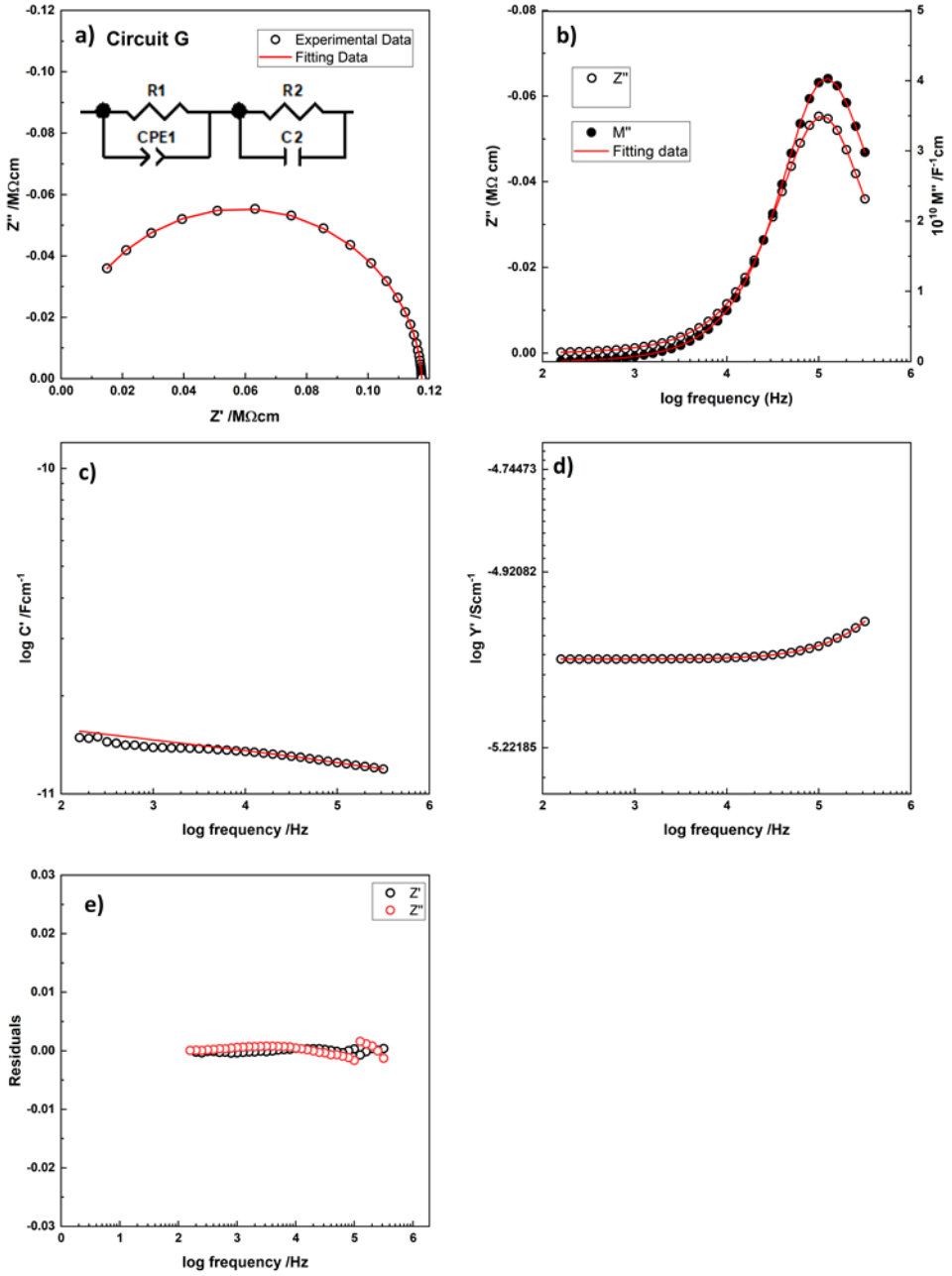

Figure S 5.8. The impedance response for BCF23, processed in air, at 21 ℃, fitted to circuit G.

Table S 5.1. Fitted parameters of circuit C, for BCF30, processed in air.

T (℃)	R_1 (kΩcm)	R_2 (kΩcm)	A_1 ($pScm^{-1}$)	n_1	C_1 ($pFcm^{-1}$)	C_2 ($pFcm^{-1}$)	Weighted sum of squares ($x10^{-3}$)
20.6	230(1)	9.9(6)	12.6	0.78	9.98(1)	797(66)	0.2
35.6	76.5(1)	4.84(7)	15.5(7)	0.78	10.3(1)	462	0.6
45.5	39.74(4)	2.82(4)	10(1)	0.78	10.8(1)	462	0.7
57	19.55(4)	1.07(4)	28(2)	0.78	10.6(1)	462	0.8
72.4	8.66(30	0.48(3)	22(2)	0.78	11.5(1)	462	0.5

Table S 5.2. Fitted parameters of circuit C, for BCF30, processed in N_2.

T (℃)	R_1 (MΩcm)	R_2 (MΩcm)	A_1 ($pScm^{-1}$)	A_3 (μScm^{-1})	n_1	n_3	C_1 ($pFcm^{-1}$)	C_2 ($pFcm^{-1}$)	Weighted sum of squares ($x10^{-3}$)
156	8.75(15)	3.20(15)	266(23)	-	0.61(1)	-	15.6(2)	93(6)	0.36
180	2.52(3)	0.78(3)	223(14)	-	0.68(1)	-	15.4(2)	125(7)	0.4
204	0.79(1)	0.21(1)	152(11)	26.3(5)	0.76(1)	0.51(1)	14.1(3)	168(13)	5
230	0.268(2)	0.072(2)	226(2)	51.5(4)	0.76	0.45(1)	14.5(1)	163(6)	3
252	0.094(2)	0.04(2)	326(10)	107(14)	0.76	0.49(1)	16.1(2)	119(6)	16
278	0.040(1)	0.015(1)	404(12)	190(1)	0.76	0.43(1)	15.5(2)	137(6)	5.9

Table S 5.3. Fitted parameters of circuit C, for BCF40, processed in air.

T (℃)	R_1 (kΩcm)	R_2 (kΩcm)	A_1 ($pScm^{-1}$)	n_1	C_1 ($pFcm^{-1}$)	C_2 ($pFcm^{-1}$)	Weighted sum of squares ($x10^{-3}$)
21.5	270	25(1)	12.8(3)	0.78	9.3	259(20)	0.16
34.5	109	10.3(2)	15(1)	0.78	9.5	259	1.1
47.5	47.26	4.8(1)	12.2(17)	0.78	10	259	0.6
62	21	2.03(3)	18(2)	0.78	10	259	0.15
78.5	8.6	8.5(3)	9.8(19)	0.78	11	259	0.46

Table S 5.4. Fitted parameters of circuit C, for BCF40, processed in N_2.

T (℃)	R_1 (MΩcm)	R_2 (MΩcm)	A_1 ($pScm^{-1}$)	A_2 (μScm^{-1})	n_1	n_2	C_1 ($pFcm^{-1}$)	C_2 ($pFcm^{-1}$)	Weighted sum of squares ($x10^{-3}$)
150	16.7(6)	6.2(5)	211(24)	-	0.63(1)	-	15.2(3)	-	0.5
172	4.61(7)	2.02(7)	189(12)	-	0.69(1)	-	15.2(2)	-	0.2
196	1.56(2)	0.75(2)	135(8)	-	0.76(1)	-	14.2(2)	-	0.1
211	0.78(1)	0.81(1)	100(6)	28.9(6)	0.81(1)	0.39(1)	12.7(4)	82(3)	4
228	0.43(1)	0.20(1)	111(9)	39.4(7)	0.81(1)	0.30(1)	12.7(5)	91(5)	4
244	0.228(1)	0.102(1)	132(2)	59.5(9)	0.81	0.33(1)	12.5(1)	91	9
263	0.120(1)	0.052(1)	151(3)	110(2)	0.81	0..36(1)	12.3(2)	91	20
278	0.057	0.025	161(3)	250(4)	0.81	0.26(1)	12.1(2)	91	10

Table S 5.5. Fitted parameters of circuit C, for BCF23, processed in air.

T (°C)	R_1 (KΩcm)	R_2 (KΩcm)	A_1 ($pScm^{-1}$)	n_1	C_2 ($pFcm^{-1}$)	Weighted sum of squares ($x10^{-3}$)
21	111.3(3)	6.3(3)	20.9(2)	0.963(1)	373	0.37
32	44.2(1)	3.45(13)	17.8(6)	0.977(2)	373	1
46	19.38(3)	1.36(1)	19.5(3)	0.973(8)	373	0.17
56	10.41(3)	0.72(3)	19.4(3)	0.976(9)	373	0.2
65	6.27(6)	0.40(6)	19.1(4)	0.980(8)	373	0.2

Table S 5.6. Fitted parameters of circuit C, for BCF23, processed in N_2.

T (°C)	R_1 (MΩcm)	R_2 (MΩcm)	A_1 ($pScm^{-1}$)	A_2 (μScm^{-1})	n_1	n_2	C_1 ($pFcm^{-1}$)	C_2 ($pFcm^{-1}$)	Weighted sum of squares ($x10^{-3}$)
152	14.9(2)	0.71(1)	143(17)	-	0.61(2)	-	14.3(2)	143(25)	0.3
181	3.19(1)	0.192(10)	177(13)	-	0.66(1)	-	15.4(1)	135	0.8
202	1.22(2)	0.093(19)	207(9)	38(2)	0.69(1)	0.62(3)	15.7(2)	135	8.7
254	0.143	0.018	414(8)	120(1)	0.72	0.38(1)	15.8(10	135	0.9
278	0.056	0.0091	569(13)	220(1)	0.73	36(1)	15	135	0.6

Chapter 6 : The effect of dc bias on the conductivity of un-doped BF and Ca-doped BF ceramics

6.1. Introduction

The effect of a small applied voltage on the electrical properties of materials is a new area of interest especially in two hot topics, memristors and flash sintering of ceramics. In recent years many research on bulk of acceptor-doped ceramics have shown a huge effect on the material conductivity in response to an application of a small dc bias. The change in the conductivity depends on several factors such as type of electronic conductivity, prescience of redox-active element and material ability to exchange oxygen with the atmosphere. The effect usually fully reversible on removing the voltage[1-4]. Ca-doped $BiFeO_3$ is one of these materials in which its resistance changes reversibly by application of a dc bias [1].

In chapter 4, a survey of the electrical properties of different Ca-doped BF compositions showed that the conductivities of these materials increased by many orders of magnitude and the properties changed from oxide-ion conduction to p-type semi-conduction with increasing pO_2 during sample processing and subsequent cooling. The transition from a high level of oxide-ion conduction to mixed ionic-electronic conduction was also demonstrated by increasing pO_2 during impedance measurements of N_2-processed samples in which the conductivities increased by a few orders of magnitude (Figures 4. 10 and 4. 11).

The introduction of electronic conduction can be studied further by application of a small dc bias during impedance spectroscopy measurements. Ca-doped BF conductivity increased reversibly by few orders of magnitude in response to application of a small dc a bias. It is the first bulk material to show this kind of resistive switching phenomenon. More recently, yttria stabilised hafnia (YSH) [5] showed similar resistive switching (RS) behaviour at higher temperature.

The resistive switching phenomenon has been a hot topic over last few years especially for memristive applications. Memristors are thin film devices in which ON-OFF switching occurs due to the formation and rupturing of conducting filaments, for example, TiO_2, ZrO_2 and NiO [6-8]. Also, RS occurs in other bulks which is associated with a phase transition such as metal-insulator transition in VO_2 and Verwey transition in magnetite [9, 10]. The RS reported in Ca-doped BF and YSH is different from those associated with the phase transition and conduction filament formation.

In this chapter, we have studied and confirmed the response of Ca-doped BF to application of a small dc bias that was reported in the literature, and extended the study by including new compositions of different Ca content and un-doped BF. Also, since the electrical properties of these materials are very dependent on processing atmosphere, we extended the study to include air- and N_2-processed samples. The magnitude of applied voltage, pO_2, temperature and voltage hold time were used as variables to study the effect of application of a small dc bias.

6.2. Results

6.2.1. Air-processed samples

6.2.1.1. Ca-doped BF

Application of a small dc bias at the same time as performing impedance spectroscopy measurements is a widely used technique to study the existence and/ or nature of electronic conduction and semi-conduction in ceramics. A small dc bias was applied across the same pellets that were used in Chapter 4. The behaviours of BCF23, 30 and 40, processed in air and O_2 were similar. Figure 6.1 shows the response of BCF23 to application of a small dc bias during impedance measurements. The impedance decreased slightly with increasing voltage (1- 4 V) in the temperature range 30- 70 ℃. The observed reduction in resistance is an indication of p-type conduction. On removal of applied voltage, the conductivities were fully recovered.

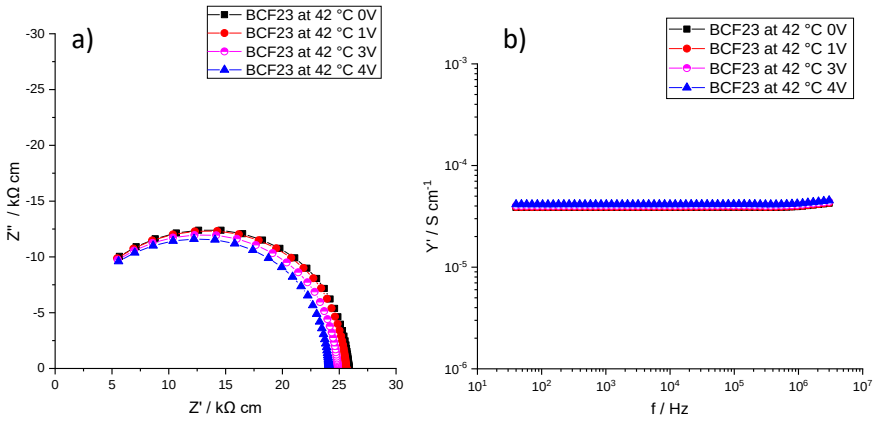

Figure 6.1. (a) Impedance complex plane plots, Z, (b) admittance spectroscopy plots, for BCF23, processed in air, at 42 ℃ under application of dc bias, as noted beside each graph.*

On application of higher voltage, in the range 5 to 20 V (60-210 V/cm), across the same pellets (thickness ~ 1- 1.3 mm), the conductivities changed considerably. The impedance data, for BCF23, are presented in Z* complex plane plots and admittance spectroscopic plots with/ without dc bias in (Figure 6.2). It shows that on application of 14 V (122V/cm) the conductivity increased by two orders of magnitude and was fully reversible on the removal of the applied voltage (Figure 6.2 b). The reversibility of the change to electrical properties indicates that no irreversible decomposition occurred in the sample during the application of the dc bias.

The resistivity of all compositions decreased significantly by up to two orders of magnitude on application of a certain voltage before reaching a steady state whose resistivity was a few hundred Ohms (Figure 6.3). A similar effect of the dc bias was observed with increasing

temperature in the range 20-60 °C. in other words, the resistivity of samples switches back and forth between ON and OFF states on application and removal of dc bias.

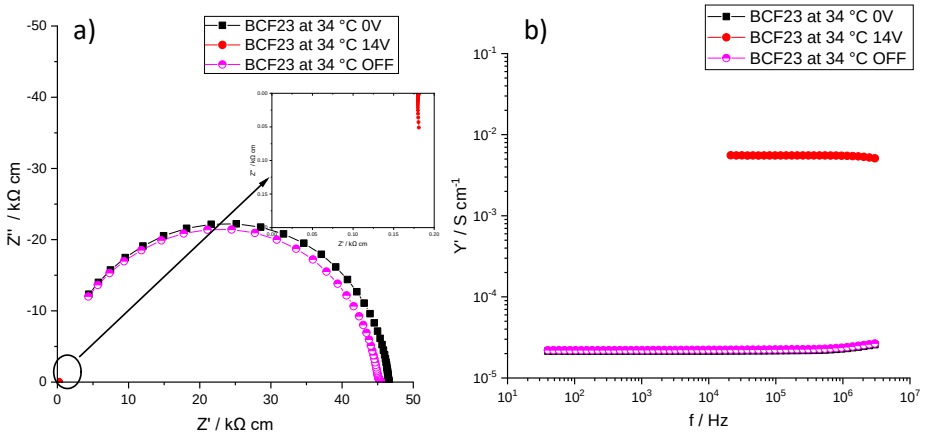

Figure 6.2. (a) Impedance complex plane plots, Z, (b) admittance spectroscopy plots, for BCF23, processed in air, at 34 °C under application of dc bias, as noted beside each graph.*

In order to understand this voltage-dependent behaviour and the important parameters, several experiments were carried out. First, the applied voltage was increased or decreased gradually from 1 to 20 V, and then the impedance was measured after reaching a steady state for each applied voltage in both directions (Figure 6.3a & c). On increasing the applied voltage, the conductivity increased slightly and steadily, but at a certain voltage (onset voltage), increased suddenly by two orders of magnitude before levelling off at an approximately constant value. On subsequent decreasing applied voltage, the high state conductivity was maintained, with hysteresis, before switching back suddenly to the low conductivity state (Figure 6.3a & c). The recovery voltage is referred to as twilight voltage.

Second, the same experiment was performed but at different temperatures, in the range 20-60 °C (e.g. Figure 6.3a). The onset voltage showed temperature-dependence which decreased with increasing temperature, while the twilight voltage was temperature-independent in this measured range. Thus the σ/V hysteresis loop became narrower with increasing temperature. It is worthwhile to mention that the sample does not switch before reaching the onset voltage at a given measurement temperature, but the conductivity does increase slightly.

Third, the ON state was measured as a function of temperature in which its impedance was measured after reaching steady state with an applied voltage of 151 V/cm at different temperatures. The Arrhenius plots (Figure 6.3b) of ON and OFF states were very different

which showed metallic behaviour with E_a= 0.007 eV for the ON state while the OFF state showed semiconducting behaviour with E_a=0.62 eV.

Fourth, the time-profile of switching behaviour was measured at different temperatures and voltages. At 35 ℃, for instance, the conductivity of BCF23 increased over a period of 10 minutes before levelling off with 132 V/ cm bias, while the sample reached steady state within 4 min with 151 V/ cm bias (Figure 6.3d).

Fifth, on increasing the temperature, the required onset voltage became smaller as shown previously, and also the time-taken to switch and reach a steady state became smaller. For example, BCF23 conductivity switched at 35 ℃, within 11 minutes with 132 V/ cm while it switched, at 45 ℃, within 7 minutes with 113 V/cm (Figure 6.4a).

In all experiments, the increase in conductivity was fully reversible on the removal of dc bias and the sample returned to its original state and the recovery time was temperature- and composition-independent. From the above results, it is clear that, the switching time is temperature- and voltage-dependent in which the sample switches to ON state faster with increasing temperature and/ or voltage.

Sixth, the switching behaviour and the time-taken to switch between ON and OFF states in both directions were measured as function of oxygen partial pressure. It showed no dependence of switching and recovery time on pO_2 during measurements and both directions were almost identical in N_2 and O_2 on application of 113 V/ cm at 43 ℃ (Figure 6.4b). Thus, the exchange between the atmosphere and sample is not an important factor for this resistive-switching behaviour in air processed samples especially at these low temperatures.

Seventh, the voltage-induced conductivity was measured as function of pO_2 in which the voltage was increased from 0 to 12 V (0-140 V/cm) and then, the sample impedance was measured after reaching a steady state Figure 6.5. The measurements were done in O_2 and N_2 sequentially at each voltage. The change in the resistivity was atmosphere-independent and the change was the same in both N_2 and O_2. These results indicate that the enhancement of conductivity is probably due to huge increase of same carriers which are holes in these materials, as discussed above, and no p-n transitions observed at high voltages similar to those observed in YSH [5] and YSZ [11].

Selective results, especially for BCF23, have been shown here as typical results to avoid unnecessary repetition. These results can be regarded as the general behaviour for BCF30 and BCF40. Furthermore, all Ca-doped BF compositions, processed in air, behaved similarly in response to the dc bias application in the different measurement conditions.

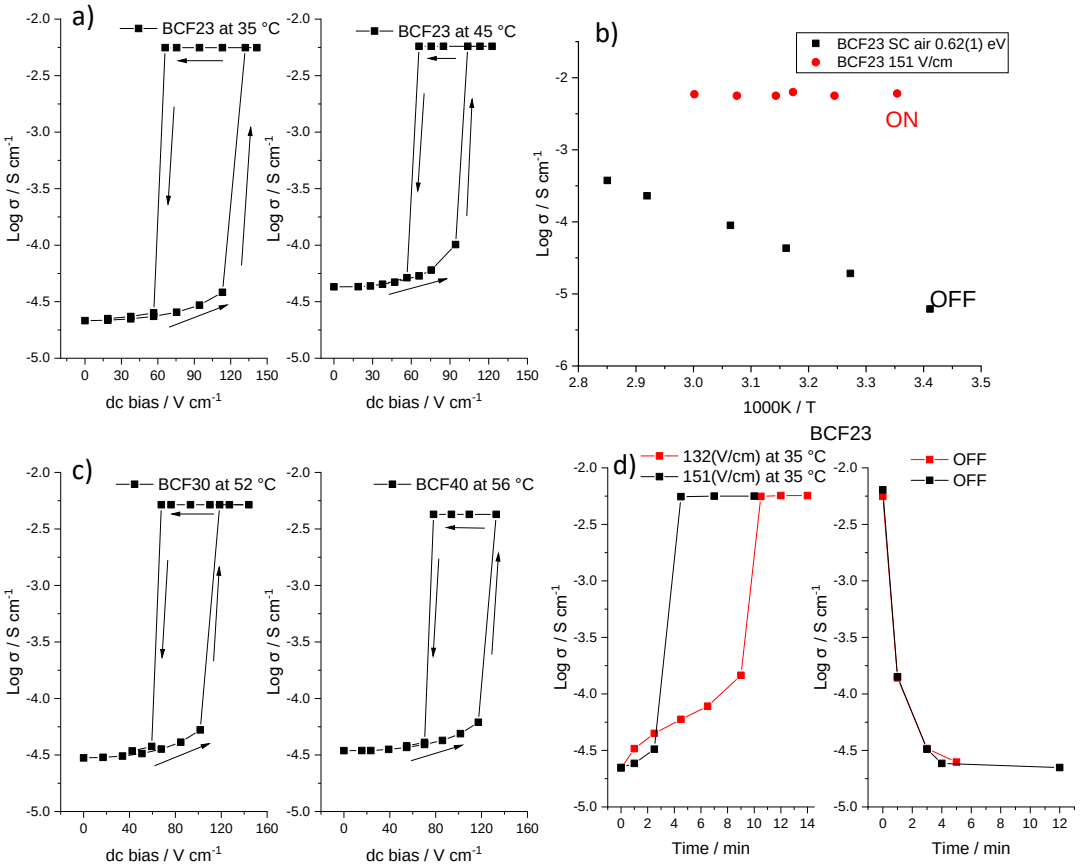

Figure 6.3. (a and c) The conductivities of samples after reaching steady state vs. applied voltage at different temperatures, as noted above each graph. (b) Arrhenius plots of the bulk conductivities during ON and OFF states. (d) The conductivities of BCF23 as function of time after applying different voltages.

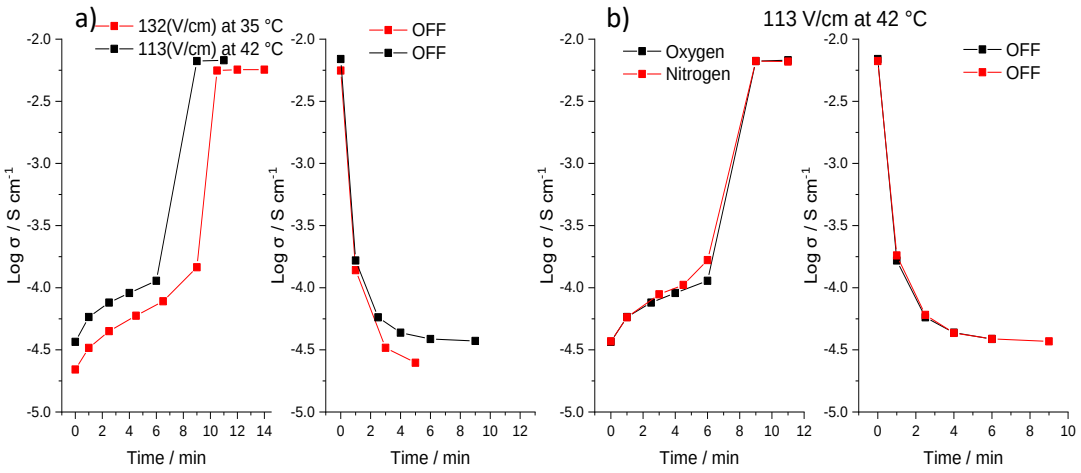

Figure 6.4. The conductivities of BCF23 as function of time after applying voltages: (a) at different temperatures and (b) in different atmospheres.

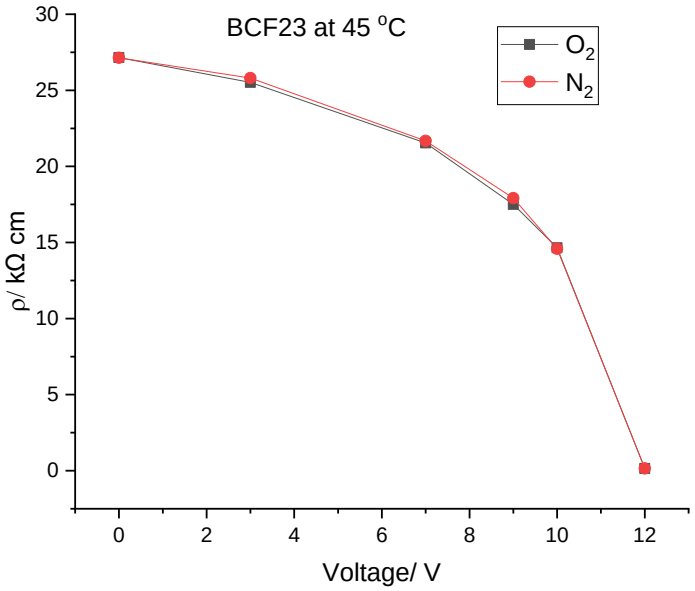

Figure 6.5. The effect of increasing voltage on BCF23 Resistivity as function of pO_2

6.2.1.2. Undoped BF

The effect of application of small dc bias (1-17 V) on undoped BF was studied in order to help understand the switching mechanism, identify which materials shows RS behaviour and the importance of oxygen vacancy and oxide-ion conduction in RS behaviour. Figure 6.6a shows that at 50 ºC and on applying 8 V (80 V/cm), the sample bulk resistivity of BF did not change and the total resistivity decreased slightly due to small reduction in the resistivity of the low frequency component. On increasing the applied voltage above 8 V, the bulk resistivity started to decrease slightly until the sample switched its resistance by two orders of magnitude at 17 V (170 V/cm) after 6 minutes (Figure 6.6a). Unlike Ca-doped BF samples, this change in BF resistivity is not reversible on removal of dc bias and did not recover its original state.

The impedance spectroscopy results for undoped BF completely changed after switching the sample, since all data sets in different formalisms were completely different to those of the original state (Figure 6.6). The sample resistivity increased by about four orders of magnitude after removing the applied voltage (Figure 6.6a). Also, the M`` peak was shifted to lower frequency and became very broad in which the peak width at half maximum was more than two decades (Figure 6.6b). The capacitance plots (Figure 6.6d) and the Z`` plots (Figure 6.6b) showed three electrical regions at low, intermediate and high frequency. These results indicate that the application of 17 V is likely to be above the electrical breakdown voltage, and the sample decomposed electrochemically. Unlike Ca-doped BF, therefore, un-doped BF does not show reversible RS under the application of dc bias.

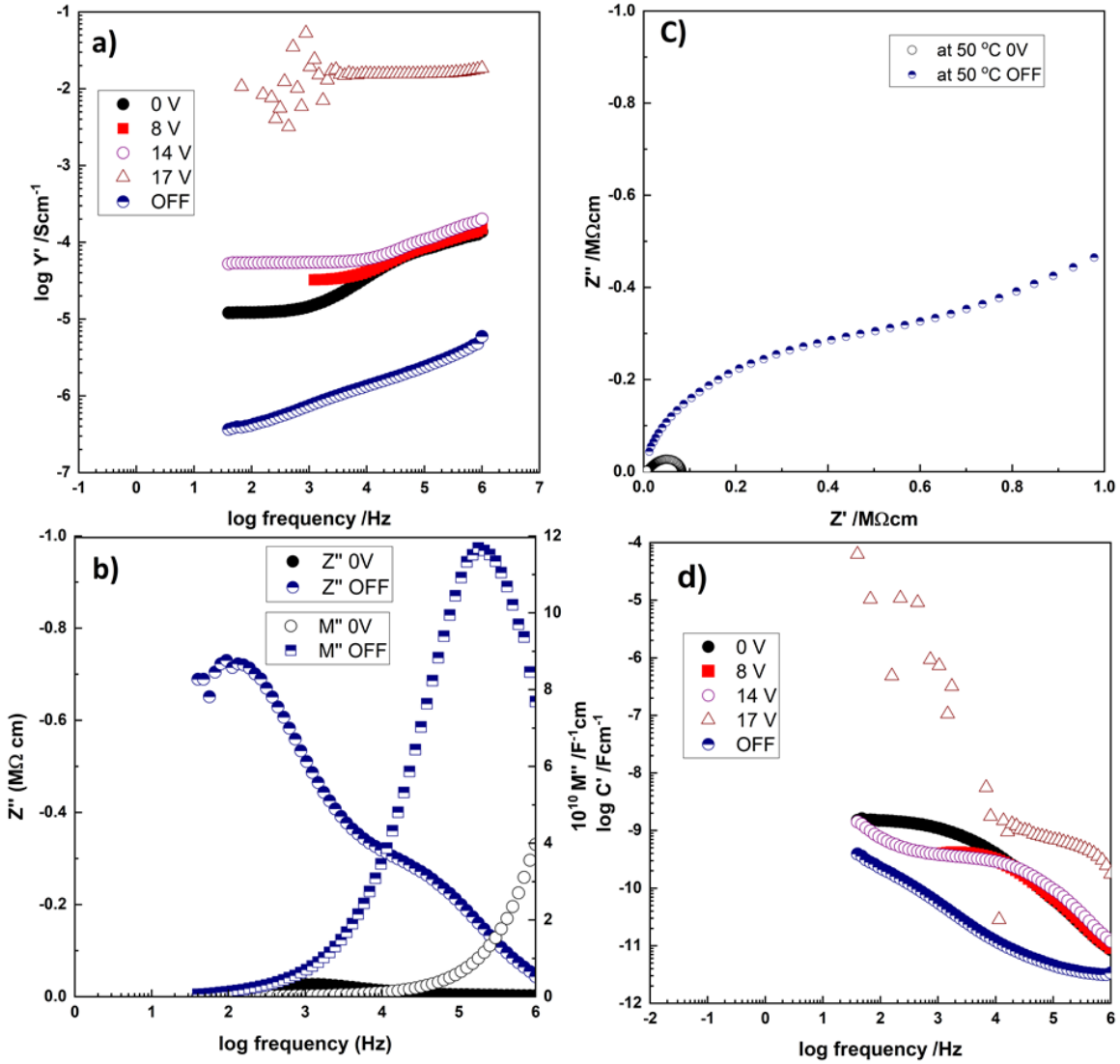

Figure 6.6. The impedance response for undoped BF, at 50 ℃, before, during and after application of different dc bias: : a) admittance spectroscopy plots, b) Z``/ M`` spectroscopy plots, c) impedance complex plane plots d) capacitances spectroscopy plots

6.2.2. N_2-processed samples

Since the N_2-processed sample conductivities decreased by a few orders of magnitude and the properties changed from p-type semi-conduction to oxide-ion conduction compared with those of air-processed samples, it is interesting to study the effect of the dc bias on these samples. Therefore, in this section, the effect of application of a very small dc (< 60 V/cm) bias on N_2-processed samples of BCF23 and 30 was studied.

The same pellets, that were used for section 6.2.1, were used here but each composition was heat-treated in N_2 at 940 ℃ for either 2 or 12h and then slow cooled to room temperature. It was found that the application of a small dc bias (below 5V (60 V/cm)) led to switching of the sample resistance by a few orders of magnitude over the temperature range (200-270 ℃) for both heating times. However, the samples responded differently to the removal of dc bias.

Firstly, Figure 6.7 shows the effect of processing time on the sample conductivities in which both samples were insulators at RT, but their conductivity-temperature profiles were different, especially at high temperatures. Therefore, they had different activation energies in which 12h-N_2-processed BCF23 and BCF30 were 0.89(1) and 0.91(1) eV, while 2h-N_2-processed were 0.71 (1) and 0.73 (1) eV, respectively. This indicates that the sample needs some time in order to lose excess oxygen and become in equilibria with the surrounding atmosphere and therefore, oxygen stoichiometric.

It is reported in chapter 4 that, these materials are primarily oxide-ion conductors when they are processed in N_2 and p-type semiconductors when processed in air or O_2. Data for 12h-processed samples were similar to those of N_2-processed samples reported in Figure 4.9 a and b.

However, 2h-processed samples had much lower activation energy than 12-N_2-processed samples with similar conductivities. Their activation energies were a little higher than air-processed BCF23 and 30 (0.62 and 0.57 eV), but still much less than normally associated with pure oxide-ion conductors. These results give a good indication that 2h-N_2-processed samples are primarily oxide-ion conductors but with higher level of electronic conduction than 12h-N_2-processed samples. Investigations of the level of electronic conduction is beyond the scope of this chapter in which the focus is on the effect of application of small dc bias on impedances of samples processed in N_2 for different times.

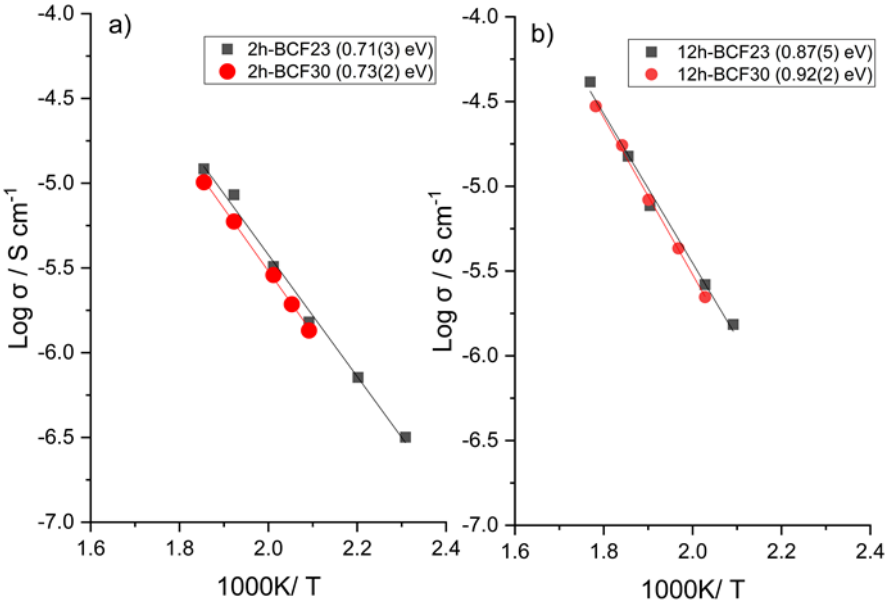

Figure 6.7. Arrhenius plots of the bulk conductivities for each sample after different processing times, as noted beside each graph. The activation energies in (eV) are shown beside each composition label.

Both 12h-processed samples respond similarly to the dc bias in which their conductivities increased by three orders of magnitude (Figure 6.8). On decreasing the applied voltage, the samples maintained the ON states and did not recover their original states (Figure 6.8), but the conductivities decreased slightly with decreasing the voltage until reaching lower conductivities at about 4.7 V/cm before a slight increase that occurred after the removal of the dc bias. This unusual effect, seen in both samples, may indicate the contribution of a capacitive discharging mechanism in which charge is stored on one electrode (probably +ve electrode) on application of a small dc bias.

Figure 6.8 shows the effect of re-application of an increasing bias on 12h-N_2-processed BCF23 after switching. The 4.7 V data are clearly different from others. They show a low frequency spike in (a) with C` rising to about 10^{-6} F in (c). This is a strong indication of oxide ion conduction. The increase in the resistance in (a) between 0 to 47 V/cm is therefore probably because the electronic charge carriers were eliminated under these conditions. At higher voltage, the resistance decrease means that electronic carriers are, somehow, created. Therefore, this can be interpreted as follows: at 0V, the conductivity was primarily electronic; at 4.7 V/cm, no electronic conductivity and only oxide-ion conductivity was seen; at higher voltages, the electronic conductivity dominated and oxide-ion conductivity cannot be detected easily.

It is clear that, the nature of the sample impedance response to the dc bias changed after switching (Figure 6.9). Both sample resistances increased on application of 4.7 V/cm and then the total resistance decreased at higher voltages (14.1 and 37.7 V/cm). The change is fully reversible on the removal of dc bias. This indicates that the samples properties have changed after switching and free electrons may be introduced. The possibility of capacitive charging in Figure 7.6 as the final step on removing bias would mean that free electrons are released and their trapping could be the source of resistance increase at 4.7 V/cm.

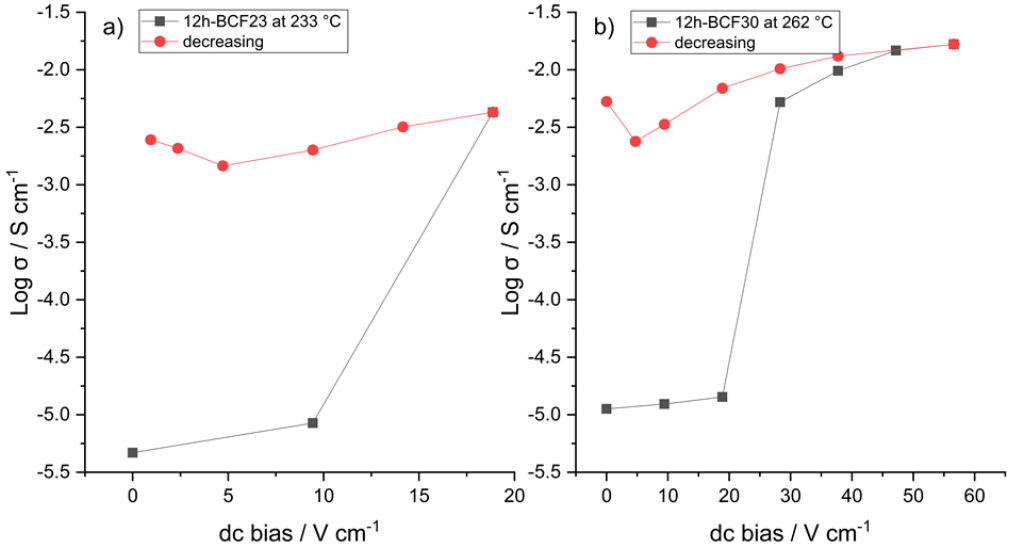

Figure 6.8. The conductivities of BCF23 (a) and BCF30 (b) processed in N_2 for 2h as function of increasing and decreasing dc bias measured in N_2.

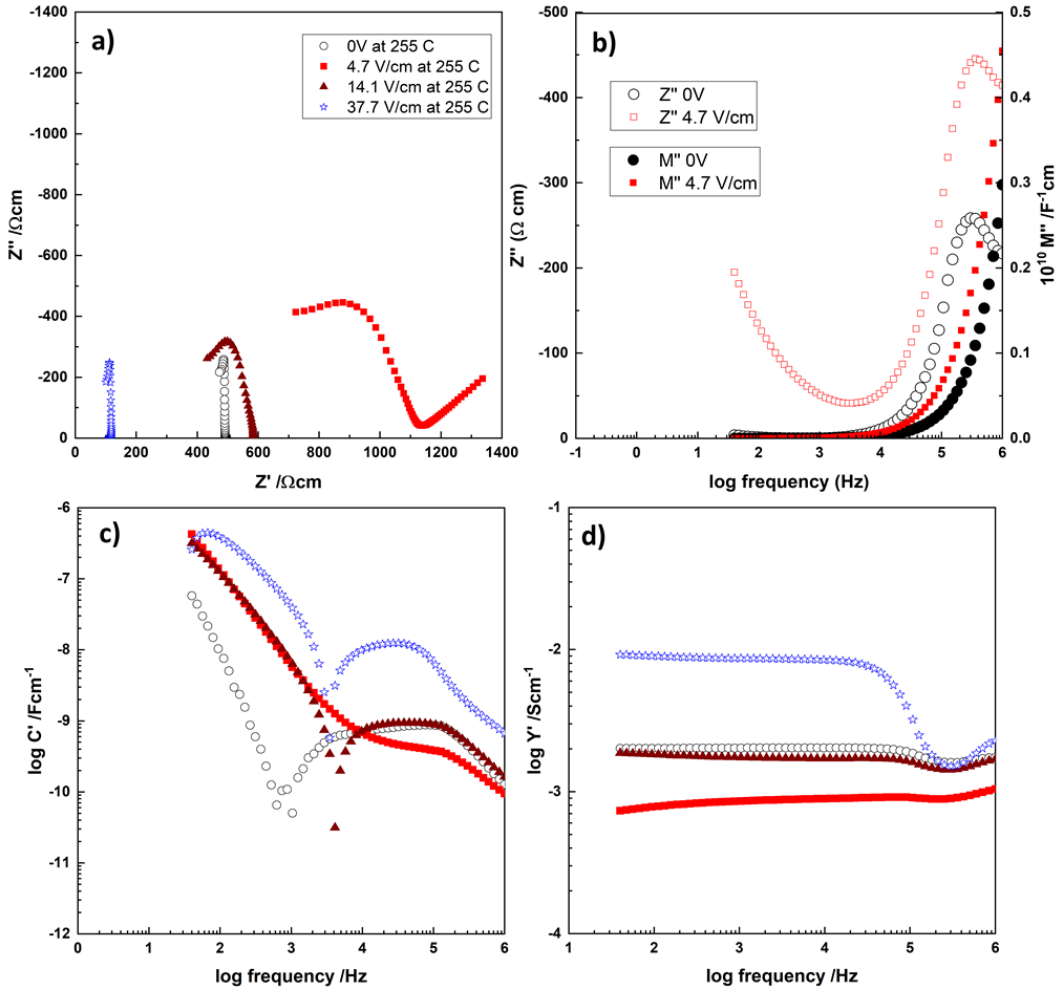

Figure 6.9. The effect of different dc bias re-application on impedance response for 12h-N_2-processed BCF23 after switching first time: a) impedance complex plane plots, b) Z``/ M`` spectroscopy plots, c) capacitances spectroscopy plots d) admittance spectroscopy plots.

Figure 6.10 a and b shows that 2h-processed-BCF23 conductivity increased by about four orders of magnitude on application of an increasing bias at 219 and 253 ℃. It also demonstrates that the onset voltage decreased with increasing temperature. The sample conductivity after switching increased slightly, and then levelled off and did not change further with increasing the applied voltage (a and b). So, this indicates that the conductivity now (in ON state) is voltage-independent and enters a new steady state. The sample recovered its original state only on removal of the dc bias.

Figure 6.10 c and d shows the effect of pO_2 on the 2h-processed BCF23 conductivity during the application and removal of 56.6 V/cm as function of time at 266 ℃. It shows that the sample switched to the above ON state again within around 17 minutes in both N_2 and O_2. The change in conductivity was larger in O_2 at each measured time. The sample recovered its original conductivity with similar times in both measured atmospheres (Figure 6.10d). Also, it is interesting that the OFF-ON switch is gradual over time.

Similarly, 2h-processed BCF30 conductivity increased faster in O_2, but this sample switched and reached a steady state more quickly in O_2 (Figure 6.11a). The sample took more than 3h to fully recover its original conductivity in N_2, while it partially recovered its original resistance in O_2 in which the sample resistance was two orders of magnitude lower than original resistivity after about 5h waiting (Figure 6.11b).

The sample maintained this new conductivity level after switching in O_2 until recharging at 102 V/cm in N_2 atmosphere. On removal of the applied 102 V/cm, the sample almost recovered its original resistance state (Figure 6.11b; pink triangles). These results indicate that the oxygen exchange between the sample and the atmosphere plays somehow an important role in switching mechanism, as discussed below. Since the change in conductivity is more rapid in O_2, this is a good indication of that the conductivity is probably p-type during the switching.

Firstly, a similar increase in p-type conductivity was reported previously in acceptor-doped perovskites such as Mg-doped $BaTiO_3$ [12], YSZ [13-15] and YSH [5]. The induced p-type conductivity was attributed to hole creation on underbonded O^{2-} by:

$$O^{2-} \rightarrow O^{-} + e^{-} \qquad (6.1)$$

And the ionised electrons may be trapped at the positive electrode, as in the charging of a capacitor. The increase in conductivities of 2h-processed BCF23 and 30 probably is due to a similar ionisation and trapping process, especially in atmospheres of low pO_2 (N_2).

The ionised electrons may also reduce oxygen molecules and cause them to ionise and dissociate to give O^- which can be absorbed by the lattice oxygen vacancies:

$$V_O^{\bullet\bullet} + \frac{1}{2}O_2 + O_O^x \leftrightarrow 2O_O^- \qquad (6.2)$$

And this can be another source of holes, especially in atmospheres of high pO_2.

It seems that, on application of a small dc bias, reaction (1) mainly lead to the increase in conductivities of 2h-processed BCF23 and 30 in N_2 while in O_2, the ionised electrons from reaction (1) may reduce oxygen molecules and they react as another source of holes according to reaction (2), as discussed above. Since there are two sources of holes in O_2 (i.e. ionised lattice oxide ions and the ionised and dissociated oxygen molecules), the conductivities of both types of BCF sample increased more rapidly in O_2 atmosphere.

On removing of the dc bias, since reaction (6.2) occurs spontaneously on increasing pO_2, the sample with higher oxygen vacancy (2h-processed BCF30) could not fully recover its original conductivity after switching in O_2.

Since the effects of reaction (6.2) are seen at temperatures above 150 °C and air-processed samples switched just above room temperature, the switching of air-processed samples was pO_2-independent and the increase of p-type conductivity was mainly due to the ionisation and trapping process in reaction (6.1).

The main differences between these materials, processed in N_2 for different times, 2h and 12h, is the level of electronic conductivity which decreased with increasing processing time. When they were processed in N_2 for 12h, they were mainly oxide ion conductors (i.e. have more oxygen vacancies). On the application of dc bias, their conductivities increased probably due to the increase in p- and n-type conductivity arising from reactions (6.1) and (6.3) at the positive electrode:

$$O^{2-} \rightarrow \frac{1}{2}O_2 + 2e^- \qquad (6.3)$$

It seems that at the positive electrode, holes are created (reaction (6.1)) and electrons are produced (reaction (6.1) and (6.3)); and the electrons are injected into the sample, at the negative electrode, similar to the mechanism reported in YSH. Since the switching occurred at relatively low temperatures, it is difficult for the sample to absorb oxygen. As result of this oxygen loss the samples did not recover their original conductivity and maintained the ON state after removing the dc bias. Also, the increase in the sample resistivity, after switching, on re-application of 4.7 V/cm is probably due to elimination of injected electrons according to (eq 6.3).

For those samples with higher level of electronic conductivity (air- and 2h-N_2-processed samples), the switching mechanism might not involve oxygen loss and be slightly different as discussed below.

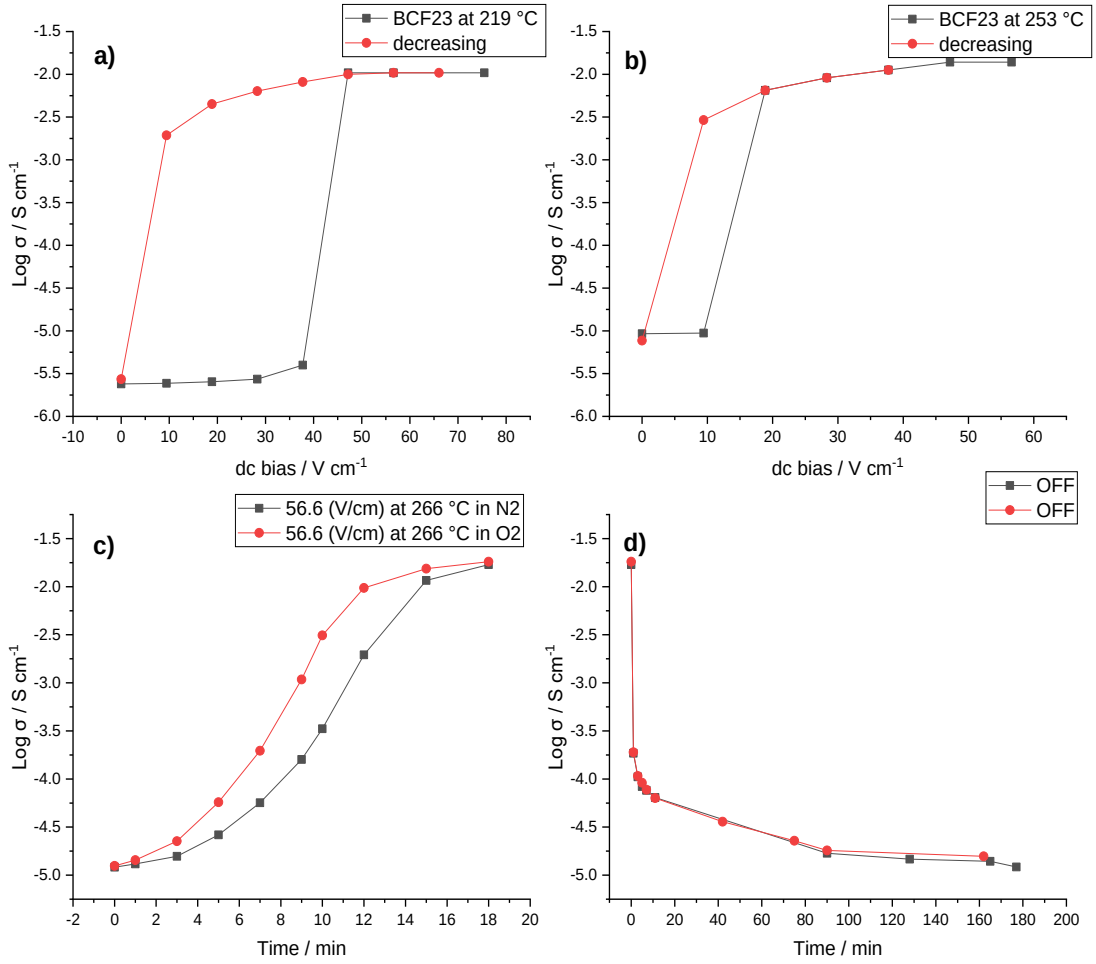

Figure 6.10. The conductivities of 2h-N_2-processed BCF23 after reaching steady state vs. applied voltage at 219 ℃ (a) and 253 ℃ (b), as noted above each graph, measured in N_2. The effect of application (c) and removal (d) of 56.6 V/cm on 2h-N_2-processed BCF23 conductivity as a function of time measured in N_2 (black)and O_2 (red).

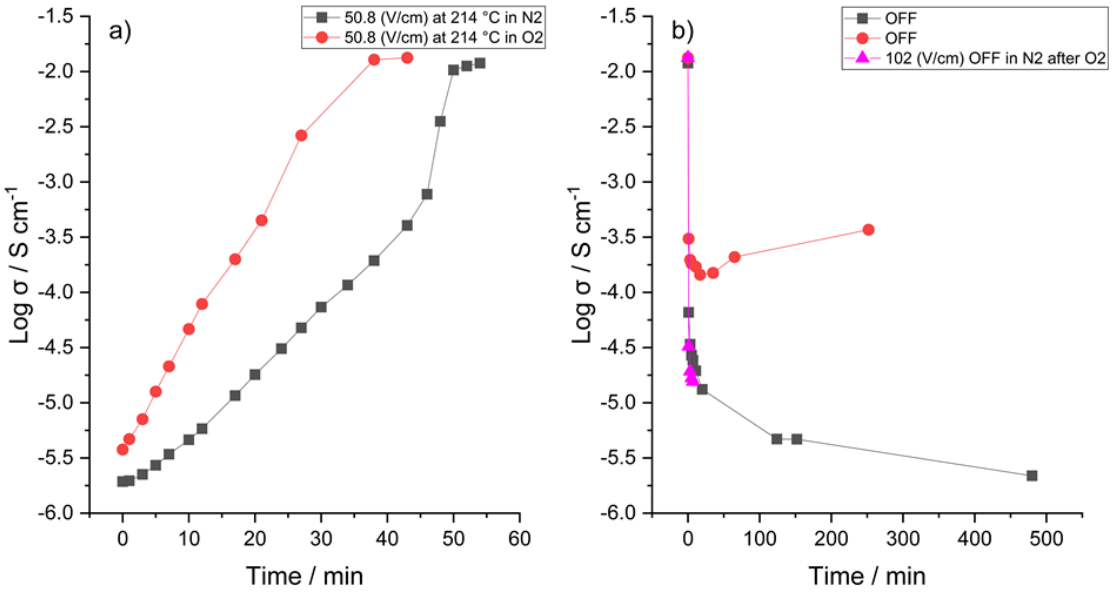

Figure 6.11. The effect of application (a) and removal (b) of 50.8 V/cm on 2h-N_2-processed BCF30 conductivity as function of time measured in N_2 (black) and O_2 (red).

In the next step, since the response of the N_2-processd sample to application of a dc bias was very slow and the samples took longer time to switch between HRS and LRS and during the recovery on the removal of the dc bias, measuring the sample impedance at different times can reveal the effect of dc bias on impedance data especially using different formalisms C` and M`` spectroscopic plots during the sample recovery.

Figure 6.12 shows the effect of application of 19 V/cm with time in all plots and formalisms of 2hN_2-BCF23. At 0V the complex plane plot (a) showed only a single semicircle attributed to the bulk response based on its capacitance (b) and the same data in Z"/ M" spectroscopic plots (d) showed a single peak in both cases which overlap indicating electrical homogeneity of the samples.

On application of 19 V/cm, the sample conductivity increased with time until full switching was obtained after 55 minutes (c). Increasing the applied voltage to 47.2 V/cm showed slight increase in the conductivity and then on further change even with increasing the voltage to 56.6 V/cm.

The C` data (b) showed an increase in the capacitance after 25 min indicating that the sample may split into two regions in which one region becomes thinner with time. The C` plot showed an inductive effect after 41 minutes at 10^3 Hz, a plateau of capacitance value about 2 nF/cm after 55 minutes at intermediate frequency, and linear decrease in the capacitance above 10^5

Hz giving rise the possibility of another region with lower capacitance at higher than instrument frequency limit.

Presenting the same data in M`` spectroscopy plots enables evaluation of the change in electrical microstructure with time. The magnitude of an M`` peak is inversely proportional to the capacitance of responsible region and therefore, relates to the region geometry. Thus, the volume fraction of the responsible region can be estimated approximately by the size of the M`` peak.

The M`` plots (e) showed that, in response to the application of 19 V/cm, the magnitude of M`` peak decreased and displaced toward higher frequency with time and became broader until becoming outside the measurement frequency range after 25 minutes. The frequency (f_{max}) at the M`` peak is related to the corresponding resistance by $2\pi f_{max}RC=1$. As the new capacitance in (b) increased and f_{max} displaced toward high frequency, the total sample resistance decreased with time.

On removal of the dc bias, the different plots recovered their original states gradually with time until they fully recovered after 16 h (Figure 6.13 and Figure 6.14). Interestingly, the M`` plot showed two peaks during the recovery (Figure 6.13d, Figure 6.14 d and f). The first peak was in the same position as the original peak but with lower magnitude, and the second peak was at higher frequency with higher magnitude than the first peak. The magnitude of the high frequency peak decreased as the first peak increased with time. Figure 6.14 d shows that the position of low frequency peak did not change with time. These results indicate that the time constant ($\tau = RC$) of low frequency region did not change with time and therefore, the resistance increased as the region got thicker. The sample recovered its original state after 16 h of the dc bias removal which showed a single M`` peak overlapping with the 0 V peak.

This splitting of the M`` peak means that the sample splits into two components during the recovery and their volume fractions change with time, and these components were in different electronic states. Therefore, the sample recovery occurs spontaneously but not homogeneously in which part of the sample recovered first and after 16 h the entire sample became one component of lower conductivity, as discussed below.

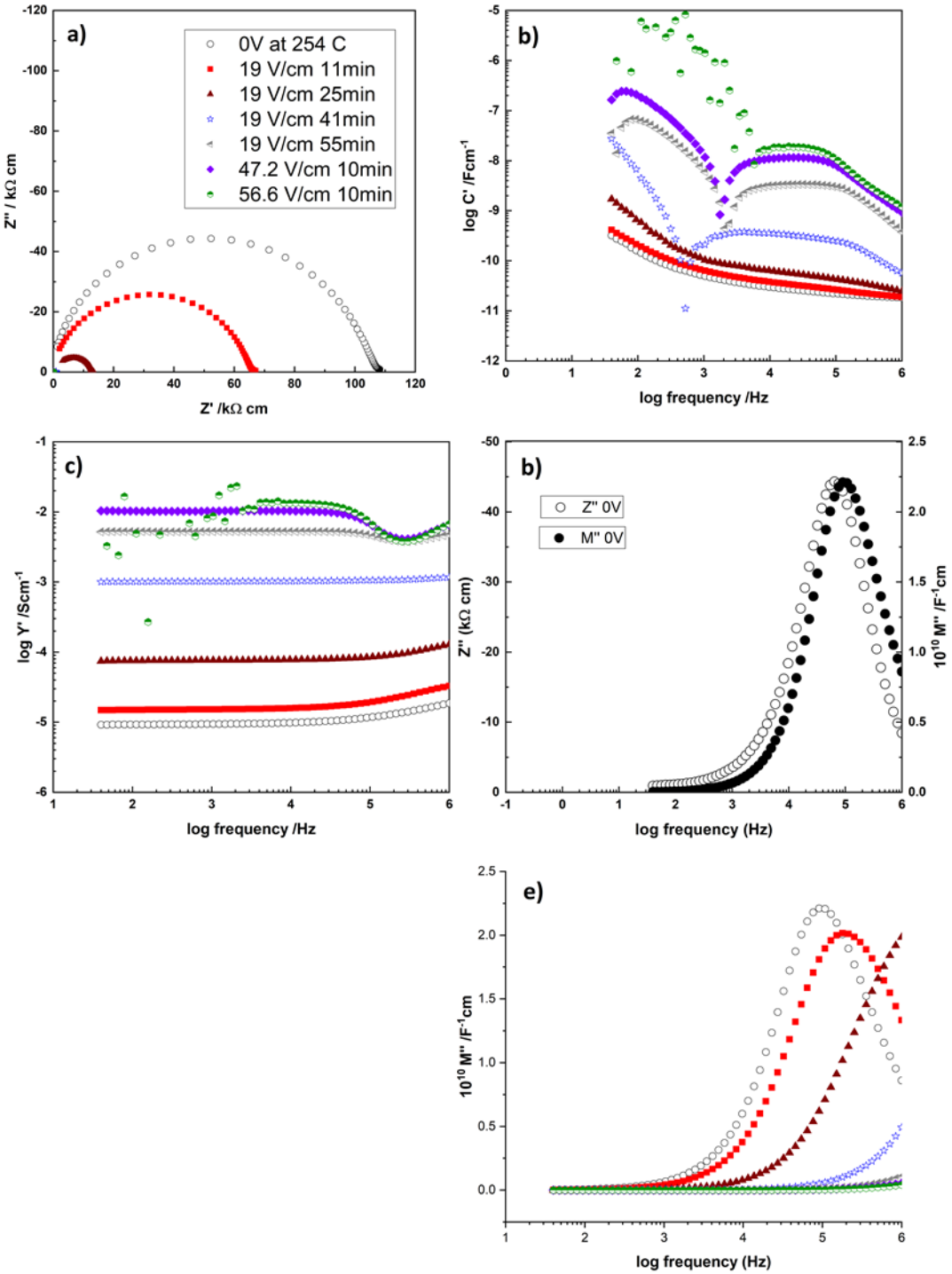

Figure 6.12. The effect of dc bias application on impedance response for 2h-N_2-processed BCF23 at 254 ℃, measured in N_2: a) impedance complex plane plots, b), capacitances spectroscopy plots, c) admittance spectroscopy plots, d) Z``/ M`` spectroscopy plots at 0 V, e) M`` spectroscopy plots at different voltages

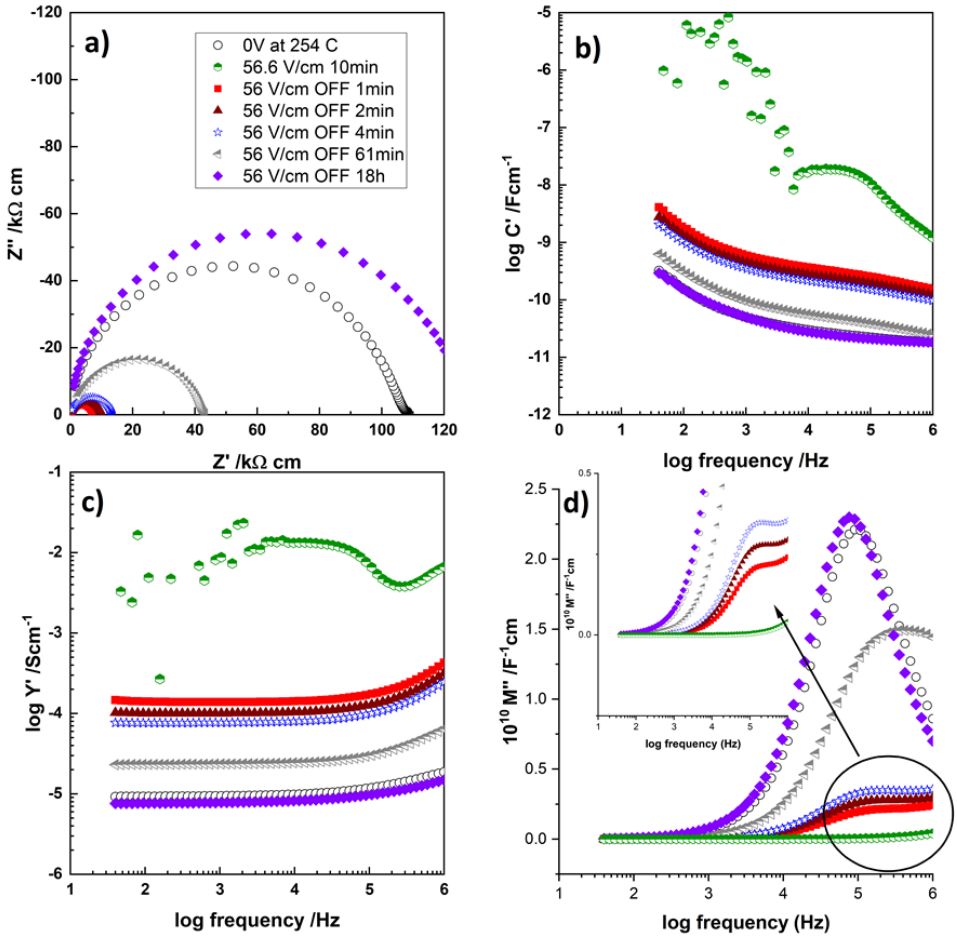

Figure 6.13. . The impedance response before, during application of 56.6 V/cm and the removal of 56.6 V/cm with time for 2h-N_2-processed BCF23 at 254 ℃, measured in N_2.

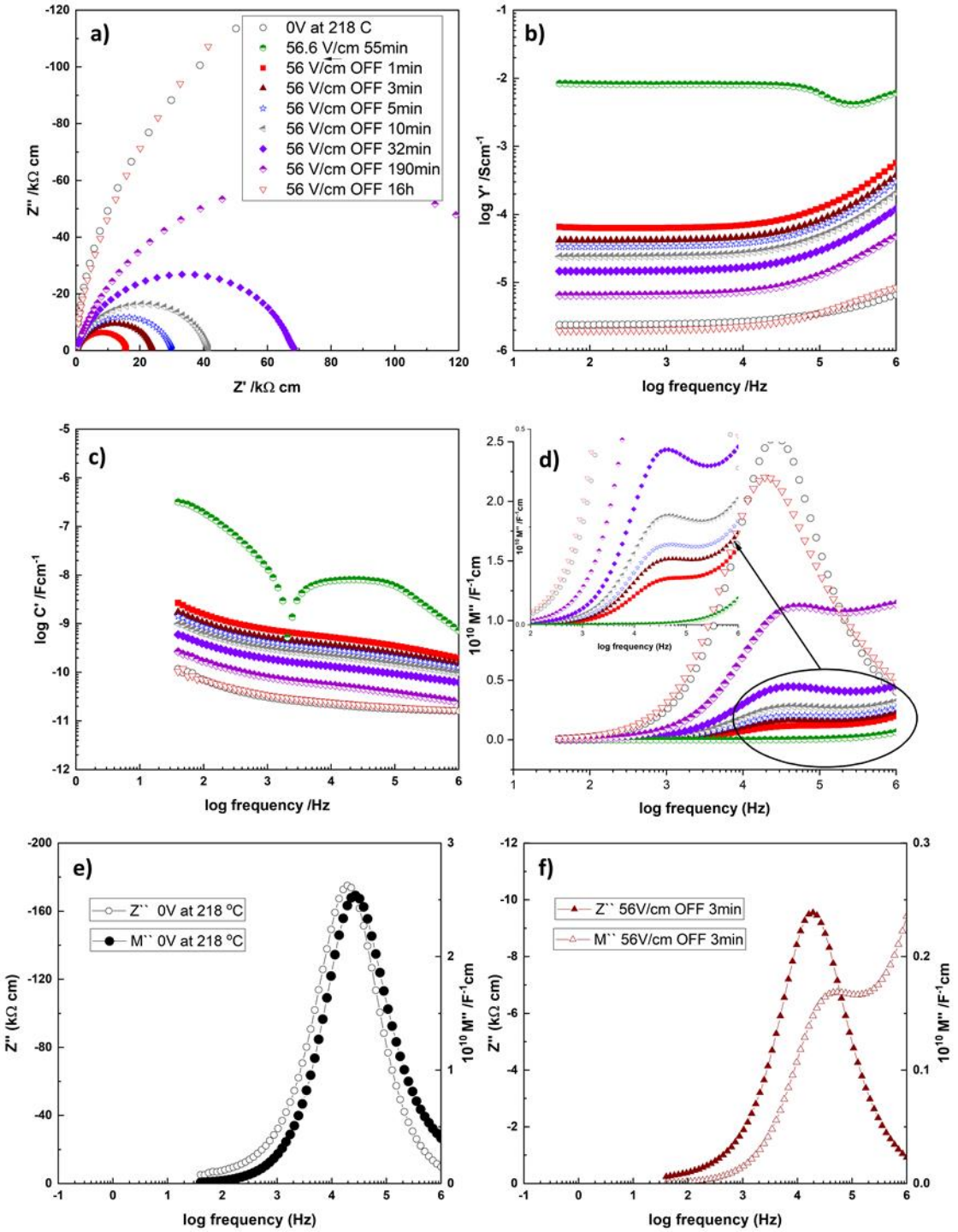

Figure 6.14. The impedance response before, during application of 56.6 V/cm and the removal of 56.6 V/cm with time for 2h-N_2-processed BCF23 at 218 °C, measured in N_2 (a-d). Z''/ M'' spectroscopic plots before (e) application of the dc bias and 3 minutes after dc bias removal (f).

Figure 6.15 shows the Arrhenius plots of total conductivity of 2h-N_2-procesed BCF23 for the same sample measured under application of 47 V/cm (On-state) and in the absence of applied voltage (Off-state). At the OFF-ON transition, the sample conductivity increased by 4 to 5 orders of magnitude at 240 ºC. Measuring the conductivity of 2h-N_2-prcessed BCF23 on cooling from 240 to 18 ºC showed two behaviours. From 290 to140 ℃, the sample conductivity showed a little reduction with activation energy of 0.13(3) eV and below 140 ºC, the conductivity decreased more with decreasing temperature with activation energy 0.65(2) eV which is almost similar to the sample activation energy in the absence of dc bias (0.72(4) eV).

The conductivity of a material with hopping conduction mechanism is given by:

$$\sigma = n\, e\, \mu \tag{6.4}$$

where n, e and μ are the number, charge and mobility of carriers, respectively. Since the activation energy of 47 V/cm data between 140-18 ℃ was similar to those obtained at 0 V data, the mobility or migration is the same, and the increase in conductivity, therefor, is attributed to an increase in the number of carriers. However, the curvature in Arrhenius plot and dramatic reduction in the activation energy in high temperature data (290-140 ℃) indicate the increase in the mobility of carriers.

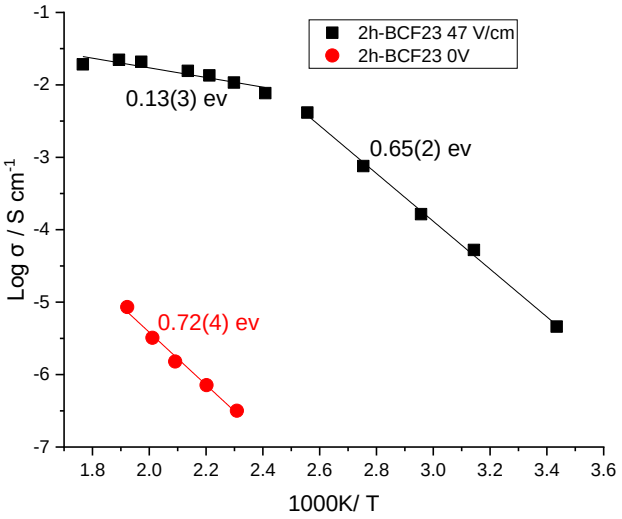

Figure 6.15. Arrhenius plots of 2h-N_2-processed BCF23 conductivity on heating in the absence of applied voltage (red) and on cooling under application of 47 V/cm (black).

6.3. Discussion

In chapter 4, it was demonstrated that Ca-doped BF materials are p-type and oxide ion mixed conductors. P-type conductivity becomes dominant if the sample was processed in high pO_2, while the oxide-ion conductivity dominates if the sample was processed in N_2.

The p-type conductivity of air-processed sample of BCF was enhanced by the application of a small dc bias (1-5 V). Recent studies of other acceptor-doped oxides, such as YSZ08 and Ca-doped BT, showed that the p-type conductivity was enhanced by either an increase of pO_2 or the application of dc bias [12, 15-17]. In those studies, the hole creation and conductivity enhancement were attributed to the ionisation of under-bonded oxygen (eq 6.1).

The driving force for ionisation of under-bonded oxygen comes from changing the equilibria at the positive electrode (anode), in which the ionised electron is attracted and trapped at the anode by forming reduced oxygen species (eq 6.2), whose net negative charge is balanced by hole creation as lattice O^-. So, several equilibria are likely to be present at a sample surface:

$$O_2(g) \leftrightarrow O_2(ads) \leftrightarrow O_2^- \leftrightarrow O_2^{2-} \,/\, 2O^- \leftrightarrow 2O^{2-}(surface) \leftrightarrow 2O^{2-}(bulk) \qquad (6.5)$$

In this chapter, it was shown that as the applied voltage is increased from 5 to 20 V, the conductivities of air-processed samples of Ca-doped BF increased steadily until reaching a certain voltage (switching voltage, V_s) and then the conductivity increased by up to three orders of magnitude. The increase of conductivity was reversible, with hysteresis, on removal of the bias. This means that Ca-doped BF ceramics have RS behaviour as has been reported in the literature [18].

Also, similar RS phenomenon was seen in N_2-processed samples. Since these samples were much more resistive than air-processed samples, they switched to LRS at higher temperatures. These materials switched at lower voltage (<5V), even with initial resistances and activation energies higher than those of air-processed samples.

The main difference between air- and N_2-processed samples during the application of dc bias was the switching temperatures. This indicates the importance of the temperatures on RS behaviour; and especially, in the initial increase of electronic conductivity which is a thermally activated process. Therefore, the created holes are localised on specific atom species rather than delocalised in the valence band.

It has been reported that RS observed in $Bi_{0.9}Ca_{0.1}FeO_3$ is due to variation of Schottky potential barrier [19]. The RS reported here appears not to be associated with a Schottky barrier since there is no component in the impedance results which can be attributed to a Schottky barrier (Figure 4.3 and 4.4); instead, the capacitance values indicate that the change in conductivity reported here is associated with bulk. Also, RS reported here is different from that reported with TiO_2-based thin layer memristor, in which the ON state is retained on removing the bias, and a reverse bias is required to switch it to OFF state. By contrast, the present switching is volatile and does not always require a reverse bias to regain the OFF state [20, 21]. So, the RS reported here is different and the first to be seen in a bulk material.

The absence of this RS in parent material (BF) indicates that the presence of oxygen vacancies is an important factor in switching behaviour. An effect of pO_2 on switching time was noticed in 2h-N_2-processed samples in which both BFC23 and BCF30 switched faster in O_2 and became more obvious in the higher dopant concentration sample. This effect aligns with the effect of increasing pO_2 during impedance measurements on N_2-processed samples, reported in chapter 4, in which the increase in conductivity was higher in the sample that has higher Ca content at the same measured temperature (Figure 4.11). This indicates the importance of oxygen exchange between the sample and atmosphere and presumably with the increase in oxygen vacancies with increasing Ca content. Also, Arrhenius plots for 2h-N_2-processed BCF23 with/ without application of dc bias (Figure 6.15), demonstrate that the dramatic change in the conductivity is attributed to the increase in carriers at low temperatures (<140 °C) and in mobility of carriers at higher temperatures.

Yttria-stabilised hafnia (YSH) is the second bulk material to show RS phenomenon. Similarly, YSH material is a p-type and oxide-ion mixed conductor. Unlike Ca-doped BF, YSH switches to LRS faster in atmosphere of low pO_2. So, the proposed switching mechanism of BCF is probably different, but with some similarity, especially in early stages of increasing p-type conductivity. Therefore, we propose a model for BCF response to the dc bias, as follows.

The model for BCF response to the applied bias is illustrated in Figure 6.16. Firstly, holes are created in the sample by the ionisation process in reaction (6.1) and the generated electrons are trapped at the positive electrode (anode), as in the charging of a capacitor. Since BCF is p-type, the attracted electrons are generated by ionisation of a redox-active element which is probably underbonded oxygen (eq 6.1).

Alternatively, the ionised electrons may undergo redox reaction with O_2 molecules leading to the formation of reduced oxygen species on the surface (eq 6.5), especially in O_2 atmosphere at high temperatures (Figure 6.16 a). These O^- may occupy the lattice vacancies, V_O, and become a source of holes (eq 6.2). Such process occurs spontaneously in response to an increase pO_2, without the need for a dc bias.

With time, further underbonded oxide ions ionise leading to thickening of the positively-charged layer, containing O^- ions, towards the sample interior. Therefore, a process of capacitive charging takes place, in which a net negative charge is developed at the anode that is offset by the net positive charge that is created in the sample interior as an accumulation of O^- ions. Since air-processed samples data did not show any p-n transition and the conductivity of 2h-N_2-processed samples switched faster in O_2, it is assumed that the enhancement of conductivity is mainly due to the increase of holes.

Secondly, As the number of positively-charged holes increases and they approach the negative electrode (cathode) surface, the sample conductivity increases by several orders of magnitude (Figure 6.16 b). After switching, the released electrons, eq 6.1, alternatively, may be injected to the sample cathode through the external circuit. These free electrons can move freely through the O^- from the negative electrode to the positive electrode (Figure 6.16 b). This explains the huge reduction in the activation at high temperature for 2h-N_2-processed samples.

The hopping of these free electrons between the created holes in lattice is assisted by the thermal energy and the applied voltage. The recovery process occurrs spontaneously on the removal of dc bias or decreasing the voltage below recovery voltage. Thirdly, when the voltage is removed or reduced below twilight voltage, the free electrons did not have sufficient energy to hope between the created holes in O^-. Thus, these free electrons recombine with the created holes cancelling the enhanced electronic conductivity and the sample starts to recover its original state (Figure 6.16 c).

During the recovery of BCF23 processed in N_2 for 2h after removing of the applied voltage, the M`` peak split into two peaks indicating that the sample was nonhomogeneous and split into two electronic states. They can be defined as ground state and excited state. The ground state is the region of the sample near to the cathode which recovered faster due to fast recombination between the free electrons, that already injected to the sample, and the created holes in O^-. The excited state is the region near to the anode, that still contain holes as O^- in

the early moment of dc bias removal. Finally, the excited region exhibits a longer recovery time probably because the change in the equilibria of surface area in (eq5) need to be reversed first, and then the released electrons diffuse back to the sample recombining with the O^- ions. Therefore, the sample now is fully recovered (Figure 6.16 d).

Studying the effect of decreasing the temperature after switching the sample to ON state (Figure 6.15) showed that below 140 ℃ the resistance started to increase with decreasing temperature with activation energy of 0.65 eV similar to 0V data, but with much lower resistance than 0V sample. This can be interpreted on the basis that below 140 ℃, the injected electrons did not have sufficient energy to hope freely through the sample, therefore they recombined with the created holes in O^- ions near the cathode. This leads to a decrease in the hole conductivity but the overall sample conductivity still is higher than 0V conductivity due to the existence of more holes than the 0 V sample especially near the anode region (Figure 6.16 c).

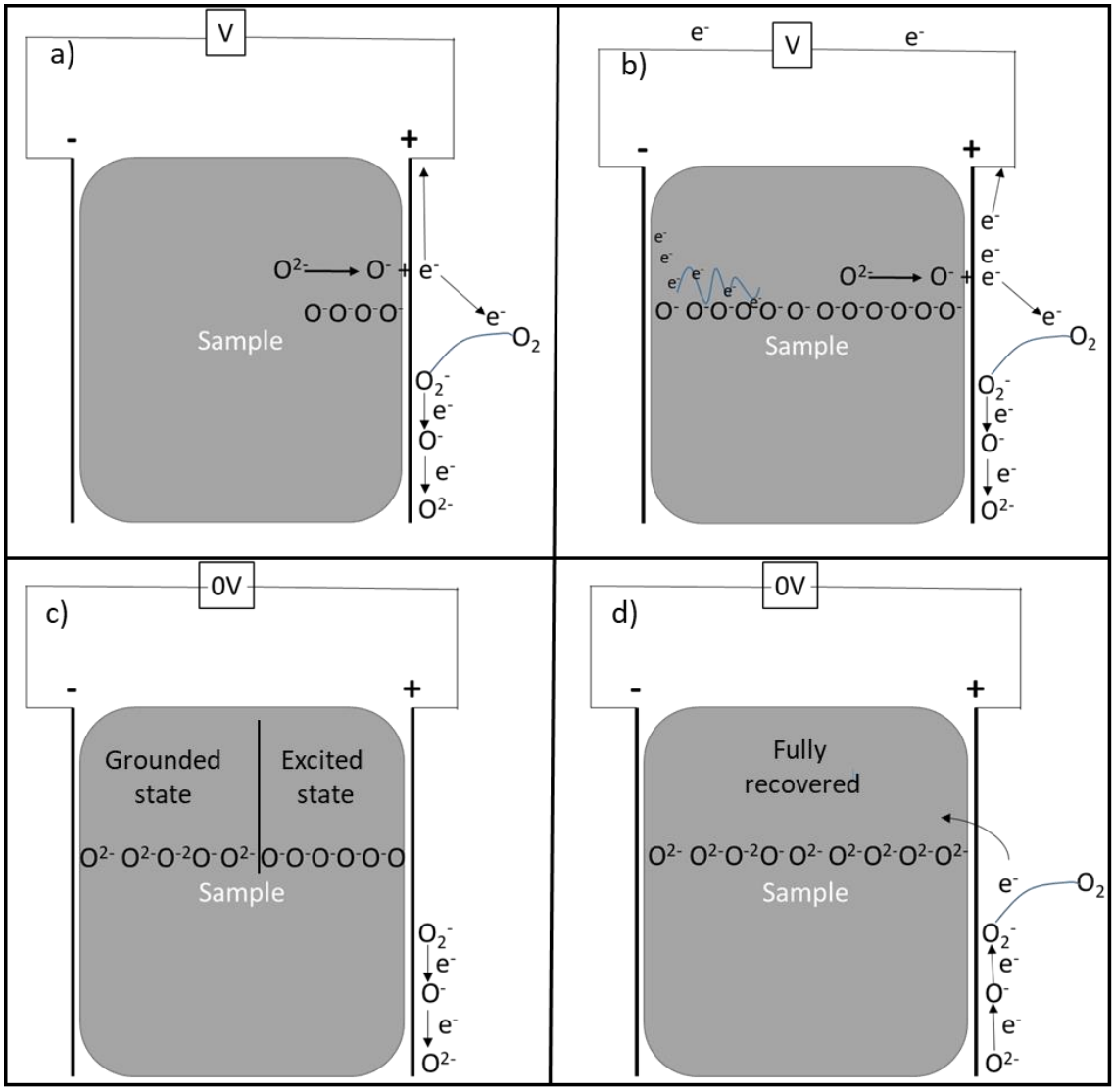

Figure 6.16. The proposed mechanism of RS of BCF, a) early stages of dc bias application, b) after switching of the sample resistance, c) first stage of the sample recovery on removal of dc bias, d) full recovery of the sample.

6.4. Conclusions

Three compositions of of $Bi_{1-x}Ca_xFeO_{3-x/2}$ (where: x = 0, 0.23, 0.3 and 0.4) were processed differently: i) in air, ii) in N_2 for 2 h and iii) in N_2 for 12h. The effect of application of a small dc bias on conductivities of all compositions were studied as function of temperature, pO_2, time and the magnitude of the applied voltage. All sample conductivities switched reversibly, ON-OFF, by 2-5 orders of magnitude on application/ removal of a dc bias.

Air-processed samples were mainly p-type semiconductors while 12-N_2-processed samples were mainly oxide-ion conductors. 2h-N_2-processed samples were mixed oxide-ion and p-type conductors with p-type conductivities higher than those of 12h-N_2-processed samples and lower than those of air-processed samples.

Air-processed samples were switched at temperature just above RT while N_2-processed samples were switched at temperatures above 200 ℃ due to the differences in their initial resistances. Resistive switching behaviour in air-processed samples was pO_2-independent since they were switched over limited temperatures, below 100 ℃ while 2h-N_2-processaed samples switched in O_2 more rapid than in N_2. The mechanism of resistive switching is attributed to huge increase in hole concentration by internal ionisation of redox active elements, which are believed to be underbonded oxygen, and trapping of the ionised electrons at the positive electrode.

6.5. References

1. Masó, N., H. Beltrán, M. Prades, E. Cordoncillo, and A.R. West, *Field-enhanced bulk conductivity and resistive-switching in Ca-doped BiFeO 3 ceramics.* Physical Chemistry Chemical Physics, 2014. **16**(36): p. 19408-19416.
2. Prades, M., N. Masó, H. Beltrán, E. Cordoncillo, and A.R. West, *Field enhanced bulk conductivity of BaTiO3 : Mg ceramics.* Journal of Materials Chemistry, 2010. **20**(25): p. 5335.
3. Liu, Y. and A.R. West, *Voltage-dependent resistance of undoped rutile, TiO2, ceramics.* Applied Physics Letters, 2013. **103**(26): p. 263508.
4. Zhang, Q.-L., N. Masó, Y. Liu, H. Yang, and A.R. West, *Voltage-dependent low-field resistivity of CaTiO3:Zn ceramics.* Journal of Materials Chemistry, 2011. **21**(34): p. 12894.
5. Alotaibi, M., F. Almutairi, and A.R. West, *Resistive-switching in yttria-stabilized hafnia ceramics.* Journal of the American Ceramic Society, 2022. **106**(2): p. 822-828.
6. Kumar, D., R. Aluguri, U. Chand, and T.Y. Tseng, *Metal oxide resistive switching memory: Materials, properties and switching mechanisms.* Ceramics International, 2017. **43**: p. S547-S556.
7. Lee, J.S., S. Lee, and T.W. Noh, *Resistive switching phenomena: A review of statistical physics approaches.* Applied Physics Reviews, 2015. **2**(3).
8. Panda, D. and T.-Y. Tseng, *Perovskite Oxides as Resistive Switching Memories: A Review.* Ferroelectrics, 2014. **471**(1): p. 23-64.
9. García, J. and G. Subías, *The Verwey transition—a new perspective.* Journal of Physics: Condensed Matter, 2004. **16**(7): p. R145.
10. Walz, F., *The Verwey transition-a topical review.* Journal of Physics: Condensed Matter, 2002. **14**(12): p. R285.
11. Jovaní, M., H. Beltrán-Mir, E. Cordoncillo, and A.R. West, *Field-induced pn transition in yttria-stabilized zirconia.* Scientific Reports, 2019. **9**(1): p. 18538.
12. Prades, M., N. Masó, H. Beltrán, E. Cordoncillo, and A.R. West, *Field enhanced bulk conductivity of BaTiO3 : Mg ceramics.* Journal of Materials Chemistry, 2010. **20**(25).

13. Vendrell, X. and A.R. West, *Electrical properties of yttria-stabilized zirconia, YSZ single crystal: local AC and long range DC conduction.* Journal of The Electrochemical Society, 2018. **165**(11): p. F966.
14. Jovani, M., H. Beltran-Mir, E. Cordoncillo, and A.R. West, *Atmosphere- and Voltage-Dependent Electronic Conductivity of Oxide-Ion-Conducting Zr(1-x)Y(x)O(2-x/2) Ceramics.* Inorg Chem, 2017. **56**(12): p. 7081-7088.
15. Masó, N. and A.R. West, *Electronic conductivity in yttria-stabilized zirconia under a small dc bias.* Chemistry of Materials, 2015. **27**(5): p. 1552-1558.
16. Ren, P., N. Masó, Y. Liu, L. Ma, H. Fan, and A.R. West, *Mixed oxide ion and proton conduction and p-type semiconduction in BaTi0.98Ca0.02O2.98 ceramics.* Journal of Materials Chemistry C, 2013. **1**(13).
17. Zhang, Q.-L., N. Masó, Y. Liu, H. Yang, and A.R. West, *Voltage-dependent low-field resistivity of CaTiO3:Zn ceramics.* Journal of Materials Chemistry, 2011. **21**(34).
18. Maso, N., H. Beltran, M. Prades, E. Cordoncillo, and A.R. West, *Field-enhanced bulk conductivity and resistive-switching in Ca-doped BiFeO3 ceramics.* Phys Chem Chem Phys, 2014. **16**(36): p. 19408-16.
19. Rubi, D., F. Gomez-Marlasca, P. Bonville, D. Colson, and P. Levy, *Resistive switching in ceramic multiferroic Bi0.9Ca0.1FeO3.* Physica B: Condensed Matter, 2012. **407**(16): p. 3144-3146.
20. Choi, B.J., S. Choi, K.M. Kim, Y.C. Shin, C.S. Hwang, S.-Y. Hwang, S.-s. Cho, S. Park, and S.-K. Hong, *Study on the resistive switching time of Ti O 2 thin films.* Applied physics letters, 2006. **89**(1): p. 012906.
21. Jeong, D.S., H. Schroeder, and R. Waser, *Mechanism for bipolar switching in aPt/TiO2/Ptresistive switching cell.* Physical Review B, 2009. **79**(19).

Chapter 7 : Resistive switching in Y-doped CeO_2 ceramics

7.1. Introduction

Resistive switching phenomena reported in bulk ceramics of Ca-doped $BiFeO_3$ (BCF) and Y-doped HfO_2 (YSH) is clearly similar in nature [1, 2]. However, it is different from those reported in other bulk materials associated with phase transitions and metal-insulator transitions, or in thin films that are associated with the formation and rupturing of conducting filaments [3-11]. Both BCF and YSH show different levels of mixed oxide-ion and p-type conductivity due to the presence of oxygen vacancies which lead to variable oxygen content for example:

$$V_O^{\bullet\bullet} + \frac{1}{2}O_2 \rightarrow O_O^x + 2h^{\bullet} \qquad (7.1)$$

Undoped BF does not show RS behaviour. In general, stoichiometric materials, such as $BaTiO_3$, do not show sensitivity to dc bias, but when they are acceptor-doped, their conductivity becomes voltage- and pO_2-dependence [12-16]. This indicates the importance of oxygen vacancies in such increase in conductivity in response to the application of a small dc bias.

Another important factor is that the presence of electronic conductivity raises the following question: is the type of electronic conductivity important. Since electronic conductivity in these materials is p-type, it is worthy of interest to study the effect of dc bias on a material with similar properties of mixed conductivity but with n-type electronic conductivity.

Pure and doped ceria (CeO_2) materials are well known mixed oxide ion and n-type conductors [17, 18]. Ceria-based materials have been intensively studied for many decades due to their various applications as electrode and electrolyte in solid oxide fuel cell (SOFC) and catalysts [19-22]. CeO_2 has fluorite structure with space group Fm3m which is stable over the whole temperature range from RT to melting point [17]. Its fluorite structure is very tolerant to doping with lower valence elements above 40% in some cases such doping with Y and rare earth oxides. The defect structure of ceria has been studied extensively for years [23]. From this extensive literature, mixed conductivity of acceptor-doped CeO_2 is discussed here.

Doped-CeO_2 has higher ionic conductivity than YSZ, the conventional electrolyte material in SOFC, at intermediate temperatures (400-700 ℃) and has good thermodynamic stability [24].

Oxygen vacancies are generated mainly by doping with lower valence such as Y^{3+} and Gd^{3+} [17]. For example, in Y-doped CeO_2, oxygen vacancies are generated via the reaction:

$$Y_2O_3 + 2Ce_{Ce}^{x} + O_O^{x} \rightarrow 2Y'_{Ce} + V_O^{\bullet\bullet} + 2CeO_2 \quad (7.2)$$

The mixed conductivity in acceptor-doped ceria materials is due to reduction of Ce^{4+} to Ce^{3+} at high temperature (< 800 °C) and/ or in reduced atmosphere [18, 22]. Under these conditions, the material tends to lose oxygen generating more oxygen vacancies and electrons according to the following reaction:

$$O_O^{x} \rightarrow \frac{1}{2} O_2 + V_O^{\bullet\bullet} + 2e' \quad (7.3)$$

And this lead to reduction of Ce^{4+} to Ce^{3+}. Therefore, Y-doped CeO_2 (YDC) becomes a mixed oxide-ion and n-type semiconductor under these condition.

The electronic conductivity may be also induced at low temperatures by an application of a small dc bias similar to YSZ [25]. Since YDC has similar mixed conductivity to YSH and BCF but with electronic conductivity of n-type, it may show similar reported RS behaviour.

In this chapter, the electrical properties of $Ce_{0.84}Y_{0.16}O_{1.92}$ were studied using impedance spectroscopy. The impedance measurements were performed as function of temperature, pO_2, voltage and a combination of both pO_2 and V. The sample conductivity was studied as function of an increased bias in different atmospheres and at different temperatures in order to discover any RS behaviour.

7.2. Results and discussion

Figure 7.1 shows the XRD pattern of $Ce_{0.84}Y_{0.16}O_{1.92}$ which confirms that the sample was single phase. Data were indexed on a cubic unit cell, consistent with the reported data in the literature [21, 24].

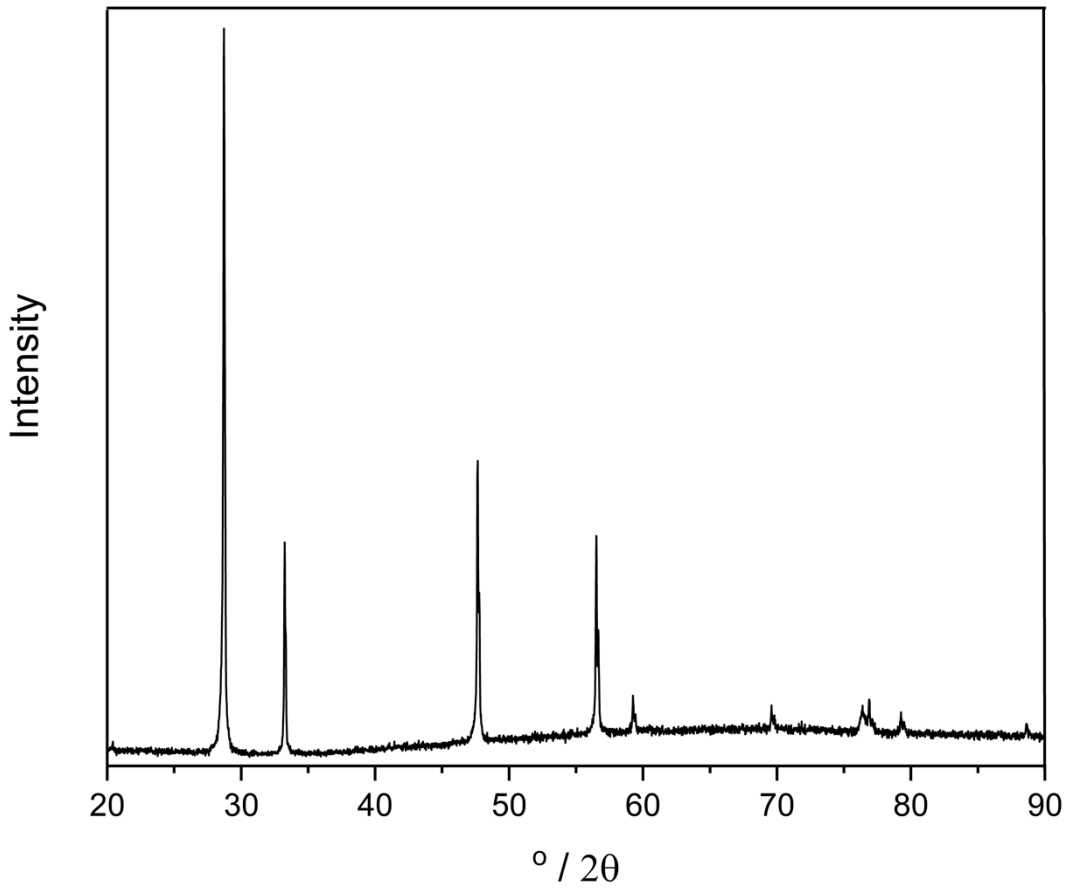

Figure 7.1. XRD patteren of $Ce_{0.84}Y_{0.16}O_{2.92}$

Typical impedance spectroscopy data are shown in Figure 7.2. The measurements were done between 150 – 506 ℃. A selection of data are shown which cover the full range of impedance response. The complex plane plot data (a and b) showed three main regions, between 300 – 379 ℃ at low, intermediate and high frequencies, while at 245 ℃ the high frequency region, and at 506 ℃ the low frequency region were outside the measurement window.

These regions were attributed to the bulk (b), grain boundary (gb) and sample electrode interface (el) with decreasing frequency. This is confirmed by capacitance values obtained from C` plots (c) for the same data sets. They show a high frequency plateau with an

approximate value 15 pF, an intermediate frequency plateau of approximate value 3 nF, and high frequency inflection of approximate value 400 μF.

The low frequency spike in (a) and high value of the sample-electrode capacitance (c) indicate that the sample is mainly an oxide-ion conductor. Presenting the 245°C data in Z``/M`` spectroscopic plots (d) showed a peak in Z`` and M`` which overlap at high frequency along with Debye-width at half maximum, FWHM, close to 1.14 decades indicating electrical homogeneity of the samples. At low frequency, there is a second peak in Z`` is related to the grain boundary.

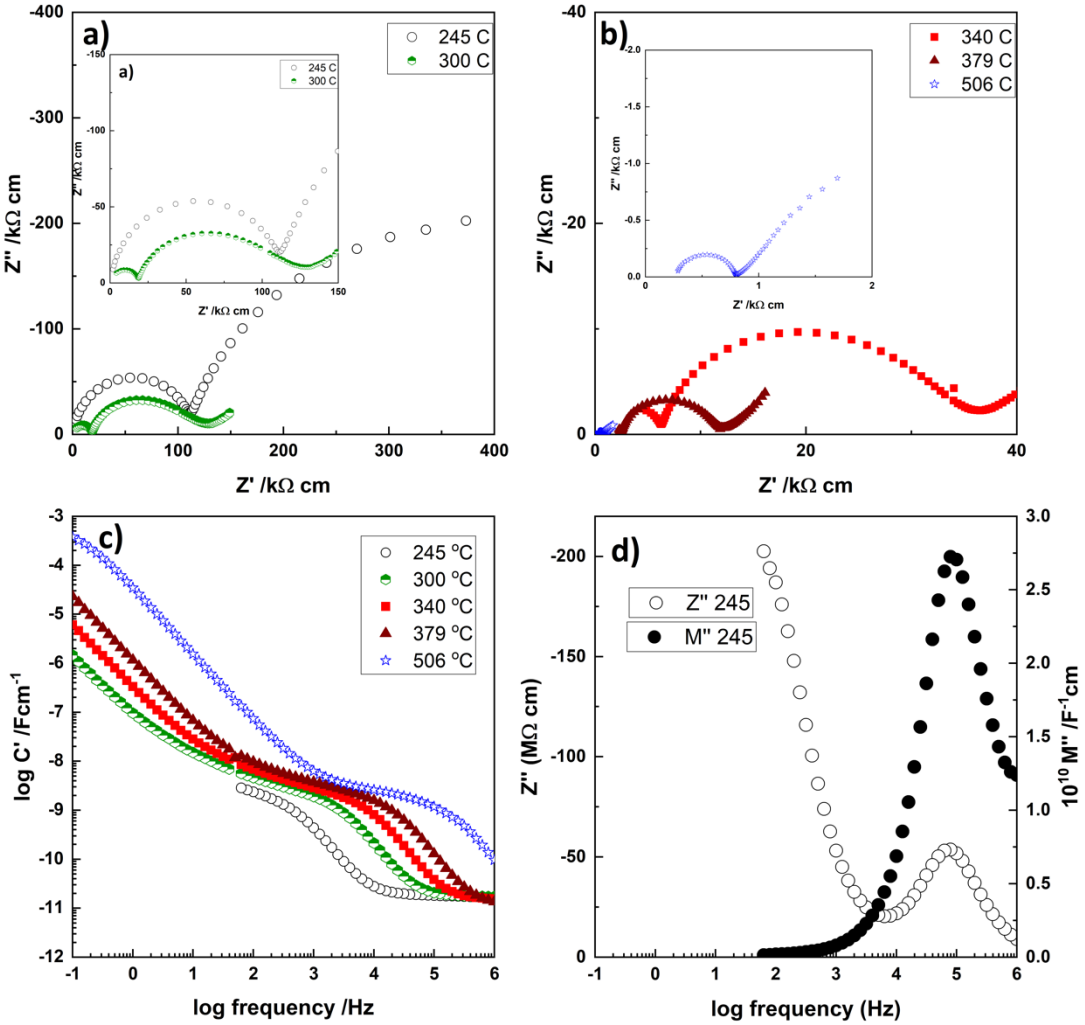

Figure 7.2. Impeance complex plane plots, Z at a) 245 and 300 °C, b) 340, 379 and 506 °C. c) C` spectroscopic plots at different temperatures. d) Z``/ M`` spectroscopic plots.*

Arrhenius plots of bulk, grain boundaries and total conductivities are shown in Figure 7.3, in which the conductivity values for each region were extracted from the intercepts of arcs on the Z` axis from data such as those in Figure 7.2a. The bulk conductivity is much larger than that

of the grain boundary and therefore the total conductivity is dominated by the gb conductivity. The bulk activation energy (0.83 eV) is smaller than that of the grain boundary (0.94 eV). This difference in activation energies indicates that the differences in the conductivity of the bulk and gb is probably due to the difference in the mobility of carriers as a consequence of small differences in structure or composition between the two regions.

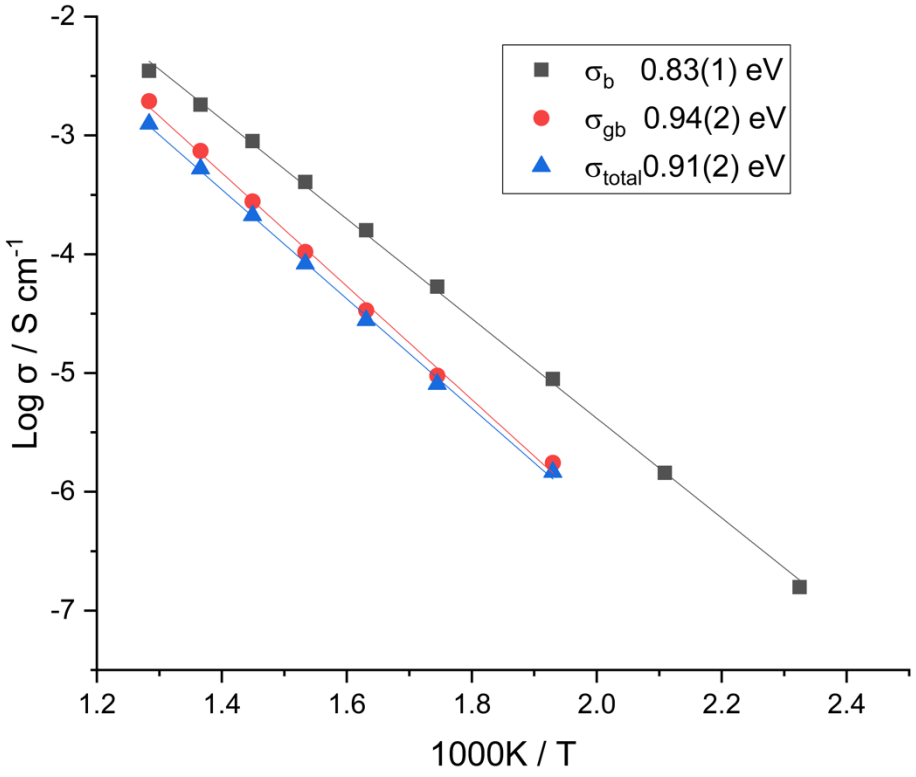

Figure 7.3. Arrhenius plot of bulk, grain bounderies and total conductivities of $Ce_{0.84}Y_{0.16}O_{2.92}$.

The effect of pO_2 on impedance data at 417 and 506 °C is shown in Figure 7.4. It shows that the sample conductivity was independent of pO_2 under these conditions. This indicates that the sample is at the electrolytic domain and mainly oxide-ion conductor at these temperatures, which is consistent with the data reported in [24]. Therefore, the level of oxide ion conductivity is insensitive to pO_2. Only, the sample-electrode interface conductivity decreased with decreasing pO_2, as shown by the dramatic decrease in Y` at low frequency (b and d) and also, the increase in size of the low frequency arc (a and c).

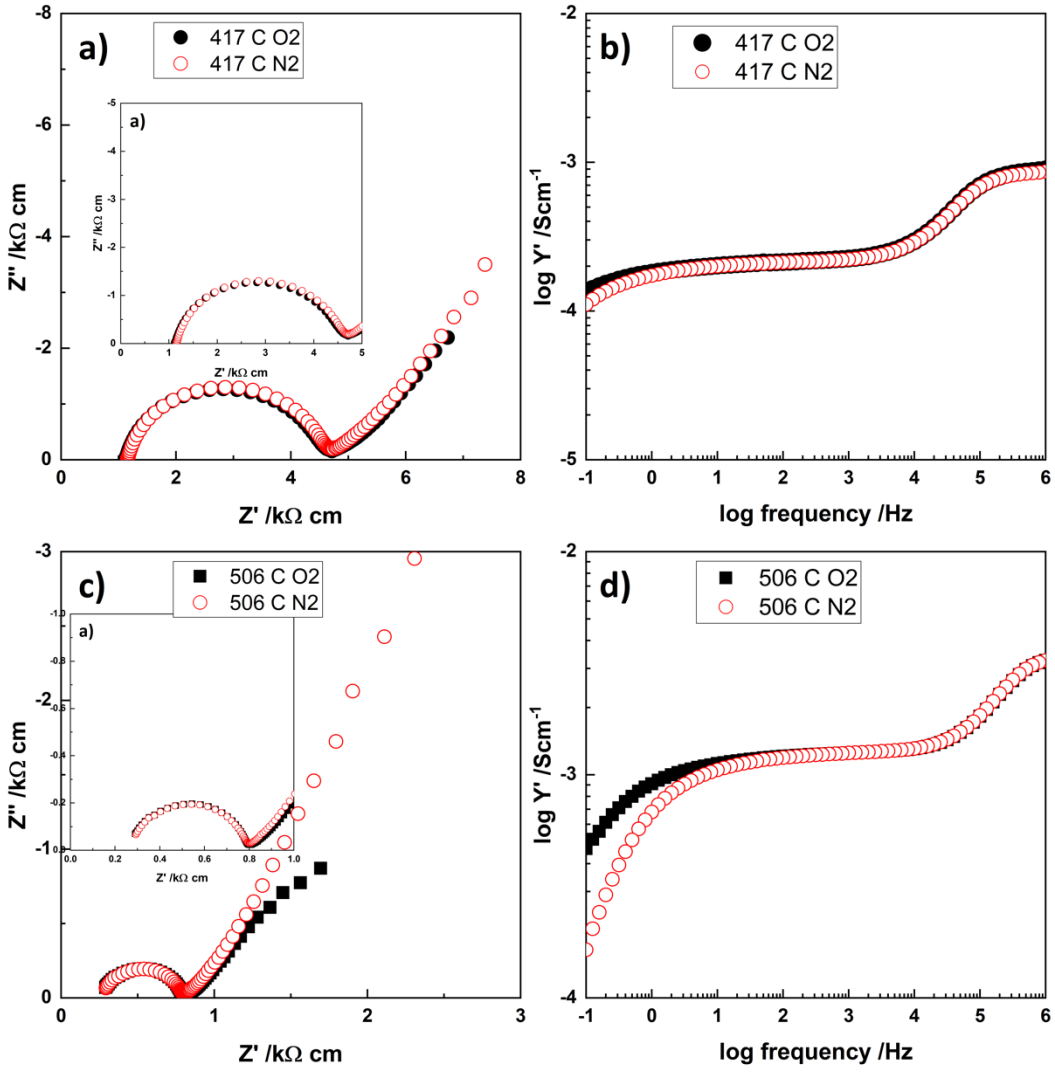

Figure 7.4. a) and c) impedance complex plane plots, b) and d) Y` spectroscopic plots of $Ce_{0.84}Y_{0.16}O_{2.92}$ measured at in O_2 and N_2 at different temperatures.

Further investigations of changing pO_2 with application of a small dc bias at the same time, on the sample impedance are shown in Figure 7.5. On application of 2 V, (a) the total resistance did not change in O_2 but slightly decreased in N_2. On increasing the voltage from 4 to 10 V, (b-d) the total resistance decreased in both atmospheres but the decrease became increasingly larger in N_2 with the voltage. So, on application of a small dc bias, both bulk and gb resistivities became pO_2-dependent in which the resistivity decreased more with decreasing pO_2. The resistivity dependence on pO_2 increased and became obvious with increasing the applied voltage. These results indicate that the electronic conductivity is induced by application of a small dc bias, similar to YSZ08 [15, 26].

The indication of intrinsic carriers, whether electrons or holes, was identified depending on the sample resistance whether it increased or decreased with changing pO_2. Since this material conductivity decreased more in N_2, the majority of carriers were n-type.

It is well known that YDC tends to lose oxygen at elevated temperatures and/ or in reduced atmosphere by the reaction (2) and this lead to reduction of Ce^{4+} to Ce^{3+}. Hence, the Ce^{3+} ions are regarded to be the main electrons carriers in this material.

It seems that as result of the existence of transition metal that can be easily reduced, the sample may lose oxygen easily even on application of a small bias (2 V). On application of higher voltage (< 6 V), the sample clearly loss more oxygen and level of n-type increased as the number of liberated electrons increased, similar to the observed behaviour in YSZ08 and YSH in which both materials show clear n-type response at higher voltages [1, 27].

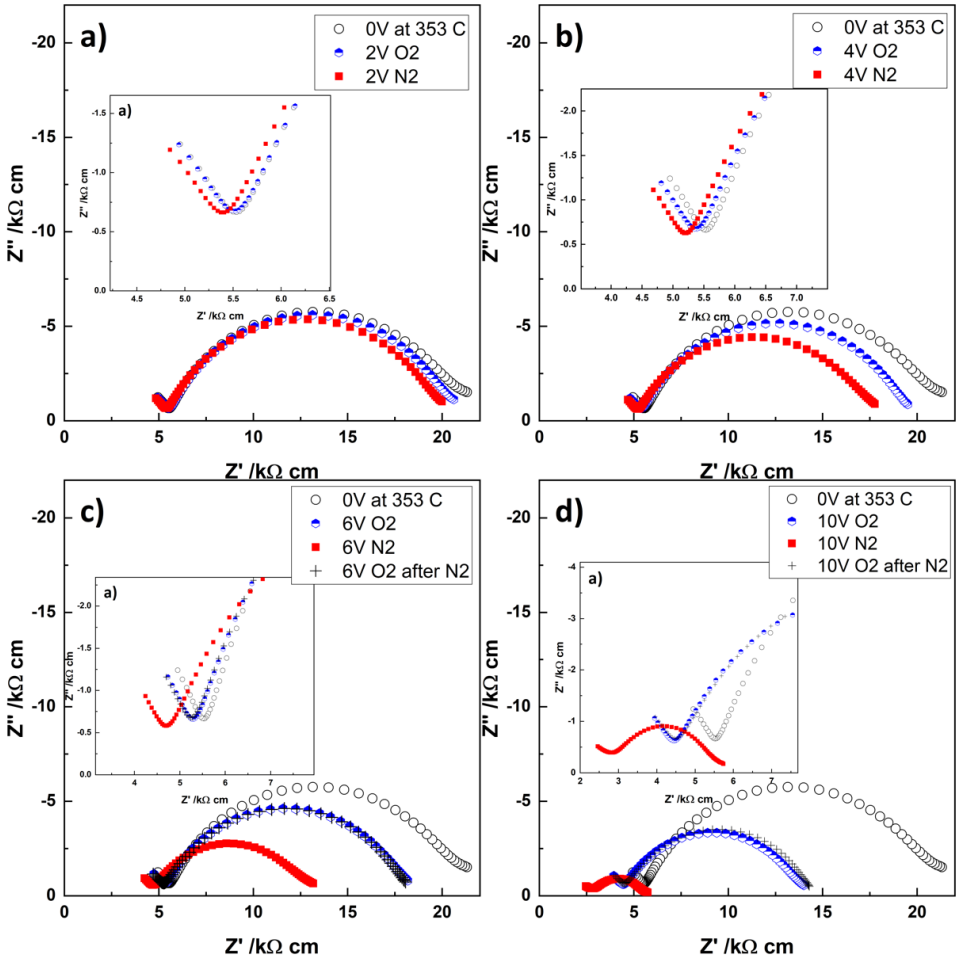

Figure 7.5. Impedance complex plane plots of $Ce_{0.84}Y_{0.16}O_{2.92}$ measured in different atmospheres on application of a) 2 V, b) 4 V, c) 6 V and d) 10 V, as noted beside each graph.

On application of an increased field, in N_2, the total resistivity of the sample decreased slightly until reaching 105 V/cm, the sample conductivity increased by about two orders of magnitude

(Figure 7.6 a). On decreasing the applied field, the high conductivity (ON) state was maintained until 55 V/cm and then the sample recovered its original conductivity (Figure 7.6 a). It is worth mentioning that the conductivity in the ON state increased slightly with decreasing applied field (104 – 65 V/cm) before starting to recover below 60 V/cm. This may indicate that the sample in the ON state is mainly n-type.

A further indication of pO_2 effect on RS behaviour is shown from the time dependence of the total conductivity in response to application of 118 and 155 V/cm at 366 ℃ in N_2 and air in (Figure 7.6). On application of 118 V/cm, (b) the conductivity in air increased slightly and then levelled off in OFF state. However, in N_2 the sample switched to the ON state, but very slowly in about 120 minutes. On application of 155 V/cm, (c) the sample switched to ON state rapidly in both N_2 and air over period 6-10 minutes, but additional time was required to switch in air. The highest ON state conductivity was seen in N_2. The time dependence of the dc bias removal results showed that the sample recovered its original conductivity rapidly with almost similar time for both air and N_2. These results indicate that the sample-oxygen exchange plays an important role in the enhancement of YDC conductivities during the application of the dc bias.

Furthermore, Figure 7.7 shows the impedance data in different formalisms before, during and after switching the sample by the application of 119 V/cm. The data were reversed to the original state after the removal of 119 V/cm indicating no crystallographic change, phase transition nor electrical damage that change the sample electrical properties.

The RS in YDC is clearly electronic in origin, and also different from those reported in unipolar and bipolar switching that required re-application of a bias voltage to recover their original conductivity. Also, YDS shows only one stable state in the absence of the applied bias, while RS associated with formation and rupturing of conduction filament shows two or multiple stable state.

Therefore, YDC is the third example, after Ca-doped BF and YSH, to show this kind of resistive switching behaviour. All cases show a reversible increase, with hysteresis, in the conductivity by few orders of magnitude in response to an application and removal of a small dc bias. All these materials are acceptor-doped and show different level of mixed oxide-ion and electronic conductivity. They have oxygen vacancies as main charge compensation mechanism. The main difference between these materials is the types of electronic

conductivities which are p-type in BCF and undergoes transition from p- to n-type in YSH while it is n-type in YDC.

The RS mechanism in YSH is attributed to the breakdown of the p-i-n junction in which the p and n-type conductivities created at the opposite electrodes in response to the application of the dc bias [1]. Whilst the RS mechanism in BCF is probably due to the creation of hole-conducting layer of O^- ions that initiated at positive electrode growing through the sample interior [2]. It shows no evidence of any introduction to n-type conductivity during or after the switching.

Unlike YSH, YDC did not show p-n transition in response to the application of an increasing bias, and was n-type at both low and high field. The presence of transition metal, that can be easily reduced (Ce^{4+} to Ce^{3+}), is the source of n-type conductivity. It is more likely that the RS mechanism in YSD is similar to BCF, but different in the carrier type and the source of the electronic conductivity.

A possible explanation for RS mechanism in YDC is that, on application of increasing bias, the sample loses oxygen at one electrode (eq 7.1), especially in atmospheres of low pO_2 and electrons produced in reaction (7.1) are injected at the opposite electrode. These electrons are most likely to be localised on Ce which can be reduced to Ce^{3+}. When these electrons distribute over large number of Ce, electron-conducting layer grows toward the opposite electrode. Once the conducting layer approach the opposite electrode and the carriers reach certain concentration, the carriers occupy a delocalised energy band, and therefore the sample conductivity increased by a few orders of magnitude. On the removal of the dc bias, electrons become more localised on Ce atoms and reaction (7.1) is displaced to the left hand side leading to the sample recovery.

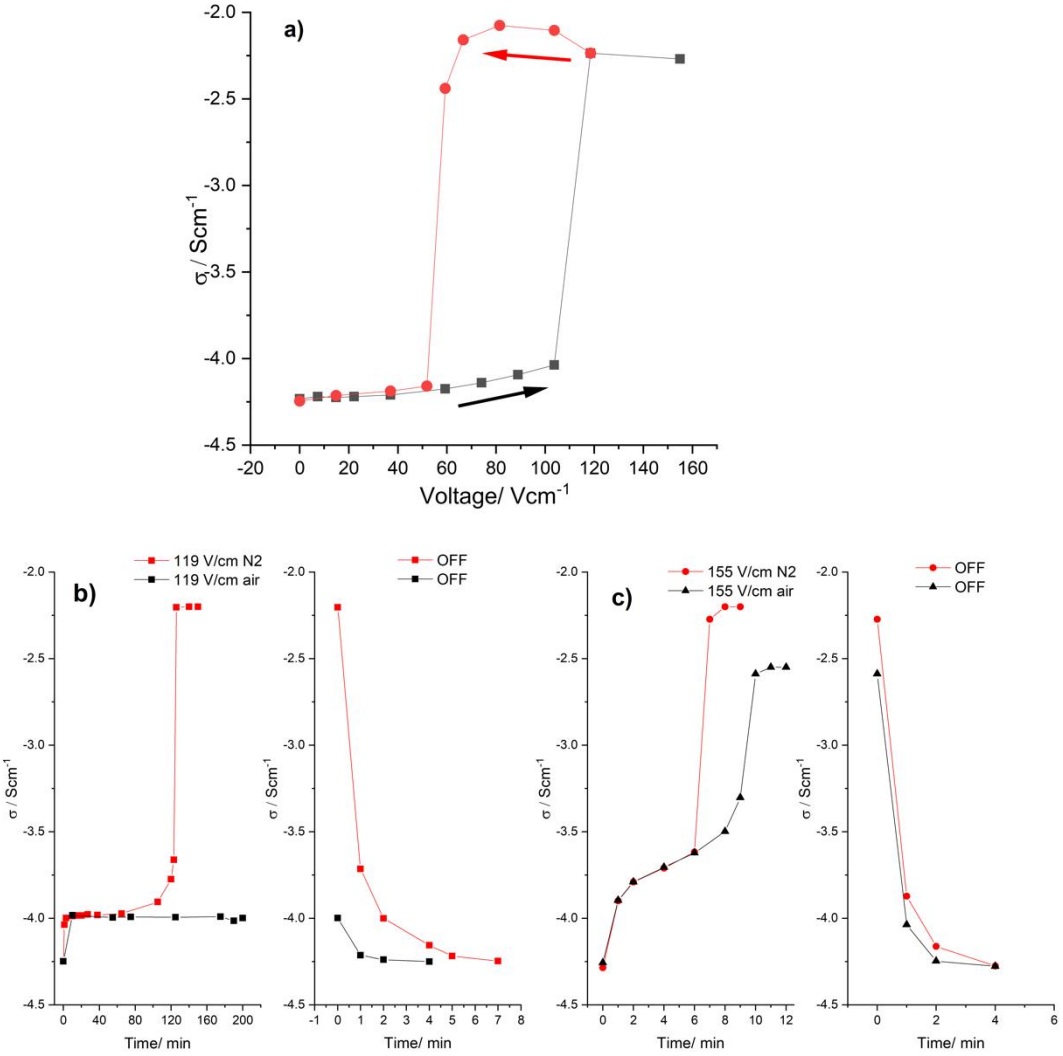

Figure 7.6. a) The total conductivity of $Ce_{0.84}Y_{0.16}O_{2.92}$ after reaching steady state vs applied voltage at 366 ℃. b) and c) the total conductivity of $Ce_{0.84}Y_{0.16}O_{2.92}$ vs time on applying and removing of 119 and 155 V/cm, respectively, at 366 ℃.

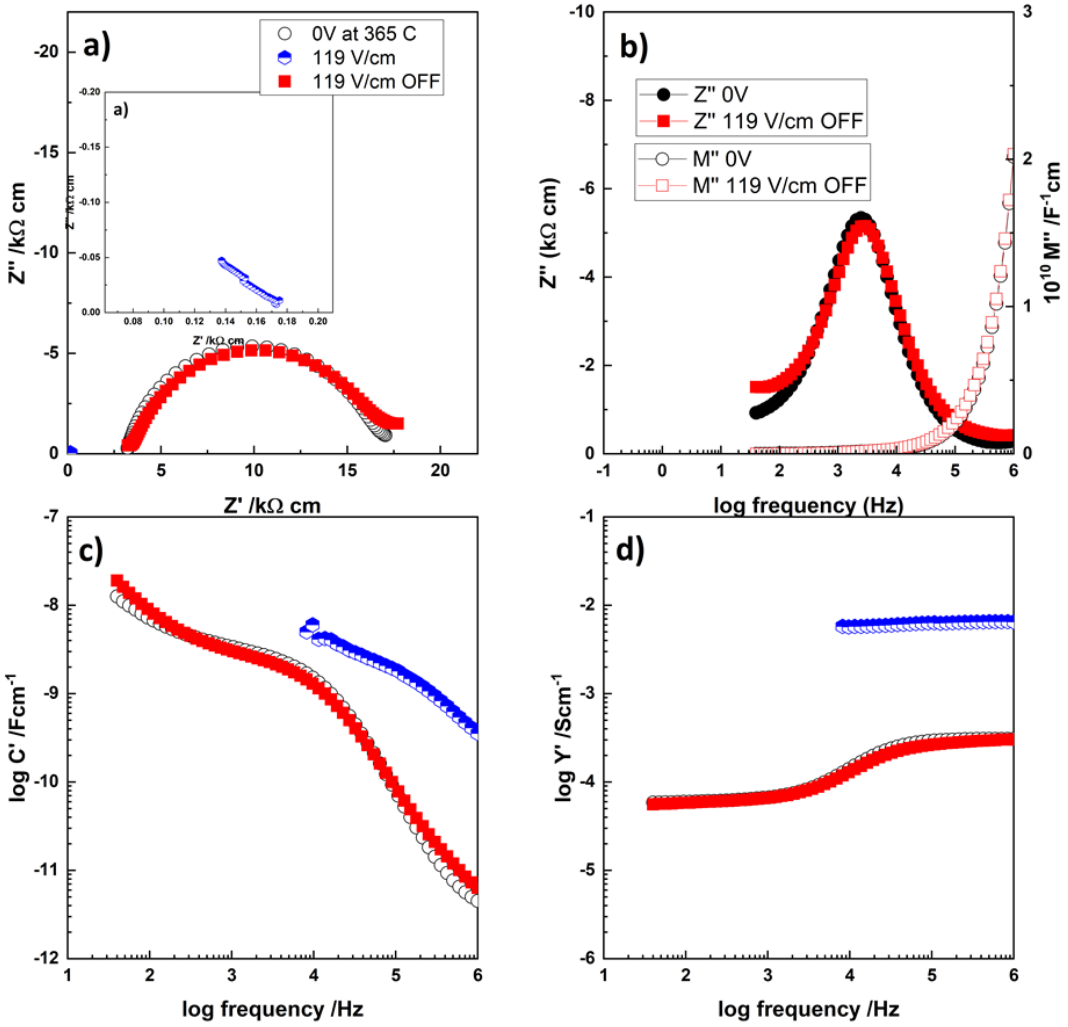

Figure 7.7. The impedance response, for $Ce_{0.84}Y_{0.16}O_{2.92}$, befor, during and after the appication of 119 V/cm

7.3. Conclusions

Single phase $Ce_{0.84}Y_{0.16}O_{1.92}$ was successfully synthesised by solid state reaction. The sample was primarily oxide-ion conductor and its conductivity was pO_2-independent at measured temperatures range (150-506 °C). Electronic conductivity was induced by applying a small dc bias. The sample resistivity decreased on application of small dc bias and the reduction increased with decreasing pO_2 indicating the introduction of n-type conductivity. The n-type conductivity introduced due to oxygen loss according to reaction (7.1) and therefore the reduction of Ce^{4+} to Ce^{3+}.

YDC is the third example to show low-field resistive switching. The sample conductivity increased reversibly by two orders of magnitude on application of a small dc bias. pO_2 plays an important role in RS behaviour. The increased conductivity is probably due to huge increase in n-type carriers as result of oxygen loss.

7.4. References

1. Alotaibi, M., F. Almutairi, and A.R. West, *Resistive-switching in yttria-stabilized hafnia ceramics.* Journal of the American Ceramic Society, 2022. **106**(2): p. 822-828.
2. Maso, N., H. Beltran, M. Prades, E. Cordoncillo, and A.R. West, *Field-enhanced bulk conductivity and resistive-switching in Ca-doped BiFeO3 ceramics.* Phys Chem Chem Phys, 2014. **16**(36): p. 19408-16.
3. Lee, J.S., S. Lee, and T.W. Noh, *Resistive switching phenomena: A review of statistical physics approaches.* Applied Physics Reviews, 2015. **2**(3).
4. Kumar, D., R. Aluguri, U. Chand, and T.Y. Tseng, *Metal oxide resistive switching memory: Materials, properties and switching mechanisms.* Ceramics International, 2017. **43**: p. S547-S556.
5. Sawa, A., *Resistive switching in transition metal oxides.* Materials Today, 2008. **11**(6): p. 28-36.
6. Panda, D. and T.-Y. Tseng, *Perovskite Oxides as Resistive Switching Memories: A Review.* Ferroelectrics, 2014. **471**(1): p. 23-64.
7. Kim, K.M., D.S. Jeong, and C.S. Hwang, *Nanofilamentary resistive switching in binary oxide system; a review on the present status and outlook.* Nanotechnology, 2011. **22**(25): p. 254002.
8. Choi, B.J., S. Choi, K.M. Kim, Y.C. Shin, C.S. Hwang, S.-Y. Hwang, S.-s. Cho, S. Park, and S.-K. Hong, *Study on the resistive switching time of Ti O 2 thin films.* Applied physics letters, 2006. **89**(1): p. 012906.
9. Lin, C.-Y., S.-Y. Wang, D.-Y. Lee, and T.-Y. Tseng, *Electrical properties and fatigue behaviors of ZrO2 resistive switching thin films.* Journal of The Electrochemical Society, 2008. **155**(8): p. H615.
10. Walz, F., *The Verwey transition-a topical review.* Journal of Physics: Condensed Matter, 2002. **14**(12): p. R285.
11. García, J. and G. Subías, *The Verwey transition—a new perspective.* Journal of Physics: Condensed Matter, 2004. **16**(7): p. R145.
12. Prades, M., N. Masó, H. Beltrán, E. Cordoncillo, and A.R. West, *Field enhanced bulk conductivity of BaTiO3 : Mg ceramics.* Journal of Materials Chemistry, 2010. **20**(25).
13. Masó, N. and A.R. West, *Electrical Properties of Ca-Doped BiFeO3 Ceramics: From p-Type Semiconduction to Oxide-Ion Conduction.* Chemistry of Materials, 2012. **24**(11): p. 2127-2132.
14. Zhang, Q.-L., N. Masó, Y. Liu, H. Yang, and A.R. West, *Voltage-dependent low-field resistivity of CaTiO3:Zn ceramics.* Journal of Materials Chemistry, 2011. **21**(34).
15. Masó, N. and A.R. West, *Electronic Conductivity in Yttria-Stabilized Zirconia under a Small dc Bias.* Chemistry of Materials, 2015. **27**(5): p. 1552-1558.
16. Gil Escrig, L., M. Prades, H. Beltrán, E. Cordoncillo, N. Masó, and A.R. West, *Voltage-Dependent Bulk Resistivity of SrTiO 3: Mg Ceramics.* Journal of the American Ceramic Society, 2014. **97**(9): p. 2815-2824.
17. Mogensen, M., N.M. Sammes, and G.A. Tompsett, *Physical, chemical and electrochemical properties of pure and doped ceria.* Solid state ionics, 2000. **129**(1-4): p. 63-94.
18. Xiong, Y., K. Yamaji, N. Sakai, H. Kishimoto, T. Horita, M.E. Brito, and H. Yokokawa, *Electronic conductivity of ZrO2–CeO2–YO1. 5 solid solutions in a wide range of temperature and oxygen partial pressure.* Journal of The Electrochemical Society, 2006. **153**(12): p. A2198.

19. Varvoutis, G., M. Lykaki, G.E. Marnellos, and M. Konsolakis, *Recent Advances on Fine-Tuning Engineering Strategies of CeO2-Based Nanostructured Catalysts Exemplified by CO2 Hydrogenation Processes.* Catalysts, 2023. **13**(2): p. 275.
20. Guo, X., S. Mi, and R. Waser, *Nonlinear Electrical Properties of Grain Boundaries in Oxygen Ion Conductors: Acceptor-Doped Ceria.* Electrochemical and Solid-State Letters, 2005. **8**(1).
21. Omar, S., E.D. Wachsman, J.L. Jones, and J.C. Nino, *Crystal Structure-Ionic Conductivity Relationships in Doped Ceria Systems.* Journal of the American Ceramic Society, 2009. **92**(11): p. 2674-2681.
22. Guo, X., W. Sigle, and J. Maier, *Blocking Grain Boundaries in Yttria-Doped and Undoped Ceria Ceramics of High Purity.* Journal of the American Ceramic Society, 2003. **86**(1): p. 77-87.
23. Tuller, H. and A. Nowick, *Defect structure and electrical properties of nonstoichiometric CeO2 single crystals.* Journal of The Electrochemical Society, 1979. **126**(2): p. 209.
24. Yang, F., X. Zhao, and P. Xiao, *Bulk conduction and relaxation in [(ZrO2) 1− x (CeO2) x] 0.92 (Y2O3) 0.08 (0≤ x≤ 1) solid solutions at intermediate temperatures.* Journal of Power Sources, 2011. **196**(11): p. 4943-4949.
25. Masó, N. and A.R. West, *Electronic conductivity in yttria-stabilized zirconia under a small dc bias.* Chemistry of Materials, 2015. **27**(5): p. 1552-1558.
26. Vendrell, X. and A.R. West, *Induced p-type semiconductivity in yttria-stabilized zirconia.* Journal of the American Ceramic Society, 2019. **102**(10): p. 6100-6106.
27. Jovaní, M., H. Beltrán-Mir, E. Cordoncillo, and A.R. West, *Field-induced pn transition in yttria-stabilized zirconia.* Scientific Reports, 2019. **9**(1): p. 18538.

Chapter 8 : Resistive Switching and Flash luminescence in Ca-doped $BiFeO_3$

8.1. Introduction

The recently-discovered flash sintering (FS) process is a novel densification technique for ceramics in which a ceramic sample is sintered under application of an electrical field over certain temperatures range in just few seconds. It is a promising technique which reduce the processing time and temperature dramatically and therefore energy consumption is reduced. The sintering process is accompanied by a dramatic increase in conductivity, power dissipation and light emission, known as flash event [1] [2].

The first material to be flash sintered was 3 mol % yttria stabilised zirconia in 2010 by the Raj group [3]. Since then many materials have been flashed sintered such as $BiFeO_3$ [4], $BaTiO_3$ [5], Al_2O_3 and 8YSZ [6]. The FS mechanism is still not well understood and the accompanied flash event is still debatable whether thermoluminescence or electroluminescence.

The accompanied increase in conductivity and flash luminescence in FS process might be related to each other and they may be attributed to the generation of electron-hole pairs. more recently, low field bulk resistive switching was reported in Ca-dope $BiFeO_3$ [7] and yttria stabilised hafnia [8] in which the material conductivity induced reversibly, OFF-ON, by several orders of magnitude on application of a small dc bias. Since the proposed mechanism for the resistive switching in these materials includes generation of carriers, holes and/ or electrons, there is a possibility that the ON state is accompanied by electroluminescence.

In this chapter, we investigate the possibility of flash luminescence in $Bi_{0.77}Ca_{0.23}FeO_3$ (BCF23) over wide range of temperatures under different pO_2.

8.2. Results and discussions

Two samples of BCF23 were processed in two different atmospheres, air and N_2. The sample conductivities were different in which the N_2-processed sample conductivity was several orders

of magnitude lower than air-processed sample with activation energy of 0.92 eV while the activation energy of air-processed sample is 0.67 eV (Figure 8.1 a). These results are consistent with those reported in chapter 4.

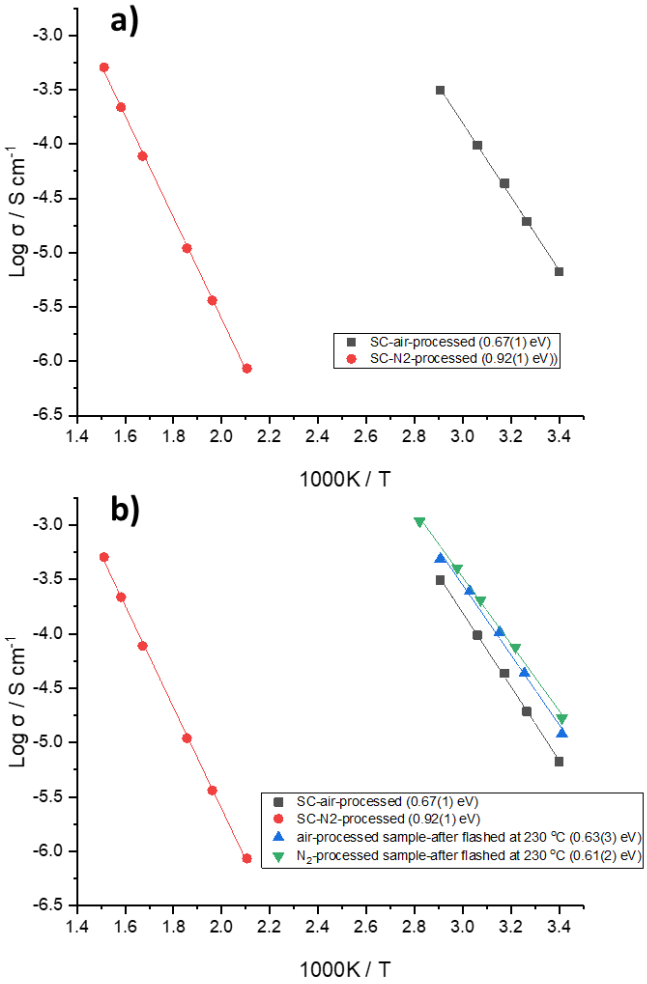

Figure 8.1. Arrhenius plots of BCF23, a) processed in different atmospheres, b) processed in different atmospheres before and after being flashed, as noted beside each graph.

The samples were attached to the conductive jig, placed inside the furnace and adjusted to allow visual inspection. The samples were First heated in air to 230°C. Then, electrical field of 198 V/cm, with limitation of maximum current density, J_{max}, to 61 mA/ mm^2, was applied to the samples. Snap shots were taken before, during and after the application of the electrical field.

For N_2-processed sample, the dc conductivity increased gradually with time before switching by 4-5 orders of magnitude, ON state, after 9 minutes (Figure 8.2 a). The sample was luminescing in the ON state for a while and then the luminesce disappeared after about 1 minute

(Figure 8.2 a). The luminescence cannot be seen before or during the application of the electrical field until the sample switch to the ON state.

The initial resistivity of air-processed sample was much lower than N_2-processed sample at 230 ℃, typically 5 Ω cm. On the application of 198 V/cm, the sample conductivity showed slight increase and then levelled off Figure 8.2 b. The sample required just few seconds to luminesce and the whole sample was luminescing within about 2 minutes after the application of the electrical field.

These results show that the sample with high initial resistance required first to switch to the ON state in order to luminesce and therefore it took about 9 minutes to luminesce. Since the air-processed sample is already in ON state at 230 ℃, the sample start to luminesce just few seconds after the application of the electrical field. Therefore, the sample resistive switching and their flash luminescence might be somehow connected to each other and the sample needs to be in highly conductive state to luminesce in an electrical field.

The Arrhenius plots of both samples after flashing at 230 ℃ (Figure 8.1 b) show that the conductivities of both samples increased and were comparable with similar activation energies. The activation energies of both samples after flashing were similar to the activation energy of air-processed samples before flashing.

After that one sample was used to see the effect of temperature and pO_2 on flash event. The sample luminesced over wide range of temperatures, typically from 200 to 915 ℃ (Figure 8.3). Clearly at all temperatures the flash event starts from the top electrode to the bottom electrode (i.e. from the negative electrode to the positive electrode). At temperatures below 200 ℃, no flash events were seen on application 198 V/cm with J_{max}=1200 mA. Also, at the higher temperatures (> 200 ℃) the flash luminescence appeared on application of 198 V/cm only if the $J_{max} \geq 1000$ mA (~ 50 mA/ mm^2).

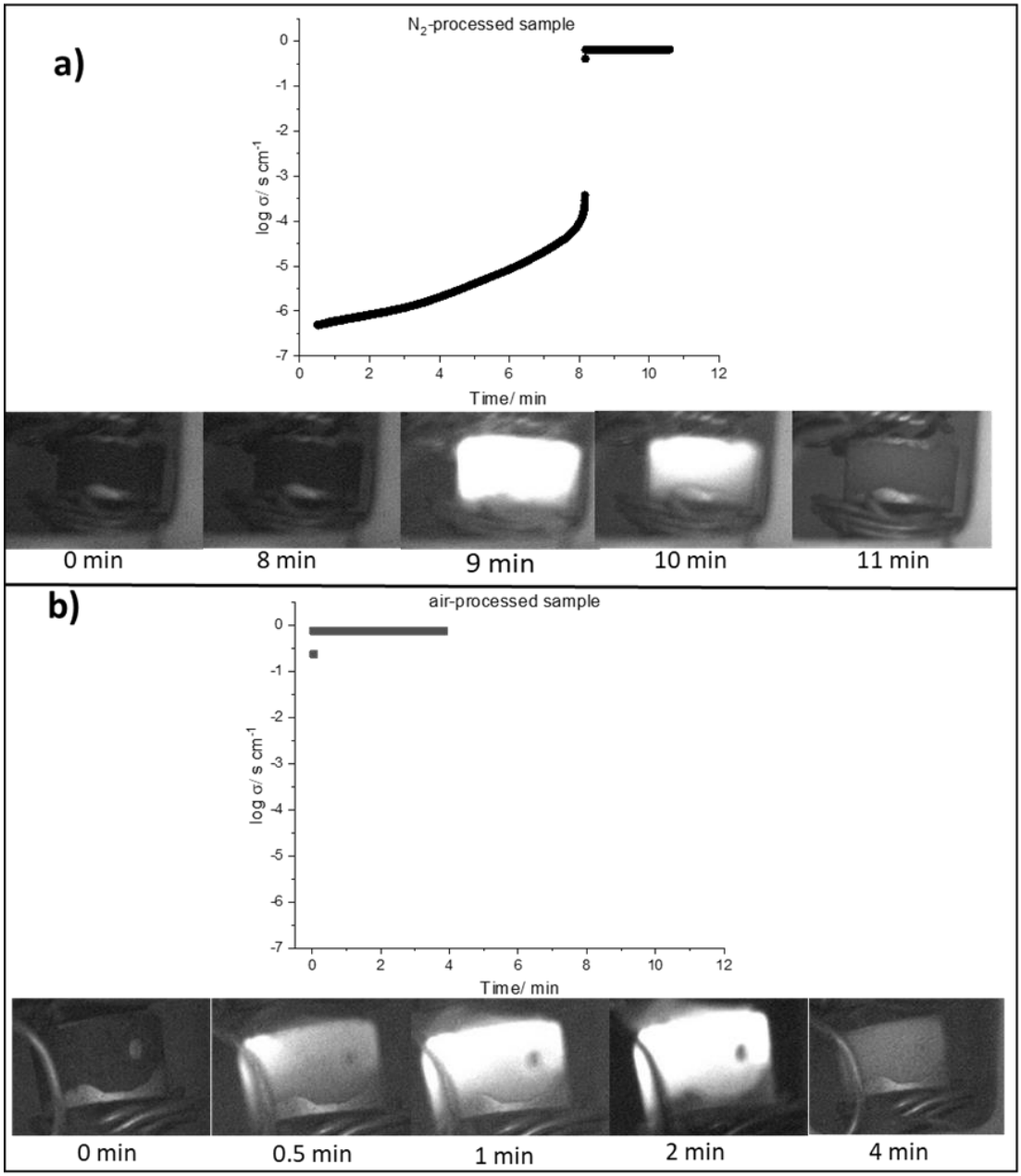

Figure 8.2. The effect of application of 198 V/cm on the conductivities of N_2-processed sample (a), and air-processed sample (b) at 230 ℃, with inclusion of snap shots of the samples before and during the electrical field application.

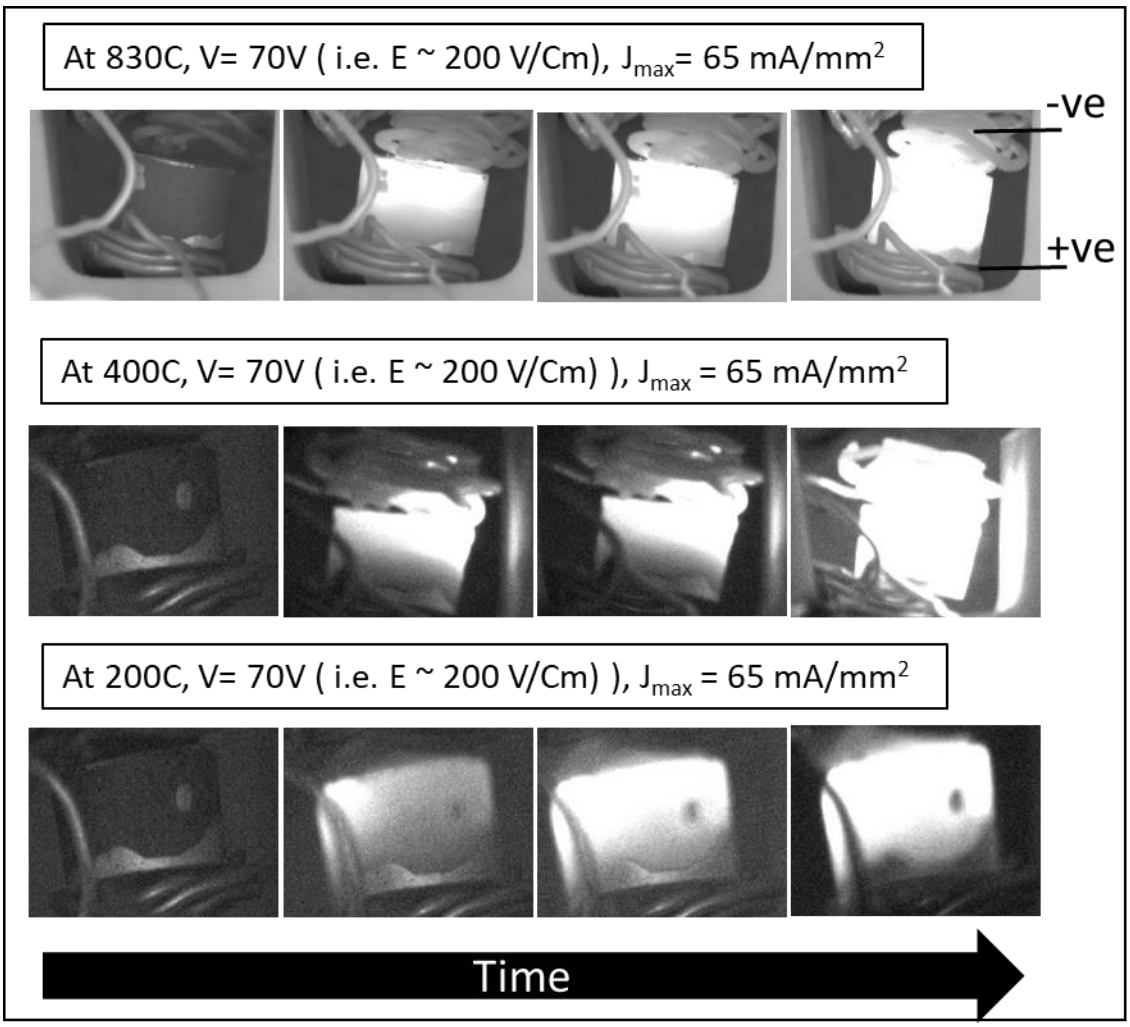

Figure 8.3. Snap shots of BCF23 processed in air on application of 198 V/cm at different temperatures, as noted above each graph.

Figure 8.4 shows the effect of heating and subsequent cooling from 790 to 945 ℃ and from 945 to 760 ℃, respectively, on the flash event. On application of 198 V/cm, the sample luminesced at 790 ℃ (b). With increasing the temperature (b), the sample maintained the same level of flashing until about 820 ℃ and then, the flash luminescence started to decay until trapped at the top electrode at 945 ℃. With decreasing the temperature (c), the flash luminescence started to recover until the whole sample flashed again below 840 ℃. This result indicates that the flash probably is not thermo-luminescence since the flash vanished at the highest temperature. Of course, the temperature is crucial and the flash starts to disappear at temperatures higher than 840 ℃ and this attributed to that the sample may lose the flash mechanism at these temperatures.

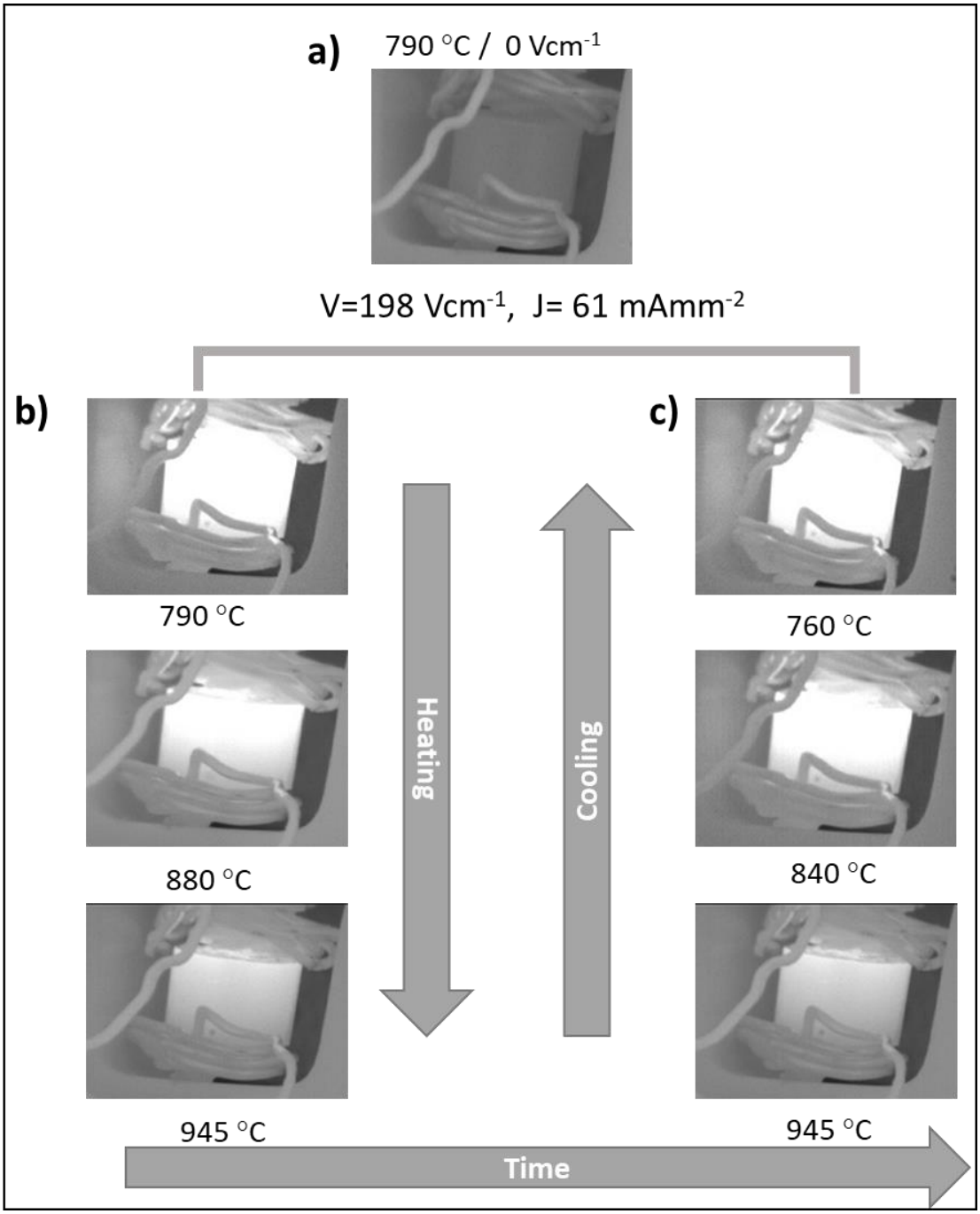

Figure 8.4. The effect of the temperature on the flash event: a) Photo of BCF23 Pellet attached to the conductive jig and placed in the furnace at 790 ℃ before applying the electrical field. Snap shots of the sample after applying 198 V/cm at different temperatures on heating, b) and on cooling, c).

It is reported that the conduction properties of this material vary from oxide-ion conduction to p-type semiconduction with increasing pO_2 during the processing and subsequent cooling [9]. At temperature around 800 ℃, the sample should be in equilibrium with the atmosphere and therefore the conductivities of the samples processed in air, O_2 and N_2 should be comparable. The equilibrium is not likely to be fully maintained on cooling in atmosphere of high pO_2

leading to various oxygen stoichiometry and therefore, the hole conduction arises according to the following reaction:

$$V_O^{\bullet\bullet} + \frac{1}{2}O_2 \rightarrow O_O^x + 2h \qquad (8.1)$$

At the equilibrium, the sample is mainly oxide-ion conductor while the sample absorbs small amount of oxygen on cooling in high pO_2 and becomes p-type semiconductor. On heating above equilibrium temperature, ~ 800 ℃, the sample can either maintain the oxygen stoichiometry or lose oxygen similar to many oxides at high temperatures and therefore, electron conduction is introduced. In both possibilities, it is less likely that the sample has hole conduction arising from reaction (8.1).

The change in conduction properties of BCF is fully reversible with changing pO_2 at temperature above 800 ℃. Therefore, studying the effect of pO_2 on flash event at higher temperature, e.g. 870 ℃, could indicate the importance of oxygen exchange between the sample and the atmosphere and especially the p-type conductivity in the mechanism of flash luminescence.

Figure 8.5 shows the effect of changing pO_2 on flash event at 870 ℃. The sample showed no luminescence before application (a) or after removal (c) of the electrical field. On the application of 198 V/cm in N_2 atmosphere (b), the sample initially luminesced in less than 1 minute and then the luminescence started to decay until almost vanished after 4 minutes. On changing the atmosphere form N_2 to air without removing the field (b), the sample luminesced again within 2 minutes. Switching the atmosphere back to N_2, the luminescence started to decay until it vanished completely after 6 minutes. These results give a good indication of that the level of p-type conductivity plays important role in the flash mechanism; when the level of p-type conductivity decreases the flash starts to decay until it disappears after sufficient time in the atmosphere of low pO_2.

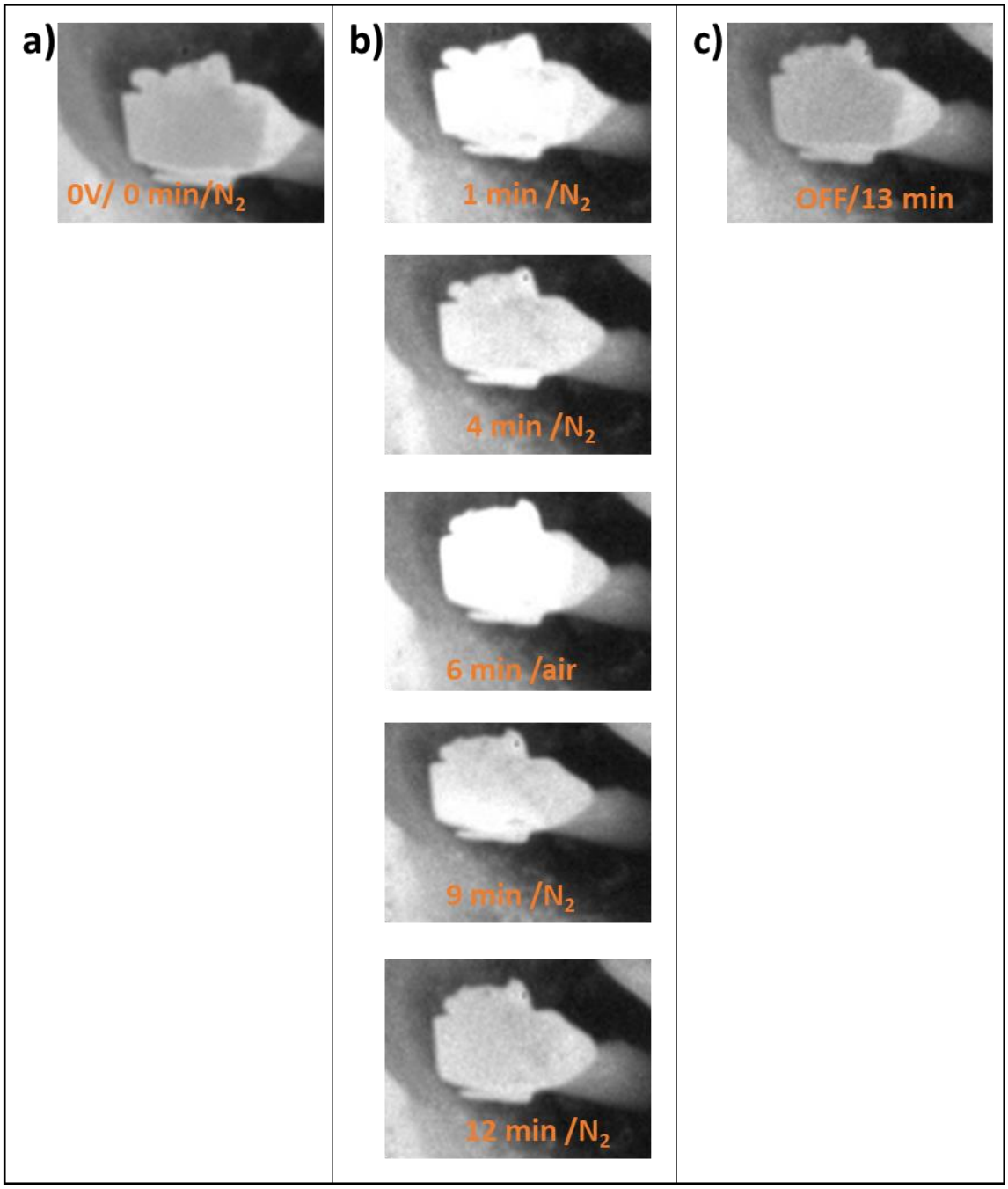

Figure 8.5. The effect of pO_2 on the flash event at 870 ℃ in BCF23: a) the sample before applying the electrical field, b) snap shots of the sample in different atmospheres, on application of 198 V/cm, c) the sample after the electrical field removal.

Two samples of BCF23 processed in air and N_2 showed luminescence during the application of an electrical field at different temperatures. The samples luminesce when they are in the high conductive state. The samples lose luminescence on either increasing the temperature above 880 ℃, or decreasing pO_2 at temperature above the equilibrium temperature, > 800 ℃. These results indicate that the light emission is probably electroluminescence due to hole-electron recombination.

The hole conduction arises in this material spontaneously from absorbing small amount of oxygen, on cooling in high pO_2 atmosphere (eq 1) [9]. Also, the p-type conductivity increases by application of a small dc bias in which holes are created in the sample interior by ionisation and trapping process [7]. It is believed that the source of holes is singly-ionised oxygen, as O^- ions. Similar induced hole conductivity has been observed in different acceptor-doped materials, such as yttria-doped zirconia (YSZ) [10, 11], yttria-doped hafnia [8] and Mg-doped barium titanate [12], in which the holes are created according to the reaction:

$$O^{2-} \rightarrow O^- + e^- \qquad (8.2)$$

The liberated electrons in reaction (8.2) are either trapped at positive electrode similar to the charging of a capacitor or react with oxygen molecules and form reduced oxygen species. The third possibility is that the released electrons are re-injected at the negative electrode through the external circuit [7, 8, 13, 14]. It is difficult to determine the trapping mechanism at this stage and one or more of these possibilities may occur.

Since the luminescence reported here was sensitive to the electronic conductivity level rather than the temperature and disappears at the highest temperature, it is more likely to be electroluminescence that arises from electron-hole recombination. The holes are already created in the sample as discussed above, and the possible source for the electrons is the injection of liberated electrons in reaction (8.2) at the negative electrode since the luminescence events reported here started from the negative electrode growing toward the positive electrode.

8.3. Conclusion

New flash electroluminescence is reported in two samples of $Bi_{0.77}Ca_{0.23}FeO_3$ processed in air and N_2. Switching the sample to high conductive state, ON state is accompanied by flash luminescence under certain conditions. Both air- and N_2- processed samples luminesced over wide range of temperatures, 200- 870 ℃. The flash event is attributed to recombination of electron-hole. Therefore, the flash luminescence was sensitive to the level of p-type conductivity. Since this material mainly is oxide-ion conductor at equilibrium, > 800 ℃ or on cooling in N_2, the luminescence stops on either increasing the temperature above 880 ℃ or decreasing pO_2 at temperature above the equilibrium temperature.

8.4. References

1. Biesuz, M. and V.M. Sglavo, *Flash sintering of ceramics.* Journal of the European Ceramic Society, 2019. **39**(2-3): p. 115-143.
2. Yu, M., S. Grasso, R. Mckinnon, T. Saunders, and M.J. Reece, *Review of flash sintering: materials, mechanisms and modelling.* Advances in Applied Ceramics, 2017. **116**(1): p. 24-60.
3. Cologna, M., B. Rashkova, and R. Raj, *Flash sintering of nanograin zirconia in< 5 s at 850 C.* Journal of the American Ceramic Society, 2010. **93**(11): p. 3556-3559.
4. Perez-Maqueda, L.A., E. Gil-Gonzalez, A. Perejon, J.M. Lebrun, P.E. Sanchez-Jimenez, and R. Raj, *Flash sintering of highly insulating nanostructured phase-pure BiFeO3.* Journal of the American Ceramic Society, 2017. **100**(8): p. 3365-3369.
5. M'Peko, J.-C., J.S. Francis, and R. Raj, *Field-assisted sintering of undoped BaTiO3: Microstructure evolution and dielectric permittivity.* Journal of the European Ceramic Society, 2014. **34**(15): p. 3655-3660.
6. Kok, D., S.K. Jha, R. Raj, and M.L. Mecartney, *Flash sintering of a three-phase alumina, spinel, and yttria-stabilized zirconia composite.* Journal of the American Ceramic Society, 2017. **100**(7): p. 3262-3268.
7. Maso, N., H. Beltran, M. Prades, E. Cordoncillo, and A.R. West, *Field-enhanced bulk conductivity and resistive-switching in Ca-doped BiFeO3 ceramics.* Phys Chem Chem Phys, 2014. **16**(36): p. 19408-16.
8. Alotaibi, M., F. Almutairi, and A.R. West, *Resistive-switching in yttria-stabilized hafnia ceramics.* Journal of the American Ceramic Society, 2022. **106**(2): p. 822-828.
9. Masó, N. and A.R. West, *Electrical Properties of Ca-Doped BiFeO3 Ceramics: From p-Type Semiconduction to Oxide-Ion Conduction.* Chemistry of Materials, 2012. **24**(11): p. 2127-2132.
10. Masó, N. and A.R. West, *Electronic Conductivity in Yttria-Stabilized Zirconia under a Small dc Bias.* Chemistry of Materials, 2015. **27**(5): p. 1552-1558.
11. Jovani, M., H. Beltran-Mir, E. Cordoncillo, and A.R. West, *Atmosphere- and Voltage-Dependent Electronic Conductivity of Oxide-Ion-Conducting Zr(1-x)Y(x)O(2-x/2) Ceramics.* Inorg Chem, 2017. **56**(12): p. 7081-7088.
12. Prades, M., N. Masó, H. Beltrán, E. Cordoncillo, and A.R. West, *Field enhanced bulk conductivity of BaTiO3 : Mg ceramics.* Journal of Materials Chemistry, 2010. **20**(25).
13. Vendrell, X. and A.R. West, *Induced p-type semiconductivity in yttria-stabilized zirconia.* Journal of the American Ceramic Society, 2019. **102**(10): p. 6100-6106.
14. Guo, M., N. Maso, Y. Liu, and A.R. West, *Electrical Properties and Oxygen Stoichiometry of Ba(1-x)Sr(x)TiO(3-delta) Ceramics.* Inorg Chem, 2018. **57**(1): p. 64-71.

Chapter 9 : Conclusions and Future work

9.1. Conclusions

Compositions of $Bi_{1-x}Ca_xFeO_{3-x/2}$ (where: x = 0, 0.23, 0.3 and 0.4) were synthesised by solid state reaction. Single phase samples were obtained. The rhombohedral distortion of the perovskite structure of BF was stabilised towards cubic by Ca^{2+} doping. Since the higher valence Bi^{3+} was substituted with the lower valence Ca^{2+}, the charge neutrality was maintained by creation of oxygen vacancies. The samples were processed in different atmospheres, air, O_2 and N_2.

The electrical properties of all compositions were analysed intensively using impedance spectroscopy. The electrical properties of doped samples were sensitive to pO_2 during processing and subsequent cooling. The conductivities decreased by few orders of magnitude and their properties changed from p-type semi-conduction to oxide-ion conduction with decreasing pO_2. N_2-processed samples were insulators at RT with activation energies about 0.90 eV while air- and O_2-samples were semiconductors with activation energies about 0.60 eV.

The variation of electrical properties is attributed to the presence of oxygen vacancies which can absorb oxygen by dissociation and ionisation process leading to variable oxygen content, given by the general formula $Bi_{1-x}Ca_xFeO_{(3-x/2)+\delta}$. Thus, if the samples are processed in high pO_2, they absorb oxygen and δ increases ($\delta > 0$) leading to hole creation and the observed p-type conductivity. The holes are believed to be located on underbonded oxygen as O^- ions. By contrast, if they are processed in N_2, they are oxygen stoichiometric (i.e. $\delta \sim 0$) and therefore, are oxide ion conductors.

The effect of changing pO_2 on the electrical properties of doped samples was seen during the impedance measurements in N_2-processed samples. The sample conductivities enhanced by 1-2 orders of magnitude and became mixed p-type/ and oxide ion conductors by increasing pO_2. The effect increased with increasing temperature and Ca^{2+} content (i.e. with increasing oxygen vacancy concentration).

Different formalisms of impedance data were dominated by the bulk response for all doped compositions processed in different atmospheres. However, good fitting was obtained only when a series or a parallel component was added to those usually used to fit bulk response (i.e.

parallel R-CPE-C). Different circuits were fitted in order to find the best equivalent circuit. It was found that the partial circuit C (i.e. parallel R_1-CPE_1-C_1 in series with parallel R_2-C_2) is the most logical circuits for air-, O_2-procesd samples and for N_2-processed samples at low temperatures in which R_1 and C_1 attributed to the bulk resistivity and capacitance, respectively and R_2 and C_2 are attributed to grain boundaries resistivity and capacitance, respectively. CPE_3 was added in series with circuit C, the complete circuit F, to fit sample-electrode interface response in N_2-processed samples at high temperature (> 200°C).

The bulk conductivities of doped samples enhanced considerably on application of small dc bias (3-20 V). The samples switched their resistances reversibly, ON-OFF, by 2-5 orders of magnitude. The required voltage to switch the samples was dependent on temperature. As the applied voltage and/ or the temperature increased, the sample switched faster. The Arrhenius plots of the sample conductivities in ON state showed a small temperature-dependence over wide range of temperatures. Also the ON state conductivities were voltage-independent. Therefore, the samples were in new steady state situation.

Air-processed samples were switched over limited temperature, < 100 °C, since their initial resistivities were much lower than those of N_2-processed samples. RS behaviour for air processed samples was pO_2-indpendent. N_2-processed samples were switched at temperatures above 200 °C and they switch faster in atmospheres of high pO_2. Since RS behaviour was independent of pO_2 or induced further with increasing pO_2, it is believed that the switching mechanism is not associated with oxygen loss at high voltages and the conductivities were p-type during switching. Therefore, the mechanism of resistive switching is attributed to huge increase in hole concentration by internal ionisation of redox active elements, which are believed to be underbonded oxygen, and trapping of the ionised electrons at the positive electrode (anode).

Also, the ionised electrons may react with oxygen molecules, especially in atmospheres of high pO_2 at high temperature, > 150 °C, causing them to reduce and dissociate by redox reaction and therefore they can be absorbed by lattice oxygen vacancies acting as another source of holes. Another possibility is that the released electrons may diffuse through the external circuit and re-injected at the negative electrode (cathode).

The evidence of electrons re-injection at the cathode was seen in chapter 8 in which under certain conditions, switching of BCF23 to high conductive state is accompanied by

electroluminescence due to electron-hole recombination starting from the cathode toward the anode. The flash luminescence was sensitive to the level of p-type conductivity. Since this material mainly is oxide-ion conductor at equilibrium, > 800 ℃ or on cooling in N_2, the luminescence stops on either increasing the temperature above 880 ℃ or decreasing pO_2 at temperature above the equilibrium temperature.

Finally, RS phenomenon was observed in new acceptor-doped material which is Y-doped CeO_2, $Ce_{0.84}Y_{0.16}O_{1.92}$. The sample conductivity increased reversibly by two orders of magnitude on application of a small dc bias. It is well-known mixed n-type and oxide ion conductors. The pO_2 plays an important role in RS behaviour. The sample conductivity induced by an application of a small dc bias and this induction increased in atmospheres of low pO_2 indicating the n-type conductivity. The sample was n-type at both low and high field. The presence of transition metal, that can be easily reduced (Ce^{4+} to Ce^{3+}), is the source of n-type conductivity. Therefore, the increase in conductivity is probably due to huge increase in n-type carriers as result of oxygen loss.

9.2. Future work

Recently, Y-rich-doped zirconia and Y-doped hafnia show that the conductivity undergoes change from p-type to n-type at voltage > 2.4 V. First, at the low voltage the p-type conduction is generated at the anode by ionisation and trapping process discussed above. Second, at higher voltage, oxygen is liberated at the anode and the released electrons are injected at the cathode leading to n-type behaviour.

Although, in general, it is possible that samples may start to decompose as result of oxygen loss and therefore, the reversibility may be partially lost on removing the bias, the conductivity of BCF was fully reversed to its original state on removing the bias, indicating no decomposition occurred in the sample.

The switching behaviour, especially for air-processed samples, was independent of pO_2 and N_2-processed samples were switching faster in O_2, indicating no oxygen loss during the switching and the increase in conductivity is probably due to huge increase in hole concentration. However, flash luminescence results demonstrate the possibility of electron re-injection at the anode. Therefore, it is expected that the reactions occurring are very probably different at the two electrodes. Also, the splitting of M" peak during the recovery of N_2-

processed samples indicating that the change is growing process and starting from one or both electrodes toward the sample interior.

In reality, one or other of these processes may dominate in response to a dc bias or both might occur. Some reactions might be important in one material but not in another material. Some of them may dominate at one electrode and others might dominate at the other electrode. The effect of dc bias on electrical properties was studied, so far, using two terminal impedance measurements. The problem with two terminal impedance is that we cannot separate them and only, the overall effect can be seen.

Therefore, 3-terminal impedance measurements are needed in order to separate the effects of pO_2 and dc bias at the two electrode-sample interfaces. These are the objectives of the next stage of the project.

Since the change of N_2-processed samples was more gradual over time and samples split into two components during switching and, especially, recovery, trying to fit them to two bulk elements to assess their volume fractions and how they change with time could provide better understanding to the OFF-ON mechanism.

In chapter 8, the sample of Ca-doped $BoFeO_3$ showed electroluminescence due to electron-hole recombination after switching the sample to high conductive state under certain conditions. The sample stopped luminescence at high temperature (~ 945 ℃) or in N_2-atmosphere at temperature above 800 ℃ Since it loses the flash mechanism under these conditions and become mainly oxide-ion conductor losing the hole conductivity. Also, the sample may start to lose oxygen and become mainly n-type conductor especially at highest temperature and on application of a dc bias. To investigate this conclusion, the sample may be quenched from high temperature under these conditions and its impedance response compared with those processed in air, O_2 and N_2.